DESIGN AND CONTROL OF PEM FUEL CELL-BATTERY-HYBRID ENERGY SYSTEM FOR LOCOMOTIVE APPLICATIONS

Upasana Sarma

DESIGN AND CONTROL OF PEM FUEL CELL-BATTERY-HYBRID ENERGY SYSTEM FOR LOCOMOTIVE APPLICATIONS

Thesis submitted to
Indian Institute of Technology, Guwahati
for the award of the degree

of

Doctor of Philosophy

by

Upasana Sarma
(166102003)

under the guidance of

Dr. Sanjib Ganguly

DEPARTMENT OF ELECTRONICS AND ELECTRICAL ENGINEERING
INDIAN INSTITUTE OF TECHNOLOGY, GUWAHATI
MAY 2021

Dedicated to

My family

Department of Electronics and Electrical Engineering
Indian Institute of Technology, Guwahati
Guwahati, India 781039.

CERTIFICATE

This is to certify that this thesis entitled “**Design and Control of PEM Fuel Cell-Battery-Hybrid Energy System for Locomotive Applications**,” submitted by **Upasana Sarma** (166102003) to Indian Institute of Technology Guwahati is a record of bona fide research work under my supervision and I consider it worthy of consideration for the award of the degree of Doctor of Philosophy of the Institute.

(Supervisor)
Dr. Sanjib Ganguly
Department of Electronics and Electrical Engineering
Indian Institute of Technology Guwahati
Guwahati, India-781039

Declaration

I certify that

a. The work contained in this thesis is original and has been done by me under the guidance of my supervisor.

b. The work has not been submitted to any other Institute for any degree or diploma.

c. I have followed the guidelines provided by the Institute in preparing the thesis.

d. I have conformed to the norms and guidelines given in the Ethical Code of Conduct of the Institute.

e. Whenever I have used materials (data, theoretical analysis, figures and text) from other sources, I have given due credit to them by citing them in the text of the thesis and giving their details in the references. Further, I have taken permission from the copyright owners of the sources, whenever necessary.

Upasana Sarma

Acknowledgements

It is my pleasure to express sincere gratitude to my supervisor, Dr. Sanjib Ganguly of the Department of Electronics and Electrical Engineering for introducing me to this area of research. His invaluable and encouraging discussions at every stage of the work helped in bringing the thesis to its present shape.

The work is supported by the Science and Engineering Research Board, the Department of Science and Technology, India, Grant no. YSS/2014/000028. I am thankful to the Deputy Head of the Department of Safety, North Eastern Frontier Railway for providing the data of the diesel locomotive. I am also grateful to the Head of the Department of Electronics and Electrical Engineering for providing me all the facilities to carry out my research work. I also express my sincere gratitude to the members of doctoral scrutiny committee and all the faculty members of the department. I would also like to acknowledge all my lab mates and co-research scholars of Electronics and Electrical Engineering Department for their help and encouragement.

My earnest thanks are to my family members who have supported this endeavor through their deeds and prayer. Their unconditional love and affection are always sources of inspiration for my future life. Many thanks to my parents for giving me the freedom of what I wanted to be. Many thanks to my friends for supporting me and making my stay in IIT Guwahati memorable.

Finally, I would like to dedicate this thesis to my family.

IIT Guwahati

Date: **(UPASANA SARMA)**


भारतीय प्रौद्योगिकी संस्थान गुवाहाटी
Indian Institute of Technology Guwahati

Abstract

The development of economically feasible renewable energy technologies to replace the fossil fuel run machineries is one of the significant areas of research in this century. Over the years, the proton exchange membrane fuel cell (PEMFC) based hybrid energy system (HES) has emerged as a promising source of electrical power for use in transportation. This is because the PEMFC has the advantages of being clean energy, low operating temperature, high efficiency, etc. In this thesis, the PEMFC-battery-HES is proposed to retrofit the diesel locomotives which are currently used to haul the passenger trains operating in North Eastern Frontier Railway (NEFR), Assam, India. However, the investment and operational costs are the important factors associated with a HES. Thus, it is important to optimise the sizes of the HES components and to design an energy management strategy (EMS) for optimum distribution of load in the HES.

In this thesis, the optimal component sizing of the PEMFC and battery that constitute the HES is carried out to provide the similar driving force as the WDM-3D class of diesel locomotives to pull the intercity passenger trains in Assam, India. To do this, single-objective and multi-objective design optimization approaches are formulated. The objective function of single-objective optimization is the minimization of the total cost of HES. The objective functions of multi-objective optimization are the simultaneous minimization of the total cost of HES and the PEMFC fuel consumption. In both the approaches, the optimization is carried out under the operational constraints of the battery state-of-charge limit, the PEMFC capacity constraint, and the instantaneous power balance between the source and load. Two EMSs are designed and are suitably incorporated into the particle swarm optimization (PSO) based solution algorithm to solve the design optimization problems.

The application of PEMFC-battery-HES in locomotives requires the maintenance of a constant DC-bus voltage across the load against the wide variation in the PEMFC output voltage with changing operating and loading conditions. This can be achieved through the use of DC/DC converters. In view of this, the design and control of a multi-input single-output (MISO)-DC/DC boost converter are carried out in this thesis. The feedback controllers regulate the pulse width modulation of the converter switches to implement the EMS and to maintain the DC-bus voltage. The performances of the designed MISO converter and the controllers are validated on MATLAB/SIMULINK and on developing an experimental set-up. Both the simulation and hardware results show that the PWM controlled MISO converter provides the desired performances.

Another vital aspect of a HES is the design of an efficient EMS to regulate the power flow in the HES based on the operational characteristics of the energy sources. Hence, two energy management optimization (EMO) approaches are devised that aim to generate the PEMFC power references at each loading point with the objective function of the minimization of the total fuel consumption of the PEMFC. The constraints of the first EMO approach include the limits on battery state-of-charge variation, the dynamic change in the PEMFC output power and the instantaneous power balance between the source and load. However, in the second EMO model, the durability limits of the energy sources are also considered in addition to the aforementioned operational constraints. The EMO approaches are executed using General Algebraic Modeling System. The performance comparison of the proposed approaches with some of the already available approaches confirms its proficiency in the reduction of fuel consumption with optimum utilization of the capacities of the energy sources.

All the above studies are carried out using the data of the dynamically varying locomotive power demand for practical drive cycle scenarios of NEFR, Assam, India.

The viable deployment of the hydrogen powered passenger trains requires a proper refueling infrastructure. In view of this, the optimal allocation planning of the hydrogen refueling stations (HRS) for the rollout of hydrogen powered passenger trains in NEFR, Assam, India is presented in this thesis. The problem of optimal allocation planning is firstly addressed as a single-objective optimization approach with the objective function of the minimization of the total cost ownership (*TCO*) of the HRS for a specified planning period. A multi-objective optimization approach is then designed with the objective functions of simultaneous minimization of the *TCO* and the average cost of refueling of the HRS. The optimization problems are solved using binary PSO based solution algorithms with the real-time data of the intercity railway traffic of NEFR, Assam, India as the input. Besides this, the total investments incurred in the HRS infrastructure development under the different scenarios of installed HRS capacity are also investigated.

Contents

3. Control approaches for the PEMFC-battery-HES for Locomotive Applications 49

List of Acronyms

ADVISOR	Advanced vehicle simulator
ARMA	Auto-regressive moving average
CCM	Continuous conduction mode
DCM	Discontinuous conduction mode
DO	Design optimization
DP	Dynamic programming
ECMS	Equivalent consumption minimization strategy
EMO	Energy management optimization
EMS	Energy management strategy
ESS	Energy storage system
FC	Fuel cell
FCLM	Flow capturing location model
FLC	Fuzzy logic control
FRLM	Flow refueling location model
GA	Genetic algorithm
GAMS	General Algebraic Modelling System
HES	Hybrid energy system
HEV	Hybrid electric vehicle
HRS	Hydrogen refueling station
IGBT	Insulated gate bipolar transistor
LFCS	Load follower charge sustaining
LHV	Lower heating value
MISO	Multi-input single-output
MOPSO	Multi-objective particle swarm optimization
MPPT	Maximum power point tracking
NEFR	North eastern frontier railway
OP	Operating point
PCB	Printed circuit board
PEMFC	Proton exchange membrane fuel cell
PLR	Part load ratio
PMP	Pontryagin’s minimum principle
PSO	Particle swarm optimization

PV	Photo-voltaic
PWM	Pulse width modulation
SC	Super-capacitor
SOC	State-of-charge
SOH	State-of-health
SPEA2	Strength Pareto Evolutionary Algorithm 2
TC	Total cost of HES
TCO	Total cost of ownership
TZ	Traffic zone
UPS	Uninterruptible power supply

List of Principal Symbols

a_0, a_1	Empirical parameters representing the activation loss of the PEMFC
$A(c)$	Total throughput in the battery (in Ah)
σ	Locomotive cross sectional area (in m^2)
β	Gradient or slope of the railway track
b	Tafel's slope
b_0, b_1	Empirical parameters representing the activation loss of the PEMFC
c	Battery c-rate
C	Capacitor across the load of the converter (in μF)
c_1, c_2	Learning factors of PSO
C_1,C_2,C_3	Capacitors constituting the model of the Type-1 and Type-3 amplifiers (in μF)
c_{bat}	Cost per unit rating of the battery (in $\$/kWh$)
C_{dl}	Double layer capacitor of the PEMFC (in F)
c_{fc}	Cost per unit rating of the PEMFC system (in $\$/kW$)
CC_k	Capital cost of the HRS located at the k^{th} potential site (in $\$$)
$C_{refuel,k}^{ct}$	Cost of refueling of the HRS located at the k^{th} potential site in the current year (in $\$$)
$C_{refuel,k}^{proj}$	Cost of refueling of the HRS located at the k^{th} potential site in the projected years (in $\$$)
D	Drag coefficient
D_1	Diode of the converter
d_j	Duty ratio of the converter switches
$\hat{d}_j$	Complement of d_j
$\tilde{d}_j$	Perturbation in d_j
$D_{k,k_{next}}$	Distance between two HRS located at the potential sites, k and k_{next} (in km)
D_{range}	Driving range of the train (in km)
$E(t_0)$	Initial battery energy (in J)
ΔE	Change in battery energy
$E_a(c)$	Activation energy of battery (in J/mol)
E_0	Open circuit voltage of the PEMFC (in V)
F	Faraday's constant (in C/mol)
F_{acc}	Force of acceleration (in N)

$f_{c,j}$	Cross-over frequencies (in *Hz*)
F_{climb}	Force to overcome the slope/gradient of the railway track (in *N*)
$FC_{k,k_{next}}$	Fraction of locomotive fuel tank capacity consumed while travelling a distance of $D_{k,k_{next}}$
F_{drag}	Aerodynamic drag (in *N*)
f_q	Traffic flow along the route, q
$f_{q,k}$	Traffic flow of q^{th} route to be refueled by the HRS at the k^{th} potential site
F_{rr}	Force of friction between the wheels and railway track (in *N*)
f_s	Switching frequency of the converter (in *Hz*)
$fuel_k$	Amount of hydrogen required for refueling of the HRS located at the k^{th} potential site which is equal to the HRS capacity (in *kg*)
FV_{bat}	Future value of the battery (in *$/kWh*)
FV_{fc}	Future value of the PEMFC stack (in *$/kW*)
FV_{H_2}	Future cost of the hydrogen fuel (in *$/kg*)
$gbest$	Global best position in the population of particles
$G_{c,j}$	Converter gain (in *dB*)
ΔH	Enthalpy of the electro-chemical reaction
$HRS_{cap,k}$	Capacity of the HRS located at the k^{th} potential site (in *kg/day*)
$HRS^{q}_{cap,used,k}$	Capacity of the HRS located at the k^{th} potential site utilized in supplying the fuel needs of the traffic flow along the route q, f_q (in *kg/day*)
HRS^{max}	Maximum number of HRS to be installed in a layout of potential railway sites
$HRS^{avg}_{refuel,cost}$	Average cost of refueling of the HRS (in *$*)
i_{bat}	Output current of the battery (in *A*)
i_{fc}	Output current of the PEMFC system (in *A*)
$i_{L,j}$	Instantaneous inductor current of the converter (in *A*)
$\tilde{i}_{L,j}$	Perturbation in $i_{L,j}$
$I_{L,j}$	Average value of the inductor current (in *A*)
$I^{peak}_{L,j}$	Peak value of the inductor current (in *A*)
$\Delta I_{L,j}$	Ripples in the inductor currents (in *A*)
I^{ref}_{L}	Current reference (in *A*)
i_{stack}	Output current of the PEMFC stack (in *A*)
$iter$	Iteration number
$iter^{max}$	Maximum number of iterations
j	Index representing the MISO converter layers (j =1 for unidirectional and j =2 for bidirectional layer)

k	Index representing the potential railway sites for HRS allocation
K	Set of all the potential railway sites
k_{bat}	Constant cost component of the battery (in *$*)
L_j	Inductors of the MISO converter (in *mH)*
m	Molecular weight of hydrogen
MC_k	Maintenance cost of the HRS located at the k^{th} potential site (in *$*)
m_{coach}	Mass of a non-air conditioned coach (in *kg*)
m_{H_2}	Mass of hydrogen consumption of the PEMFC (in *kg*)
$\dot{m_{H_2}}$	Rate of hydrogen consumption (in *kg/s*)
m_0, m_1	Empirical parameters representing the concentration loss of the PEMFC
m_{loco}	Locomotive mass (in *kg*)
M_{veh}	Vehicle mass (in *kg*)
n	Emperical parameter representing the concentration loss of the PEMFC
N	Number of sample data
N_{bat}	Life-time of the battery (in years)
η_{bat}	Efficiency of the battery
N_{bat}^{rep}	Number of replacements of the battery during the planning period
$N(c)$	Number of battery charge/discharge cycles
η_{chg}/η_{dis}	Charging/discharging efficiencies of the battery
n_{coach}	Number of non-air conditioned coaches
n_{e^-}	Number of electrons generated in the electro-chemical reaction
N_{end}	Set of all the origin-destination terminuses of the railway routes
N_{fc}	Life-time of the PEMFC (in years)
η_{fc}	Overall efficiency of the PEMFC system
N_{fc}^{rep}	Number of replacements of the PEMFC stack during the planning period
n_{pop}	PSO population size
N_q	Set of all the potential sites that lies on the route, *q*
$N_{refuel,k}$	Frequency of refueling of the HRS located at the k^{th} potential site in the current year
$N_{refuel,k}^{proj}$	Frequency of refueling of the HRS located at the k^{th} potential site in the projected (T_{plan}-1) year
N_s	Number of cells in the PEMFC stack
η_{stack}	Efficiency of the PEMFC stack
η_{sys}	Transmission system efficiency
N_{trip}	No. of trips of the passenger train per day

ρ	Air density (in kg/m^3)
P_{aux}	Power consumed by the auxiliaries of the train, such as, the traction motor blower, air brakes, lighting loads, etc. (in *W*)
$P_{bat}(t)$	Instantaneous output power of the battery (in *W*)
$pbest$	Particle's own best position
PB_j	Amplifier phase boost
$P_{c,j}$	Converter phase shift
P_{H_2}	Power available in the hydrogen consumed (in *W*)
p_{H_2O}	Partial pressure of water (in *atm*)
p_{H_2}	Partial pressure of hydrogen (in *atm*)
p_{O_2}	Partial pressure of oxygen (in *atm*)
$P_{fc}(t)$	Instantaneous net output power of the PEMFC system (in *W*)
ΔP_{fc}	Change in PEMFC output power (in *W*)
P_{fc}^{aux}	Power consumed by the PEMFC auxiliary components (in *W*)
$P_{fc}^{constant}$	Constant power (in *W*)
P_{fc}^{0}	PEMFC output power at the beginning of the acceleration/deceleration period (in *W*)
P_{fc}^{min}	Lower limit of the output power of the PEMFC (in *W*)
P_{fc}^{rated}	Power rating of the PEMFC (in *W*)
P_{fc}^{ref}	References for the PEMFC output power (in *W*)
P_{fc}^{stack}	Power output of the PEMFC stack (in *W*)
$P_{load}(t)$	Instantaneous power demand of the train for the original drive cycle (in *W*)
P_{load}^{avg}	Average power demand of the train (in *W*)
$P_{load}^{scaled}(t)$	Instantaneous power demand of the train for the reduced scaled drive cycle (in *W*)
PM_j	Phase margin
PV_{H2}	Current cost of the hydrogen fuel (in *$/kg*)
q	Index representing the intercity railway routes
Q	Set of all the railway routes of NEFR, Assam, India
Q_{bat}^{rated}	Rated capacity of the battery (in *Wh*)
Q_{heat}	Amount of heat generated due to burning of hydrogen fuel (in *J*)
R	Universal gas constant (in *J/K/mol*)
R_1,R_2,R_3	Resistances constituting the model of the Type-1 and Type-3 amplifiers (in *Ω*)
$rand_1$, $rand_2$	Random number between [0, 1]
r_{bat}	Discounting rate of the PEMFC stack

r_{fc}	Discounting rate of the battery
r_{H_2}	Discounting rate of hydrogen fuel
R_{load}	Load resistance (in Ω)
R_{max}	Maximum rate of change of PEMFC output power (in *W/s*)
R_{ohm}	Ohmic resistance associated with the ohmic loss of the PEMFC (in Ω)
$R_{ohm,0}$, $R_{ohm,1}$	Empirical parameters associated with the ohmic loss of the PEMFC
R_r	Coefficient of rolling resistance
R_{total}	Resistance representing the total voltage drop due to concentration and activation losses of the PEMFC (in Ω)
S_{ij}^{iter}	Position of the *j*th dimension of the *i*th particle in *iter*th iteration of PSO
$SOC(t)$	Instantaneous state-of-charge of the battery
$SOC(t_0)$	SOC at the start of the drive cycle, i.e., at $t = 0$.
$SOC(t_f)$	SOC at the end of the drive cycle, i.e., at $t = t_f$.
SOC_{max}	Upper limit of *SOC*
SOC_{mean}	Mean value of *SOC*
SOC_{min}	Lower limit of *SOC*
SOH_{bat}	State-of-health of the battery
ΔSOH_{bat}	Change in SOH_{bat}
$SOH_{bat}(t_0)$	SOH at the start of the drive cycle, i.e., at $t = 0$.
$SOH_{bat}(t_f)$	SOH at the end of the drive cycle, i.e., at $t = t_f$.
$\Delta SOH_{bat,max}$	Maximum deterioration in the battery SOH per trip
SW_1	IGBT without the anitpararallel diode
SW_2, SW_3	IGBTs with the anitpararallel diode
T	Cell temperature (in *K*)
Δt	Change in time (in *s*)
$tank_{cap}$	Fuel tank capacity of the train (in *kg*)
T_{delay}	Delay in the range of microseconds or nanoseconds incurred in the response times of the controller, communication channels, DC-DC converter, etc.
t_f	Final/total duration of the drive cycle (in *s*)
TF	Total traffic flow of the intercity passenger trains operating under the Department of NEFR in Assam, India
$TF_j^{Type-1}(s)$	Transfer function models of the Type-1 PWM controller
$TF_j^{Type-3}(s)$	Transfer function models of the Type-3 PWM controller
$TF_j^{c}(s)$	Transfer function models of the converter used in the design of the PWM controllers

t_0	Initial/starting time of the drive cycle (in *s*)
T_{plan}	Planning period (in *years*)
$\vartheta(t)$	Instantaneous speed of the train (in *m/s*)
v_{act}	Voltage drop due to the activation loss of the PEMFC (in *V*)
v_{bat}	Output voltage of the battery (in *V*)
$\tilde{v}_{bat}$	Perturbation in v_{bat}
v_C	Voltage across the capacitor, *C* (in *V*)
$\tilde{v}_C$	Perturbation in v_C
$v_{c,dl}$	Voltage across the double layer capacitor, C_{dl} (in *V*)
v_{conc}	Voltage drop due to the concentration loss of the PEMFC (in *V*)
v_{DC}	Instantaneous DC-bus voltage (in *V*)
$\tilde{v}_{DC}$	Perturbation in v_{DC}
V_{DC}	Average value of the DC-bus voltage (in *V*)
ΔV_{DC}	Ripple in the DC-bus voltage
V_{DC}^{ref}	Voltage reference (in *V*)
v_{fc}	Output voltage of the PEMFC system (in *V*)
$\tilde{v}_{fc}$	Perturbation in v_{fc}
$V_{in,j}$	Average value of the converter input voltage (in *V*)
V_{ij}^{iter}	Velocity of the *j*th dimension of the *i*th particle in *iter*th iteration of PSO
V_{OC}	Open circuit voltage of the battery (in *V*)
v_{ohm}	Voltage drop due to the ohmic loss of the PEMFC (in *V*)
v_{rev}	Theoretical cell potential or reversible voltage of the PEMFC (in *V*)
v_{stack}^{exp}	Experimental PEMFC stack voltage (in *V*)
v_{stack}^{model}	Voltage of the PEMFC model (in *V*)
x_k	Binary variable representing the HRS location at the *k*th potential site
y_q	Binary variable representing if the traffic flow, f_q is refueled by the HRS layout
z	Power law factor

List of Figures

List of Tables

Chapter 1

Introduction and Literature Review

1.1. Introduction

Since the last few decades, the natural world has been facing massive degradation in its biodiversity and climate, with its extended effects being reflected on human welfare and all other life on earth. Even today, most of the energy demand of the world is met with the conventional fossil fuels. However, the fossil fuel reserve on earth is finite. Thus, it may be only a matter of time when these reserves would run out. Also, burning of fossil fuels releases greenhouse gases which causes environmental pollution and global warming. Hence, to overcome this crisis, the millennials have been given the urgent task of reversing the damages of industrial civilization and overcoming the greatest challenge humanity has ever faced - to secure the stability of our future environmentally, economically and socially. In contrast to the fossil fuels, the renewable energy resources are constantly replenished and will never run out. Thus, scientists all over the world have come up with new technological innovations that utilize green energy, such as hydrogen, biodiesel, natural gas, or electricity with the goal of replacing the fossil fuel run machineries in various applications. However, the renewable energy sources are usually intermittent in nature. Using a hybrid energy system (HES), in which the different energy sources are used in conjunction, can achieve better utilization of renewable energy. The energy storage system (ESS) plays a vital role in a HES, especially when a HES is used in applications, where constant adjustments to the power supply are needed for predictable changes in power demand. For example, when there is more power generation than demand, the excess energy can be stored in the ESS. Similarly, the ESS can supply energy when the demand exceeds the generation of the primary sources.

From the last decade, the popularity of fuel cell (FC) has greatly increased. The FC is a green energy technology which converts the chemical energy of hydrogen into electricity, with water and heat as the by-products. The FCs are basically classified by the kind of electrolyte they employ. This classification determines the kind of electrochemical reactions that take place in the cell, the catalysts and the fuel required, the temperature range in which the FC operates, etc. These characteristics, in turn, determine the applications for which the FCs are most suitable. There are several types of FCs currently under development, each with its own advantages, limitations and potential applications. Examples of some of the FC technologies are the alkaline FC, direct methanol FC, phosphoric acid FC, molten carbonate FC, proton exchange membrane fuel cell (PEMFC) and solid oxide FC. In transportation, stationary power generation and portable applications, the use of PEMFC is preferred over the other FC technologies since this FC has the benefit of low operating temperature (~ 80 to 120 ^{0}C). In [1], the various aspects of PEMFC, from theory and fundamentals to its practical applications are provided.

The two vital components of the PEMFC system are the PEMFC stack and the auxiliary components. The PEMFC stack generates electricity by means of an electro-chemical reaction between hydrogen and oxygen of air. The stack consists of a number of individual cells which are connected in series/parallel combinations in order to provide the necessary voltage and power output. Each cell comprises of some critical intrinsic components, such as, the membrane, electrodes, layer of catalyst, etc. A schematic diagram of the PEMFC exhibiting the electro-chemical reaction is given in Fig. 1.1. As seen in this figure, the hydrogen atom undergoes oxidation reaction at the anode to generate H^+ ions and electrons, e^-. The e^-s through an external circuitry pass to the cathode, and constitute the electric current supplied by the PEMFC stack. The H^+ ions reach the cathode through the polymer electrolyte membrane. At the cathode, the H^+ ions, e^-s and oxygen of air combine and undergo reduction reaction to produce water and heat as the by-products. In this way, the electricity is generated in a PEMFC without the release of any harmful by-products. The auxiliary components, on the other hand, are responsible for keeping the stack operational by supplying air and hydrogen, by humidifying the reactant gases, and by cooling the stack. However, the PEMFC is not devoid of technical drawbacks. Some of the notable disadvantages in deploying the PEMFC are the high cost, shorter lifetime, slow dynamic response, etc. Thus, the PEMFC cannot be used as a sole source of energy. In [2]–[4], it is shown that the hybridization of PEMFC with ESS is always beneficial, in terms of improved dynamic response of the system, reduced fuel consumption, improved efficiency of the overall system, etc. The different types of batteries and/or super-capacitor (SC) are used in the ESS. Nevertheless, the investment and operational costs are the important factors associated with a HES. Thus, it is important to optimize the sizes of the HES components, and to design an efficient energy management strategy (EMS) for the optimum distribution of power demand to the components of the HES. Hence, the same forms an important area of research.

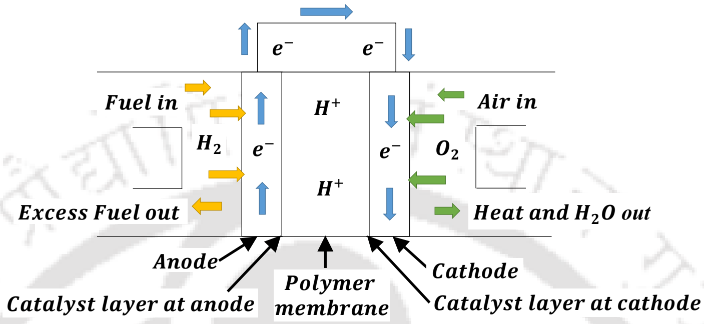

$$\text{At anode, } 2H_2 = 4H^+ + 4e^-$$

$$\text{At cathode, } O_2 + 4H^+ + 4e^- = 2H_2O + heat$$

$$\text{Overall redox reaction, } 2H_2 + O_2 = 2H_2O + heat$$

Fig. 1.1: Schematic of the electrochemical reaction of the PEMFC.

1.2. Brief Review of the Existing Literature on PEMFC based HES

In the recent years, a lot of research is reported in the field of application of PEMFC based HES. However, a few studies are reported on its application in tractions. The concerned research area is classified in a three-level tree structure as shown in Fig.1.2. The level 1 classification includes the two broad areas of study in this field. The first area of study is based on the development of EMS to control the power/energy flow in the HES [5]–[55]. However, the various EMS proposed under this category of study may or may not result into optimal power distribution among the energy sources. The second area of study is based on the development of design optimization (DO) and/or energy management optimization (EMO) approaches. Whereas, the aim of the DO is to determine the optimal rating requirements for each component of the HES, EMO aims at developing an optimal power flow control strategy for the hybrid power plant. It is known that, the vehicle performance is affected not only by the powertrain component sizes but also by the EMS involved. Therefore, both DO and EMO play important roles in developing an efficient HES for vehicular application. Relatively many literature can be found in these areas, some of which are reported in [2]–[4], [34], [47], [56]–[89]. Both the optimization approaches are carried out under some operational constraints, with a view to maximize or minimize one or more objective functions. Some of the objective functions of the optimization approaches, reported in literature, are the minimization

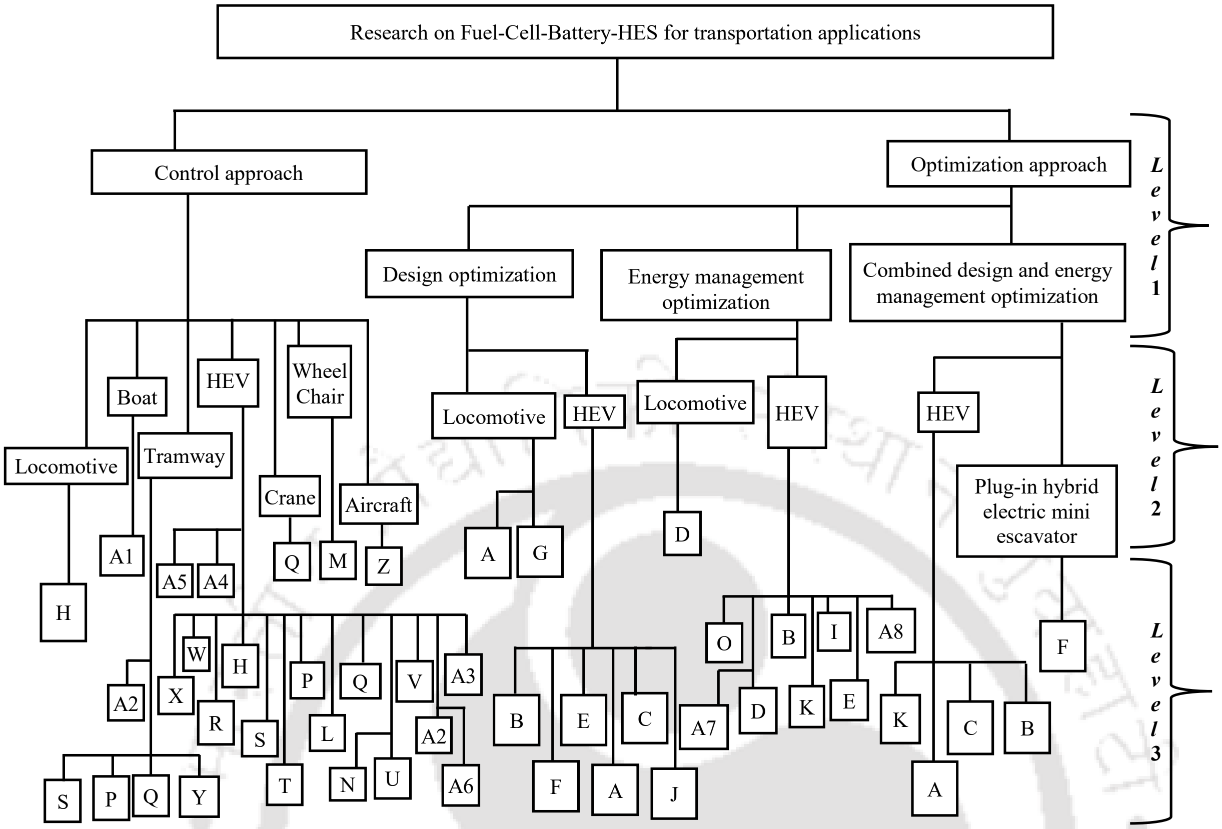

Level 1: It consists of the two broad areas of study in this field: control approach and optimization approach.

Level 2: It is based on the various transportation areas where PEMFC based HES has been used so far.

Level 3: It is based on the different types of solution strategies used.

A: Heuristic search
B: Genetic Algorithm
C: Particle Swarm Optimization
D: Pontryagin's Minimum Principle
E: Deterministic algorithm
F: Branch and bound algorithm
G: Bisection method
H: Fuzzy Logic Control (FLC)
I: Matlab optimization toolbox
J: Non-linear programming
K: Dynamic Programming
L: Adaptive supervisory control
M: Control strategy with FC as range extender
N: Passivity based EMS
O: Global Extremum Seeking
P: Equivalent Consumption Minimization Strategy
Q: Rule based EMS
R: EMS based on PEMFC operation in constant or quasi state power regime
S: Model predictive control
T: EMS based on reinforcement learning
U: ARMA based EMS
V: Hysteresis control
W: Finite state machine based EMS
X: Two-stage control
Y: State-machine control based EMS
Z: Decentralized control
A1: Combined MPPT-FLC
A2: Combined wavelet transform-FLC
A3: Time delay control
A4: Controller based on AVR technology
A5: Feedback closed loop control based EMS
A6: Artificial neural network
A7: Line search algorithm
A8: Co-evolutionary algorithm

Fig. 1.2: Classification of the research on PEMFC-battery-HES for transportation applications.

of the investment and operating costs of the HES [47], [56]–[60], [62], [63], [65], [71], [83], [84], [86], [88], minimization of the mass/volume of the HES [3], [4], [57], [58], [60], [61], minimization of the PEMFC fuel consumption [4], [34], [59], [65]–[70], [72], [73], [75], [77]–[81], [83]–[89], minimization of the PEMFC degradation [68], [77], minimization of the battery usage [66], [73], [83], [85], maximization of the overall efficiency of the HES [3], [60], [64], [67], [72], maximization of the braking energy recovery by the ESS [74], maximization of the fuel consumption efficiency [78], maximization of the fuel economy [82], etc. The constraints involved in optimization include mainly the vehicle performance constraints in terms of acceleration time, gradeability, etc. [47], [60], [66], [68], [70], [89], the constraint of the dynamic behavior of the energy sources [60], [66], [68], [70], [85], [88], the maximum size limitation of the hybrid powertrain components [89], maintenance of the state-of-charge (SOC) of the ESS [34], [70], [72], [75], [80], [81], regulation of the energy level of the ESS [79], maximum output current of the FC [80], constraint on the air-flow and fuel-flow rates [82], etc.

The level 2 further categorizes the level 1 classification based on the various transportation areas where PEMFC based HES has been used so far. Examples of some of the transportation areas are hybrid electric vehicle (HEV) [2]–[5], [10]–[22], [24]–[29], [32]–[35], [37]–[46], [48]–[50], [53]–[62], [64]–[67], [67]–[73], [75]–[82], [85]–[89], tramway [6]–[8], [30], [36], [51], crane [9], wheelchair [23], aircraft [31], locomotive [47], [63], [74], boat [52], plug-in mini excavator [83], [84], etc.

The level 3 classification presents the various types of solution strategies used. This includes both control and optimization approaches. There are several control approaches proposed in literature. Among these, the equivalent consumption minimization strategy (ECMS) is proposed in [5] and [6]. In this type of EMS, the power split among the energy sources is determined so as to minimize the real PEMFC fuel consumption, and an additional fictitious fuel consumption for the ESS usage. The fictitious fuel consumption can be either positive or negative depending on the instantaneous SOC of the ESS. To further enhance the voltage stabilization and to minimize the fuel consumption of the PEMFC, the conventional ECMS is modified, and the ECMS based on dynamic penalty control is implemented in [7]. In [8]–[21], some rule based EMSs are presented. These EMSs are devised based on some pre-defined rules which determine the operating points of the energy sources to be followed depending on various factors such as, the instantaneous power demand, vehicle speed, SOC of the ESS, etc. The authors in [22] propose the EMS based on adaptive supervisory control. In this EMS, the distribution of load among the energy sources is performed in four sequential phases, i.e., the ECMS, vehicle accessorial power estimating algorithm, battery charge-sustaining algorithm and recursive least squares algorithm. In the first phase, the ECMS generates the PEMFC power references at each loading point of the vehicular power demand. The vehicle accessorial power is then calculated in the second phase. The battery SOC may deviate from its target while supplying the load. In addition to this, the PEMFC output power may also decline over time. These phenomena are taken care of by the battery charge-sustaining algorithm and recursive least squares algorithm in the third and fourth phases, respectively. As mentioned in section 1.1, the PEMFC suffers from the technical drawback of slow dynamic response. Hence, to compensate for this phenomenon, the EMS with PEMFC as range extender [23], and the EMS based on PEMFC operation in constant and/or quasi state power regime [24]–[28] are proposed. In [29] and [30], the model predictive control based EMSs are developed which aim to generate the power references for the hybrid energy sources with a view to satisfy some operational constraints, such as, the instantaneous power balance between the source and load, maintenance of the SOC of the ESS, etc. The main objective of the predictive controller is to hold the power outputs of the energy sources at the reference values by adjusting the manipulated variables. The manipulated variables are estimated based on the future behaviour of the HES, and the data collected during its previous operation. The authors in [31] implement the decentralized EMS based on mixed droop strategy. The proposed EMS aims to split the load power into low and high-frequency components, and allocate them to the FC and SC units, respectively. In a similar way, the frequency decoupling of the energy sources according to the power requested is done by the DC-bus filters in [32]. A passivity based controller is then designed in [32] to force the currents of the energy sources to follow the references. The hysteresis algorithm based EMSs are proposed in [33] and [34]. The hysteresis control developed in [33] aims to enhance the FC durability by reducing the active operation time and the number of on-off switching of the FC. On the other hand, the objective of the hysteresis algorithm based EMS devised in [34] is to decide the operating mode of the battery in order to maintain its SOC level around the chosen reference while supplying the power demand. To do this, the proposed EMS determines the SOC thresholds. Based on this thresholds, the high power mode to track the maximum power, and the low power mode to track the maximum efficiency point of the battery are chosen. In [35], the finite state machine control based EMS is devised. This EMS divides the problem of energy management into finite states with transitions between them, often triggered by events and conditions defined by the various factors, such as, the vehicular power demand, the SOC and charge/discharge power of the ESS, etc. Likewise, the state-machine control based EMS is proposed in [36] which determines the operational states of the energy sources according to the demanded load, tramway speed and different levels of the battery SOC, i.e., high SOC (65%), normal SOC (42–65%) and low SOC (<42%). The two-stage controller based EMS is implemented in [37]. The proposed control system is composed of two controllers connected in sequential stages: predictive control and tracking control. The predictive control generates the PEMFC power references using the ECMS. The tracking controller uses some rule-based control logics in order to track the FC power reference obtained in the previous stage. To regulate the PEMFC output current in order to prevent the starvation of air in the PEMFC, the time delay control is employed in [38]. To do this, the proposed time delay control based EMS regulates the optimum stoichiometric amount of oxygen irrespective of the dynamic fluctuations that exist in the PEMFC output power. Similarly, the central controller based on AVR technology is implemented in [39] to achieve the load distribution in the PEMFC-battery-HES by regulating the air stoichiometry and stack temperature of the PEMFC in accordance to the dynamically varying power demand. The authors in [40] develop a feedback closed loop control based EMS with the objectives of minimization of the energy cost, the maintenance of the battery operation in the desired SOC range, and the regulation of the transients on the battery and SC of the proposed PEMFC-battery-SC-HES. To do this, a cost function in terms of the square error between the desired variable settings and the current sensed values is formulated. The developed feedback control based EMS then determines the power split in the HES with the aim of minimization of the cost function. Besides these, several EMSs based on fuzzy logic control (FLC) are proposed in [41]-[49], where the power split among the energy sources is determined by applying fuzzy theory on various vehicular elements, such as, the power demand, the SOC of the ESS, the vehicle speed, etc. The combined wavelet theory-FLC [50], [51] and the maximum power point tracking (MPPT)-FLC based EMS [52] are also proposed. The basic idea behind these combined strategies is to minimize the transients on the PEMFC output power in order to increase its lifetime. However, most of the aforementioned EMS methods are either based on some predefined rules or prediction that may not be adaptive to real-time driving conditions. Hence, to address this issue, the authors present the auto-regressive moving average (ARMA) controller based EMS [53], an intelligent EMS based on reinforcement learning [54] and radial-basis-function networks based adaptive optimal control [55]. In [53], the ARMA controller is developed, and tuned based on the observations and analysis of the HES's behaviour obtained for multiple drive cycles using pontryagin's minimum principle (PMP). The design and tuning of the ARMA controller is done to mimic the optimal results of PMP in order to obtain sub-optimal fuel consumption results. Thus, the designed ARMA based EMS leads to the minimum fuel consumption of the PEMFC, maintains the physical limitations of the energy sources, regulates the SOC of the ESS within the desired operating region during the driving period, and ensures charge sustaining behaviour of the ESS (i.e., the SOC level at the beginning of the drive cycle is equal to the SOC level at the end). Likewise, the EMS based on reinforcement learning [54] autonomously learns and determines the power split in the HES in real time through interaction with the onboard HES. In [55], the adaptive optimal control based EMS is designed using neural network. For this, the radial-basis-function networks are implemented and trained for different drive cycles so that all possible driving situations are taken into account. The trained neural network can then be applied for real-time load distribution in the HES without prior knowledge of the future driving patterns.

Under the category of optimization approaches, various solution strategies are used in literature to solve the DO and/or the EMO problems. The concerned solution strategies can be categorized as follows:

(i) **Mathematical and enumerative approaches**, such as, bisection method [47], rule based deterministic algorithm [56], [57], [68], heuristic search [2]–[4], [62]–[65], [89], non-liner programming [60], branch and bound algorithm [61], [83], [84], PMP [34], [66], [73]–[76], dynamic programming (DP) [66], [73], [77], [85], [87], line search algorithm [79], etc.

(ii) **Meta-heuristic approaches**, such as, genetic algorithm (GA) [58], [59], [66], [70]–[72], [80], [86], [87], particle swarm optimization (PSO) [58], [88], global extremum seeking algorithm [78], [82], co-evolutionary algorithm [81], etc.

A comprehensive review on each of the approaches are given in Table 1.1.

Table 1.1: A comprehensive review of the research on the PEMFC-battery-HES used in transportation applications.

Ref. No.	**Approach**	**Solution Strategy**	**Objective**	**Application**
2	DO	Heuristic search	To determine the optimal degree of hybridization	HEV
3	DO	Heuristic search	To maximization the energy efficiency, and minimize the mass/volume of HES	HEV
4	DO	Heuristic search	To minimize the hydrogen consumption and vehicle mass	HEV
5	Control approach	ECMS	To minimize the fuel consumption and SOC deviation from its target	HEV
6	Control approach	ECMS	To minimize the fuel consumption and SOC deviation from its target	Tramway
7	Control approach	ECMS based dynamic penalty control	To enhance voltage stabilization, and to minimize the fuel consumption	Tramway
8	Control approach	Rule based EMS	To improve the operational efficiency of the HES	Tramway
9	Control approach	Rule based EMS	To maintain the DC bus voltage and the SC SOC	Crane
10	Control approach	Rule based EMS	To minimize the PEMFC hydrogen consumption	HEV

11	Control approach	Rule based EMS	To satisfy the PEMFC slow dynamic response, to recover the energy during deceleration phase, and to maintain the SC voltage	HEV
12	Control approach	Rule based EMS	To minimize the number of FC startup and shut down	HEV
13	Control approach	Rule based EMS	To maintain the DC bus voltage	HEV
14	Control approach	Rule based EMS	To maintain the battery SOC, and to improve the system's energy efficiency and energy density	HEV
15	Control approach	Rule based EMS	To maintain a steady FC power in order to extend the FC lifetime	HEV
16	Control approach	Rule based EMS	To limit the battery load to a threshold min-max according to the SOC, and to charge the battery under braking and traction mode	HEV
17	Control approach	Rule based EMS	To maintain the SOC, and to enhance the FC durability	HEV
18	Control approach	Rule based EMS	To enhance the FC durability	HEV
19	Control approach	Rule based EMS	To limit the battery load to a threshold min-max according to the SOC, and to ensure the battery charging during braking	HEV
20	Control approach	Rule based EMS	To maintain the charging/discharging currents of the ESSs within their threshold limits	HEV
21	Control approach	Rule based EMS	To regulate the DC-bus voltage regulation, and to minimize the FC power demand transitions	HEV
22	Control approach	EMS based on adaptive supervisory control	To maximize the fuel economy	HEV
23	Control approach	EMS with FC as range extender	To maximize the efficiency of HES, and to minimize the size of the FC	Wheelchair
24	Control approach	EMS based on PEMFC operation in constant and/or quasi state power regime	To minimize the fuel starvation	HEV
25	Control approach	EMS based on PEMFC operation in constant and/or quasi state power regime	To maximize the fuel economy and FC life time	HEV
26	Control approach	EMS based on PEMFC operation in constant	To increase the PEMFC lifetime by reducing the transients on FC	HEV

		and/or quasi state power regime		
27	Control approach	EMS based on PEMFC operation in constant and/or quasi state power regime	To maintain a constant FC output in order to extend FC lifetime	HEV
28	Control approach	EMS based on PEMFC operation in constant and/or quasi state power regime	To maintain a constant FC output in order to extend FC lifetime	HEV
29	Control approach	Nonlinear model predictive control	To track the maximum efficiency point of the FC	HEV
30	Control approach	Model predictive control based EMS	To provide the power demanded by the tramway while meeting the battery, and SC SOC constrains and ordering the operation of the braking resistor, when necessary, during regenerative braking	Tramway
31	Control approach	Decentralized EMS based on mixed droop strategy	To ensure the SC's SOC recovery and lossless accommodation of regenerative energy	Aircraft
32	Control approach	Passivity based control scheme	To reduce the transients on the FC	HEV
33	Control approach	Hysteresis algorithm based EMS	To improve the fuel economy and FC durability	HEV
34	Control approach (EMO)	Hysteresis control (PMP based EMS)	To maintain the SOC, and to minimize the fuel consumption	HEV
35	Control approach	Finite state machine based EMS	To maximize the FC net power without causing oxygen starvation, and to satisfy the charge and discharge capabilities of the ESS	HEV
36	Control approach	State-machine control based EMS	To reduce the transients on FC and to enable the operation of braking resistor when required during regenerative braking	Tramway
37	Control approach	Two-stage controller based EMS	To minimize the fuel consumption and SOC deviation from its target	HEV
38	Control approach	Time delay control	To prevent the starvation of air in the PEMFC	HEV
39	Control approach	Central controller based on AVR technology	To improve the transient response of the PEMFC by regulating the air stoichiometry and stack temperature in accordance to the power demand	HEV
40	Control approach	Feedback closed loop control based EMS	To minimize the energy cost, to maintain the battery operation in the desired SOC operating range, and to maintain the transients on the battery and SC.	HEV

41	Control approach	EMS based on FLC	To maximize the efficiency of HES	HEV
42	Control approach	EMS based on FLC	To maximize the efficiency of HES	HEV
43	Control approach	EMS based on FLC	Maximization of fuel economy and lifetime of FC	HEV
44	Control approach	EMS based on FLC	To maximize the efficiency of HES	HEV
45	Control approach	EMS based on FLC	To maximize the efficiency of HES	HEV
46	Control approach	EMS based on FLC	To maximize the fuel economy	HEV
47	Control approach (DO)	EMS based on FLC (Bisection method)	To reduce the dynamic load of FC, and to maintain the battery SOC (Minimization of cost)	Locomotive
48	Control approach	Fuzzy charging strategy based EMS	To regulate the battery SOC to increase its lifetime	HEV
49	Control approach	EMS based on FLC	To stabilize the DC-bus voltage	HEV
50	Control approach	Combined wavelet theory and FLC based EMS	To maximize the fuel economy and lifetime of power sources	HEV
51	Control approach	Combined FLC and Haar wavelet transform based EMS	To maximize the fuel economy and lifetime of power sources	Tramway
52	Control approach	Combined MPPT and FLC based EMS	To optimize the solar power, and to maintain the battery SOC	Boat
53	Control approach	Auto-regressive moving average regulator	To minimize the PEMFC fuel consumption	HEV
54	Control approach	EMS based on reinforcement learning	To minimize the variation of battery SOC	HEV
55	Control approach	Radial-basis-function networks based adaptive optimal control	To minimize the fuel consumption and the difference between the initial and final SOC levels of the ESS	HEV
56	DO	Rule based deterministic algorithm	To minimization the investment and operating costs	HEV
57	DO	Deterministic algorithm with gradient technique	To minimize the cost and mass of the overall system	HEV
58	DO	GA, and PSO	To minimize the mass, cost and volume of the HES	HEV
59	DO	GA	To minimize the hydrogen consumption and vehicle cost	HEV

60	DO	Non-linear programming	To maximize the efficiency, and minimize the mass and cost of the overall system	HEV
61	DO	Branch and bound algorithm	To minimize the mass of the hybrid energy storage system	HEV
62	DO	Exhaustive search on feasible objective space	To minimize the cost of the HES	HEV
63	DO	Heuristic search	To minimize the cost of the HES	Locomotive
64	DO	Heuristic search	To maximize the efficiency of the HES	HEV
65	DO of ESS	Heuristic search	To minimize the ESS costs, and maximize the fuel economy	HEV
66	EMO	DP, PMP, and GA	To minimize the fuel consumption and battery power contribution	HEV
67	EMO	MATLAB optimization toolbox	To minimize the fuel consumption, and maximize the efficiency of the hybrid power system	HEV
68	EMO	Rule based deterministic algorithm	To minimize the fuel consumption and FC degradation	HEV
69	EMO	Global optimisation algorithm based on optimal control theory	To minimize the hydrogen consumption	HEV
70	EMO	GA	To minimize the hydrogen consumption and difference between initial and final battery SOC	HEV
71	EMO	GA	To minimize the daily operation cost	HEV
72	EMO	GA	To minimize the fuel consumption, to maximize the efficiency of the HES, to minimize the difference between required and achieved speed, and SOC value at the end of drive cycle	HEV
73	EMO	PMP, and DP	To minimize the hydrogen cost of the FC system, and battery charge/discharge cost	HEV
74	EMO	PMP	To maximize the SC absorption of braking energy	Locomotive
75	EMO	PMP	To minimize the fuel consumption while keeping the SOC in an acceptable range	HEV
76	EMO	Adaptive EMS based on PMP	To request the PEMFC power reference based on its real behavior	HEV
77	EMO	Stochastic DP based EMS	To minimize the fuel consumption and PEMFC degradation	HEV
78	EMO	Gobal Extremum Seeking	To maximize the fuel economy and fuel consumption efficiency	HEV
79	EMO	Line search algorithm	To minimize the fuel consumption, and maintain the energy level of the ESS	HEV

80	EMO	GA	To minimize the fuel consumption	HEV
81	EMO	Co-evolutionary algorithm	To minimize the fuel consumption and keep the system states near the best working point	HEV
82	EMO	Global Extremum Seeking	To maximize the fuel economy	HEV
83	DO + EMO	Branch and bound algorithm	To minimize the component purchase cost, fuel cost, maintenance cost and cost of energy required for battery charging	Plug-in hybrid electric mini-excavator
84	DO + EMO	Branch and bound algorithm	To minimize the component purchase cost, fuel cost and maintenance cost	Plug-in hybrid electric mini-excavator
85	DO + EMO	Stochastic DP	To minimize the fuel consumption and battery energy usage	HEV
86	DO + EMO	GA	To maximize the fuel economy, and minimize the HES cost	HEV
87	DO + EMO	GA for DO, and DP for EMO	To minimize the hydrogen consumption	HEV
88	DO + EMO	PSO	To minimize the vehicle cost and fuel consumption	HEV
89	DO + EMO	Exhaustive search on feasible objective space for DO. EMS is based on classical optimal control theory.	To minimize the hydrogen consumption	HEV

The application of PEMFC based HES is not limited to transportation alone. Similar research on PEMFC based HES for other applications is also reported. For example, under the area of control approach, the moving average filter based EMS with supervisory control, model predictive control based EMS, and EMS based on Hybrid Automata are developed in [90], [91], and [92], respectively for the application of PEMFC based HES in micro-grid. The role of moving average filter in [90] is to separate the average and fluctuating power components. These power components are further modified by the proposed EMS based on the operational limits of the energy sources, such as, the ramp rate constraint of the PEMFC, SOC of the ESS, etc. The modified power components are then fed as the input references to the current controllers of the DC/DC converters connected at the output terminals of the respective energy sources. The primary goal of the model predictive control proposed in [91] is to ensure a stable delivery of electrical power to its local load consumers without compromising the durability of the energy sources. The EMS based on Hybrid Automata [92] aim to regulate the interaction between the discrete and continuous operating states of the HES. The operation cycle of the HES is described by seven discrete states which include the system standby mode, battery charging by the renewable energy system, battery charge preservation by the FC or diesel generator, discharge mode of FC, discharge mode of battery, discharge mode of diesel generator, and hydrogen production by the electrolyser. The continuous transition between the states is defined by the propositional based logic rules which are derived from the knowledge of the operating conditions of the HES, such as, the SOC of the battery, the amount of hydrogen in the storage tank, etc. Similarly, combined MPPT and rule based EMS is implemented in [93] for the operation of photovoltaic (PV)-wind-PEMFC-battery HES in power generation system. While the MPPT technique concurrently tracks the maximum power points of both the PV and wind system, the rule based EMS regulates the distribution of load between the PEMFC and battery.

In the field of optimization approaches, an approach for optimal component sizing of a stand-alone HES consisting of PV, wind generator, diesel generator, FC and battery is reported in [94] for domestic power distribution. In this research article, the harmony search algorithm is adopted to solve the problem of DO. Similar approaches for the optimal sizing of a standalone PV-wind-FC-HES, standalone wind-FC-HES, and a grid connected wind-FC-HES combining heat and power system are reported in [95], [96] and [97], respectively for residential application. In [95], four different heuristic algorithms, namely, the PSO, Tabu search, simulated annealing and harmony search are applied, and the results are compared in terms of the total annual cost of the HES. Likewise, the PSO based solution algorithms are implemented for DO in [96], [97]. In [98], the optimal component sizing of a stand-alone micro-grid using GA is provided considering the degradation models of the FC electrolyzer and battery. Such degradation models are included in the optimization model to study the effect of degradation on component sizing. The authors in [99] present the DO problem to determine the optimal rating requirements of the components of a FC-PV-wind-battery-HES for its application in desalination systems. In this paper, improved bee algorithm is used to solve the DO problem. In [100], the DO approach is formulated for the application of a PEMFC-battery-PV-HES in radio base station. In this optimization approach, the sizes of the HES components are heuristically chosen. With regard to EMO, the evolutionary programming based EMO approaches are presented in [101] and [102] for the optimal operation of the PEMFC based hybrid distributed power generation plants. In [103], similar EMO problem is reported and solved using GA to optimize the power flow control of a stand-alone FC-PV–diesel–battery–HES.

An important challenge associated with the application of a PEMFC based HES is to maintain a constant DC-bus voltage across the load against the wide variation in the PEMFC output voltage with varying operating and loading conditions. This can be achieved through the use of pulse width modulation (PWM) controlled DC/DC converter. In literature, there are several research articles where the use of different DC/DC converter topologies is reported for the implementation of the PEMFC based HESs in various applications. In these HESs, the energy sources are either directly connected to the DC-bus or are connected via. DC/DC converters. The authors in [104] show the use of a PEMFC-SC-HES in laptop. In this HES, the traditional DC/DC buck converter is implemented. In [105], three different topologies of the PEMFC-battery-HES, i.e. the series hybrid, parallel hybrid and series-parallel hybrid topologies are reported for application in distributed generation system. In these HESs, the closed loop controlled DC/DC boost converters are implemented to interface the HES with the load, and to control the power flow in the HES in accordance to the EMS. In transportation too, similar research on the PEMFC based HES and DC/DC converters are reported. Examples of such HES include the PEMFC-battery-HES [28], [34], [36], [38], [47], [53], [77], [79], PEMFC-battery-PV-HES [14], PEMFC-SC-HES [9], [13], [21], [26], [27], [32], [55] and PEMFC-SC-battery-HES [30], [40], [51], [66]. The different transportation areas include the HEV [13], [14], [21], [26]–[28], [32], [34], [38], [40], [53], [55], [66], [77], [79], locomotive [47], tramway [30], [36], [51] and crane [9]. To regulate the converter duty-cycle in order to provide constant boost to the DC-bus voltage, and to control the PEMFC output current, the dynamic evolution control and time delay control are employed in [38], respectively. Likewise, the rule based control scheme [9], [13], [14], [21], [36], predictive control based EMS [30], passivity based control scheme [32], hysteresis control [34], PMP based EMS [34], [66], FLC [47], combined FLC-wavelet transform based EMS [51], ARMA regulator [53], EMS based on DP [66], [77], real-time optimal power splitting method based on line search algorithm [79], and adaptive optimal control based on neural network [55] are used to generate the current/power references for the DC/DC converters connected at the output terminals of the hybrid energy sources. In [26]–[28], the converter switching is carried out in such a way that the ESS operates to supply/absorb the transient power at high rates, and the PEMFC operates at constant power. In [40], for optimal load distribution in the HES, the entire HES is split into two sub-systems, i.e., the PEMFC-battery and battery-SC. These are individually controlled through DC/DC converters with controllers based on optimal control theory. However, in all the above mentioned articles, the study is carried out only through computer simulation. No hardware results are presented.

However, there are some research papers reported in literature where the HES dynamics, and the performance of the closed loop controlled DC/DC converters are tested on an experimental platform [6], [12], [15], [18]–[20], [31], [39], [49], [74]–[76], [93], [106], [107]. In these research articles, the PEMFC based HES finds application in electric aircraft [31], locomotive [74], HEV [12], [15], [18]–[20], [39], [49], [75], [76], tramway [6], power generation system in remote areas

[93] and uninterruptible power supply (UPS) system [106], [107]. The different types of PEMFC based HES reported in these works are PEMFC-battery-HES [12], [15], [18], [19], [39], [75], [76], [107], PEMFC-SC-HES [31], [74], [106], PEMFC-battery-SC-HES [6], [20], [49] and PV-wind-PEMFC-battery-HES [93]. To regulate the power flow in these HES by generating the desired current/power references for the DC/DC converters, different EMS are devised, such as, the EMS based on a modified droop control [31], PMP based EMS [74]–[76], central controller based on the AVR technology [39], rule based EMS [12], [15], [18]–[20], FLC based EMS [49], ECMS [6] and combined MPPT-rule based EMS [93]. For the reduction of the current ripples in the UPS system, a push–pull DC/DC converter with active-clamp circuit is presented in [106]. In [107], an intelligent comprehensive controller is designed to control the PEMFC power generation by constantly monitoring the operational parameters of the energy sources. A comprehensive review on some of the converter topologies is given in Table 1.2.

Table 1.2: Comprehensive information on some of the converter topologies used for the implementation of PEMFC based HES in different applications.

Ref. No.	DC/DC Converter topology (power switch)	PWM control scheme	Application	If PWM control design presented?	If hardware test done?
[6]	U-BC (IGBT) and Bi-BBC (IGBT)	Cascade bi-loop control	Tramway	No	Yes
[9]	U-BC and Bi-BC	Two step CC for U-BC; Cascade VC and CC for Bi-BC.	Crane	No	No
[12]	BC	CC	HEV	No	Yes
[13]	BC and Bi-BBC	Interconnection and damping assignment passivity based control	HEV	Yes	No
[14]	BuC	CC	HEV	No	No
[15]	BuC (IGBT)	CC	HEV	No	Yes
[18]	U-BC	CC	HEV	No	Yes
[20]	U-PT isolated BC (MOSFET) and Bi-BBC (IGBT)	VC for U-PT isolated BC; CC for Bi-BBC.	HEV	No	Yes
[21]	U-BC and Bi-C	VC for Bi-C; CC for U-BC	HEV	No	No
[26]	U-BC and Bi-BBC	Converters controlled to maintain DC bus voltage constant	HEV	No	No
[27]	U-BC and Bi-BBC	VC for U-BC; CC for Bi-BBC.	HEV	No	No
[30]	U-BC, Bi-BC and Bi-BuC	CC for U-BC, and Bi-BuC; Cascade VC and CC for Bi-BC.	Tramway	No	No
[31]	U-BC and Bi-BBC	Virtual resistor droop control for U-BC; Virtual impedance droop control for Bi-BBC.	Aircraft	Yes	Yes

[32]	U-BC and Bi-BC	Cascade VC and CC	HEV	No	No
[36]	BC with two switches: main switch and safety switch	Cascade CC	Tramway	No	No
[38]	Bi-BC	Dynamic evolution based CC	HEV	No	No
[39]	U-BuC	CC	HEV	No	Yes
[47]	U-BC	CC	Locomotive	No	No
[51]	U-BC and Bi-BC	CC for U-BC; Cascade VC and CC for Bi-BC.	Tramway	No	No
[55]	U-BC and Bi-BBC	VC and CC	HEV	No	No
[93]	U-PT isolated BC (N-MOSFET) and Bi-BBC (IGBT).	VC for U-PT based BC of solar/wind; CC for U-PT isolate BC of FC, and Bi-BBC.	Power generation in remote areas	No	Yes
[104]	BuC (MOSFET)	VC	Laptop	No	No
[106]	PPC with active clamp circuits	Current ripple reduction based control	UPS	No	Yes
[107]	PPC	VC	UPS	No	Yes
[108]	MISO converter	Combined VC and CC	-	No	Yes

Note. BB: buck-boost, B: boost, Bi: bidirectional, Bu: buck, C: converter, CC: current control, MPPT: maximum power point tracking, PP: push-pull, PT: pulse transformer, U: unidirectional, VC: voltage control.

1.3. Motivations behind this Thesis

The use of PEMFC as an electric power source in transportation is still in the preliminary stage. This is because there are many technical challenges yet to be overcome for the PEMFC to stand in competition with the conventional internal combustion engines in various aspects. These are explained below:

- Cost: According to the report published by the U.S. Department of Energy [109], the platinum remains one of the costliest cost components of the PEMFC and its cost increases with the increase in the rating of the PEMFC. That is why, significant emphasis is being laid on approaches that will increase the utilization and reduce the content of current platinum metal and platinum-alloy catalysts for long-term applications. Besides the development of low-cost FC stack, the development of advanced high-volume manufacturing approaches to reduce the overall system cost is also going on. Keeping this in mind, it is important to optimise the rating of the PEMFC so that it suffices to supply the power demand in different applications with minimum capital and maintenance costs incurred in its deployment.

- Performance: The slow dynamics of the PEMFC is another concern of the current PEMFC technologies. Hence, rapid work is going on in developing innovative materials and integration strategies to improve the PEMFC efficiency and performance. Some of these innovative techniques include developing ion-exchange membrane electrolytes with enhanced efficiency and durability at reduced cost; improving membrane electrode assemblies with high power density; modeling to understand system design and operating conditions; developing stacks with high-performance air management components with low parasitic losses, etc.

- Durability: The presence of various critical components in the PEMFC stack raises the concern of the PEMFC durability, since these components are prone to damage when subjected to frequent load variations. Hence, rapid research is going on in identifying and understanding the FC degradation mechanisms and developing materials and strategies to mitigate their effects.
- Energy Management: The aforementioned technical drawbacks of the current PEMFC technology demands its use in conjunction with some ESS to form a HES. However, the optimal energy management in such HES is crucial in order to minimise the operating cost of the HES and to ensure the optimum utilization of the energy sources without causing their wear and tear.

In view of the above discussion, the present thesis is basically focused on the development of a PEMFC-battery-HES for locomotive applications which can offer satisfactory performance both in terms of the capital and operational investments. Furthermore, from the literature survey carried out so far, the following research gaps are identified:

- Very few research articles [47], [63], [74] are reported on the application of the PEMFC based HES in locomotives.
- In [47] and [63], the problem of DO is addressed. In [47], the modelling, simulation and analysis of PEMFC-battery-HES for locomotive applications are provided using the software package called advanced vehicle simulator (ADVISOR). The sizing of the HES components is done using bi-section method. In [63], the potential benefits and implementation difficulties of PEMFC-battery-HES for various types of locomotives are provided. The best combination of the PEMFC-battery-HES in terms of minimum system cost is heuristically chosen. However, in none of these works, the determination of the component sizes of the HES is not done with the formulation of an optimization approach.
- A critical requirement of a HES is to design an efficient EMS to regulate the power flow in the HES based on the operational characteristics of the energy sources. In locomotive

applications, a FLC based EMS is implemented in the PEMFC-battery-HES in [47], and its efficiency is tested through simulation in ADVISOR software. No optimization based EMS is presented in this paper. In [74], the PMP based optimal EMS with the objective function of maximizing the regenerative energy absorption by the SC is proposed. However, the study presented in this paper is only concentrated on the braking region of the speed curve. The performance analysis of the PEMFC-SC-HES under a practical drive cycle scenario with multiple acceleration/deceleration period, variable constant speed regimes and stops is not carried out in [74].

- Since both the PEMFC and battery exhibit variation in their output voltages in relation to the variation in operating and loading conditions, the PEMFC-battery-HES needs a DC/DC converter to maintain a stable DC-bus voltage across the load. A control action is also required to ensure the power sharing among the components of the HES in accordance to the EMS. This can be done through proper PWM control of the converter switches. In literature, different DC/DC converter topologies and PWM control approaches are proposed. Out of these, the study on the design and control of converters for PEMFC based HES application in locomotives are reported in [47] and [74]. In [47], the performance analysis of the PEMFC-battery-HES is carried out through simulation using ADVISOR. No experimental analysis is carried out in this paper. Conversely, in [74], the dynamics of the PEMFC-SC-HES and the DC/DC converters are experimentally tested on a real time-lab platform. However, in these papers, the design procedures of the DC/DC converters and the PWM controllers are not discussed.
- The integration of FC vehicles faces a “chicken-egg dilemma” as vehicles need a proper refueling infrastructure to provide a safe and continuous hydrogen supply, but a viable deployment of the hydrogen refueling stations (HRS) needs the support of an initial market of the vehicles [110]. In view of this, several research on the alternative refueling infrastructure planning are carried out in [110]–[135]. However, in none of these works, studies on the HRS infrastructure planning for the deployment of hydrogen powered locomotives are reported.

These research gaps are the motivations behind the present work.

1.4. Objectives of this Thesis

Based on the research gap discussed in the previous section, the following objectives are proposed in the present thesis:

- Use of the PEMFC-battery-HES powered locomotives to replace the conventional diesel locomotives operating in Indian Railways.
- Determination of the rating requirements of the PEMFC and battery that constitute the HES such that the proposed HES is capable of supplying the locomotive power demand under different driving conditions.
- Development of the control approaches to regulate the power flow in the PEMFC-battery-HES and to maintain the DC-bus voltage across the locomotive load.
- Optimal energy management in the PEMFC-battery-HES to supply the locomotive load with the aim of minimizing the PEMFC fuel consumption without violating the operational constraints of the energy sources.
- Determination of the optimal locations of the HRS for the deployment of the hydrogen powered intercity passenger trains in the North Eastern Frontier Railway (NEFR), Assam, India.
- Infrastructure planning of the HRS in terms of the capital and operational costs for different scenarios of installed HRS capacity.

1.5. Organization of this Thesis

This thesis is organized as follows:

- In Chapter-2, the single-objective and multi-objective DO approaches for optimal component sizing of the PEMFC-battery-HES are presented so that the designed HES is capable of providing the driving force required to haul the intercity passenger trains operating on short to medium distant routes. The variation in the sizes of the PEMFC and battery with the choice of EMS, the drive cycle, etc. is also highlighted in this chapter.
- In Chapter-3, the design of the PWM control approaches for the multi-input single-output (MISO) DC/DC boost converter is carried out to meet the requirements of the application of the PEMFC-battery-HES in locomotives, i.e., the regulation of the DC-bus voltage and the implementation of the EMS. The performance of the PWM controlled MISO converter is verified both through computer simulation, and on developing the experimental setup of the HES and MISO converter for a practical drive cycle scenario.
- In Chapter-4, two different EMO approaches with and without the durability constraints of

the energy sources are formulated for the optimal distribution of load in the PEMFC-battery-HES for locomotive applications. Execution of the EMO approach is done using General Algebraic Modelling System (GAMS). Simulation study to test the proficiency of the proposed EMO approaches for practical drive cycle scenarios is also presented in this chapter.

- In Chapter-5, the optimal allocation planning of the HRS for the rollout of the hydrogen powered intercity passenger trains in NEFR, Assam, India is presented. For this, single-objective and multi-objective optimization approaches are formulated to satisfy the constraints and deployment feasibility of the HRS in locomotive applications. The total investments incurred in the HRS infrastructure development under the different scenarios of installed HRS capacity, in terms of their capital costs including the annual maintenance and refueling costs of the HRS are also investigated in this chapter.
- In Chapter-6, the conclusions of the whole work and some of the future research directions in this area are presented.

1.6. Contributions of this Thesis

The main contributions of this thesis are summarized below:

- Mathematical modelling of the PEMFC-battery-HES is carried out to retrofit the WDM-3D class of diesel locomotives which are currently used to drive the intercity passenger trains operating under the department of NEFR, Assam, India.
- The single-objective and multi-objective DO approaches are formulated to determine the optimal rating requirements for the PEMFC and battery that constitute the HES. This is done so that the designed HES is capable of providing the tractive force to pull the intercity passenger trains operating on short to medium distant routes. To solve the DO approaches, two different EMSs based on the operational constraints of the energy sources are developed, and are used as the support sub-routines in the PSO based solution algorithms.
- The design and control of the MISO DC/DC boost converter are carried out to interface the PEMFC-battery-HES to the load. The performance of the PWM controlled MISO converter is tested through computer simulation, and on developing an experimental setup. For simulation study, a reduced scale prototype model of the proposed HES and the PWM controlled MISO converter is developed. The PWM controllers are simulated following the mathematical concept of Venable K-factor, and aim to regulate the DC-bus voltage and the

power flow control in the HES. For experimental study, the (printed circuit board) PCB layout of the MISO converter is designed, and the PWM control system is implemented through MATLAB simulation and using the DSP kit as an interface between the simulation software and hardware setup.

- Mathematical formulation of two EMO approaches with and without the durability constraints of the energy sources is carried out for the optimal distribution of load in the PEMFC-battery-HES for locomotive applications. Both the EMO approaches are executed as offline optimization processes using GAMS.

The single-objective and multi-objective optimization approaches are developed to determine the optimal location of the HRS for the commercial deployment of the hydrogen powered intercity passenger trains in NEFR, Assam, India. For this, the network of existing intercity railway stations of Assam, India is considered as the potential base layout for allocating the HRS. Suitable solution strategies are also devised, and are used as the support subroutine in the binary PSO algorithm to solve the optimization problems.

Chapter 2

Design Optimization of PEMFC-battery-HES for Locomotive Applications

2.1. Introduction

Rapid industrialization, environmental degradation and diminishing fossil fuel reserves have motivated the research community around the globe to work on the development of economically feasible renewable energy systems. A major part of the energy demand is still met by fossil fuels which draw on finite resources that will eventually dwindle, becoming too expensive and environmentally damaging to retrieve. Thus, the development of economically feasible renewable energy systems to replace the fossil fuel run machineries is one of the major challenges facing the globe. Hydrogen is one such green energy source. In the recent years, the pace of investment in developing technologies for hydrogen fueled energy sources is greatly increased. The PEMFC is one such technology [1]. It has several advantages, such as, high power density, low operating temperature, high efficiency, etc. Due to the relatively lower operating temperature of the PEMFC, this form of FC can be used in replacing the traditional petroleum-based drives. However, owing to the technical drawbacks of high cost, shorter lifetime, slow dynamic response, etc., the hybridization of the PEMFC with some ESS is preferred. The investment and operational costs are the important factors associated with a PEMFC based HES. Thus, it is important to optimize the sizes of the HES components and to design an efficient EMS for optimum load distribution among the hybrid energy sources. In literature, several research papers are reported on the use of PEMFC based HES in different transportation applications [2]–[79], [83]–[89]. The research is multidirectional and is classified based on the following attributes:

- ***Development of control strategy***: This include those research articles where the design of some EMS to control the power flow in the HES is carried out. Examples of some of the control approaches are the ECMS [5]–[7], rule based EMS [8]–[21], EMS based on adaptive supervisory control [22], EMS with constant/quasi state power operation of the PEMFC [23]–[28], model predictive control [29], [30], decentralized EMS based on mixed droop strategy [31], passivity based control scheme [32], hysteresis control [33], [34], state-machine control based EMS [35], [36], two-stage controller based EMS [37], time delay control [38], central controller based on AVR technology [39], feedback closed loop control based EMS [40], EMS based on FLC [41]–[49], combined FLC-wavelet transform based EMS [50], [51], combined MPPT-FLC based EMS [52], ARMA regulator [53], EMS based on reinforcement learning [54], and neural network based adaptive optimal control [55], etc.
- ***DO and EMO for PEMFC-based HES***: The formulation of the DO approaches for the optimal component sizing of the HES, and the EMO approaches for optimal energy management in the HES are carried out in [56]–[65] and [66]–[82], respectively. The studies on the combined DO and EMO approaches are reported in [83]–[89].
- ***Different transportation applications***: This includes the HEV [2]–[5], [10]–[22], [24]–[29], [32]–[35], [37]–[46], [48]–[50], [53]–[62], [64]–[67], [67]–[73], [75]–[82], [85]–[89], tramway [6]–[8], [30], [36], [51], crane [9], wheelchair [23], aircraft [31], locomotive [47], [63], [74], boat [52], plug-in mini excavator [83], [84], etc.
- ***Solution approach for the DO and EMO problems***: The solution strategies can be categorized into: (i) **mathematical and enumerative approaches**, such as, bisection method [47], rule based deterministic algorithm [56], [57], [68], heuristic search [2]–[4], [62]–[65], [89], non-liner programming [60], branch and bound algorithm [61], [83], [84], PMP [34], [66], [73]–[76], DP [66], [73], [77], [85], [87], line search algorithm [79], etc., and (ii) **meta-heuristic approaches**, such as, GA [58], [59], [66], [70]–[72], [80], [86], [87], PSO [58], [88], Co-evolutionary algorithm [81], Global Extremum Seeking algorithm [78], [82], etc.

From the above literature survey, it is seen that there are very few published works where the DO of the PEMFC based HES is reported for locomotive application, [47] and [63]. In [63], the potential benefits and implementation difficulties of PEMFC-battery-HES for various types of locomotives are provided. The best combination of PEMFC-battery-HES in terms of the minimum system cost is heuristically chosen. In [47], the modelling, simulation and analysis of PEMFC-battery-HES for locomotive application are provided using the software package called ADVISOR. The sizing of the HES components is done using bi-section method. The FLC based EMS is used to meet the dynamically varying power demand of the locomotive. However, neither the determination of the component sizes of the HES nor the design of the EMS is done with the formulation of an optimization approach. Thus, from the literature review, it is seen that the mathematical formulation of the DO and EMO approaches for the PEMFC-battery-HES in locomotive applications is not reported, till date. This research gap is the motivating factor behind the proposed work which aims at the development of an optimization approach for the component sizing of the PEMFC-battery-HES. Thus, the objectives of this chapter are:

(i) Development of a PEMFC-battery-HES model which is capable of providing similar tractive effort as the diesel locomotive, WDM-3D, which is used to haul the intercity passenger trains running over short to medium distances in NEFR, Assam, India.

(ii) Formulation of the single-objective and multi-objective optimization approaches to determine the sizes of the HES components.

(iii) Development of the EMS and appropriate solution strategies for solving the optimization problems formulated.

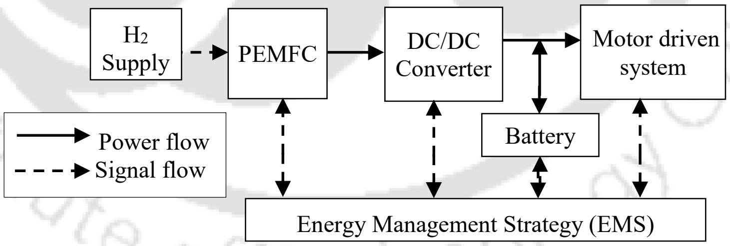

Fig. 2.1: Topology of the PEMFC-battery-HES.

2.2. Modelling of the PEMFC-battery-HES

The proposed HES consists of the PEMFC as the primary energy source and a pack of lithium-ion batteries as the ESS. Lithium-ion battery is chosen here, since it has the advantage of high power density, high energy density, longer lifetime, low cost per watt-hour rating, etc. The topology of the HES is shown in Fig. 2.1. The HES is designed so that it is capable of providing similar tractive effort as the diesel engine of the Indian locomotive class, WDM-3D, which is used to drive the intercity passenger trains in India. An intercity passenger train operates between two terminal stations over short to medium distant routes with a number of intermediate stops in different stations. The train speed varies throughout the driving period, and accordingly the power demand also varies. This implies that the proposed PEMFC-battery-HES is designed to meet the dynamically varying power demand of the train.

2.2.1. Model of PEMFC

The PEMFC system consists of a FC stack and some auxiliary components. The stack comprises of a number of cells connected in series-parallel combination to generate the required voltage and output power. The theoretical cell potential of the PEMFC is dependent on the cell temperature, and the partial pressures of oxygen and hydrogen. The theoretical cell potential or the reversible voltage of the PEMFC, v_{rev} is obtained from the Nernst equation [1] as follows:

$$v_{rev} = E_0 - \frac{RT}{n_{e^-}F} ln \left\{ \frac{p_{H_2O}}{p_{H_2}(p_{O_2})^{1/2}} \right\} \tag{2.1}$$

Where, E_0 is the open circuit voltage of the PEMFC; R is the universal gas constant (8.314 *J/K/mol*); T is the cell temperature; F is the faraday's constant (96,450 *C/mol*); n_{e^-} is the number of electrons generated in the electro-chemical reaction (which is 2); p_{H_2O} is the partial pressure of water (assumed to be 1 *atm*); and p_{O_2} and p_{H_2} are the partial pressures of oxygen and hydrogen, respectively. The value of E_0 is 1.229V, if water produced as the by-product of the electro-chemical reaction is in liquid state, and 1.18V if the water is in gaseous state. These values of E_0 correspond to the temperature of 298.5K, and p_{O_2}, p_{H_2} of 1 *atm*. However, the actual cell potential is lower than the theoretical cell potential due to the several losses occurring in the FC. These losses mainly include the activation loss which occurs due to the slowness of the reaction taking place on the surface of the electrodes; ohmic loss due to the resistance offered to the flow of electrons through the electrodes and the ions through the electrolyte; and the concentration loss due to the decrease in the reactant concentration at the surface of the electrodes. Thus, the actual FC voltage, v_{fc} is given by Eq. (2.2) as follows:

$$v_{fc} = v_{rev} - v_{act} - v_{ohm} - v_{conc} \tag{2.2}$$

Where, v_{rev} is the theoretical cell potential of the PEMFC; and v_{act}, v_{ohm} and v_{conc} is the voltage drop corresponding to the activation loss, ohmic loss and concentration loss, respectively.

A typical polarization curve showing v_{fc} as a function of the current density is given in Fig. 2.2(a). Thus, the electrical output power of the PEMFC stack, P_{fc}^{stack} is defined mathematically as follows:

$$P_{fc}^{stack} = v_{fc} i_{stack} \tag{2.3}$$

Where, i_{stack} is the current generated by the PEMFC stack. The efficiency of the PEMFC stack, η_{stack} is defined as the ratio of the electrical power generated by the PEMFC stack (P_{fc}^{stack}) to the power available in the hydrogen consumed (P_{H_2}). Mathematically, η_{stack} is expressed as follows:

$$\eta_{stack} = \frac{P_{fc}^{stack}}{P_{H_2}} = \frac{P_{fc}^{stack}}{\dot{m}_{H_2} \Delta H} \tag{2.4}$$

Where,

$$\dot{m}_{H_2} = \frac{m i_{stack}}{n_{e^-} F} \tag{2.5}$$

Where, $\dot{m}_{H_2}$ is the rate of hydrogen consumption; ΔH is the enthalpy of the electro-chemical reaction; and *m* is the hydrogen molecular weight. A fraction of the power generated by the PEMFC stack is consumed by the PEMFC auxiliary components, P_{fc}^{aux} which are responsible for keeping the stack operational by supplying air and hydrogen, by humidifying the reactant gases, and by cooling the stack, etc. Thus, the net power output of the PEMFC system, P_{fc} is defined as follows:

$$P_{fc} = P_{fc}^{stack} - P_{fc}^{aux} \tag{2.6}$$

Accordingly, the overall efficiency of the PEMFC system (η_{fc}) is expressed as follows,

$$\eta_{fc} = \frac{P_{fc}}{P_{H_2}} = \eta_{stack} \frac{P_{fc}^{stack} - P_{fc}^{aux}}{P_{fc}^{stack}} = \eta_{stack} \left(1 - \frac{P_{fc}^{aux}}{P_{fc}^{stack}}\right) \tag{2.7}$$

The PEMFC efficiency map as a function of part load ratio (PLR) is taken from [136], and is shown in Fig. 2.2(b). The term PLR represents the ratio of the electrical power output of the PEMFC system to the PEMFC rated power, i.e., $\left(\frac{P_{fc}}{P_{fc}^{rated}}\right)$. The mathematical equations to approximate $\eta_{fc}(PLR)$ is given by Eqs. (2.8) and (2.9).

$$\eta_{fc}(PLR) = 0.2716; if\ PLR(t) < 0.05 \tag{2.8}$$

$$\eta_{fc}(PLR) = 0.9033. PLR(t)^5 - 2.996. PLR(t)^4 + 3.6503. PLR(t)^3 - 2.0704. PLR(t)^2$$
$$+0.4623. PLR(t) + 0.3747; if\ PLR(t) \geq 0.05 \tag{2.9}$$

The total fuel consumption of the PEMFC (m_{H_2}), and the corresponding heat generated, Q_{heat}, during the driving period can be derived from Eqs. (2.4) and (2.5), as follows:

$$m_{H_2} = \int \frac{P_{fc}}{\Delta H \eta_{fc}(PLR)} dt = \int \frac{P_{fc}}{LHV \eta_{fc}(PLR)} dt \qquad (2.10)$$

$$Q_{heat} = m_{H_2}.LHV \qquad (2.11)$$

Where, *LHV* is the lower heating value of hydrogen (120 *MJ/kg*). However, the slow dynamic response of the PEMFC auxiliary components imposes a limit on the rate of change of P_{fc}. This limit is represented by the ramp rate constraint, R_{max}. In this study, R_{max} is calculated considering that P_{fc} takes about 30 seconds to reach 90% of its rated power, P_{fc}^{rated} [137]. Thus, R_{max} and the instantaneous $P_{fc}(t)$ are defined as follows:

$$\frac{dP_{fc}}{dt} = R_{max} = \frac{90\% \; of \; P_{fc}^{rated}}{t = 30 \; sec} \qquad (2.12)$$

$$\int dP_{fc} = \int R_{max} dt \qquad (2.13)$$

$$P_{fc}(t) = R_{max} t + P_{fc}^{0} \qquad (2.14)$$

Where, P_{fc}^{0} is the PEMFC output power at the beginning of the acceleration/deceleration period.

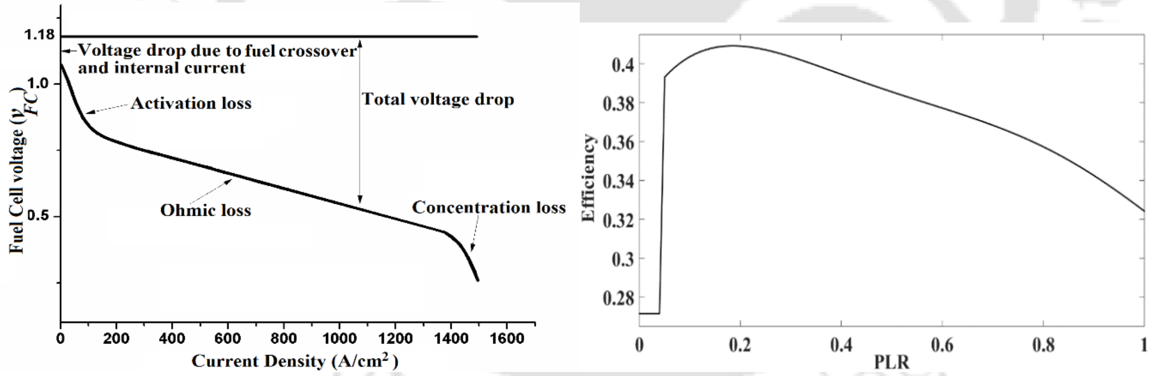

(a) (b)

Fig. 2.2: Overview of the PEMFC: (a) Polarization curve and (b) Efficiency map.

2.2.2. Model of Lithium-ion battery

The lithium-ion battery is designed in the proposed HES to assist the PEMFC power output during transient conditions. The instantaneous output power of the battery, $P_{bat}(t)$ is computed as follows,

$$P_{bat}(t) = P_{load}(t) - P_{fc}(t) \qquad (2.15)$$

Where, $P_{load}(t)$ is the instantaneous locomotive power demand. Thus, $P_{bat}(t)$ can be either positive or zero or negative. The positive (negative) $P_{bat}(t)$ implies the discharging (charging) state of the operation. If $P_{bat}(t)$ is zero, the battery remains idle. Accordingly, the *SOC* of a battery at any instant of time is mathematically calculated as given in Eq. (2.16).

$$SOC(t) = SOC(t - \Delta t) - \boldsymbol{\eta_{bat}} \frac{P_{bat}(t)}{Q_{bat}^{rated}} \Delta t \tag{2.16}$$

Where, η_{bat} is computed as follows:

$$\eta_{bat} = \begin{cases} \frac{1}{\eta_{chg}}, & for\ P_{bat}(t) \leq 0, during\ battery\ charging \\ \eta_{dis}, & for\ P_{bat}(t) > 0, during\ battery\ discharging \end{cases} \tag{2.17}$$

Where, η_{chg} and η_{dis} are the charging and discharging efficiency of the battery; Q_{bat}^{rated} is the battery capacity; and Δt is the small increment in time.

2.2.3. *Model of Instantaneous Power Demand of a Train*

The $P_{load}(t)$ represents the summation of the instantaneous power demand of a train, and the power consumed by the auxiliaries of the train, such as, the traction motor blower, air brakes, lighting loads, etc., P_{aux}. The instantaneous power demand of a train is governed by the simple law of physics which defines power as the product of the mechanical forces acting on it and the instantaneous speed of the train, $\vartheta(t)$. These mechanical forces include the aerodynamic drag (F_{drag}), force of friction between the wheels and railway track (F_{rr}), force to overcome a slope/gradient (F_{climb}), and the force of acceleration (F_{acc}). The mathematical model representing the $P_{load}(t)$ of an inter-city passenger train is given below:

$$P_{load}(t) = [\{F_{rr}(t) + F_{drag}(t) + F_{climb}(t) + F_{acc}(t)\}\vartheta(t)]/\eta_{sys} + P_{aux} \tag{2.18}$$

$$F_{drag}(t) = 0.5\rho D\sigma v(t)^2 \tag{2.19}$$

$$F_{rr}(t) = M_{veh} g R_r cos\beta \tag{2.20}$$

$$F_{acc}(t) = M_{veh} \frac{dv(t)}{dt} \tag{2.21}$$

$$F_{climb}(t) = M_{veh} g sin\beta \tag{2.22}$$

$$M_{veh} = m_{loco} + n_{coach} m_{coach} \tag{2.23}$$

Where, η_{sys} is the transmission system efficiency; ρ is air density (1.293 kg/m^3); D is drag coefficient; σ is cross sectional area; ϑ is locomotive velocity; M_{veh} is vehicle mass; R_r is coefficient of rolling resistance; β is gradient or slope of the railway track on which the train runs,

Table 2.1: Parameters of the locomotive and train coaches.

WDM-3D locomotive					
Bogie type	Co-Co	*Width* (in *m*)	2.95	R_r	0.05
m_{loco} (in *kg*)	117000	*Height* (in *m*)	4.077	*D*	0.75
Non-air conditioned coaches					
m_{coach} (in *kg*)		45300	n_{coach}		10

Table 2.2: Parameters of the drive cycle.

Drive cycle parameters	*Drive cycle 1*	*Drive cycle 3*	*Drive cycle 3*
Time (in *s*)	15960	8700	15360
Distance (in *km*)	167.52	113	151
Maximum speed (in *mph*)	39.7	44	38
Average speed (in *mph*)	23.8	30	21.9
Number of stops	15	7	21

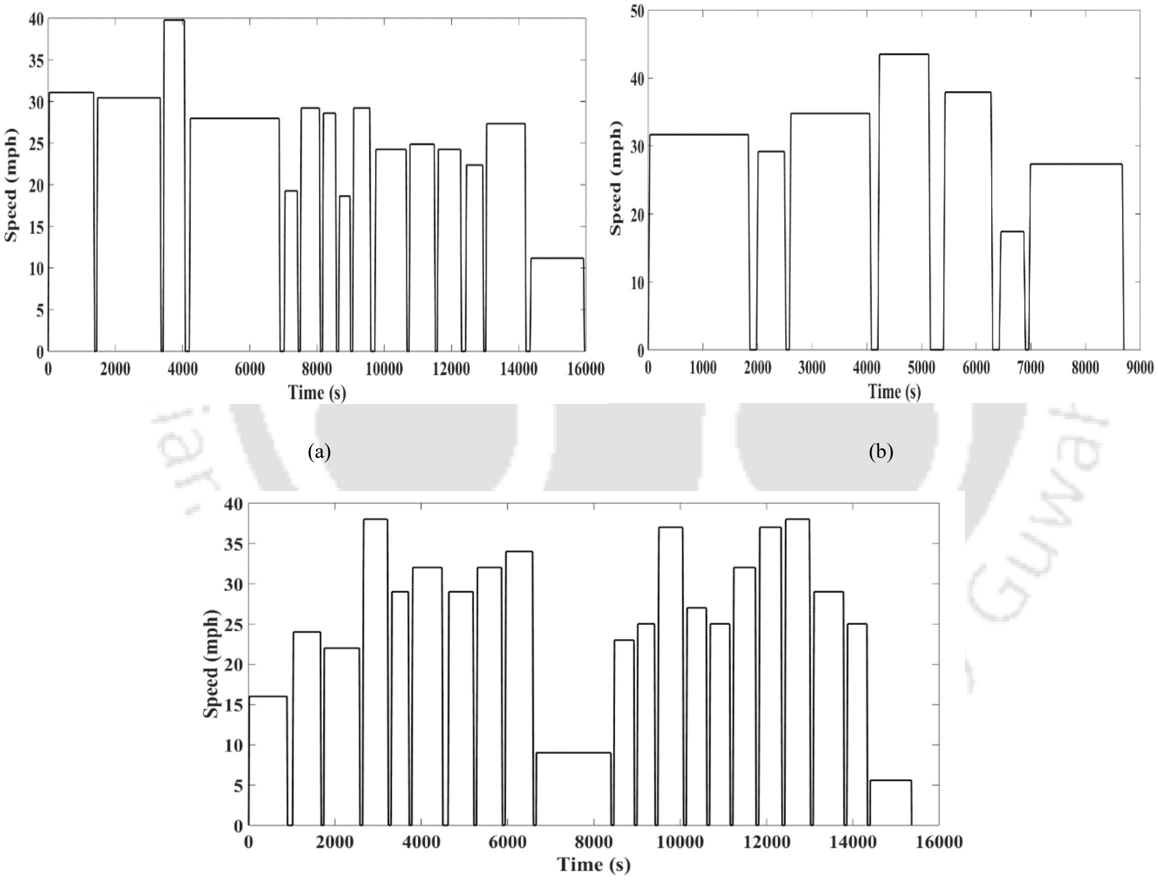

(a)

(b)

(c)

Fig. 2.3: Drive cycles of intercity passenger trains running in Indian railways: (a) drive cycle 1, (b) drive cycle 2 and (c) drive cycle 3.

m_{loco} is the locomotive mass; m_{coach} and n_{coach} are the mass and number of train compartments/coaches. Here, M_{veh} represents the mass of the entire train which includes the locomotive mass and the mass of the train coaches as given in Eq. (2.23). The locomotive class, WDM-3D is considered in this study. The details of the locomotive parameters are taken from [138], and are listed in Table 2.1. It is assumed that all the compartments/coaches are non-air-conditioned coaches. The assumption is valid for most of the intercity passenger trains running in India. The value of m_{coach} is taken from [139], and is also provided in Table 2.1.

2.2.4. *Drive cycle*

A drive cycle is the time-dependant variation of the speed of a vehicle. The instantaneous power demand of the vehicle varies with the drive cycle. In this study, the drive cycles of three intercity passenger trains, operating in Assam, India are considered, and are shown in Fig. 2.3. The drive cycles are developed according to the data provided in [140]. The data provided in [140] is based on the average of the driving patterns followed by the passenger train while running between two terminal stations. However, the actual driving pattern may slightly vary from the average driving pattern on a daily basis. The details of the drive cycle parameters are listed in Table 2.2.

2.2.5. *Energy management strategy*

The purpose of the EMS is to determine the instantaneous output power of the individual HES components to meet the power demand. Two EMSs are proposed in this work. The first EMS, i.e., EMS1 is developed based on the following assumptions/considerations:

a) The $P_{fc}(t)$ increases to its rated value, P_{fc}^{rated} and then operates at P_{fc}^{rated} during acceleration and during the period when the train is running at constant speed. During braking, $P_{fc}(t)$ reduces. In other words, the PEMFC output power varies in accordance to the dynamically varying $P_{load}(t)$. However, the rate of change of $P_{fc}(t)$ is limited by R_{max} as given in Eqs. (2.12) - (2.14).

b) Conversely, the battery operates either in its charging or discharging mode during the entire driving period depending on the power requirement of the train. The battery discharges to assists the PEMFC output power if the PEMFC alone is deficit to meet $P_{load}(t)$. On the other hand, the battery operates in charging mode if $P_{fc}(t)$ is greater than $P_{load}(t)$. In other words, the battery discharges, i.e., $P_{bat}(t)$ is positive when $\left[P_{load}(t) - P_{fc}(t)\right]$ is positive. The battery charges, i.e., $P_{bat}(t)$ is negative when $\left[P_{load}(t) - P_{fc}(t)\right]$ is negative. In other times, the battery remains idle, i.e., $P_{bat}(t)$ is zero.

The second EMS, i.e., EMS2 is developed keeping in mind the slow dynamic response of the PEMFC. This EMS aims to reduce the dynamics on the PEMFC. This EMS is described as follows:

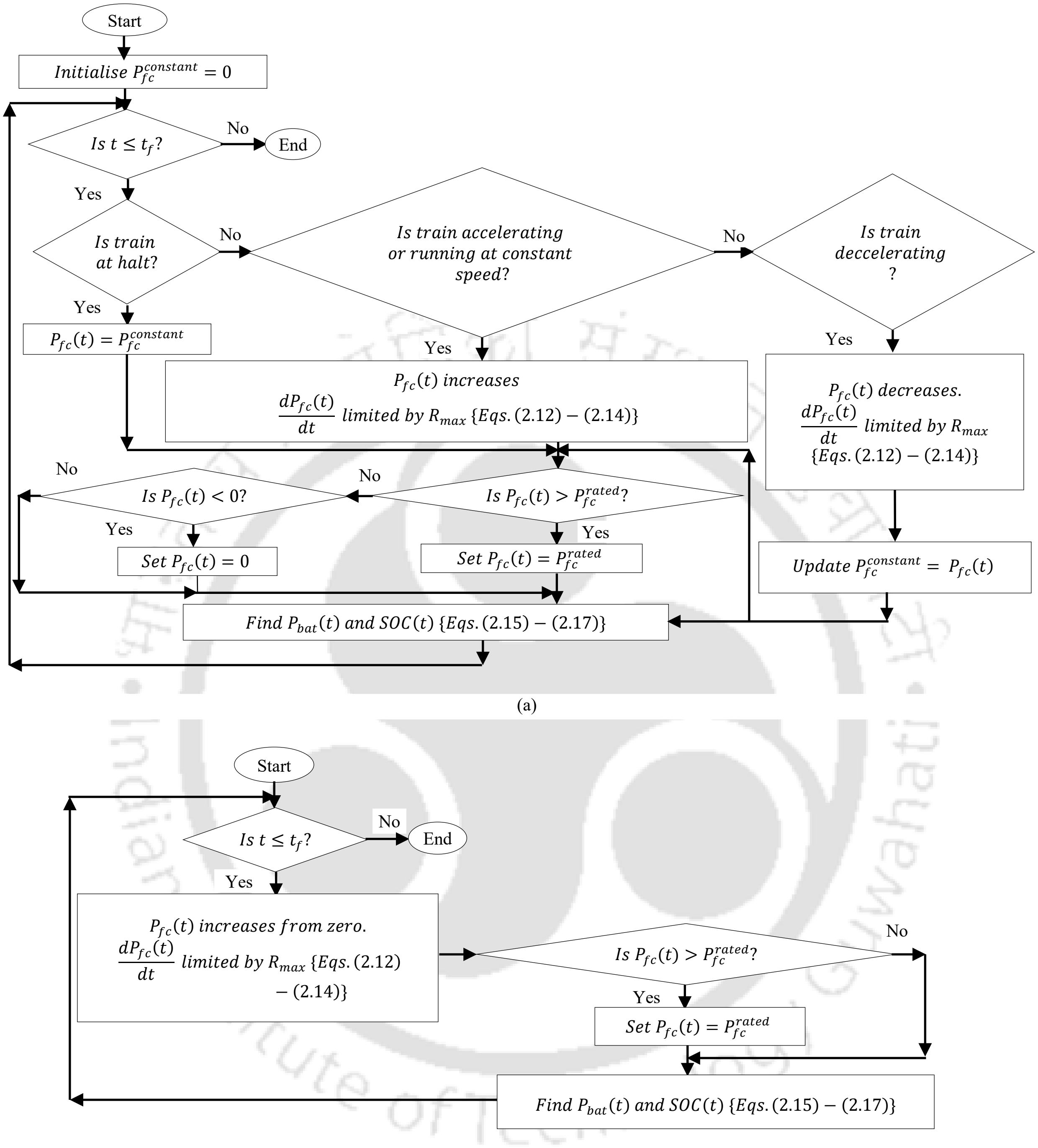

Fig. 2.4: Flowcharts of the EMSs: (a) EMS1 and (b) EMS2.

a) The $P_{fc}\ (t)$ increases initially, the rate of increase of $P_{fc}\ (t)$ is limited by R_{max}. Once $P_{fc}\ (t)$ reaches P_{fc}^{rated}, the PEMFC operates at its rated power throughout the driving period irrespective of the dynamically varying power demand of the train.

b) The battery is designed to operate in charging or discharging mode in a similar manner as in the EMS1 depending on the power requirement and the instantaneous output power of the PEMFC.

The flowcharts of the two EMSs are shown in Figs. 2.4(a) and 2.4(b), respectively.

2.2.6. Cost model of the PEMFC-battery-HES

The cost of the HES includes the cost of the HES components, and the periodical replacement costs of the PEMFC stack and battery over a planning period. Mathematically, the total cost of the HES, *TC* is defined as follows:

$$TC = c_{fc}.P_{fc}^{rated} + \left(c_{bat}.Q_{bat}^{rated} + k_{bat}\right) + \frac{FV_{fc}.P_{fc}^{rated}}{(1+r_{fc})^{N_{fc}}}.N_{fc}^{rep} + \frac{FV_{bat}.Q_{bat}^{rated}}{(1+r_{bat})^{N_{bat}}}.N_{bat}^{rep} \tag{2.24}$$

Where, c_{fc} and c_{bat} are the costs per unit rating of the PEMFC system and battery, respectively; k_{bat} is the constant cost component of the battery; FV_{fc} (FV_{bat}) is the future value of the PEMFC stack (battery); r_{bat} (r_{fc}) is the discounting rate of battery (PEMFC stack) which is assumed to be 7% [141]; $N_{fc}(N_{bat})$ is the life-time of PEMFC stack (battery) in years, and $N_{fc}^{rep}\left(N_{bat}^{rep}\right)$ is the number of replacements of the PEMFC stack (battery) during the planning period. While, the first and second terms of Eq. (2.24) represent the capital cost of the PEMFC system and battery, respectively, the maintenance cost of the PEMFC and battery are given by the third and fourth terms, respectively. The values of the cost co-efficient are taken from [141]. Assuming an annual production of 500,000 units of PEMFC, the value of c_{fc} is considered as 47.67 *S/kW*. Likewise, the values of c_{bat} and k_{bat} are obtained as 651.2 *\$/kWh* and 680 *\$*, respectively. The most critical components of the PEMFC system which require periodical replacement are the polymer membrane, the electrodes and the platinum catalyst [1]. Hence, the replacement cost of the PEMFC stack alone is considered in this study. According to the report of U. S. Department of Energy [142], the life-time of the FC stack for transportation applications is projected to be 8000 operating hours. Thus, considering 8 hours of operation of the passenger train per day, the value of N_{fc} is estimated as 4 years. According to [141], the lithium-ion batteries need replacement in every 10 years, i.e., N_{bat} is 10 years. Thus, for a planning period of 20 years, the values of N_{fc}^{rep} and N_{bat}^{rep} are obtained as 3 and 1, respectively.

2.3. Single-Objective DO approach for PEMFC-battery-HES

In this section, a single-objective DO approach is formulated to determine the ratings of the

PEMFC and battery. The details of the DO model, PSO based solution strategy and simulation results are discussed in separate sub-sections.

2.3.1. *Single-Objective DO model*

The single-objective DO model is formulated with the objective function of minimization of the *TC* of the HES components which subject to the constraints of battery *SOC* limit, rate of change of PEMFC output power, and instantaneous power balance between the demand and supply. A constraint on P_{fc}^{rated} is also considered. As discussed before, the battery is designed to operate as an energy buffer in the proposed HES. Thus, the size of the PEMFC should be such that it can suffice to supply the average power demand of a train alone. This puts a lower limit on P_{fc}^{rated}. Mathematically, the single-objective DO problem is defined as follows:

$$Minimise \;\; f(x) = TC \tag{2.25}$$

$$where, x = \left[P_{fc}^{rated}, Q_{bat}^{rated}\right]^T \tag{2.26}$$

$$subject\ to\ the\ following\ constraints,$$

$$P_{load}(t) = P_{fc}(t) \pm P_{bat}(t) \tag{2.27}$$

$$SOC_{min} \leq SOC(t) \leq SOC_{max} \tag{2.28}$$

$$0 \leq P_{fc}(t) \leq P_{fc}^{rated} \tag{2.29}$$

$$P_{fc}^{rated} \geq P_{load}^{avg} \tag{2.30}$$

Where, SOC_{max} and SOC_{min} are the upper and lower limits of SOC, respectively; and P_{load}^{avg} is the average power demand of the train.

2.3.2. *PSO based solution strategy*

PSO is a population based meta-heuristic search technique inspired by social behavior of bird flocking or fish schooling [143], [144]. PSO has various advantages, such as, broad applicability, easy implementation, ability to incorporate nonlinear objectives/constraints, etc. In PSO, each solution is called a particle. A particle consists of a position which is iteratively updated with its velocity. The velocity directs the movement of the particle in the search space. Each particle is characterized with a fitness value which is evaluated by the objective function to be optimized. The PSO algorithm starts with an initial population of particles with randomly chosen positions and velocities. The position corresponding to the best fitness value for a particle is called *pbest*. The position of the particle with the best fitness value in the population of solutions/particles is called *gbest*. The velocity and position update equations are given below:

$$V_{ij}^{iter} = V_{ij}^{iter-1} + c_1 rand_1 \left(pbest_{ij}^{iter-1} - S_{ij}\right) + c_2 rand_2 \left(gbest_{ij}^{iter-1} - S_{ij}\right) \tag{2.31}$$

$$S_{ij}^{iter} = S_{ij}^{iter-1} + V_{ij}^{iter} \tag{2.32}$$

Where, *iter* is the iteration number; V_{ij}^{iter} (S_{ij}^{iter}) is the velocity (position) of the j^{th} dimension of the i^{th} particle in $iter^{th}$ iteration; $rand_1$ and $rand_2$ is a random number between [0, 1]; c_1 and c_2 are learning factors. In this work, PSO is used as the solution strategy to solve the single objective DO problem. Each particle in PSO encodes the information of P_{fc}^{rated} and Q_{bat}^{rated}. The EMS proposed in Section 2.2.5, is embedded into the main PSO algorithm as its support subroutine. However, only one EMS, i.e., either EMS1 or EMS2, is used at a time to obtain a pair of optimal solutions, P_{fc}^{rated} and Q_{bat}^{rated}. The flowchart of the overall solution strategy is given in Fig. 2.5.

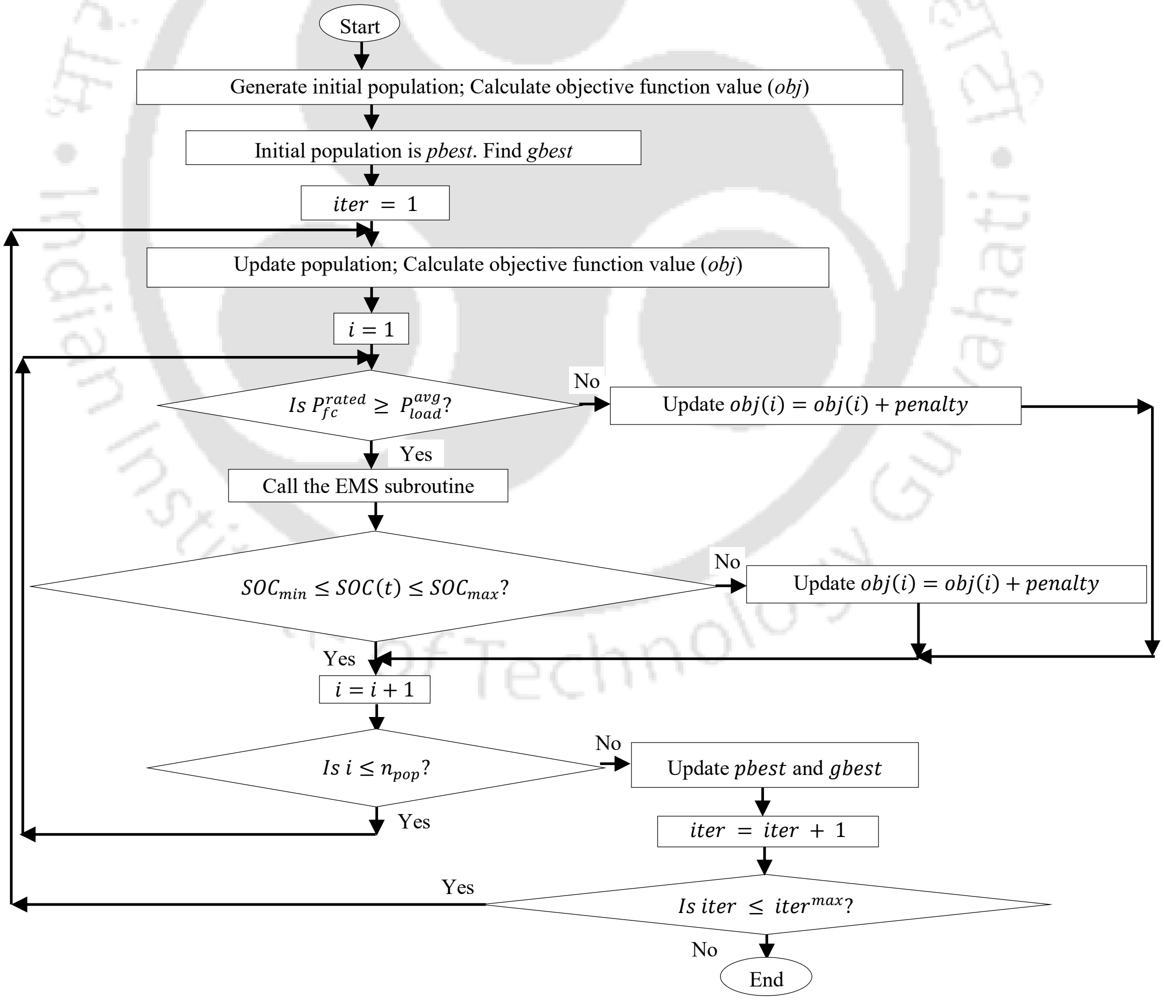

Fig. 2.5: Flowchart of the PSO based solution strategy for handling the operational constraints in single-objective DO.

2.3.3. Results and discussion of single-objective DO approach

This sub-section provides the numerical results obtained from computer simulation study. The aim of this work is to determine the sizes of the HES components, i.e., the PEMFC and lithium-ion battery. To determine the sizes of the HES components, the $P_{load}(t)$ corresponding to the three drive cycles (section 2.2.4) should be known. The $P_{load}(t)$ is calculated using Eqs. (2.18 - 2.23) for three different values of β, i.e., 0%, 1%, and 2% with P_{aux} assumed as 82 kW. Furthermore, the values of P_{load}^{avg} for the different values of β under the three drive cycle scenarios are determined, and are given in Table 2.3. The values of SOC_{min}, SOC_{max} and $SOC(t_0)$ are set as 0.3, 0.9 and 0.8, respectively. The PSO parameters are optimized by taking multiple simulation runs. The best results are obtained with n_{pop} of 200 and $iter^{max}$ of 100.

Table 2.3: Values of P_{load}^{avg}.

Slope (β) in %	*Drive cycle 1*	*Drive cycle 2*	*Drive cycle 3*
0	2900 kW	3514 kW	2667 kW
1	3520 kW	4533 kW	3134 kW
2	4115 kW	5094 kW	3691

Table 2.4: Values of the PEMFC and battery sizes obtained using PSO for drive cycle 1.

Slope (β) in %	*EMS1*		*EMS2*	
	P_{fc}^{rated}	Q_{bat}^{rated}	P_{fc}^{rated}	Q_{bat}^{rated}
0	3.3212×10^6	2.1235×10^6	2.9691×10^6	2.6867×10^6
1	3.9628×10^6	2.5395×10^6	3.5422×10^6	3.2129×10^6
2	4.6153×10^6	2.9618×10^6	4.1251×10^6	3.7476×10^6

Table 2.5: Values of the PEMFC and battery sizes obtained using PSO for drive cycle 2.

Slope (β) in %	*EMS1*		*EMS2*	
	P_{fc}^{rated}	Q_{bat}^{rated}	P_{fc}^{rated}	Q_{bat}^{rated}
0	3.8329×10^6	1.4391×10^6	3.4418×10^6	1.6931×10^6
1	4.9208×10^6	1.8435×10^6	4.4174×10^6	2.1350×10^6
2	5.7342×10^6	2.1426×10^6	5.1461×10^6	2.4426×10^6

Table 2.6: Values of the PEMFC and battery sizes obtained using PSO for drive cycle 3.

Slope (β) in %	*EMS1*		*EMS2*	
	P_{fc}^{rated}	Q_{bat}^{rated}	P_{fc}^{rated}	Q_{bat}^{rated}
0	2.800×10^6	2.9663×10^6	2.7001×10^6	3.1427×10^6
1	3.4085×10^6	$3.0602 * 10^6$	3.2001×10^6	3.2963×10^6
2	3.800×10^6	$3.5521 * 10^6$	3.7140×10^6	3.6741×10^6

2.3.3.1. Determination of the sizes of the PEMFC and battery

The optimal sizes of the PEMFC and battery for the three different drive cycles are obtained using PSO. The corresponding results are given in Tables 2.4, 2.5 and 2.6. Following conclusions can be inferred from the analysis of the results:

a) The size of the PEMFC obtained using EMS1 in PSO is found to be larger than the PEMFC size obtained using EMS2. From the description of the EMS provided in section 2.2.5, it is evident that the PEMFC is subjected to higher dynamics while following EMS1 as compared to that in EMS2. Hence, the sizes of the PEMFC are obtained to be 10.6%, 10.2% and 2.5% higher for EMS1 than EMS2 for drive cycles, 1, 2 and 3, respectively.

b) Larger the size of the PEMFC, smaller is the size of the battery, and vice versa. This trend of variation in the sizes of the PEMFC and battery establishes a trade-off between the two HES components.

c) The sizes of the PEMFC and battery basically depend on the power demand, which is a function of the mass of the train, frontal area of the locomotive, average speed of the drive cycle, and the slope/gradient (β) of the railway track on which the train is operating. In this study, the two varying parameter in the calculation of power demand are the average locomotive speed and β. Higher the value of β, higher is the power demand of the train. This subsequently leads to the larger sizes of the PEMFC and battery for all the drive cycles. The increase in the sizes of the PEMFC (battery) is observed to 19.32% and 39% (19.60% and 39.50%) as β increases from 0% to 1% and 2%, respectively for drive cycle 1. The corresponding increase in the PEMFC (battery) sizes is 38.40%, 49.60% (28.35%, 49.52%), and 21.73%, 35.71% (18.52%, 37.56%), for drive cycles 2 and 3, respectively.

d) The value of P_{fc}^{rated} increases with the increase in the value of P_{load}^{avg}, which is a function of the average speed of the drive cycle. Since, drive cycle 2 has the highest value of average speed, therefore, the size of P_{fc}^{rated} is the largest for drive cycle 2. The increase in the PEMFC sizes is almost 15.41% to 24.25%, and 37% to 51.14% for drive cycle 2 as compared to drive cycles 1 and 3, respectively.

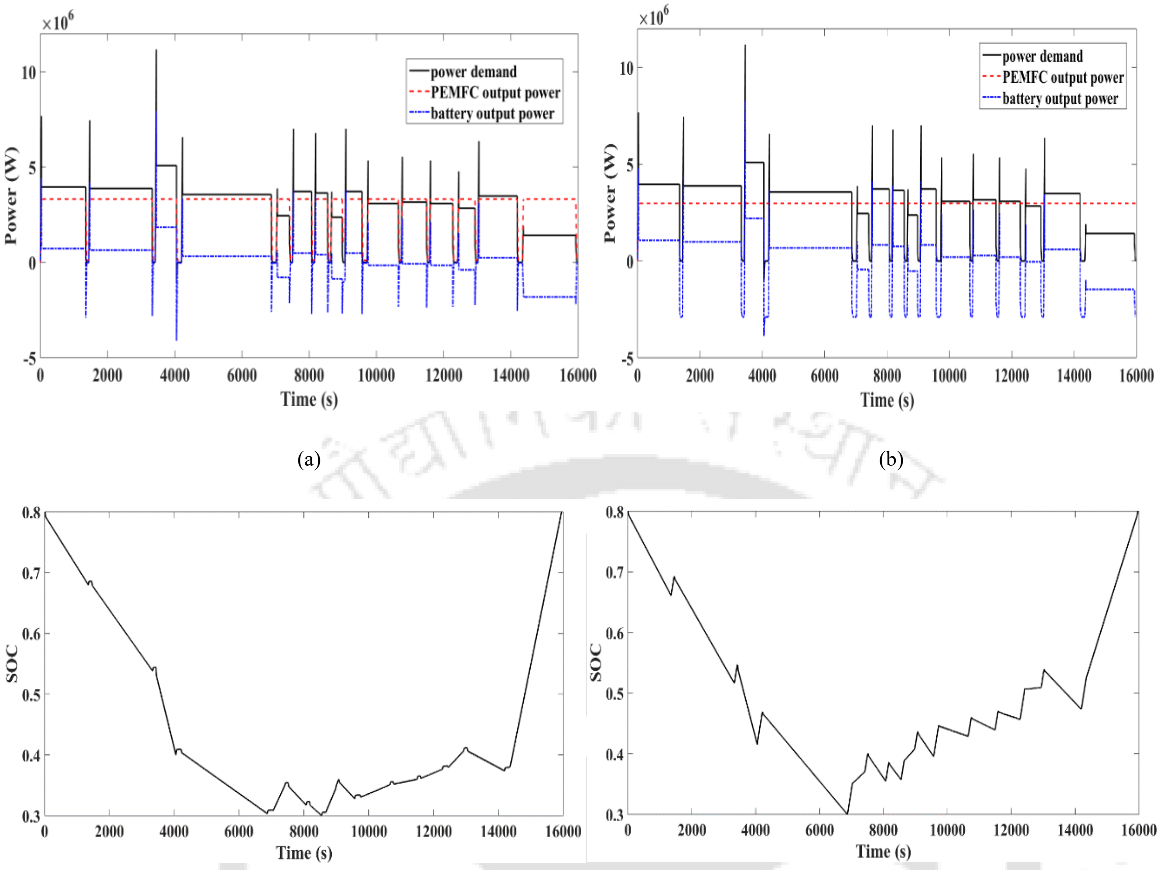

(a)

(b)

(c)

(d)

Fig. 2.6: Plots depicting the variation of power and battery SOC with time for the case of 0% slope of the railway track for drive cycle 1: (a) variation of PEMFC and battery output power with time for EMS1, (b) variation of PEMFC and battery output power with time for EMS2, (c) variation of SOC with time for EMS1, and (d) variation of SOC with time for EMS2.

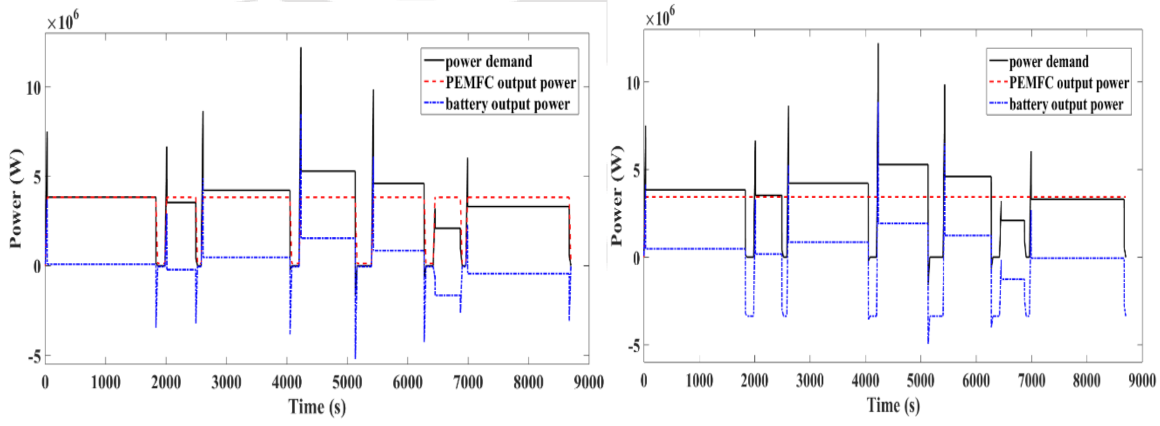

(a)

(b)

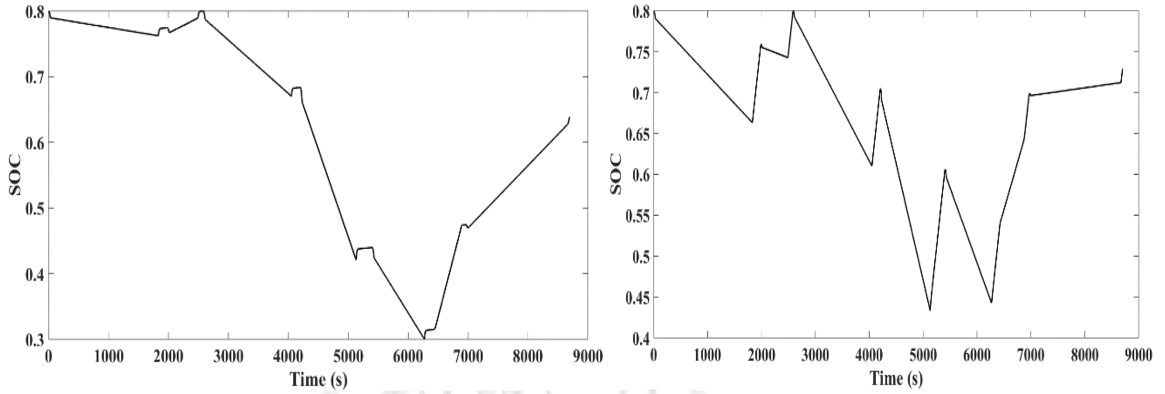

(c) (d)

Fig. 2.7: Plots depicting the variation of power and battery SOC with time for the case of 0% slope of the railway track for drive cycle 2: (a) variation of PEMFC and battery output power with time for EMS1, (b) variation of PEMFC and battery output power with time for EMS2, (c) variation of SOC with time for EMS1, and (d) variation of SOC with time for EMS2.

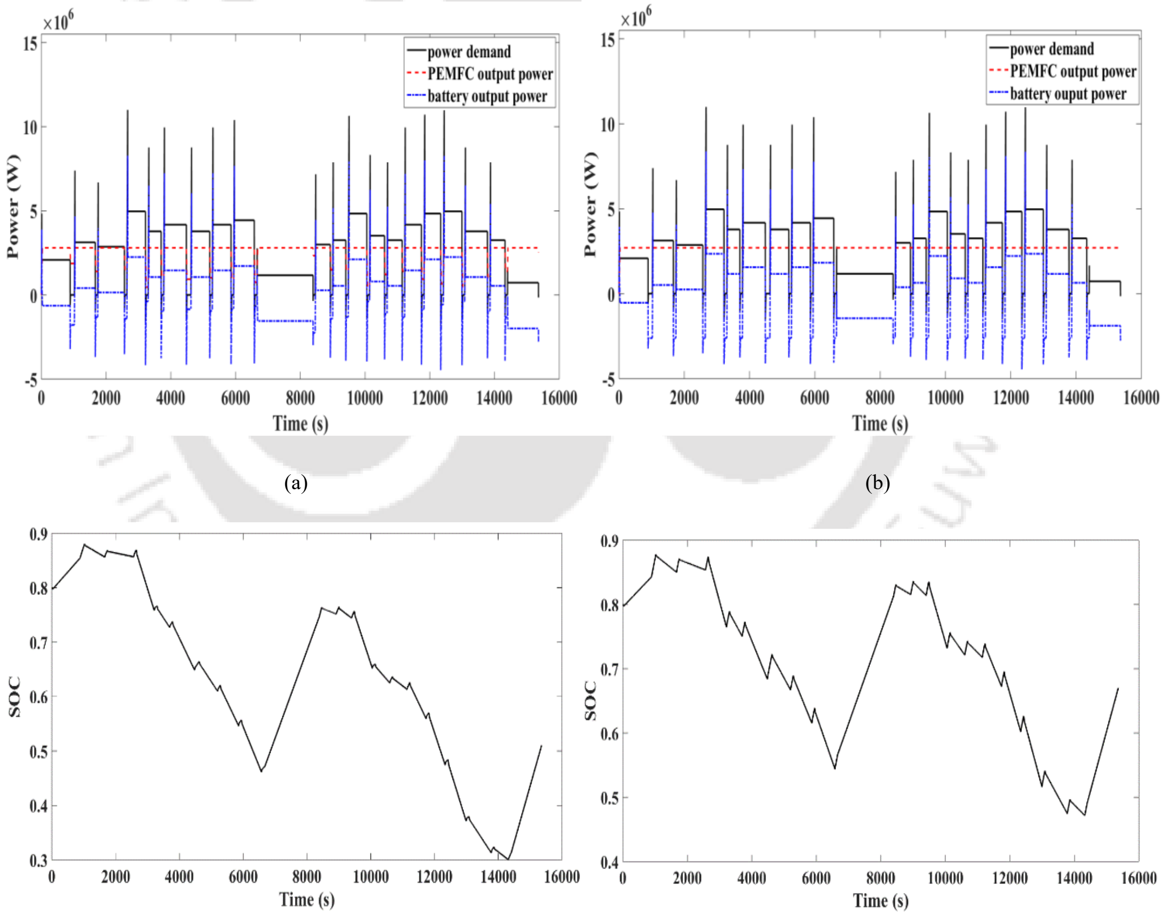

(a) (b)

(c) (d)

Fig. 2.8: Plots depicting the variation of power and battery SOC with time for the case of 0% slope of the railway track for drive cycle 3: (a) variation of PEMFC and battery output power with time for EMS1, (b) variation of PEMFC and battery output power with time for EMS2, (c) variation of SOC with time for EMS1, and (d) variation of SOC with time for EMS2.

2.3.3.2. Analysis of the dynamics of the PEMFC and battery

In this sub-section, the analysis of the dynamic behavior of the PEMFC and battery under the different drive cycle scenarios is carried out. Plots depicting the variation of the PEMFC output power, battery output power and SOC with time for the case of 0% slope of the railway track for drive cycles 1, 2 and 3 are shown in Figs. 2.6, 2.7 and 2.8, respectively. As already discussed in section 2.2.5, in EMS1, the $P_{fc}(t)$ increases to P_{fc}^{rated}, and then operates at P_{fc}^{rated} during acceleration and during the period of constant power demand. During deceleration, the $P_{fc}(t)$ decreases. The battery charges or discharges according to the power requirement of the train. The battery discharges, i.e., $P_{bat}(t)$ is positive when $\left[P_{load}(t) - P_{fc}(t)\right]$ is positive. The battery charges, i.e., $P_{bat}(t)$ is negative when $\left[P_{load}(t) - P_{fc}(t)\right]$ is negative. Accordingly, the *SOC* of the battery varies. The battery *SOC* rises when the battery charges, and falls when the battery discharges. On the other hand, in EMS2, $P_{fc}(t)$ increases to P_{fc}^{rated} initially, and then remains at P_{fc}^{rated} for the remaining driving period. The battery charges and discharges in a similar manner as in EMS1 based on the power demand of the train. Accordingly the $SOC(t)$ varies. This dynamic behavior of the PEMFC and battery in response to the dynamically varying power demand of the train are clearly exhibited in Figs. 2.6 – 2.8. It is to be noted that the level of $SOC(t)$ variation or the ripples in $SOC(t)$ are seen to be higher for EMS2 as compared to EMS1 for all the drive cycles. This characteristic variations in the $SOC(t)$ are quite evident from the description of the EMS, where the battery has to supply or absorb higher power while following EMS2 as compared to EMS1. However, the $SOC(t)$ always remains within its limits for both the EMS for all the drive cycles. Similar variation in the output power of the HES components is observed for the remaining cases of slope of the railway track, and hence, they are not discussed in this sub-section.

Table 2.7: Values of the *TC* of HES obtained using PSO (in *\$*).

Slope (β) *in %*	*Drive cycle 1*		*Drive cycle 2*		*Drive cycle 3*	
	EMS1	*EMS2*	*EMS1*	*EMS2*	*EMS1*	*EMS2*
0	2.1312×10^6	2.4886×10^6	1.73×10^6	1.8634×10^6	2.66×10^6	2.775×10^6
1	2.5215×10^6	2.9488×10^6	2.18×10^6	2.3339×10^6	2.82×10^6	2.963×10^6
2	2.9181×10^6	3.3946×10^6	2.52×10^6	2.6359×10^6	3.23×10^6	3.308×10^6

Table 2.8: Values of the fuel consumed by the PEMFC (in *kg*) under the three drive cycle scenarios.

Slope (β) *in %*	*Drive cycle 1*		*Drive cycle 2*		*Drive cycle 3*	
	EMS1	*EMS2*	*EMS1*	*EMS2*	*EMS1*	*EMS2*
0	1358.8	1230.4	808	777	1032.3	1000
1	1621.2	1468	1073.6	997	1256.7	1110
2	1905	1709.5	1288.4	1161.5	1490.5	1350

2.3.3.3. *Comparison between the two EMSs in terms of the total cost of the HES*

In this sub-section, a comparison between the two EMSs in terms of the TC of the HES is carried out. The values of the cost function are provided in Table 2.7. Observation of the results shows that although the TC of the HES is a function of the sizes of both the PEMFC and battery, the values of TC are found to be higher for EMS2 than EMS1 for all the drive cycles. This is because almost 26.41% increase in battery size is observed in EMS2 as compared to EMS1. On the contrary, the increase in the PEMFC size is relatively less (almost 10.6%) in EMS1 than EMS2 as compared to the battery. This subsequently leads to higher TC of the HES in EMS2 for all the drive cycles. However, under a particular drive cycle, the values of the cost function increase with the increase in the slope of the railway track for both the EMSs. This is because with the increase in slope of the railway track, larger size of the PEMFC and battery are obtained. This results in higher values of TC for higher values of β. For drive cycle 1, the increase in TC of the HES with the increase in β from 0% to 1% and 2% is found to be 18% and 37%, respectively for both the EMSs. The corresponding increase in TC is 26%, 45.67% and 6%, 21.43% for drive cycles 2 and 3, respectively. Nevertheless, the EMS2 has an advantage over EMS1. The advantage is that the PEMFC is subjected to fewer dynamics in EMS2 than EMS1. Thus, following EMS2 may result in relatively longer lifetime of the PEMFC as compared to EMS1.

2.3.3.4. *Comparison between the two EMSs in terms of the PEMFC fuel consumption*

The fuel, i.e., the hydrogen consumption of the PEMFC during the driving period is determined, and the results obtained are given in Table 2.8. The results show that the fuel consumption would approximately be 5% to 10% higher if EMS1 is chosen. This is due to the larger sizes of the PEMFC required to adopt EMS1. The total fuel consumption also varies with the travel distance of a drive cycle. Thus, the PEMFC hydrogen consumption is highest for drive cycle 1, and decreases by 32% to 40.5%, and 21% to 25% in drive cycles 2 and 3, respectively for both the EMSs. The total fuel consumption also increases with the increase in the value of β. Thus, the fuel economy, i.e., hydrogen consumption per km of a PEMFC-battery-HES is found to be varying with the drive cycles, the choice of EMS, and the slope of the railway track. According to the fuel consumption, the fuel storage of the locomotive and the refuel facilities need to be designed.

2.4. Multi-Objective DO approach for PEMFC-battery-HES

In this section, a multi-objective DO approach is formulated to determine the sizes of the PEMFC and battery of the proposed HES. The details of the DO model, the MOPSO based solution strategy and the simulation results are presented in separate sub-sections.

2.4.1. *Multi-objective DO model*

The multi-objective DO model is formulated with the objective functions of simultaneous minimization of the *TC* of the HES and the total fuel consumption of the PEMFC during the driving period. The optimization is carried under the operational constraints of the battery *SOC* limit, PEMFC output power rate, and the instantaneous power balance between the demand and supply. Mathematically, the multi-objective DO problem is defined as follows:

$$Minimise\begin{cases} f_1(x) = TC \\ f_2(x) = m_{H_2} \end{cases} \tag{2.33}$$

$$where, x = [P_{fc}^{rated}, Q_{bat}^{rated}]^T \tag{2.34}$$

$$subject\ to\ the\ following\ constraints$$

$$P_{load}(t) = P_{fc}(t) + P_{bat}(t) \tag{2.35}$$

$$0 \le P_{fc}(t) \le P_{fc}^{rated} \tag{2.36}$$

$$SOC_{min} \le SOC(t) \le SOC_{max} \tag{2.37}$$

```
Begin
Generate initial population of particles;
Obtain the initial non-dominated solutions and store them in elite archive;
While $iter \le iter^{max}$
    For $i = 1{:}n_{pop}$
        Update particle velocity and position using Eqs. (2.31), and (2.32);
        Call the EMS subroutine for the energy management;
        Calculate objective function and assign the finesses using SPEA2;
    End for
    Find the new set of non-dominated solutions;
    Update the elite archive;
    iter=iter+1;
End while
Elite archive contains the optimal sets of PEMFC and battery sizes.
End
```

Fig. 2.9: Pseudo-codes of SPEA2-MOPSO based DO algorithm.

2.4.2. *SPEA2-MOPSO based Solution Strategy*

As mentioned in the Section 2.3.2, the PSO is an iterative optimization technique that mimics the social behavior of bird flocking or fish schooling. In a multi-objective optimization problem, it is very important to obtain the Pareto optimal set of solutions with better diversity among the solutions

[145], [146]. Obtaining the best Pareto set of solutions depends on the selection of *pbest* and *gbest* which in turn is dependent on the fitness assignment scheme. In this chapter, Strength Pareto Evolutionary Algorithm-2 (SPEA2) is used for assigning the fitness value to the particles. The details of SPEA2 and SPEA2-based multi-objective particle swarm optimization (MOPSO) are given in [139] and [140], respectively. The particles of MOPSO encode the information of P_{fc}^{rated} and Q_{bat}^{rated}. Each EMS is used as the subroutine in the SPEA2-MOPSO based optimization algorithm at a time to obtain one Pareto set of solutions. Thus, two different Pareto fronts are obtained, one for each EMS. The Pareto front comprises of the non-dominant optimal solution sets of P_{fc}^{rated} and Q_{bat}^{rated}. The pseudo-codes for the optimization algorithm are shown in Fig. 2.9. The particles violating constraints are penalized as in [146].

2.4.3. Results and discussion of multi-objective DO approach

In this section, the results obtained with the computer simulation study are presented and discussed. The optimal sizes of the HES components are determined for drive cycle 1. The values of SOC_{max}, SOC_{max} and $SOC(t_0)$ are set as 0.9, 0.3 and 0.8, respectively. The values of n_{pop} and $iter^{max}$ are chosen to be 1000 and 100, respectively. These PSO parameters are chosen after performing multiple simulation runs.

2.4.3.1. Determination of the sizes of HES components

The optimal sizes of the PEMFC and battery are determined for the drive cycle 1 using the proposed multi-objective DO model. Two Pareto fronts are obtained, one corresponding to each EMS, and are shown in Fig. 2.10. Three different solutions are chosen from each Pareto front, and are listed in Table 2.9. The solution set 1 corresponds to the highest value of the *TC* of HES and the lowest value of fuel consumption. The solution set 3 corresponds to the lowest value of the *TC* of the HES and the highest value of fuel consumption. The solution set 2 corresponds to an intermediate solution in the Pareto-front. The PEMFC and battery sizes corresponding to these three solutions are shown in Table 2.10. It is observed that larger the size of the PEMFC smaller is the size of the battery, and vice-versa. This variation in PEMFC and battery size shows a trade-off between the two energy sources. The above observation is valid for both the EMSs. Furthermore, as shown in Fig. 2.10, two Pareto fronts are obtained corresponding to EMS1 and EMS2. This implies that the sizes of the HES component are also dependent on the choice of EMS. The PEMFC is subjected to comparatively larger dynamic variation in its output power when EMS1 is used for energy management, and the battery needs to undergo comparatively higher dynamics when EMS2 is implemented for energy management. Thus, adopting EMS1 results in larger size of the PEMFC (almost 11% to 13% higher as compared to that of EMS2), and hence higher fuel consumption. The choice of EMS2 results in larger size of the battery (almost 18.20% larger than that of EMS1), and hence, a higher value of the *TC* of HES. This observation is clearly depicted in Tables 2.9 and 2.10. The results show that the choice of EMS2 provides a solution which is approximately 2.5% to 3% costlier as compared to that of EMS1. On the contrary, the solutions obtained with EMS1 results in the fuel consumption of approximately 1.5% to 4% higher than that of the EMS2. Furthermore, the results also show that choice of solution sets 2 or 3 reduces the *TC* of HES to approximately 50% and 75% to that of the solution 1, respectively. Conversely, the choice of solution set 1 results in zero fuel consumption. The fuel consumption increases from solution set 2 to solution set 3. The choice of solution set 3 increases the fuel consumption of the PEMFC by 75% that of the solution set 2. Correspondingly, the battery size of the solution set 1 is found to be approximately 8 to 10 times larger than that of the solution set 3, and it is almost double of the size of solution set 2. The PEMFC size is found to be approximately 75% higher in solution set 3 as compared to solution set 2.

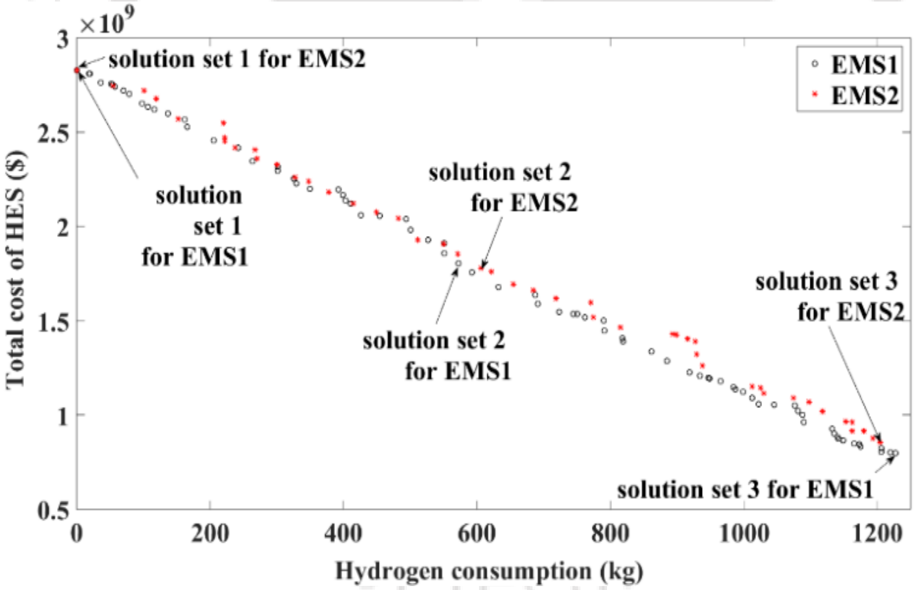

Fig. 2.10: Pareto fronts obtained using SPEA2-MOPSO for drive cycle1.

Table 2.9: Values of the PEMFC fuel consumption and *TC* of HES corresponding to the solution sets indicated in Fig. 2.10.

Solution Set No.	*EMS1*		*EMS2*	
	Fuel Consumption (kg)	*TC of HES ($) (*10^8)*	*Fuel Consumption (kg)*	*TC of HES ($) (*10^8)*
1	0	28.3	0	28.3
2	718	15.8	691.5	16.2
3	1246	7.73	1227	7.98

Table 2.10: Values of the PEMFC and battery sizes obtained using SPEA2-MOPSO corresponding to the solution sets indicated in Fig. 2.10.

Solution Set No.	EMS1		EMS2	
	P_{fc}^{rated} (MW)	Q_{bat}^{rated} (MWh)	P_{fc}^{rated} (MW)	Q_{bat}^{rated} (MWh)
1	0	25.13	0	25.13
2	1.92	11.59	1.67	13.65
3	3.33	2.52	2.96	3.08

2.4.3.2. Analysis of the dynamic behaviour of the HES

The analysis of the dynamic behavior of the HES for drive cycle 1 is carried out to validate the sizes of the PEMFC and battery shown in Table 2.10. Plots depicting the variation of battery $SOC(t)$ with time, for each set of PEMFC and battery sizes are obtained and are shown in Fig. 2.11. The analysis of the plots shows that the SOC remains within the specified limits throughout the driving period. This implies that the sizes of the PEMFC and battery obtained in Table 2.10 are appropriate, and suffice to meet the dynamically varying power demand for drive cycle 1.

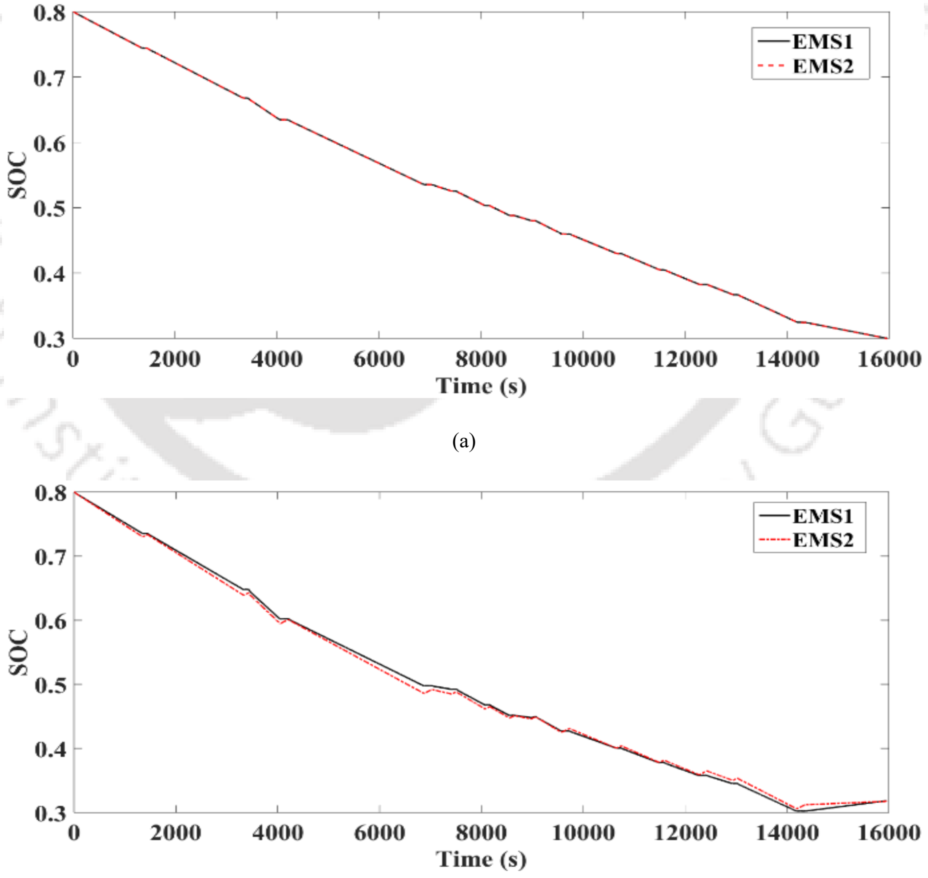

(a)

(b)

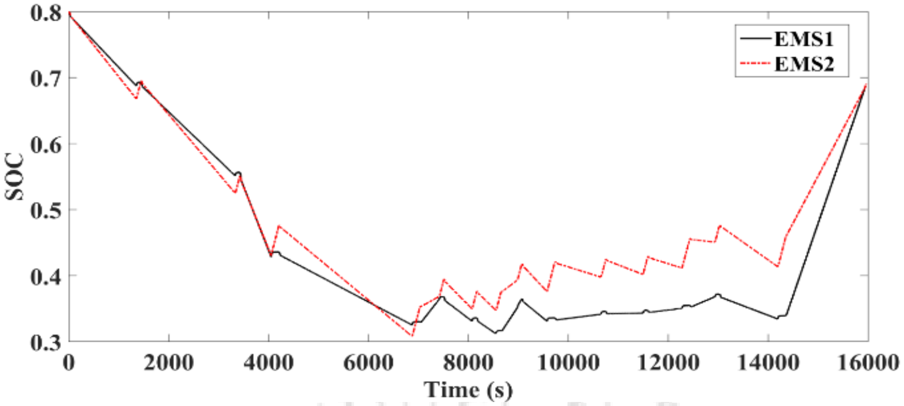

(c)

Fig. 2.11: Plots of battery SOC for PEMFC and battery sizes corresponding to each solution set of Table 2.10 for drive cycle1 scenario: (a) solution set 1, (b) solution set 2 and (c) solution set 3.

2.5. Summary of the present work

In this work, the DO approaches have been proposed to determine the optimal sizes of the HES components, i.e., the PEMFC and battery capable of providing similar tractive efforts as the traditional diesel locomotive class, WDM-3D, which is currently used to haul most of the intercity passenger train in India. The problem of DO has been firstly addressed as a single-objective optimization approach. The objective function of optimization is the minimization of the total cost of the HES. The cost function is defined as the summation of the capital costs of the PEMFC and battery, and the periodical replacement costs of the PEMFC stack and battery for the specified planning period. The optimization has been carried out for different practical drive cycle scenarios. However, besides capital expenditure, the operational cost also influences the feasibility of the application of a PEMFC-battery-HES in locomotives. The operational cost is a function of the PEMFC hydrogen consumption which in turn is dependent on the size of the PEMFC. To address this issue, the problem of DO of the PEMFC-battery-HES has now been formulated as a multi-objective optimization approach. The objective functions of the multi-objective optimization approach are the simultaneous minimization of the total cost of the HES and the hydrogen consumption of the PEMFC over the driving period. The single-objective and multi-objective DO problems have been solved using PSO and SPEA2-MOPSO based solution strategies, respectively. Two EMSs have been devised in this chapter to regulate the distribution of load in the HES. The proposed EMSs have been used as the subroutines in the solution strategies. The conclusions derived from the simulation study are discussed below.

- The sizes of the PEMFC and battery are found to be primarily dependent on the average power demand, which is basically a function of the average speed of the drive cycle and the slope of the railway track. This implies the HES component sizes vary with the drive cycle.
- The HES component sizes are also dependent on the choice of EMS. Larger sizes of the PEMFC and battery are obtained when EMS1 and EMS2 are adopted for energy management, respectively.
- Comparison between the two EMS in terms of the total cost of the HES and fuel consumption of the PEMFC shows their dependency on the size of the HES components. Although the total cost of the HES is a function of both the PEMFC and battery sizes, yet the increase in battery size when EMS2 is employed for energy management is comparatively higher than the increase in PEMFC size when EMS1 is implemented for load distribution in the HES. Therefore, the value of cost function is found to be higher for EMS2 than EMS1. On the other hand, the amount of fuel consumed, and the corresponding heat energy generated is directly proportional to the PEMFC size. Therefore, the fuel consumption is found to be higher for EMS1 than EMS2, since the size of the PEMFC is larger for EMS1 than EMS2. The dependency of the total cost and hydrogen consumption on the sizes of the HES components is found to be valid for all the drive cycles considered in this chapter.
- Performance analysis of the HES for the two EMS reveals that the battery is subjected to larger dynamics in EMS2 as compared to EMS1. Hence larger ripples in the battery SOC are observed for EMS2.
- The proposed multi-objective DO approach for the PEMFC-battery-HES can provide a set of alternative solutions with different component sizes, from which a planner can select a solution according to its capital expenditure and operational expenditure budget.

Chapter 3

Control approaches for the PEMFC-battery-HES for Locomotive Applications

3.1. Introduction

As already mentioned in the previous chapter, the PEMFC is turning out to be a promising sustainable energy technology for use in several applications, especially in stationary, portable and transportation applications. However, the use of PEMFC in conjunction with the ESS, such as battery, SC, etc., is always beneficial to compensate for the technical shortcomings of the PEMFC. An important challenge associated with the application of a PEMFC based HES is to maintain a constant DC-bus voltage across the load against the wide variation in the PEMFC output voltage with varying operating and loading conditions. This can be achieved through the use of PWM controlled DC/DC converter. The DC/DC converters basically aim to provide the constant boost to the DC-bus voltage, and to control the power flow in the HES in accordance to the EMS. In literature, several research articles related to the use of DC/DC converters for the application of PEMFC based HES are reported [6], [9], [12]–[15], [18]–[21], [26]–[28], [30]–[32], [34], [36], [38]–[40], [47], [49], [51], [53], [55], [66], [74]–[77], [79], [93], [104]–[107]. The concerned research area is classified based on the following attributes:

- ***Types of PEMFC based HES***: This include the PEMFC-battery-HES [12], [15], [18], [19], [28], [34], [36], [38], [47], [53], [77], [79], PEMFC-SC-HES [9], [13], [21], [26], [27], [31],

[32], [55], [74], [106], PEMFC-SC-battery-HES [6], [20], [30], [40], [49], [51], [66], PEMFC-battery-PV-HES [14], and PV-wind-PEMFC-battery-HES [93].

- ***Application areas***: The different application areas are HEV [12]–[15], [18]–[21], [26]–[28], [32], [34], [38]–[40], [49], [53], [55], [66], [75]–[77], [79], locomotive [47], [74], tramway [6], [30], [36], [51], crane [9], electric aircraft [31], power generation system in remote areas [93], and UPS system [106], [107].
- ***Converter topologies***: Examples of some of the converter topologies used to interface the PEMFC based HES to the load are unidirectional boost converter [6], [9], [12], [13], [18], [21], [26], [27], [30]–[32], [36], [47], [51], [55], bidirectional boost converter [9], [30], [32], [38], [51], bidirectional buck-boost converter [6], [13], [20], [26], [27], [31], [55], [93], buck converter [14], [15], [39], [104], bidirectional buck converter [30], unidirectional pulse transformer isolated boost converter [20], [93], push-pull converter [106], [107], etc.
- ***PWM control schemes***: To regulate the converter duty cycle in order to achieve the DC-bus voltage regulation and the execution of the EMS the different kinds of PWM control schemes adopted are current control [12], [14], [15], [18], [20], [21], [27], [30], [39], [47], [51], [55], [93], voltage control [20], [21], [27], [55], [93], [104], [107], cascade current control [9], [36], cascade current, and voltage control [9], [30], [32], [51], virtual resistor droop control and virtual impedance droop control [31], etc.

In the aforementioned research papers, the dynamic performance of the HES and the closed loop controlled DC/DC converters are tested either through computer simulation [9], [13], [14], [21], [26]–[28], [30], [32], [34], [36], [38], [40], [47], [51], [53], [55], [66], [77], [79], [104], [105] or on an experimental platform [6], [12], [15], [18]–[20], [31], [39], [49], [74]–[76], [93], [106], [107]. However, the literature survey shows that very few published works are reported on the application of PEMFC based HES in locomotive [47], [74]. In [47], the performance analysis of the PEMFC-battery-HES is carried out through simulation using the vehicle simulation software, ADVISOR. No experimental analysis is presented in this paper. In [74], the dynamics of the PEMFC-SC-HES and the DC/DC converters are experimentally tested on a real time-lab platform. However, the study aims at the maximization of the regenerative energy recovery by the SC. Thus, the performance analysis of the PEMFC-SC-HES is concentrate only on the braking region of the speed curve, and not for a complete driving horizon. In addition to these, the design procedures of the DC/DC converters and PWM controllers are not discussed in these papers. Keeping this in mind, the design of the PWM control approaches for the MISO-DC/DC boost converter are proposed in this chapter for the application of the PEMFC-battery-HES in locomotives. The MISO converter proposed in [103] is adopted for connecting the PEMFC-battery-HES with the DC-bus, since this converter topology allows the independent power control of the input sources having different power levels. The MISO converter is operated in closed loop control mode to achieve the DC-bus voltage regulation and to implement the EMS. The dynamics of the proposed PEMFC-battery-HES and the PWM controlled MISO converter are investigated through simulation in MATLAB/SIMULINK, and on the experimental setup of the HES. For hardware study, the PCB layout of the MISO converter is designed. The PWM controllers are developed utilizing the concept of Venable K-factor presented in [147]. The advantage of the concept of K-factor is that it helps the circuit designers to realize the electrical circuit of the controllers by providing simple algebraic equations to determine the values of the circuit elements, (such as the resistors, capacitors, etc.). The contributions of this chapter are summarized below:

- Development of the PWM control approaches for a MISO DC/DC boost converter to meet the requirements of the implementation of the PEMFC-battery-HES in locomotives, i.e., the maintenance of the DC-bus voltage, and the distribution of power demand between the hybrid energy sources in accordance to the EMS.
- Design of the PCB layout of the PWM controlled MISO converter.
- Simulation and experimental verification of the dynamics of the MISO converter and the PWM controllers for a practical drive cycle scenario of an intercity passenger train operating in NEFR, Assam, India.

3.2. Modelling of the PEMFC-battery-HES

In the proposed HES, the PEMFC and battery are connected to the load via. the MISO-DC/DC boost converter. An overview of the HES and the MISO converter is presented in Fig. 3.1. The details of the HES components are discussed in separate sub-sections.

3.2.1. PEMFC model

In this study, the operation of the PEMF in steady-state and dynamic modes is represented by the equivalent electrical circuit model which is shown in Fig. 3.2. The corresponding mathematical model of the PEMFC is presented below:

$$v_{fc} = v_{rev} - v_{act} - v_{ohm} - v_{conc} \tag{3.1}$$

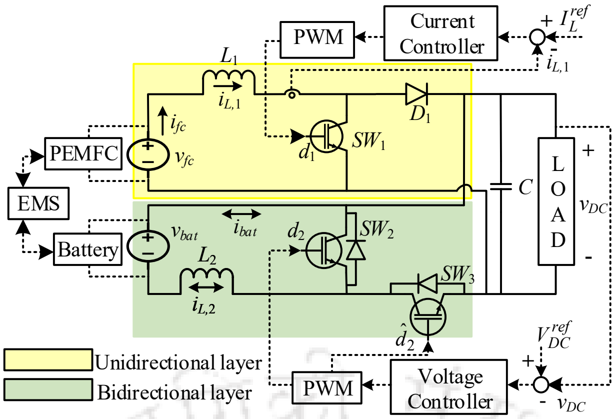

Fig. 3.1: Configuration of the PEMFC-battery-HES and PWM controlled MISO-DC/DC boost converter.

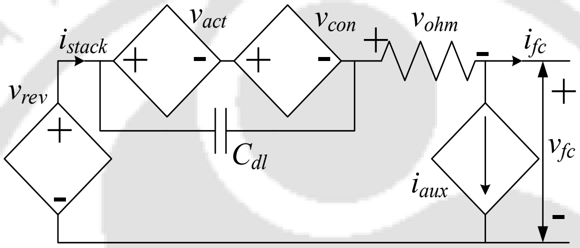

Fig. 3.2: Equivalent electrical circuit of the PEMFC.

$$v_{rev} = E_0 - \frac{RT}{n_{e^-}F} ln\left\{\frac{p_{H_2O}}{p_{H_2}(p_{O_2})^{1/2}}\right\} \tag{3.2}$$

$$v_{act} = N_s\{a + bln(i_{stack})\} \tag{3.3}$$

$$v_{conc} = N_s\{me^{(n.i_{stack})}\} \tag{3.4}$$

$$v_{ohm} = N_s R_{ohm} i_{stack} \tag{3.5}$$

$$a = a_0 + a_1 T \tag{3.6}$$

$$b = b_0 + b_1 T \tag{3.7}$$

$$m = m_0 + m_1 T \tag{3.8}$$

$$R_{ohm} = R_{ohm,0} + R_{ohm,1} T \tag{3.9}$$

$$\frac{dv_{c,dl}}{dt} = \frac{1}{C_{dl}}\left(i_{stack} - \frac{v_{c,dl}}{R_{total}}\right) \tag{3.10}$$

Where, v_{fc} is the PEMFC output voltage; v_{rev} is the reversible voltage of the PEMFC; E_0 is theoretical cell potential; R is the universal gas constant; T is the cell temperature (in K); F is the faraday's constant; n_{e^-} is the number of electrons generated in the electro-chemical reaction (which is 2); p_{H_2O}, p_{O_2} and p_{H_2} are the partial pressure of water (assumed to be 1 atm), oxygen and hydrogen, respectively; i_{stack} is the PEMFC stack current; N_s is the number of cells in the stack (which is 36); v_{act}, v_{conc} and v_{ohm} are the voltage drops due to the activation, concentration and ohmic losses, respectively; b is the Tafel's slope; R_{ohm} is the ohmic resistance of the FC stack; a_0, a_1, b_0, b_1, m_0, m_1 n, $R_{ohm,0}$ and $R_{ohm,1}$ are the empirical parameters; C_{dl} is the double layer capacitor; $v_{c,dl}$ is the voltage across C_{dl}; and R_{total} is the resistance representing the total voltage drop due to the concentration and activation losses. Equations (3.1) to (3.9) represent the steady-state characteristics of the PEMFC, and Eq. (3.10) represents its dynamic behaviour. The dynamic characteristics of the PEMFC are associated with the double charge effect of the PEMFC which occurs due to the accumulation of the ionic and electronic charges at the interface between the electrode and electrolyte. The charge transfer occurs during the oxidation and reduction half reactions taking place at the electrode-electrolyte interface of the PEMFC. These layers can store the electrical energy and behave like a capacitor, C_{dl}. Due to this, even if there is a sudden change in the current, it will take certain time for the charges to build up or dissipate. Accordingly, the operating voltage changes gradually to its new equilibrium point. This is called the double charge effect.

In this study, the experimental setup of the NEXA 1200 PEMFC system of Ms. Heliocentris is considered. The plots depicting the PEMFC characteristics of NEXA 1200 system are presented in Fig. 3.3. The experimental data obtained from the NEXA 1200 PEMFC system shows that i_{stack} differs from the actual current demanded from the PEMFC system (i_{fc}). This is because the auxiliary components of the PEMFC system consume a part of the electrical power generated by the PEMFC stack. Additionally, the T and p_{H_2} also exhibit variations in relation to i_{fc}. The mathematical equations to approximate this variation are obtained from the method of curve fitting on the experimental data and are given below:

$$i_{stack} = 1.7 + 1.1 i_{fc} \tag{3.11}$$

$$T = 46.71 + 0.1635 i_{fc} + 0.0045 {i_{fc}}^2 \tag{3.12}$$

$$p_{H_2} = 1.3 - 0.0026 i_{fc} \tag{3.13}$$

In this sub-section, the estimation of the PEMFC model parameters, i.e., a_0, a_1, b_0, b_1, m_0, m_1, n, $R_{ohm,0}$, $R_{ohm,1}$ and C_{dl} is done through the formulation of an optimization model. The objective function of optimization is the error minimization between the experimental stack voltage and the voltage of the PEMFC simulation model.

$$Err = \left[\frac{1}{N}\left\{\sum_{i=1}^{N}\left(v_{fc,i}^{exp} - v_{fc,i}^{model}\right)^{2}\right\}\right]^{1/2} \tag{3.14}$$

Where, v_{fc}^{exp} is the experimental stack voltage; v_{fc}^{model} is the voltage of the PEMFC model; and N is the number of sample data. To solve the optimization problem, the experimental data of 1.2 *kW* NEXA PEMFC system of Ms. Heliocentris is utilised, and PSO [143] is used as the solution algorithm. The values of the PEMFC model parameters obtained using PSO are listed in Table 3.1. With the obtained parameter values, plots depicting the comparison between the PEMFC experimental setup and the PEMFC SIMULINK model in terms of their steady state and dynamic responses are obtained. These steady-state and dynamic plots are shown in Figs. 3.4(a) and 3.4(b), respectively. From these figures, it is observed that both the curves are in good agreement with each other. This implies that the values of the model parameters are appropriate. Hence, the developed SIMULINK model is a good approximation of the experimental PEMFC setup.

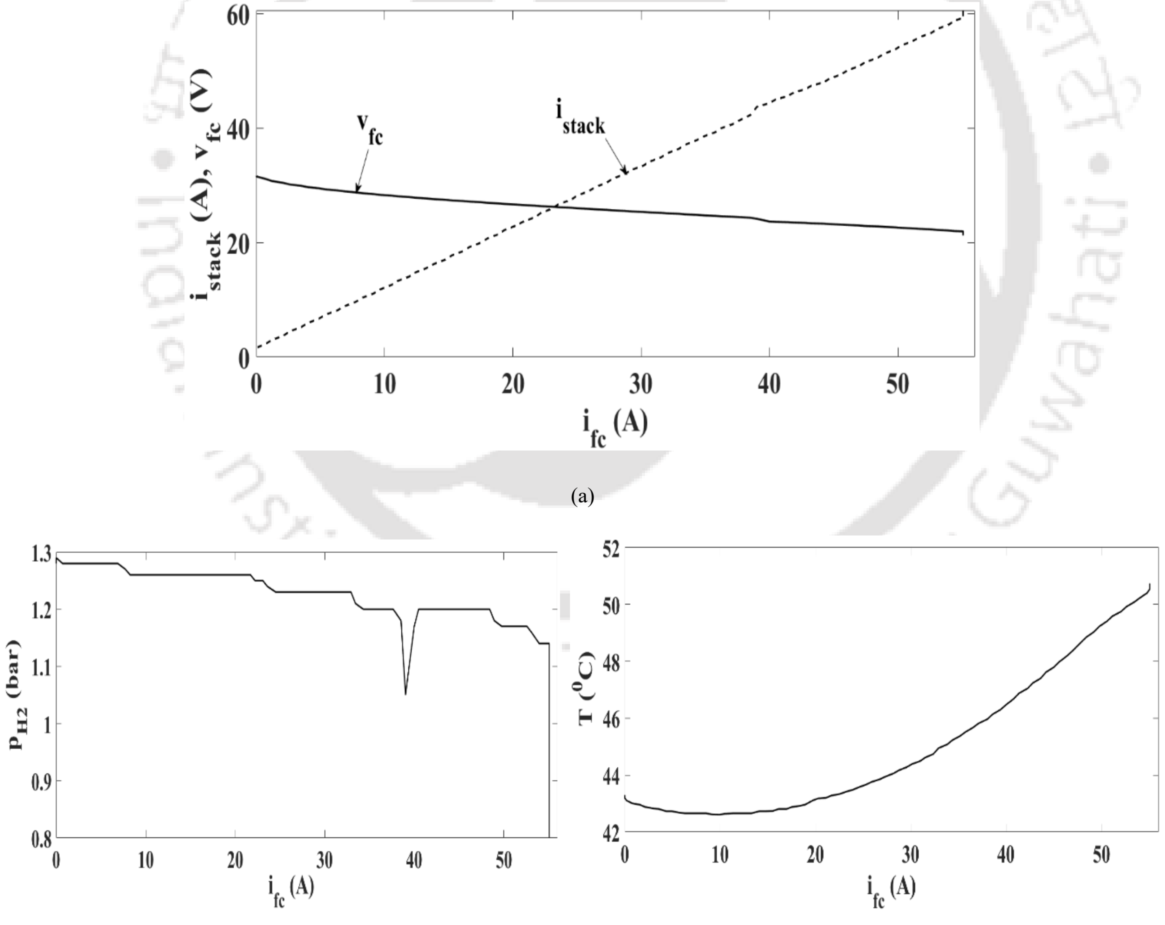

(a)

(b)

(c)

Fig. 3.3: Plots depicting the characteristics of the NEXA 1200 PEMFC system: (a) i_{stack}, v_{fc} vs i_{fc}, (b) p_{H_2} vs i_{fc} and (c) T vs i_{fc}.

Table 3.1: Optimal values of the PEMFC model parameters.

Values of the steady state model parameters					
a_0 (*V*)	0.6897	a_1 (*VA⁻¹*)	0.0012	b_0 (*V*)	0.0623
b_1 (VA^{-1})	9.94×10^{-5}	m_0 (*V*)	0.01764	m_1 (VA^{-1})	4.446×10^{-5}
n (A^{-1})	0.055	$R_{ohm,0}$ (ohm)	0.004	$R_{ohm,1}$ ($ohmT^{-1}$)	-4.04×10^{-6}
Values of the dynamic model parameters					
C_{dl} (F)	0.1389		R_{total} (ohm)	6.998×10^{-2}	

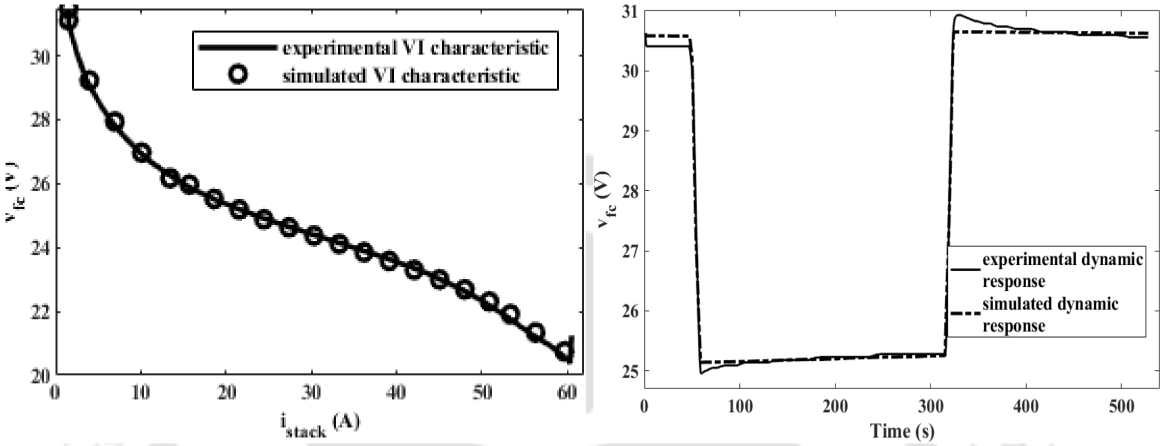

(a) (b)

Fig. 3.4: Comparison between the 1200 NEXA PEMFC setup and PEMFC SIMULINK model in terms of: (a) steady state VI characteristic and (b) dynamic response.

3.2.2. Battery model

As discussed in section 2.2., the battery is chosen to serve as the secondary energy source. Technically, the battery dynamics are characterized by its state-of-charge, $SOC(t)$ which is a function of the battery output power, $P_{bat}(t)$ and the battery rated capacity, Q_{bat}^{rated}. The model of the battery is vividly presented in section 2.2.2.

3.2.3. Load model

The load, $P_{load}(t)$ represents the dynamically varying power demand of an intercity passenger train operating in Indian railways. Mathematically, the $P_{load}(t)$ is defined as the summation of the instantaneous power demand of the train (which is a function of the total mass, and instantaneous speed of the train), and a constant power representing the power consumed by the auxiliary components of the train, P_{aux}. The mathematical model of the load is given in section 2.2.3.

3.2.4. Energy Management Strategy

In this sub-section, a rule-based EMS which is almost similar to the EMS2 proposed in section

2.2.5. This EMS is devised keeping in mind the durability constraint of PEMFC. The durability constraint arises, since the PEMFC stack comprises of some critical intrinsic components, such as, the membrane, electrodes, catalyst layer, etc., which are prone to damage when subjected to frequent load variation, and thereby affecting the durability or the life span of the PEMFC. In addition to this, the slow transport of reactants in the FC stack during the electro-chemical reaction, and the slow dynamics of the PEMFC auxiliaries impose a limitation on the rate of change of its output power, $P_{fc}(t)$. Conversely, the batteries can withstand sudden and faster dynamics without compromising its lifetime. The proposed EMS aims to operate the PEMFC in quasi-steady state without undergoing rapid changes in its operating point. According to the proposed EMS, the $P_{fc}(t)$ and $P_{bat}(t)$ varies as follows:

- PEMFC is set to operate at its rated power, P_{fc}^{rated} throughout the driving period.
- The battery is set to supply the power demand when $P_{load}(t) > P_{fc}(t)$. It absorbs the excess power when $P_{load}(t) < P_{fc}(t)$, and store it in the form of chemical energy for future use. Thus, the battery either charges/discharges, i.e. $P_{bat}(t)$ is either negative/positive throughout the driving period.

3.3. Design of the MISO-DC/DC boost converter

The MISO-DC/DC boost converter is designed to operate in continuous conduction mode (*CCM*) for a switching frequency, f_s of 20 *kHz*. As shown in Fig. 3.1, the converter layer connected to the PEMFC and battery is a unidirectional and bidirectional in nature, respectively. In the unidirectional converter layer, the IGBT without the anitparallel diode is chosen as the switch, SW_1. Conversely, in the bidirectional converter layer, the IGBT switches comprising of the anti-parallel diodes operate as the switches, SW_2 and SW_3 to allow the bidirectional power flow between the source and load. Thus, the bidirectional converter layer allows the charging and discharging of the battery. The values of the inductors (L_1, L_2) and the capcitor (C) (Fig. 3.1) are determined using the mathematical Eqs. (3.15 - 3.18). The values of L_1 and L_2 are chosen to satisfy the operating conditions of the PEMFC and battery, respectively. On the other hand, the value of C is obtained under the operating conditions of both the energy sources.

$$L_j = \frac{V_{in,j} d_j}{\Delta I_{L,j} f_s} \tag{3.15}$$

$$\Delta I_{L,j} = I_{L,j}^{peak} = 2 I_{L,j}, \text{ at the boundary of } CCM \text{ and } DCM \tag{3.16}$$

$$C = \frac{V_{DC} d_j}{R_{load} \Delta V_{DC} f_s} \tag{3.17}$$

$$d_j = 1 - \frac{V_{in,j}}{V_{DC}} \tag{3.18}$$

Where, j is the index representing the layers of the MISO converter (j =1 for the unidirectional converter layer, and j =2 for the bidirectional converter layer); d_j is the duty ratio of the converter switches; DCM stands for the discontinuous conduction mode of converter operation; $V_{in,j}$ is the average value of converter input voltage; V_{DC} is the average value of the converter DC-bus voltage which is also the converter output voltage; $I_{L,j}$ is the average value of the inductor current; $I_{L,j}^{peak}$ is the peak value of the inductor current; $\Delta I_{L,j}$ (ΔV_{DC}) is the ripple in the inductor current (DC-bus voltage); and R_{load} is the load resistance. The design specifications of the MISO converter are discussed in the following sub-sections.

3.3.1. Unidirectional converter layer

The values of L_1 and C are determined using Eqs. (3.15 - 3.18) for the PEMFC operating voltage range of 20 to 34V corresponding to the load variation of 15 to 1200W. The variable, $V_{in,1}$ of Eq. (3.15) is the PEMFC output voltage, V_{fc}. To determine C, the values of V_{DC} and ΔV_{DC} of Eq. (3.17) are taken as 48V and 5% , respectively. Two different values of L_1 and C for the maximum and minimum loading operating points (*OP*) are obtained. Finally, the larger values of L_1 and C are chosen.

3.3.2. Bidirectional converter layer

The values of L_2 and C of the bidirectional converter layer are obtained for the battery nominal voltage of 24V, the loading range of 4.8 to 1200W, V_{DC} of 48V, and ΔV_{DC} of 5%. The variable $V_{in,2}$ of Eq. (3.15) is the battery output voltage, V_{bat}. Similar to section 3.3.1, two different values of L_2 and C are obtained for the maximum and minimum loading *OP*s of the battery of which the larger values of L_2 and C are chosen.

Thus, four different values of C are obtained for the MISO converter layers under the maximum and minimum loading *OP*s. Among these, the largest value of C is chosen for deployment.

3.4. Pulse width modulation of the DC/DC converter

In this section, the details of the PWM schemes implemented for generating the switching pulses for the DC/DC converter are presented. Besides this, the design procedures of the PWM controllers are also discussed here.

3.4.1. PWM control scheme

In this study, the current control and voltage control schemes are implemented for controlling the PWM of the switches of the unidirectional and bidirectional layers of the MISO converter, respectively. The PWM control schemes are depicted in Fig. 3.1. The controller of the unidirectional converter layer is designed to operate in current control mode to ensure the load distribution in the HES in accordance to the EMS. According to this control scheme, the current controller generates the switching pulses based on the error between the instantaneous inductor current, $i_{L,1}(t)$ and the current reference, I_L^{ref}. The I_L^{ref} is given by $\left(P_{fc}(t)/v_{fc}(t)\right)$ in which the $P_{fc}(t)$ is determined by the specific EMS adopted, and $v_{fc}(t)$ represents the instantaneous value of the PEMFC output voltage. According to the EMS proposed in this work, the $P_{fc}(t)$ is maintained at P_{fc}^{rated} throughout the driving period. Hence, I_L^{ref} is a fixed current reference whose value corresponds to the P_{fc}^{rated} *OP*. Since the PEMFC and battery operate in parallel, hence, controlling $i_{L,1}(t)$ or $i_{fc}(t)$ in reference to I_L^{ref} results in the simultaneous control of $i_{L,2}(t)$ or $i_{bat}(t)$. In this way, the current controller assists in implementing the EMS.

For controller of the bidirectional converter layer, the voltage control scheme is adopted, and is used to regulate the DC-bus voltage. In this scheme, the switching pulses are generated based on the error between the instantaneous DC-bus voltage, $v_{DC}(t)$ and the reference voltage, V_{DC}^{ref}. Thus, the controller assists in maintaining a constant DC-bus voltage across the load irrespective of the variations in the loading and operating conditions.

3.4.2. Design of the PWM controllers

The PWM controllers are designed following the mathematical concept of Venable K-factor, and the amplifier models proposed in [147]. The steps involved are summarized below:

Step 1: The transfer function models of the MISO converter are determined. To do this, the average state space model of the MISO converter is firstly derived considering $(\tilde{i}_{L,1}, \tilde{i}_{L,2}, \tilde{v}_C)$ as the state variables, $[x_1\ x_2\ x_3]^T$; $(\tilde{v}_{fc}, \tilde{v}_{bat}, \tilde{d}_1, \tilde{d}_2)$ as the input variables, $[u_1\ u_2\ u_3\ u_4]^T$; and $\tilde{v}_{DC}$ as the output variable, y. The state space model is given in Eqs. (3.19) and (3.20).

$$\begin{bmatrix}\dot{x}_1\\ \dot{x}_2\\ \dot{x}_3\end{bmatrix}=\begin{bmatrix}0 & 0 & \frac{D_1-1}{L_1}\\ 0 & 0 & \frac{D_2-1}{L_2}\\ \frac{1-D_1}{C} & \frac{1-D_2}{C} & \frac{-1}{RC}\end{bmatrix}\begin{bmatrix}x_1\\ x_2\\ x_3\end{bmatrix}+\begin{bmatrix}\frac{1}{L_1} & 0 & \frac{V_C}{L_1} & 0\\ 0 & \frac{1}{L_2} & 0 & \frac{V_C}{L_2}\\ 0 & 0 & \frac{-I_{L,1}}{C} & \frac{-I_{L,2}}{C}\end{bmatrix}\begin{bmatrix}u_1\\ u_2\\ u_3\\ u_4\end{bmatrix} \tag{3.19}$$

$$\dot{y}=\begin{bmatrix}0 & 0 & 1\end{bmatrix}\begin{bmatrix}x_1\\ x_2\\ x_3\end{bmatrix} \tag{3.20}$$

Where, $\tilde{\imath}_{L,1}, \tilde{\imath}_{L,2}, \tilde{v}_C, \tilde{v}_{fc}, \tilde{v}_{bat}, \tilde{d}_1, \tilde{d}_2, \tilde{v}_{DC}$ represent the perturbations in the inductor currents $(i_{L,1}, i_{L,2})$, the voltage across the capacitor (v_C), the duty ratios (d_1, d_2), and the DC-bus voltage (v_{DC}), respectively. The transfer function models, $TF_1^c(s)$ and $TF_2^c(s)$ which are the used in the design of the current controller and voltage controller, respectively are derived from the state-space model, and are given in Eqs. (3.21) and (3.22), respectively.

$$TF_1^c(s)=\frac{\tilde{\imath}_{L,1}(s)}{\tilde{d}_1(s)}=\frac{L_2CV_C.s^2+\left[\left(\frac{L_2V_C}{R_{load}}\right)+I_{L,1}L_2(1-D_1)\right].s+V_C(1-D_1)^2}{(L_1L_2C).s^2+\left(\frac{L_1L_2}{R_{load}}\right).s+L_2(1-D_1)^2+L_1(1-D_2)^2} \tag{3.21}$$

$$TF_2^c(s)=\frac{\tilde{v}_{DC}(s)}{\tilde{d}_2(s)}=\frac{(1-D_2).V_C.L_1-\left(L_1L_2I_{L,2}\right).s}{(L_1L_2C).s^2+\left(\frac{L_1L_2}{R_{load}}\right).s+L_2(1-D_1)^2+L_1(1-D_2)^2} \tag{3.22}$$

Step 2: Suitable crossover frequencies, $f_{c,j}$ and desired phase margins, PM_j are chosen.

Step 3: The values of the converter gain, $G_{c,j}$ and phase shift, $P_{c,j}$ at f_c is obtained from the bode plots of $TF_j(s)$.

Step 4: The values of the amplifier gain, $G_{a,j}$ and phase boost, PB_j are determined using Eqs. (3.23) and (3.24), respectively.

$$G_{a,j}={}^{1}/_{G_{c,j}} \tag{3.23}$$

$$PB_j=PM_j-P_{c,j}-90 \tag{3.24}$$

Step 5: Based on the criteria given in [147], the amplifier models which serve as the PWM controllers are chosen. After selecting the suitable amplifier type, the values of the amplifier model parameters are determined. There are three types of amplifiers presented in [147]. Each amplifier type has its own set of mathematical equations to determine the values of its model parameters. These mathematical equations use the values of $G_{a,j}$ and PB_j.

Following the above steps, the PWM controllers are designed in this study.

3.5. Results and discussions

In this section, the simulation and hardware results are presented and discussed. The present work aims to examine the dynamic performance of the PWM controlled MISO-DC/DC boost converter to implement the PEMFC-battery-HES in locomotives. The study is firstly carried out in MATLAB/SIMULINK, and then on the experimental setup of PEMFC-battery-HES. For this study, a reduced-scale simulation model and an experimental setup of the PEMFC-battery-HES are developed. The $P_{load}(t)$ of a train is determined considering the WDM-3D locomotive and a practical drive cycle scenario. The details of the locomotive [138] and the train compartments [139] are provided in Table 2.1. The drive cycle is chosen from the Indian railway website [140], and represents the average driving pattern of an intercity passenger train operating on the Guwahati-Bongaigaon route in Assam, India. The chosen drive cycle is shown in Fig. 3.5, and its details are listed in Table 3.2. The model of the load presented in section 2.2.3 shows that $P_{load}(t)$ is a function of M_{veh} and $\vartheta(t)$. Thus, the large value of locomotive mass, mass of the train compartments, high value of speed and longer driving period (Fig. 3.5) result in high value of $P_{load}(t)$ in terms of its magnitude (in the range of *MW*) and simulation time. The high value of $P_{load}(t)$ makes it infeasible to carry out the present study because of the following reasons:

- The longer duration of $P_{load}(t)$ will result in longer simulation time.
- The NEXA 1200 PEMFC setup has a power rating of 1.2 *kW* and hence, it is incapable of supplying $P_{load}(t)$ alone. Conversely, since the batteries supply/absorb the difference of power $\{P_{load}(t) - P_{fc}^{rated}\}$, this will require a high capacity rating of the battery.
- The high value of $P_{load}(t)$ will require a MISO converter of higher rating which is infeasible to develop in a laboratory due to the risk of high voltage damage and large space requirement.
- It is not possible to model $P_{load}(t)$ for experimental study using the available electronic load of 2.4 *kW* rating.

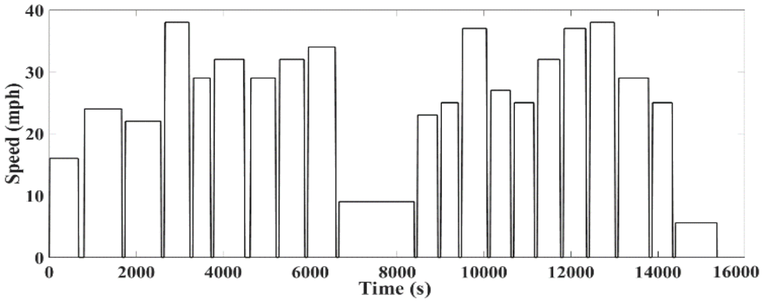

Fig.3.5: Drive cycle of an intercity passenger train operating in Indian railways.

Table 3.2: Details of the drive cycle of Fig. 3.3.

Driving time	4 hrs 26 mins	*Maximum speed (mph)*	38	*Distance (km)*	151	*Number of stops*	20

Hence, some assumptions are made to obtain the reduced scale value of the instantaneous power demand, $P_{load}^{scaled}(t)$ of the original drive cycle scenario. The assumptions are listed below:

- The train mass, locomotive cross-sectional area, $\vartheta(t)$, and the duration of constant speed regime are scaled down to 1/10,000, 1/10,000, (1/3) and (1/100) times of their respective original values.
- The value of acceleration is maintained at the same value as the original drive cycle.
- The duration of stop is considered as 3s.
- The P_{aux} is scaled down to 4.8 W from 8.2 kW.
- The first two repetitions of the drive cycle are considered to reduce the overall simulation time.

Based on the above assumptions, the $P_{load}^{scaled}(t)$ is determined. The dynamic performance of the PWM controlled MISO converter is now examined for the newly simulated $P_{load}^{scaled}(t)$ scenario.

3.5.1. Computer simulation results

In this section, the results obtained from computer simulation study are presented and discussed.

3.5.1.1. Development of the simulation model

For this study, the reduced scale prototype model of the proposed PEMFC-battery-HES (Fig. 3.1) is developed in MATLAB/SIMULINK, and is shown in Fig. 3.6(a). The PEMFC system is the equivalent electrical circuit of the NEXA 1200 PEMFC of Ms. Heiocentris (Fig. 3.2). In the simulation model, the battery model provided in SIMULINK library is implemented. The voltage and ampere-hour ratings of the battery model are set as $24V$ and $12Ah$, respectively. As per the criteria mentioned in section 2.3.1, the value of P_{fc}^{rated} is set as $75W$ in the EMS which is higher than the average value of $P_{load}^{scaled}(t)$. For the MISO-DC/DC boost converter, the values of L_1, L_2 and C are set as 0.5 mH, 1 mH and 390 μF, respectively. These values of L_1, L_2 and C are obtained based on the design procedure presented in section 3.3. Both the current and voltage controllers are simulated in terms of their transfer function models, TF_1^{Type-3} and TF_2^{Type-3}, respectively. In this study, the Type-3 amplifier is chosen to serve as the feedback controllers. The configuration of the Type-3 amplifier is shown in Fig. 3.6(b) and its transfer function is given in Eq. (3.25).

$$TF_1^{Type-3}(s) = TF_2^{Type-3} = \frac{R_2C_1C_3(R_1+R_3).s^2+[R_2C_1+C_3(R_1+R_3)].s+1}{(R_1R_2R_3C_1C_2C_3).s^3+[R_1R_2C_1C_2+R_1R_3C_3(C_1+C_2)].s^2+R_1(C_1+C_2).s} \quad (3.25)$$

Following the steps described in section 3.4.2, the Type-3 amplifier is designed. The values of $G_{c,j}$ and $P_{c,j}$ at the chosen value of $f_{c,j}$ are obtained from the bode plots of the plant transfer functions, $TF_1^c(s)$ and $TF_2^c(s)$, respectively. These bode plots are depicted in Fig. 3.7. The details of the controller design specifications and the amplifier model parameters are given in Table 3.3.

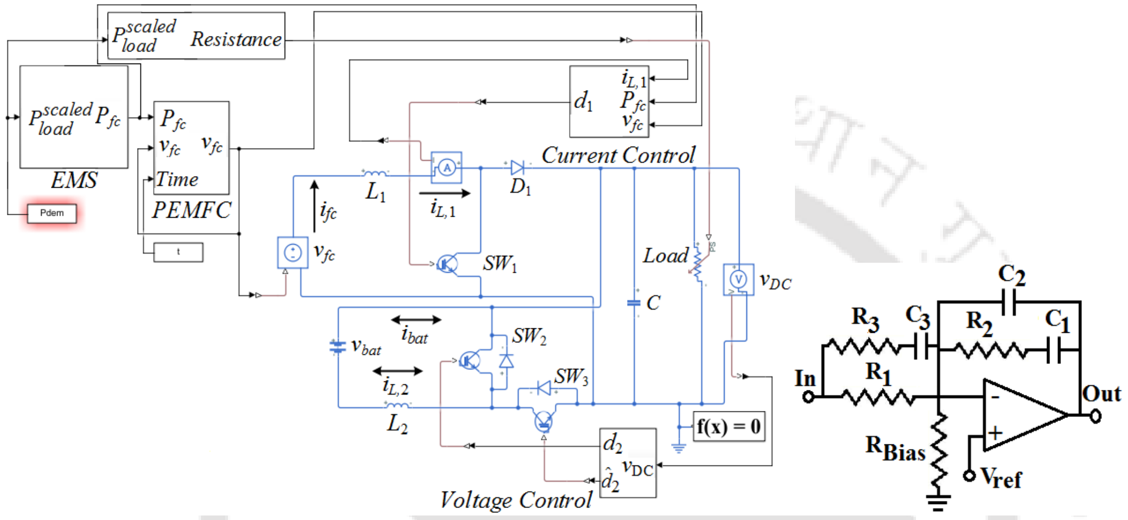

(a) (b)

Fig. 3.6: Configuration of: (a) the MATLAB/SIMULINK model of the PEMFC-battery-HES and (b) the Type-3 amplifier.

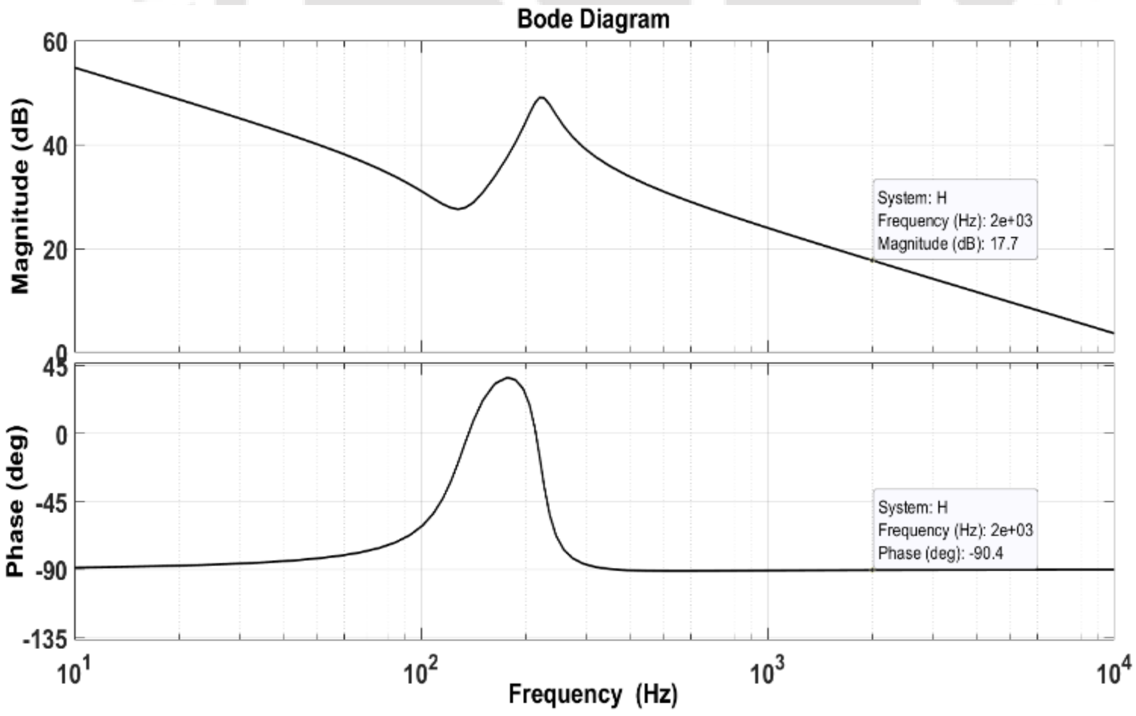

(a)

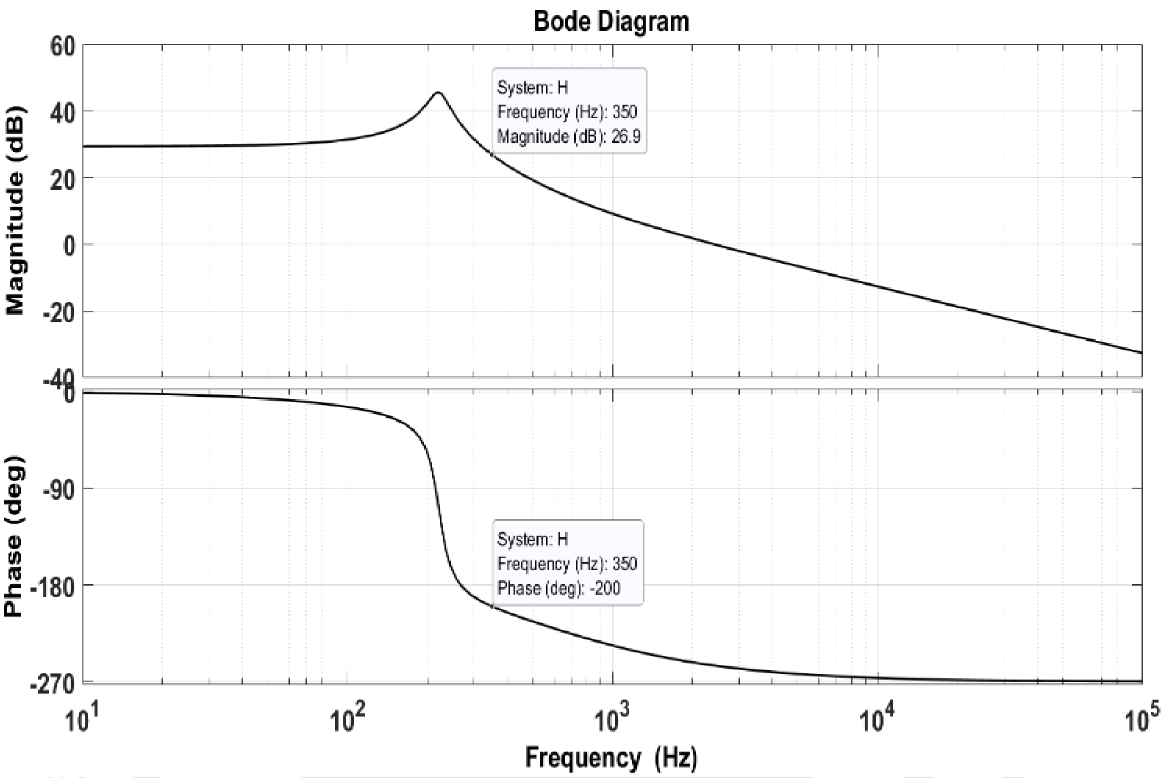

(b)

Fig. 3.7: Bode plot of the MISO converter transfer functions: (a) $TF_1^c(s)$ and (b) $TF_2^c(s)$.

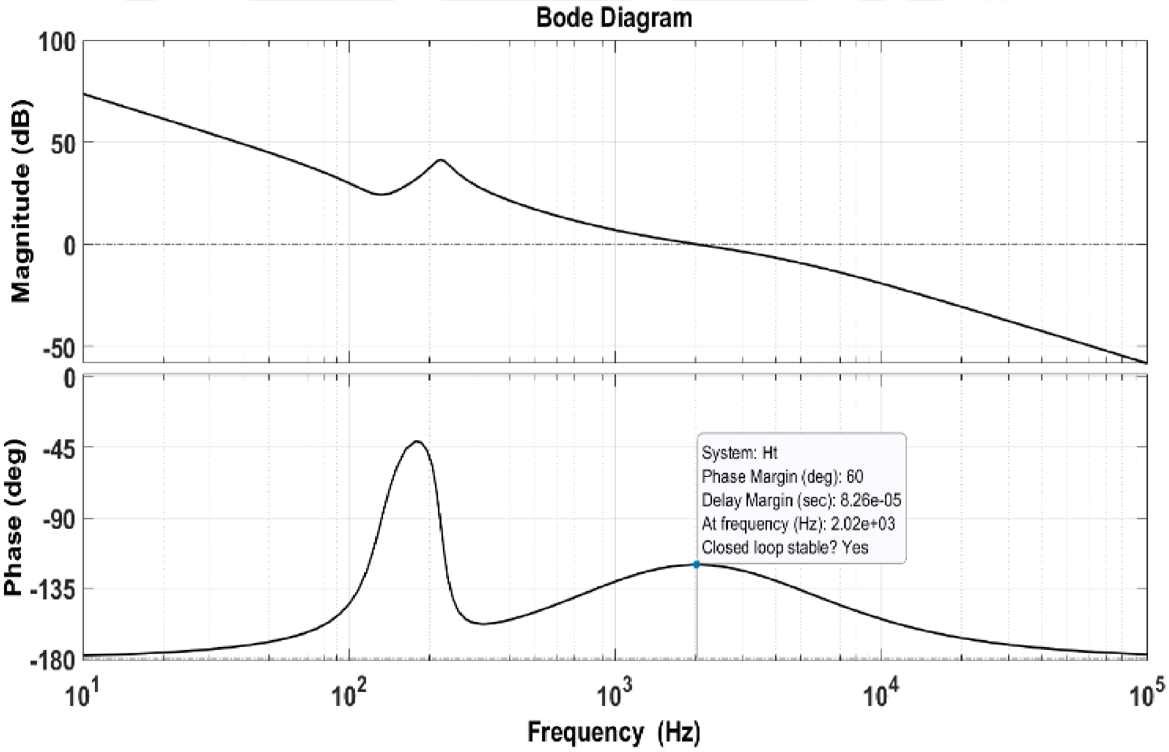

(a)

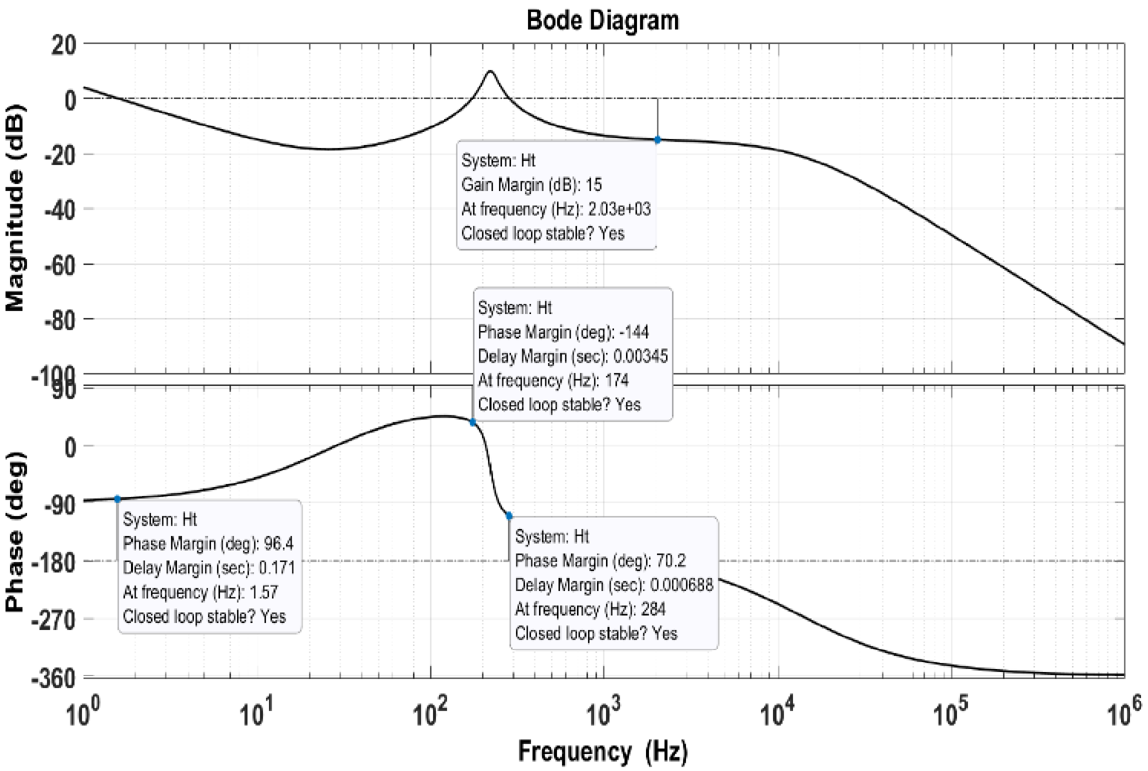

(b)

Fig. 3.8: Bode plots of the closed loop transfer functions for the two PWM control modes: (a) current control and (b) voltage control.

Table 3.3: Details of the design specifications and amplifier model parameters.

PWM controller	*Current Controller*		*Voltage Controller*	
	Amplifier type	*Type-3*	*Amplifier type*	*Type-3*
Design specifications	$f_{c,1}, G_{c,1}, P_{c,1}, PM_1$	2000 *Hz*, 17.7, -90.4°, 60°	$f_{c,2}, G_{c,2}, P_{c,2}, PM_2$	350 *Hz*, 26.9, -200°, 60°
	$G_{a,1}, PB_1$	0.1298 (*abs*), 60.4°	$G_{a,2}, PB_2$	0.0455 (*abs*), 170°
Model parameters	$C_1, C_2, C_3\,(\mu F)$	1.23, 0.61, 0.0926	$C_1, C_2, C_3\,(\mu F)$	3000, 5.68, 5.9
	$R_1, R_2, R_3\,(\Omega)$	1000, 112.6, 494	$R_1, R_2, R_3\,(\Omega)$	1000, 1.98, 1.90
Stability analysis	Closed loop stability	Yes	Closed loop stability	Yes

3.5.1.2. Analysis of the dynamic behavior of the HES

The performances of the designed MISO converter and the PWM controllers are now examined using the simulation model presented in Fig. 3.6. For this study, the plots of $P_{load}^{scaled}(t)$, $P_{fc}(t)$ and $P_{bat}(t)$ are firstly obtained, and are shown in Fig. 3.9. Observation of this figure shows that $P_{fc}(t)$ is maintained at $75W$, and $P_{bat}(t)$ varies to supply/absorb the deficit/excess power. Thus, the variation in $P_{fc}(t)$ and $P_{bat}(t)$ conform to the proposed EMS.

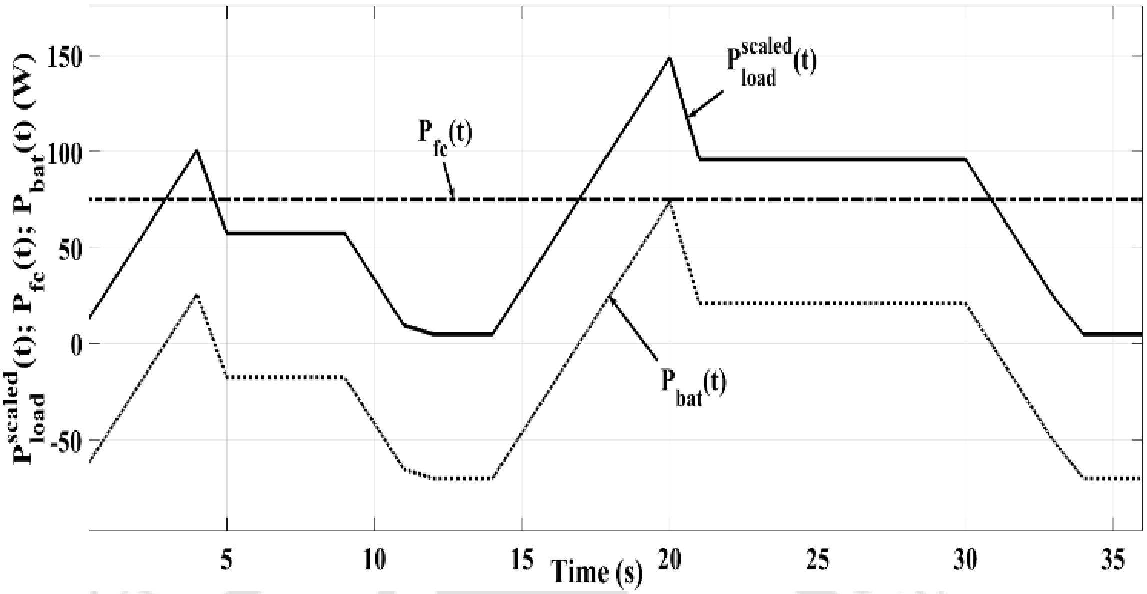

Fig. 3.9: Plot of $P_{load}^{scaled}(t), P_{fc}(t)$ and $P_{bat}(t)$ vs. time.

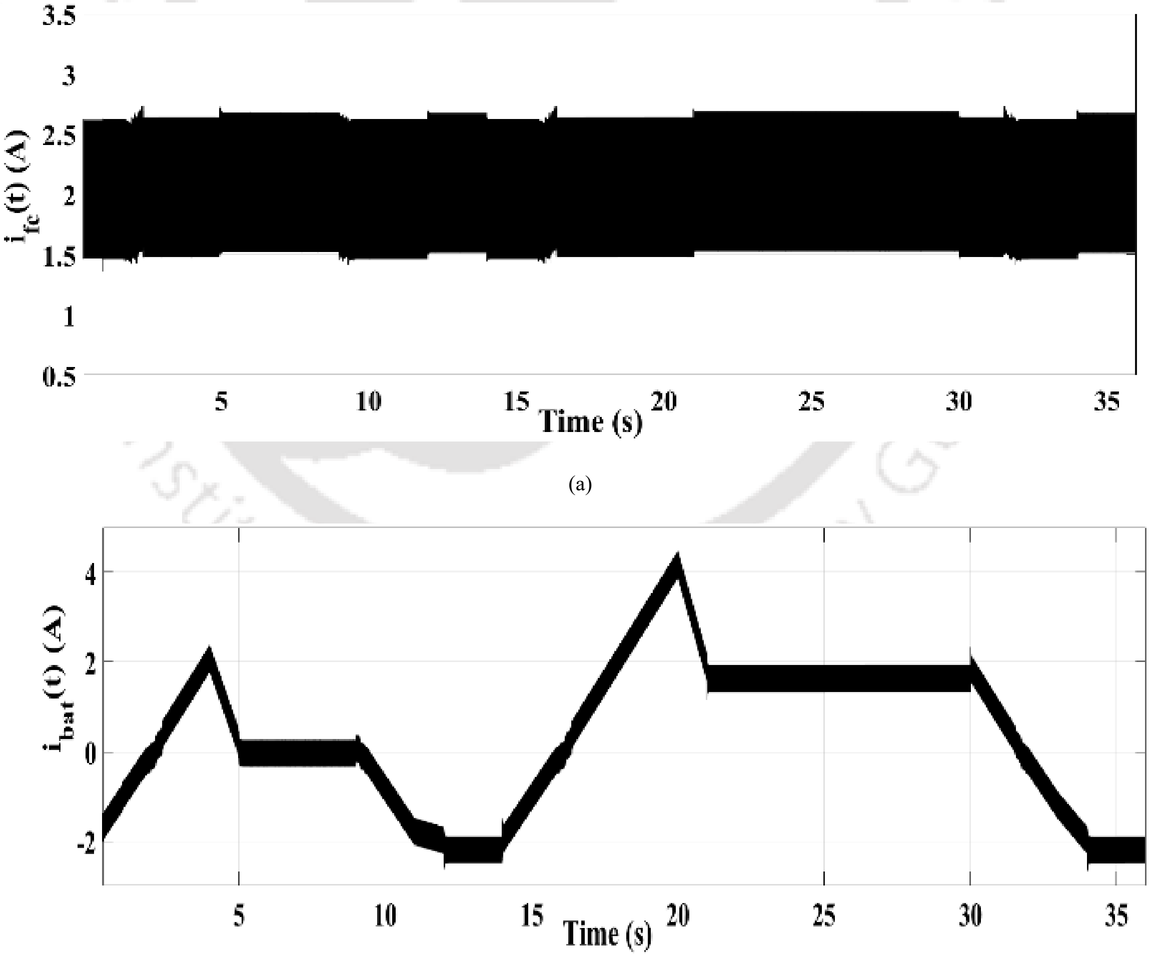

(a)

(b)

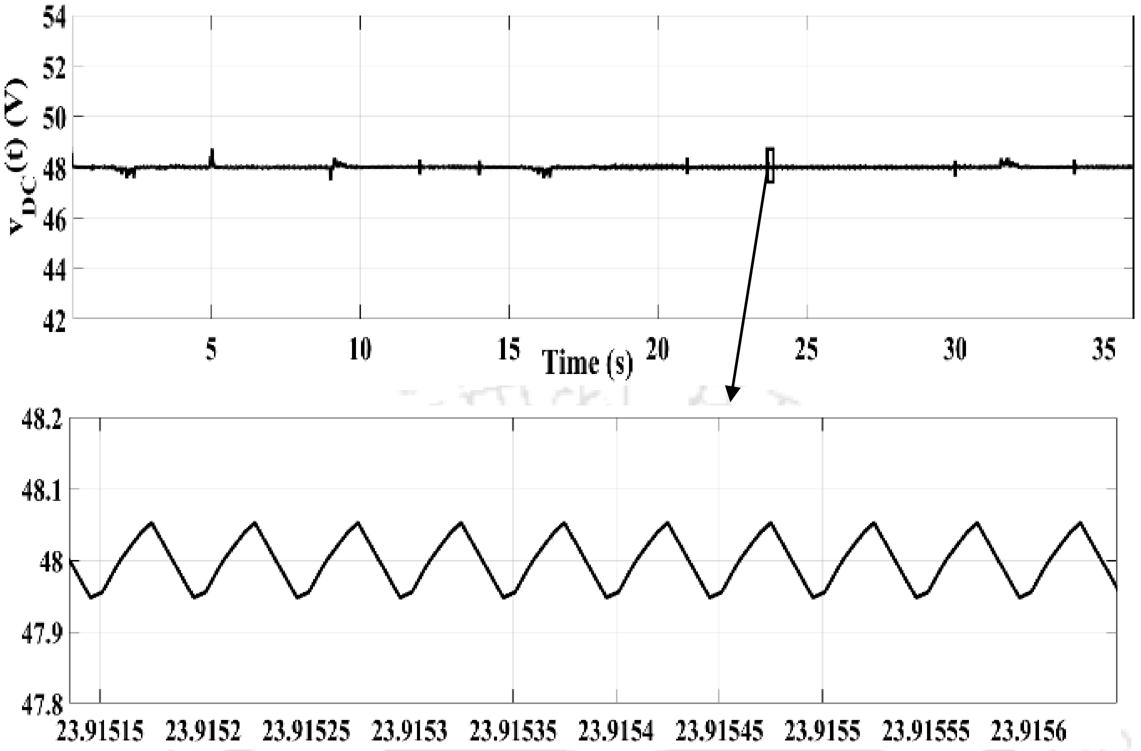

(c)

Fig. 3.10: Plots depicting the variation of: (a) $i_{fc}(t)$, (b) $i_{bat}(t)$ and (c) $v_{DC}(t)$.

Thereafter, to examine the performance of the current controller, plots of $i_{fc}(t)$ and $i_{bat}(t)$ are obtained, and are presented in Figs. 3.10(a) and 3.10(b), respectively. Based on the value of P_{fc}^{rated}, i.e., $75W$, and the value of $v_{fc}(t)$ corresponding to P_{fc}^{rated} OP, i.e., $34V$, the value of I_L^{ref} is obtained as $2.2A$. In Fig. 3.10(a), it is observed that $i_{fc}(t)$ is maintained close to the desired I_L^{ref} of $2.2A$. The $i_{bat}(t)$ varies throughout the simulation period to maintain the instantaneous power balance between the supply and load. Thus, as seen in Fig. 3.10(b), the $i_{bat}(t)$ is positive/negative, i.e. the battery discharges/charges depending on the instantaneous power demand and the power output of the PEMFC. In addition to this, the current ripples of around $1A$ and $0.5A$ are observed in $i_{fc}(t)$ and $i_{bat}(t)$, respectively. These confirms to the design specifications of the MISO converter which are discussed in section 3.3. The above observation implies that the designed current controller performs appropriately to maintain $i_{fc}(t)$ at I_L^{ref}, and to assists in the effective load distribution between the PEMFC and battery in accordance to the EMS.

Next, to examine the performance of the voltage controller, the plot of $v_{DC}(t)$ is obtained, and is presented in Fig. 3.10(c). Observation of the plot shows that $v_{DC}(t)$ is maintained at the chosen

V_{DC}^{ref} of $48V$ irrespective of the dynamically varying locomotive load. Some voltage ripples, Δv_{DC} are also observed in $v_{DC}(t)$ at steady-state, and its magnitude increases/decreases with increasing/decreasing load. However, Δv_{DC} remains within the pre-specified maximum allowable value of 5%. This observation shows that the voltage controller works appropriately to maintain $v_{DC}(t)$ at V_{DC}^{ref} throughout the driving period.

Thus, the simulation study verifies that the designed PWM controlled MISO-DC/DC boost converter operates satisfactorily to achieve the DC-bus voltage regulation and the implementation of the EMS in the HES.

3.5.2. Hardware results

In this section, the hardware results are presented. The aim is to validate the computer simulation results presented in section 3.5.1, and to examine the performances of the PWM controllers and the MISO converter with the experimental setup of the PEMFC-battery-HES.

3.5.2.1. Development of the hardware setup

An overview of the experimental setup of the HES is presented in Fig. 3.11(a). The enlarged view of the NEXA 1200 PEMFC setup of Ms. Heliocentris is provided in Fig. 3.11(b). The primary energy source is the PEMFC stack. The secondary energy source or the ESS is the stack of lead-acid batteries having the voltage rating of $24V$. The MISO-DC/DC boost converter is designed as per the design procedure discussed in section 3.3. The PCB layout of the MISO converter is shown in Fig. 3.11(c). The PWM controllers are designed following the concept of Venable K-factor. In the hardware setup, the PWM control system is implemented through simulation in MATLAB/SIMULINK, and using the TMS320F28335 DSP as the interface between the hardware setup of the MISO converter and the MATLAB simulation software. The PWM controllers are simulated in terms of their transfer function models, TF_1^{Type-3} and TF_2^{Type-3} of Eq. (3.25). The feedback signals of the PWM control system, i.e., the DC-bus voltage, the inductor current of the unidirectional converter layer and the PEMFC output voltage are provided using the 12-bit analog-digital-conversion pins (module A) of the TMS320F28335 DSP. The feedback input signals are sampled at a frequency of $2kHz$. The output of the PWM control system, i.e., the gate pulses for the IGBT switches are obtained using the enhanced PWM pins, ePWM1 and ePWM2 pins of the TMS320F28335 DSP kit. However, the DSP kit can receive or send signals within the voltage range of 0 to $3.3V$. Hence, the sensor circuits are designed to sense the feedback signals and to scale them down to signals with voltage level between 0 to $3.3V$. Similarly, the gate driver circuits are designed for each IGBT switch to boost the voltage of the gate pulses (obtained from DSP kit) from 0 and 3.3V to -8.7 and 15V required to drive the IGBTs. The PCB layout of the sensor and gate driver circuits are shown in Fig. 3.11(c). The block diagrams of the gate driver circuit and sensor circuits are depicted in Figs. 3.12 and 3.13, respectively. The PCB layout of the MISO converter is designed using the Designspark software package. The particulars of the components comprising the experimental setup are listed in Tables 3.4 and 3.5.

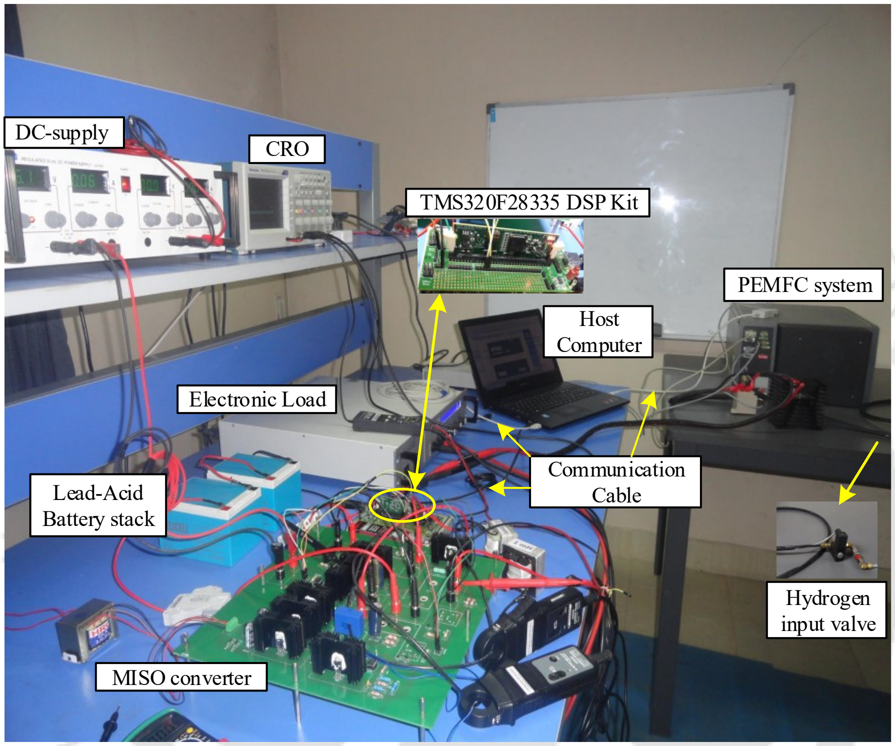

(a)

(b)

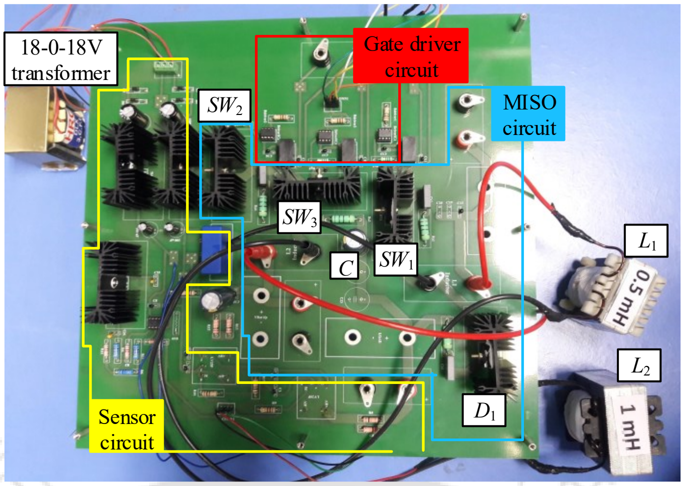

(c)

Fig. 3.11: Overview of: (a) the experimental setup of PEMFC-battery-HES, (b) enlarged view of the NEXA 1200 PEMFC system, and (c) PCB layout of the MISO converter, sensor circuit and gate driver circuit.

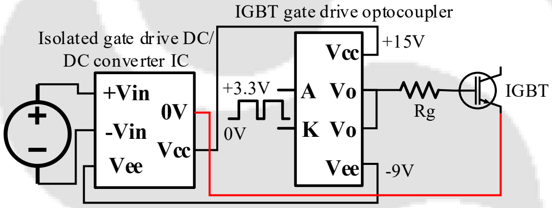

Fig. 3.12: Gate Driver circuit for the IGBT switch.

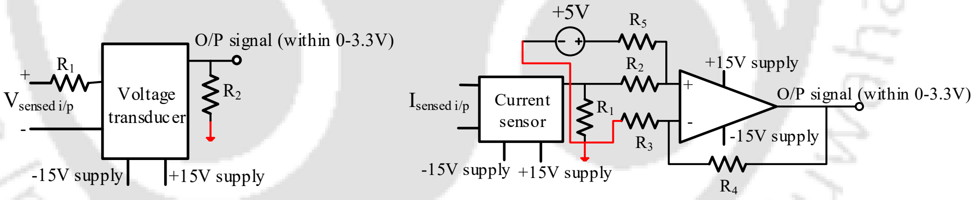

(a) (b)

Fig. 3.13: Sensor circuit to sense: (a) voltage and (b) current.

Table 3.4: Details of the components comprising the experimental setup and amplifier model parameters.

PEMFC system		
Power rating		1.2 *kW*
No. of cells constituting the PEMFC stack		36
Operating voltage range		18-36 *V*
Lead-acid battery		
Nominal voltage and ampere-hour ratings		12 *V*, 12 *Ah*
No. of batteries constituting battery stack		2
DC Electronic Load		
Nominal voltage, current, power ratings		160 *V*, 100 *A*, 2400 *W*
Regulated dual DC power supply		
Voltage, current ratings		16 *V*, 2 *A*
Type-3 Amplifier	*As Current Controller*	*As Voltage Controller*
C_1, C_2, C_3 (μF)	1.23, 0.61, 0.092	3000, 5.68, 5.9
R_1, R_2, R_3 (Ω)	1000, 112.6, 494	1000, 1.98, 1.90

Table 3.5: Details of the circuit components comprising the PCB layout of MISO converter, gate driver circuit and sensor circuits (Figs. 3.9, 3.10, 3.11).

MISO-DC/DC Boost converter			
VA rating		200 VA	
C		390 μF	
Snubber circuit		10 Ω, 10 nF	
Unidirectional layer		*Bidirectional layer*	
L_1	0.5 mH	L_2	1 mH
SW_1	IRG7PH50UPBF, IGBT	SW_2, SW_3	IRGP4266DPBF, IGBT with ultrafast soft recovery diode
D_1	STTH60W03C,Turbo 2 ultrafast high voltage rectifier diode		
Gate driver circuit			
Gate drive Optocoupler		HCPL-3120, 2.5A Output Current IGBT Gate Drive Optocoupler	
Isolated DC/DC converter		MGJ2D151509SC, 5.2kV DC Isolated 2W Gate Drive DC-DC Converter	
Gate drive resistance, R_g		10 Ω	
Voltage sensor circuit			
Voltage sensor		LV 25-P, Voltage transducer	
R_1, R_2		5 $k\Omega$, 100 Ω (to sense DC-bus voltage)	
		5 $k\Omega$, 200 Ω (to sense PEMFC output voltage)	
Current sensor circuit			
Current sensor		LA 55-P, Current transducer	
R_1, R_2, R_3, R_4, R_5		0.01, 1, 5, 1, 3 ($k\Omega$)	

3.5.2.2. Experimental verification of the HES dynamics

To examine the performances of the feedback controllers and the MISO converter under the dynamically varying $P_{load}^{scaled}(t)$ (Fig. 3.9), plots of $i_{fc}(t)$ or $i_{L,1}(t)$, $i_{bat}(t)$ or $i_{L,2}(t)$, and $v_{DC}(t)$ are obtained, and are shown in Fig. 3.14(a). The variation in load as per the dynamically varying $P_{load}^{scaled}(t)$ is done using the DC electronic load. Furthermore, the plots depicting the variation of $i_{fc}(t)$, $i_{bat}(t)$ and $v_{DC}(t)$ at five different loading/operating points, i.e., $OP_i|_{i=1,\ldots,5}$ are also obtained, and are presented in Figs. 3.14(b) – 3.14(f).

The performance of the current controller is firstly examined. Observation of the plots of $i_{fc}(t)$ and $i_{bat}(t)$ in Figs. 3.14(a) – 3.14(f) shows that $i_{fc}(t)$ varies at around the desired I_L^{ref} with small fluctuation between 1.9 to 2.21A. The $i_{bat}(t)$ varies depending on the instantaneous values of $P_{load}^{scaled}(t)$ and $P_{fc}(t)$. Thus, throughout the driving period, $i_{bat}(t)$ is observed to be sometimes positive when $P_{load}^{scaled}(t) > P_{fc}(t)$ {Figs. 3.14(b) – 3.14(d)}, and negative when $P_{load}^{scaled}(t) < P_{fc}(t)$ {Figs. 3.14(e) – 3.14(f)}. Furthermore, as calculated using Eqs. (3.15) and (3.16), current ripples of around 1.1A and 0.5A are observed in $i_{fc}(t)$ and $i_{bat}(t)$, respectively at all the OP_i. Thus, from the above observations it can be concluded that the current controller operates satisfactorily to maintain the PEMFC output current at I_L^{ref} while the battery charges/discharges to absorb/supply the excess/deficit power. This implies that the current controller effectively works to implement the load distribution in the HES as per the EMS.

The performance of the voltage controller is now tested. Examination of the plot of $v_{DC}(t)$ in Figs. 3.14(a) – 3.14(f) shows that $v_{DC}(t)$ is maintained close to the V_{DC}^{ref}. However, some transients are observed in $v_{DC}(t)$ during switching, i.e., at the instant of turn ON and turn OFF of the IGBT switches. These transients persist only for few microseconds and their peak overshoots/undershoots lie within 60-20V. This observation shows that the designed voltage controller works effectively to maintain $v_{DC}(t)$ at the desired V_{DC}^{ref} irrespective of the variation in the operating and loading conditions. Thus, the hardware results show that the design and the control of the MISO-DC/DC boost converter are effective and work satisfactorily to achieve the DC-bus voltage regulation and the implementation of the EMS in the HES.

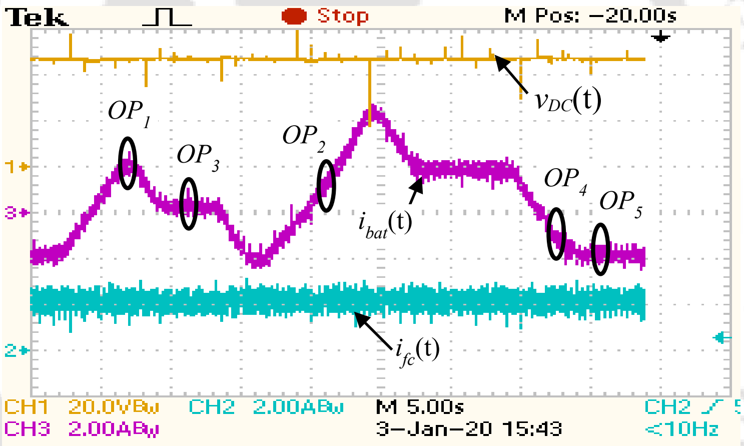

(a)

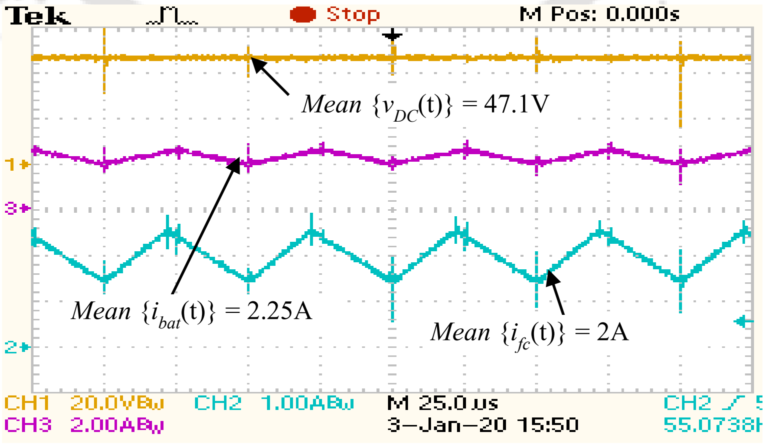

(b)

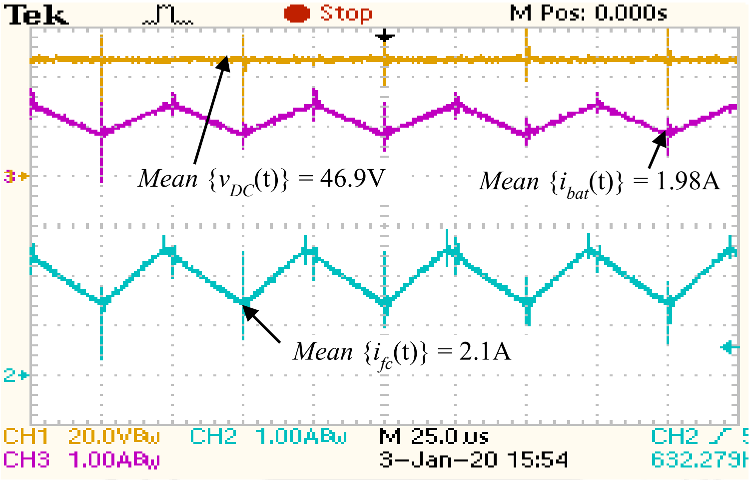
Tek
Stop
M Pos: 0.000s
3
2
Mean $\{v_{DC}(t)\}$ = 46.9V
Mean $\{i_{bat}(t)\}$ = 1.98A
Mean $\{i_{fc}(t)\}$ = 2.1A
CH1 20.0VBW CH2 1.00ABW M 25.0µs CH2 ⁄
CH3 1.00ABW 3–Jan–20 15:54 632.279

(c)

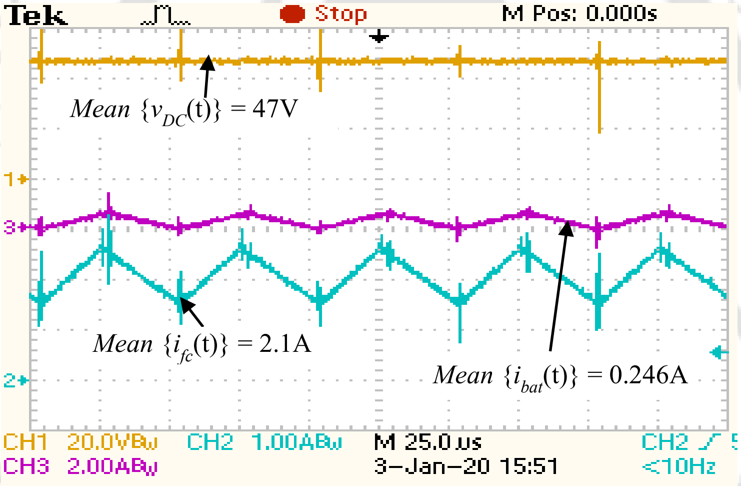
Tek
Stop
M Pos: 0.000s
1
3
2
Mean $\{v_{DC}(t)\}$ = 47V
Mean $\{i_{fc}(t)\}$ = 2.1A
Mean $\{i_{bat}(t)\}$ = 0.246A
CH1 20.0VBW CH2 1.00ABW M 25.0µs CH2 ⁄
CH3 2.00ABW 3–Jan–20 15:51 <10Hz

(d)

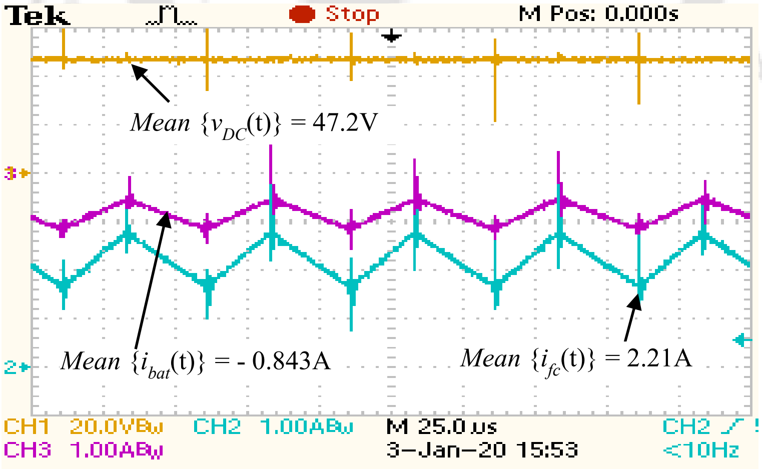
Tek
Stop
M Pos: 0.000s
3
2
Mean $\{v_{DC}(t)\}$ = 47.2V
Mean $\{i_{bat}(t)\}$ = - 0.843A
Mean $\{i_{fc}(t)\}$ = 2.21A
CH1 20.0VBW CH2 1.00ABW M 25.0µs CH2 ⁄
CH3 1.00ABW 3–Jan–20 15:53 <10Hz

(e)

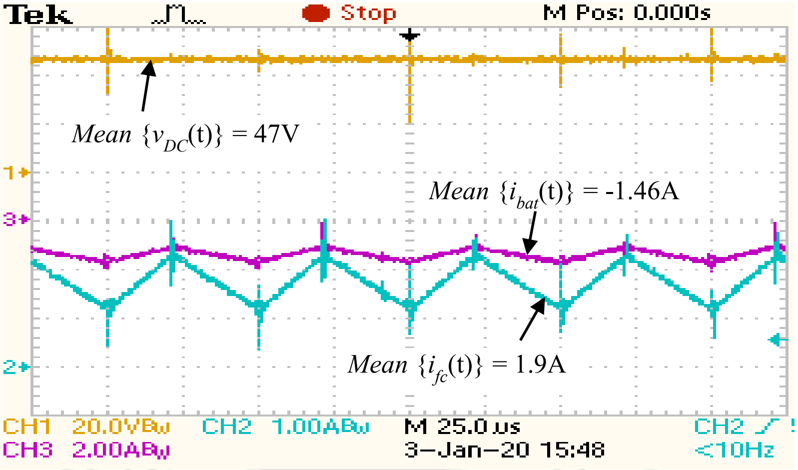

(f)

Fig. 3.14: Plots of $v_{DC}(t)$, $i_{bat}(t)$ and $i_{fc}(t)$: (a) under the dynamically varying $P_{load}^{scaled}(t)$, (b) at OP_1 of 100.8W/2.1A, (c) OP_2 of 76.8W/1.6A, (d) OP_3 of 57.6W/1.2A, (e) OP_4 of 33.6W/0.7A and (f) OP_5 of 4.8W/0.1A.

3.5.2.3. Comparison between the simulation and hardware results

In this subsection, the results obtained from simulation and hardware studies are compared. The outcomes of the comparison study are as follows:

1. Some spikes are observed in the current and voltage waveforms obtained through hardware study at the instant of switching of the IGBT switches. These switching transients are due to the Turn On and Turn Off characteristics of the IGBT switches. The switching transients are absent in the simulation results since the IGBT switches are considered to be ideal with no delays incurred during Turn On and Turn Off. However, transients at the instant of load change are observed in the current and voltage waveforms of both the simulation and experimental results.

2. In the simulation results, the DC-bus voltage $\{v_{DC}(t)\}$ is maintained perfectly at the desired voltage level of 48V. On the contrary, the $v_{DC}(t)$ varies in the range of 46.9 to 47.2V. Thus, a steady-state error of around 2% is observed in $v_{DC}(t)$ of the experimental results. This is due to the voltage drop across the resistance of the tracks, external connection wires, etc.

3. Similarly, simulation results show that the instantaneous inductor current of the unidirectional MISO converter layer or the PEMFC output current $\{i_{fc}(t)\}$ is maintained perfectly at the reference current signal of 2.2A. This reference current is generated by the EMS proposed in Chapter 3. Unlike the simulation results, the hardware studies show that

the $i_{fc}(t)$ varies in the range of 1.9 to 2.21A. Thus, current fluctuation of -13.6% to +0.45% is observed in $i_{fc}(t)$ around the reference current signal of 2A in the hardware results.

4. Simulation study is carried out without the use of snubber circuits across the switching devices, i.e., the IGBTs and diode. However, the absence of snubber circuit did not have any effect on the performances of the switching devices during simulation. On the contrary, the snubber circuits are designed and implemented across the switching devices while carrying out the experimental study to protect it from malfunctioning/damage owing to overcurrent and overvoltage conditions.

Thus the simulation study was carried out to analyse the performance of the proposed control approaches. Once verified, the competence of the PWM control approaches was tested on the prototype hardware setup of the PEMFC-Battery-HES and the MISO converter. The experimental study gave us an overview of the dynamic performance of the control approaches and the PEMFC-Battery-HES when implemented on a real-time locomotive platform.

3.6. Summary of the present work

In this work, the design and control of a MISO-DC/DC boost converter have been carried out for the application of the PEMFC-battery-HES powered locomotive. In the proposed HES, the PEMFC has been used in conjunction with the battery as it can withstand larger load dynamics as compared to the PEMFC. Besides, the battery can also serve as the ESS to absorb the excess power and store it for future use. For the effective load distribution in the HES, a rule based EMS has been devised keeping in mind the durability constraint of the PEMFC. According to this EMS, the PEMFC operates at constant power without undergoing rapid changes in its operating point. However, one of the most important criteria related to the application of the PEMFC-battery-HES in locomotive is the maintenance of a constant DC-bus voltage across the load against the wide variation in the PEMFC output voltage with dynamically varying locomotive load. In order to achieve this, a PWM controlled MISO-DC/DC boost converter has been designed. The MISO converter has been developed to satisfy the operating conditions of both the energy sources. The PWM controllers regulate the converter switching in order to achieve the DC-bus voltage regulation and to the implement the EMS. The controllers have been designed utilizing the concept of Venable K-factor. The dynamic performances of the PWM controlled MISO converter have been firstly examined through simulation in MATLAB/SIMULINK. For this study, a reduced scale prototype model of the proposed PEMFC-battery-HES has been simulated. In the simulation model, the PEMFC model is the equivalent electrical circuit of the NEXA 1200 PEMFC system of Ms.

Heliocentric. Thereafter, the performances of the designed controllers and the MISO converter have been tested on the experimental setup of the HES. In this experimental setup, the PCB layout of the MISO converter has been designed and the PWM control scheme has been implemented through MATLAB simulation, and using the TMS320F28335 DSP kit as an interface between the simulation software and the hardware setup of the MISO converter. Both the simulation and hardware results show that the designed PWM controlled MISO converter operates satisfactorily to maintain the DC-bus voltage and to ensure the load distribution in the HES in accordance to the EMS. Thus, the proposed prototype of the PEMFC-battery-HES can serve as an effective benchmark based on which the real setup of the HES for locomotive can be designed.

Chapter 4

Energy Management Optimization Strategy for PEMFC-Battery-HES for Locomotive Applications

4.1. Introduction

The depletion of conventional energy resources, increase in energy demand, and need for pollution free power generation are the prime motivations behind the integration of PEMFC based HES in transportation, power generation systems and portable applications. In chapter 2, the problem of DO of the HES components is presented to optimize the capital cost of the PEMFC-battery-HES for locomotive applications. In chapter 3, the PWM control approaches are designed to regulate the switching of the MISO-DC/DC boost converter switches in order to meet the requirements of the implementation of the PEMFC-battery-HES in locomotives, i.e., the maintenance of the DC-bus voltage, and the power flow control in the HES. However, another vital aspect that determines the competence of a PEMFC based HES is to optimize the operational cost of the HES without compromising the operational constraints of the energy sources, such as, the sluggish dynamic response of the PEMFC including the FC starvation and flooding, long charging times of the battery and SC with limited driving distance per charge, the intermittent nature of the renewable energy technology, especially the PV, and wind power technology, etc. These technical drawbacks of the energy sources need to be compensated when they are used in conjunction to form a HES. This can be achieved through the design of an efficient EMS. In literature, several EMS are reported, and can be categorized as follows:

- ***Non-optimization based EMS***: Examples of such EMS includes the ECMS [5], [6], [7], rule based EMS [8]–[21], [23], [24]–[28], adaptive supervisory control [22], [90], model predictive control based EMS [29], [30], [91], decentralized EMS based on mixed droop strategy [31], passivity based controller [32], hysteresis algorithm based EMS [33], [34], state-machine control based EMS [35], [36], two-stage controller based EMS [37], time delay control [38], central controller based on AVR technology [39], EMS based on FLC [41]–[49], combined wavelet theory-FLC [50], [51], combined MPPT-FLC [52], ARMA controller based EMS [53], EMS based on reinforcement learning [54], radial-basis-function networks based adaptive control [55], EMS based on Hybrid Automata [92], combined MPPT-rule based EMS [93], and load follower charge sustaining (LFCS) based EMS [86]. These EMSs are basically based on some pre-defined rules, and may or may not result into optimal power split among the energy sources of the HES.
- ***Optimization based EMS/EMO approaches***: The EMO approaches aims at developing an optimal power flow control strategy for the hybrid power plant. The goal of EMO approaches is to either maximise or minimise one or more objective functions by systematically choosing the input values from within an allowed set of operational constraints. Some of the objective functions of the EMO approaches proposed in literature are the minimization of the PEMFC fuel consumption [66]–[70], [72], [73], [75], [77]–[81], minimization of the PEMFC degradation [68], [76], [77], minimization of the battery usage [66], minimization of the levelised cost of energy of the hybrid renewable energy system, renewable energy system exploitation and pollutant emission [100], maximization of the overall efficiency of the HES [67], [72], maximization of the braking energy recovery by the ESS [74], maximization of the fuel consumption efficiency [78], minimization of the daily operational cost [71], [101]–[103], maximization of fuel economy [82], etc. These EMO approaches are solved using either the **mathematical and enumerative strategies,** such as, the rule based deterministic algorithm [68], PMP [34], [66], [73]–[76], DP [73], [77], line search algorithm [79], etc., or the **meta-heuristic solution strategies**, such as, the GA [66], [70]–[72], [80], [103], global extremum seeking algorithm [78], [82], evolutionary programming [81], [101], [102], etc.

A comprehensive review of the aforementioned EMSs is presented in section 1.2. Based on the literature survey, the following research gaps are observed:

- In most of the research articles, i.e., [5]–[39], [41]–[55], [86], [90]–[93], the deployment of non-optimization based EMSs is reported. Among these papers, a FLC based EMS is implemented for power flow control in the PEMFC-battery-HES for locomotive application, and its efficiency is tested through simulation in the vehicle simulation software, ADVISOR in [47]. The designed FLC takes the locomotive power demand and SOC of the battery as inputs, and the required power of the PEMFC as the output. While designing the rules of FLC, two basic principles are considered, i.e., to reduce the dynamic load of the FC, and to make the battery undertake the quick change of required power demand while maintaining the battery SOC within its limits. Likewise, the ECMS [6], [7], rule based EMS [8], model predictive control [30], state-machine control [36], and combined FLC-Haar wavelet transform based EMS [51] are proposed for tramway applications.

- There are few research works where optimization based EMSs are presented [66]–[82], [101]–[103]. Among these papers, the EMO of a PEMFC-SC-HES is carried out for locomotive applications only in [74]. In this paper, the authors propose a PMP based EMS with the objective function of maximizing the regenerative energy absorption by the SC. Thus, the study carried out on the EMS is basically focussed on the braking region of the speed curve, and not for a complete driving horizon.
- In none of the above papers, [47], [74], the durability of the energy sources are taken into consideration.

Keeping this in mind, the problem of EMO for optimizing the operational performance of the PEMFC-battery-HES for locomotive applications is addressed in this chapter. The contributions of this chapter are summarized below:

- Mathematical formulation of two different EMO approaches is carried out for the optimal distribution of the locomotive load in the PEMFC-battery-HES. The two EMO approaches are:
  (a) EMO1 approach: In this EMO approach, the durability constraints of the energy sources are not considered.
  (b) EMO2 approach: This EMO approach is designed considering the durability model of the battery as one of the operational constraints of optimization.
- The proposed EMO approaches are solved by using the linear and non-linear programming solvers.
- Simulation study is carried out to test the proficiency of the proposed EMO approaches for

some practical drive cycle scenarios of intercity passenger trains operating in NEFR, Assam, India. The competence of the EMO approaches is measured in terms of the reduction in the fuel consumption of the PEMFC and the improvement in the dynamic performances of the energy sources.

4.2. EMO1 approach

In this section, the EMO1 approach is proposed for the optimal energy management in the PEMFC-battery-HES to supply the locomotive load. The performance of the proposed EMO1 approach is tested through comparison with some of the already available energy management approaches, and on the prototype MATLAB/SIMULINK model of the PEMFC-battery-HES. The aforementioned studies are discussed in the following sub-sections.

4.2.1. Mathematical formulation of the EMO1 approach

The proposed EMO1 approach aims to determine the PEMFC power references for each loading point of the dynamically varying locomotive power demand. Formulated as a discrete linear optimization model, the objective function of the EMO1 approach is to minimize the PEMFC fuel consumption during the driving period under the operational constraints of the instantaneous power balance between the source and load, the rate of change of PEMFC output power, and the variation in $SOC(t)$. The mathematical model of the EMO1 approach is given below:

$$Minimise\ f(x) = m_{H_2} = \sum_{t=t_0}^{t_f} \frac{P_{fc}(t)}{LHV\eta_{fc}} \Delta t \tag{4.1}$$

$$where, x = P_{fc}(t) \tag{4.2}$$

$$subject\ to$$

$$P_{fc}(t) + P_{bat}(t) = P_{load}(t) \tag{4.3}$$

$$\frac{\Delta P_{fc}}{\Delta t} \leq R_{max} \tag{4.4}$$

$$P_{fc}^{min} \leq P_{fc}(t) \leq P_{fc}^{rated} \tag{4.5}$$

$$SOC_{min} \leq SOC(t) \leq SOC_{max} \tag{4.6}$$

$$where,$$

$$R_{max} = \frac{\Delta P_{fc}|_{0-90\%\ of\ P_{fc}^{rated}}}{\Delta t = 30s} \tag{4.7}$$

$$P_{fc}^{min} = P_{aux} \tag{4.8}$$

$$SOC(t) = SOC(t - \Delta t) - \eta_{bat} \frac{P_{bat}(t)}{Q_{bat}^{rated}} \Delta t \tag{4.9}$$

$$\eta_{bat} = \begin{cases} \frac{1}{\eta_{chg}}, if\ P_{bat}(t) \le 0 \\ \eta_{dis}, if\ P_{bat}(t) > 0 \end{cases} \tag{4.10}$$

Where, m_{H_2} is the hydrogen consumption of the PEMFC; $t_0(t_f)$ is the starting (final) time of the driving period; $P_{fc}(t)$ $\{P_{bat}(t)\}$ are the instantaneous output power of the PEMFC (battery); $P_{load}(t)$ is the instantaneous power demand of the train; LHV is the lower heating value of hydrogen; η_{fc} (η_{chg}/η_{dis}) is the efficiency of the PEMFC (charging/discharging efficiency of the battery); ΔP_{fc} (Δt) is the change in PEMFC output power (time); R_{max} is the maximum rate of change of PEMFC output power; P_{fc}^{min} is the lower limit of PEMFC output power; P_{fc}^{rated} is the rated power of the PEMFC; $SOC(t)$ is the instantaneous state-of-charge of the battery; SOC_{min} (SOC_{max}) is the lower (upper) limit on $SOC(t)$; P_{aux} is the constant power component representing the power consumption of the auxiliaries of the train, such as, the traction motor blower, lighting loads, etc.; and Q_{bat}^{rated} is the rated battery capacity. Equation (4.1) define the objective function of optimization, i.e., the minimization of the PEMFC fuel consumption. The optimizing/decision variable is $P_{fc}(t)$, and is defined in Eq. (4.2). The operational constraints of the optimization model are given in Eqs. (4.3 - 4.6). The constraint of instantaneous power balance between the source and load is defined in Eq. (4.3). Equation (4.4) imposes an upper limit, R_{max} on the rate of change of $P_{fc}(t)$ so as to prevent the phenomenon of FC starvation, flooding, etc., and also to account for the slow transport of reactants in the FC stack during the electro-chemical reaction. The variation in $P_{fc}(t)$ is restricted within the range of $[P_{fc}^{min}, P_{fc}^{rated}]$ in Eq. (4.5). Likewise, the battery dynamics in terms of the $SOC(t)$ is constrained to vary within $[SOC_{min}, SOC_{max}]$ in Eq. (4.6). Equations (4.7 - 4.10) present the mathematical definitions of the terms, R_{max}, P_{fc}^{min} and $SOC(t)$, respectively as considered in this study. According to the report published by the U.S Department of Energy [137], by 2020 the PEMFC will be able to reach from 0 to 90% of its rated power in 30*s*. Based on this, the value of R_{max} is computed in Eq. (4.7). The values of η_{fc} and η_{chg} (η_{dis}) are taken as 50% [148] and 90%, respectively.

4.2.2. Solution strategy for the EMO1 approach

In this chapter, the proposed EMO1 approach is implemented as an offline optimization process using GAMS. For this, the mathematical model of the EMO1 approach is fitted into GAMS, a high-level modeling software used for mathematical programming and optimization. GAMS consists of a set of integrated high-performance solvers which can be used to solve large scale linear, nonlinear and mixed integer optimization problems. The CPLEX solver of GAMS is used to solve the EMO1 approach, since it is a kind of linear optimization problem. In the EMO1 model, the optimal values of P_{fc}^{rated} and Q_{bat}^{rated} that meet the requirements of supplying the $P_{load}(t)$ of the intercity passenger trains operating under the different drive cycle scenarios are firstly determined. The chosen drive cycles are shown in Fig. 4.1, and their details are listed in Table 4.1. These drive cycles are simulated based on the real-time data provided in [140]. The $P_{load}(t)$ is computed using the load model of section 2.2.3. In the calculation of $P_{load}(t)$, the value of the vehicle mass is determined as the summation of the masses of the WDM-3D locomotive [138] and the non-air conditioned coaches [139]. The corresponding details are listed in Table 2.1. The P_{aux} is taken as 82 kW. For reference, the $P_{load}(t)$ obtained for drive cycle 1 is plotted in Fig. 4.2. The ratings of the HES components for the different drive cycles are now determined using the optimization model formulated in section 2.3.1. Three different sets of $[P_{fc}^{rated},\ Q_{bat}^{rated}]$ for the three drive cycles are obtained. From these ratings, the approximate values of P_{fc}^{rated} as $4.9MW$ and Q_{bat}^{rated} as $2MWh$ that suffices to meet the locomotive power demand for all the drive cycles are chosen.

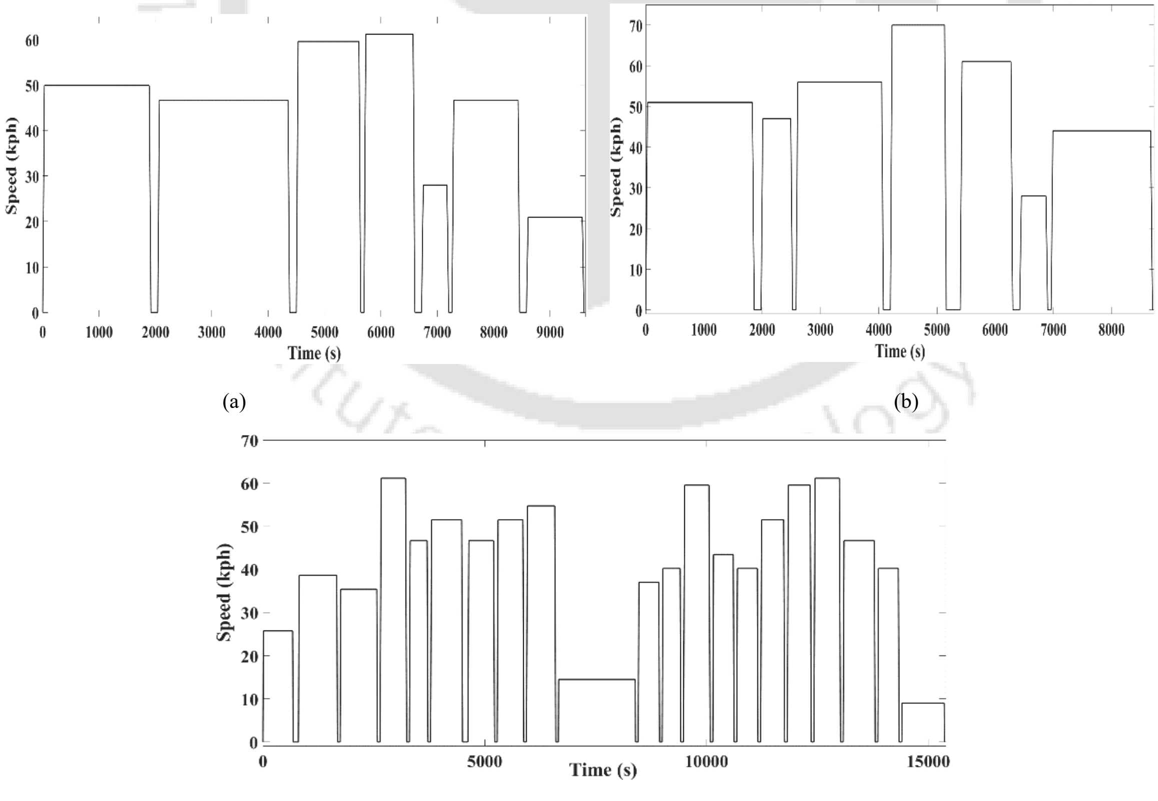

(a)

(b)

(c)

Fig. 4.1: Plots depicting the variation of locomotive speed vs. time: (a) drive cycle 1, (b) drive cycle 2 and (c) drive cycle 3.

Table 4.1: Details of the drive cycles of Fig. 4.1.

	Total duration	*Distance (in km)*	*Maximum speed (in kph)*	*No. of halts*
Drive cycle 1	2 hours 40 minutes	116	61	6
Drive cycle 2	2 hours 25 minutes	113	71	6
Drive cycle 3	4 hours 16 minutes	151	61	21

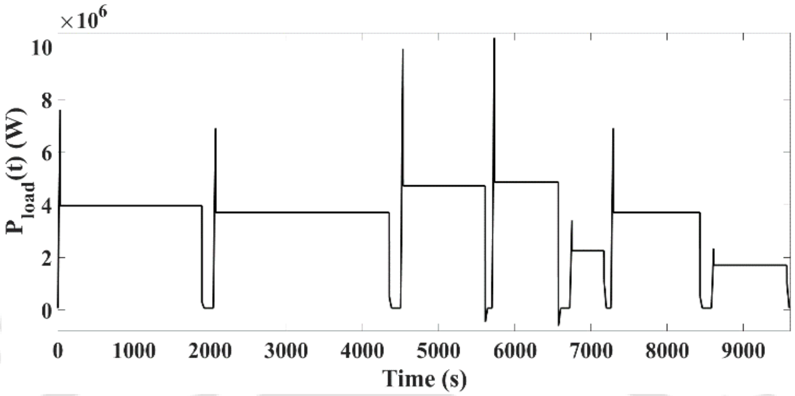

Fig. 4.2: The $P_{load}(t)$ of an intercity passenger train while operating under drive cycle 1 scenario.

Secondly, in the EMO1 model, the $SOC(t)$ is restricted to vary in the range of $[SOC_{min}, SOC_{max}]$, i.e., (0.4, 0.6) with $SOC(t_0)$ set as 0.5. Thirdly, the data of the dynamically varying $P_{load}(t)$ is provided as an input to GAMS. The input data is sampled at every $1s$. The EMO is now carried out using GAMS to determine the references for the PEMFC output power, P_{fc}^{ref} at each loading point of the locomotive power demand. The optimization takes about 47 seconds to converge to an optimal solution which is acceptable considering the large size of the input data file. The block diagram exhibiting the offline EMO execution using GAMS is shown in Fig. 4.3. A snapshot for the solution obtained with the CPLEX solver of GAMS is shown in Fig. 4.4.

4.2.3. Results of EMO1 approach

The results of the EMO1 approach are presented and discussed in this sub-section. The study is carried out in two sequential phases:

- Phase 1 presents the performance comparison of the EMO1 approach with some of the already available energy management approaches for the different drive cycle scenarios of intercity passenger trains of NEFR, Assam, India.
- Phase 2 aims to examine the competence of the EMO1 approach on the prototype model of the PEMFC-battery-HES (Fig. 3.1) to meet the requirements of its application in locomotives.

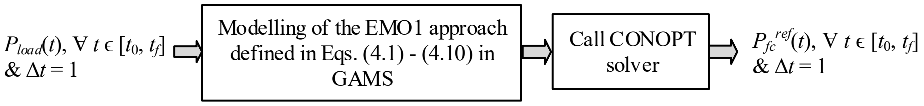

Fig. 4.3: Block diagram depicting the determination of PEMFC power references through offline EMO using GAMS.

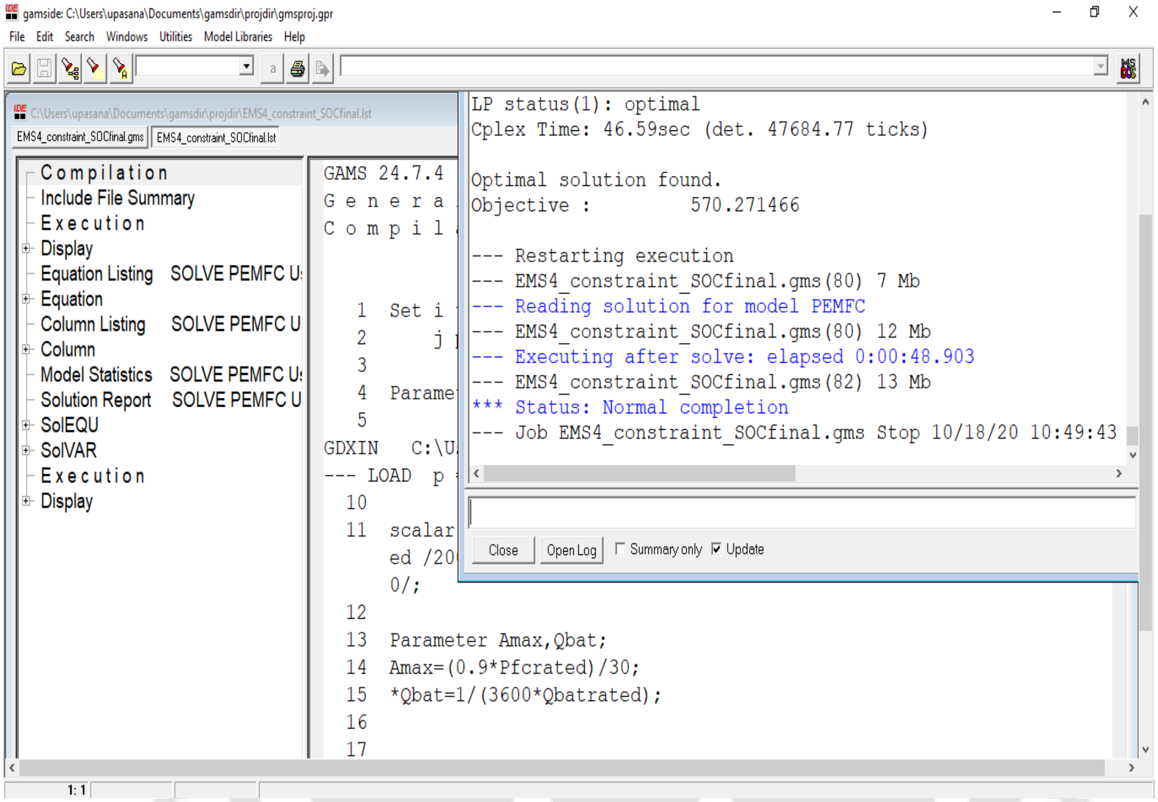

```
LP status(1): optimal
Cplex Time: 46.59sec (det. 47684.77 ticks)

Optimal solution found.
Objective :          570.271466

--- Restarting execution
--- EMS4_constraint_SOCfinal.gms(80) 7 Mb
--- Reading solution for model PEMFC
--- EMS4_constraint_SOCfinal.gms(80) 12 Mb
--- Executing after solve: elapsed 0:00:48.903
--- EMS4_constraint_SOCfinal.gms(82) 13 Mb
*** Status: Normal completion
--- Job EMS4_constraint_SOCfinal.gms Stop 10/18/20 10:49:43
```

```
GAMS 24.7.4
G e n e r a
C o m p i l

  Set i
      j

  Parame

GDXIN   C:\U
--- LOAD  p

  scalar
  ed /20
  0/;

  Parameter Amax,Qbat;
  Amax=(0.9*Pfcrated)/30;
  *Qbat=1/(3600*Qbatrated);
```

Fig. 4.4: Snapshot for a solution obtained using GAMS.

4.2.3.1. Performance analysis of the EMO1 approach

To examine the performance of the proposed EMO1 approach, the plots depicting the variation of $P_{fc}(t)$ and $P_{bat}(t)$ to supply the dynamically varying $P_{load}(t)$ of drive cycle 1 (Fig. 4.2) are obtained, and are shown in Fig. 4.5. The observation of this figure shows that following the EMO1 approach, the PEMFC operates mostly near the region of its rated power. Although, the PEMFC exhibits fluctuations in its output power, the variation in $P_{fc}(t)$ is limited by the constraint of R_{max} as defined in Eq. (4.4). The battery charges/discharges throughout the driving period depending on the instantaneous values of $P_{load}(t)$ and $P_{fc}(t)$. Accordingly, the $SOC(t)$ varies and is depicted in Fig. 4.6(a). As seen in this figure, the $SOC(t)$ rises and falls with small ripples around it. However, the variation in $SOC(t)$ is always maintained within (0.4, 0.6) with $SOC(t_f)$ lying close to SOC_{min}. Similar characteristic variations in $P_{fc}(t)$, $P_{bat}(t)$ and $SOC(t)$ are observed for the drive cycles 2 and 3, and hence, they are not discussed in this section.

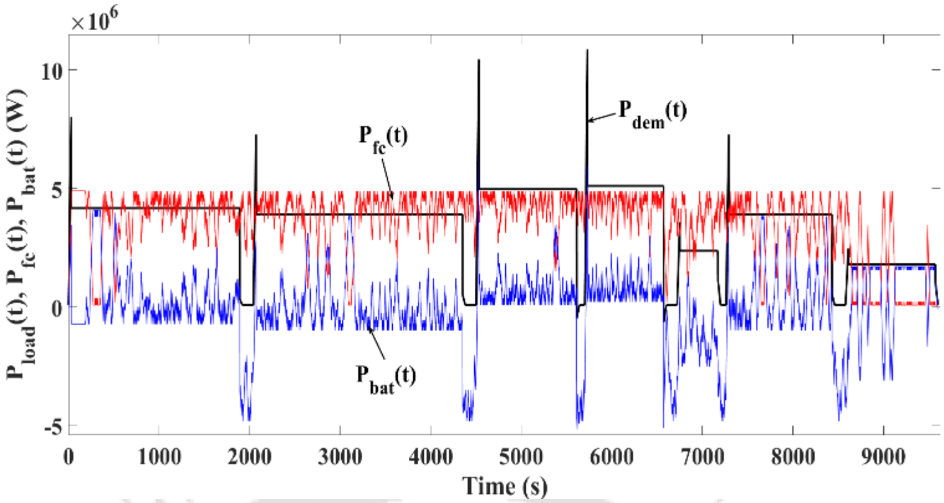

Fig. 4.5: Plots depicting the variation of $P_{fc}(t)$ and $P_{bat}(t)$ to supply $P_{load}(t)$ of drive cycle 1 following the EMO1 approach.

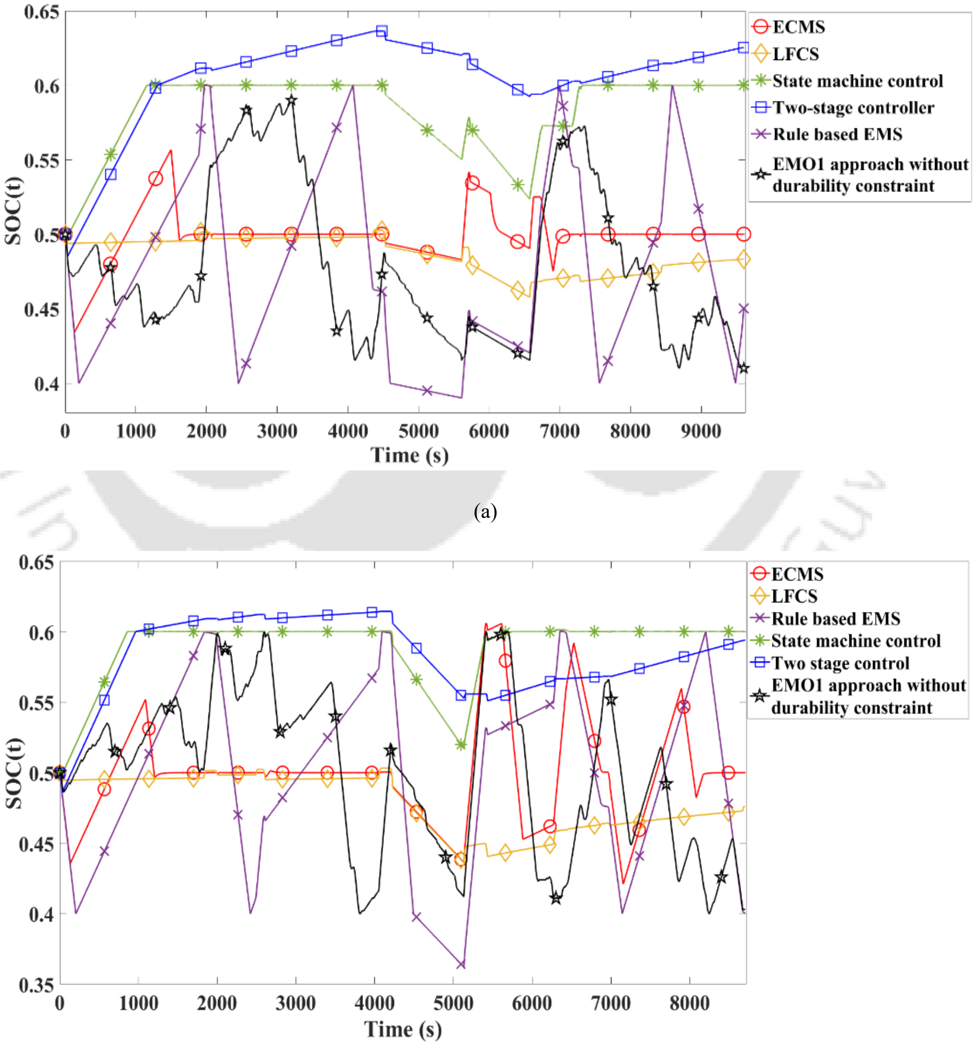

(a)

(b)

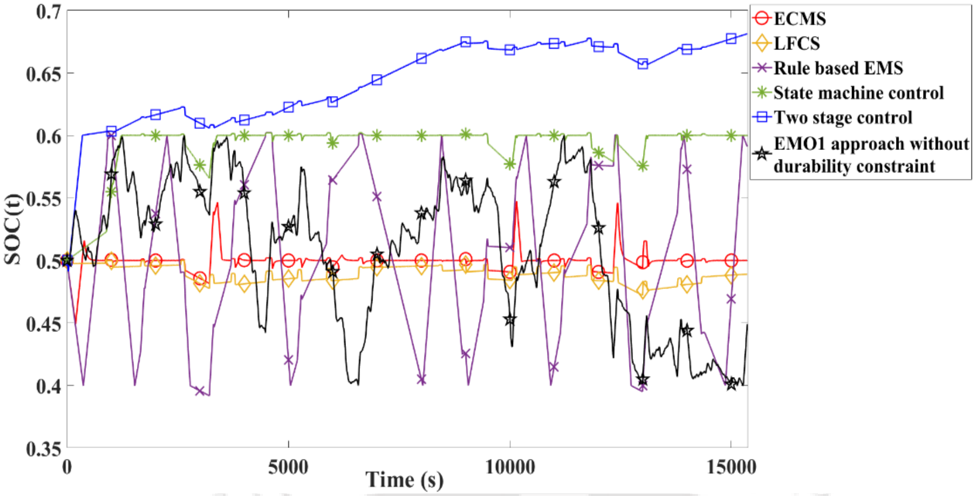

(c)

Fig. 4.6: Comparison among the EMO1 approach and the already available EMSs of literature in terms of their $SOC(t)$ variation under the dynamically varying locomotive load of: (a) drive cycle 1, (b) drive cycle 2 and (c) drive cycle 3.

Table 4.2: Performance analysis of the proposed EMO1 approach and some of the EMSs used in literature in terms of their $SOC(t)$ variation.

EMS	*Drive cycles*	$SOC(t_f)$	*Remarks*
State-machine control [36]	1	$SOC(t_f) = 0.6$	The battery initially charges to SOC_{max}. Thereafter, $SOC(t)$ varies close to SOC_{max}.
	2		
	3		
Two-stage controller [37], [149]	1	$SOC(t_f) = 0.625$	The $SOC(t)$ fluctuates around SOC_{max} with occasional charging beyond SOC_{max}.
	2	$SOC(t_f) = 0.594$	
	3	$SOC(t_f) = 0.681$	
ECMS [5]	1	$SOC(t_f) = 0.5$	$SOC(t)$ is maintained around SOC_{mean} of 0.5 with slight deviations around it.
	2		
	3		
LFCS [86], [150]	1	$SOC(t_f) = 0.483$	$SOC(t)$ varies in a similar way as the ECMS with $SOC(t_f)$ falling slightly below SOC_{min}.
	2	$SOC(t_f) = 0.476$	
	3	$SOC(t_f) = 0.489$	
Rule based EMS [12]	1	$SOC(t_f) = 0.433$	The battery charges, and discharges alternately throughout the driving period.
	2	$SOC(t_f) = 0.4$	
	3	$SOC(t_f) = 0.591$	
Proposed EMO1 approach	1	$SOC(t_f) = 0.41$	Occasional rises, and dips are observed in $SOC(t)$ without violation of its limits.
	2	$SOC(t_f) = 0.403$	
	3	$SOC(t_f) = 0.45$	

Table 4.3: Details of the PEMFC hydrogen consumption (in *kg*) for the EMO1 approach, and the different EMSs for the different drive cycles of Fig. 4.1.

EMS	*Drive cycle 1*	*Drive cycle 2*	*Drive cycle 3*
Two-stage controller [37], [149]	590.20	537.02	779.36
State-machine control [36]	586.81	534.81	768.53
ECMS [5]	573.50	521.50	755.20
LFCS [86], [150]	571.30	520.87	753.75
Rule based [12]	570.27	518.28	767.36
Proposed EMO1 approach	566.85	515.21	749.80

Next, to test the competence of the proposed EMO1 approach, the performance comparison between the EMO1 approach and some of the EMSs previously used in literature, i.e., the two-stage controller [37], [149], state-machine control [36], LFCS [86], [150], ECMS [5], and rule based EMS [12] is carried out. The comparison among these EMSs in terms of their battery $SOC(t)$ variation is presented in (Fig. 4.6 and Table 4.2). Likewise, the PEMFC hydrogen consumption of the EMSs for the different drive cycle scenarios are compared, and are listed in Table 4.3. The following inferences are obtained from this comparison study:

- In Fig. 4.6, it is seen that the two stage controller and state-machine control based EMSs aim to sustain the $SOC(t)$ variation around SOC_{max}. However, unlike the state machine control based EMS, the two stage controller occasionally charges the battery beyond SOC_{max} in all the drive cycle scenarios.

- The ECMS and LFCS based EMSs operate to maintain the $SOC(t)$ close to SOC_{mean} $\{SOC_{mean} = 0.5(SOC_{max} + SOC_{min})\}$ with small fluctuations around it. However, for the LFCS based EMS, the $SOC(t)$ tends to fall slightly below SOC_{mean} towards the end of the driving period.

- The above observations imply that following the two-stage controller, state-machine control, LFCS and ECMS based EMSs, the $P_{fc}(t)$ undergoes larger dynamic load variation as compared to the battery. Hence, these EMSs are useful for applications where the preservation of $SOC(t)$ holds prior importance. However, these EMSs do not guarantee the optimum utilization of the battery capacity to supply the load.

- Alternate charging/discharging patterns in the $SOC(t)$ are observed for the rule based EMS. Moreover, while supplying the locomotive power demand in accordance to the rule base EMS for drive cycles 1 and 2, the battery $SOC(t)$ decreases to a lower level towards the end of the driving period as compared to the two-stage controller, state-machine control, ECMS and LFCS based EMSs. The decrease in $SOC(t_f)$ level is almost 11.55% to 50% in the rule based EMS. This implies that the battery capacity is utilized more than the PEMFC to supply the power demand in the rule based EMS in these drive cycle scenarios. This subsequently leads to reduced fuel consumption of the PEMFC in the rule base EMS for drive cycles 1 and 2. However, the battery $SOC(t_f)$ is maintained at a higher level (almost 15.40% to 17.26% higher) for drive cycle 3 following the rule based EMS as compared to the ECMS and LFCS based EMSs. This is because while alternatively supplying/absorbing the deficit/excess power in accordance to the rule based EMS, the battery tends to follow the charging pattern towards the end of the drive cycle 3. This implies that more amount of PEMFC output power is utilized to supply the locomotive load and to charge the battery in the rule based EMS for drive cycle 3. This subsequently leads to higher fuel consumption for drive cycle 3 in the rule based EMS as compared to the ECMS and LFCS based EMSs. Hence, in terms of reduced fuel consumption, the rule based EMS may be advantageous under certain driving conditions. However, occasional violation of the SOC limits is seen in Fig. 4.6 for this EMS.

- These technical drawbacks are taken care of by the EMO1 approach. The proposed EMO1 approach generates the set points for the PEMFC output power using GAMS so as to minimize the PEMFC hydrogen consumption while simultaneously limiting the rate of change of $P_{fc}(t)$ by R_{max}, and the variation of $SOC(t)$ within $[SOC_{min}, SOC_{max}]$. Thus, it is observed in Table 4.3 that the EMO1 approach results in the least hydrogen consumption of the PEMFC. For drive cycle 1, the hydrogen consumption for the EMO1 approach decreases by 4.12%, 3.52%, 1.17%, 0.79% and 0.6% as compared to the two stage controller, state-machine control, ECMS, LFCS and rule based EMSs, respectively. Similarly, for drive cycles 2 and 3, the corresponding decrease in the hydrogen consumption is observed to be 4.23%, 3.80%, 1.22%, 1.10%, 0.60% and 3.94%, 2.50%, 0.72%, 0.53%, 2.34%, respectively.
- Unlike the proposed EMO1 approach, the two stage controller, state-machine control, ECMS, LFCS and rule based EMSs are based on some pre-specified rules, and hence may not work for all driving scenarios.

From the above comparison study, it can be concluded that the proposed EMO1 approach operates satisfactorily to minimize the PEMFC fuel consumption with optimum utilization of the capacity of the energy sources without violating the operational constraints.

4.2.3.2. Implementation of the EMO1 approach on the PEMFC-battery-HES prototype

In this section, the execution of the EMO1 approach on the prototype MATLAB/SIMULINK model of the PEMFC-battery-HES {Fig. 3.4(a)} is analyzed. For this study, the $P_{load}(t)$ for the original drive cycle 1 scenario {Fig. 4.1(a)} is firstly scaled down to $P_{load}^{scaled}(t)$ in terms of its magnitude and simulation time based on the following assumptions:

- The train mass, locomotive cross-sectional area, speed, duration of constant speed regime and stop are scaled down to 1/2000, 1/100, 1/5, 1/200 and 1/60 times of their respective original values. The acceleration is kept at the same value as the original drive cycle.
- The P_{aux} is scaled down to 4.8 W.
- The first three recurrences of the drive cycle are chosen.

The P_{fc}^{ref} at each loading point of $P_{load}^{scaled}(t)$ are now obtained by solving the EMO1 approach using the CPLEX solver of GAMS. In the optimization model, the values of P_{fc}^{rated} and Q_{bat}^{rated} set as $380W$ and $6Wh$, respectively. These values of P_{fc}^{rated} and Q_{bat}^{rated} are obtained using the optimization approach defined in section 2.3.1 for the newly simulated $P_{load}^{scaled}(t)$ scenario. The corresponding data of P_{fc}^{ref} is fitted in the EMS block of the simulation model of the PEMFC-battery-HES. For the PWM control system, the Type-3 and Type-1 amplifiers [147] are chosen to serve as the current and voltage controllers, respectively. The configurations of the amplifiers are shown in Fig. 4.7. These controllers are designed following the concept of Venable K-factor in a similar way as described in section 3.4.2. In the MATLAB/SIMULINK model of the HES, these controllers are simulated in terms of their transfer function models given by Eqs. (4.11) and (4.12), respectively. The values of the amplifier model parameters are listed in Table 4.4.

$$TF_1^{Type-3} = \frac{R_2C_1C_3(R_1+R_3).s^2+[R_2C_1+C_3(R_1+R_3)].s+1}{(R_1R_2R_3C_1C_2C_3).s^3+[R_1R_2C_1C_2+R_1R_3C_3(C_1+C_2)].s^2+R_1(C_1+C_2).s} \tag{4.11}$$

$$TF_2^{Type-1} = \frac{1}{R_1C_1s} \tag{4.12}$$

(a) (b)

Fig. 4.7: Configurations of the PWM controllers: (a) Type-1 amplifier and (b) Type-3 amplifier.

Table 4.4: Details of the Amplifier model parameters.

Type-1 amplifier		*Type-3 amplifier*	
C_1 (μF)	*100.52*	C_1, C_2, C_3 (μF)	*2.24, 1.0345, 0.097*
R_1 (Ω)	*1000*	R_1, R_2, R_3 (Ω)	*1000, 63, 461.05*

The simulation is now carried out to obtain the plots of $P_{load}^{scaled}(t)$, $P_{fc}(t)$, $P_{bat}(t)$, $i_{fc}(t)$, $i_{bat}(t)$ and $v_{DC}(t)$, and are depicted in Fig. 4.8. The interpretations of this study are:

- In Fig. 4.8(a), the PEMFC operates to follow P_{fc}^{ref}. The variation in $P_{fc}(t)$ lies close to P_{fc}^{rated} for major part of the reduced scale driving scenario. However, towards the end of the driving period, the $P_{fc}(t)$ decreases and varies around P_{fc}^{min}. Accordingly, the $P_{bat}(t)$ varies to maintain the instantaneous power balance between the source and load.

- In Fig. 4.8(b), it is seen that $i_{fc}(t)$ varies to track I_L^{ref}. The I_L^{ref} is determined from the values of P_{fc}^{ref} and $v_{fc}(t)$ corresponding to the P_{fc}^{ref} operating point. Accordingly, the battery charges/discharges depending on the values of $P_{fc}(t)$ and $P_{load}^{scaled}(t)$. Thus, $i_{bat}(t)$ is observed to be either positive (discharging mode of battery operation) or negative (charging mode of battery operation) in Fig. 4.8(c). In addition to this, the current ripples of around $1A$ and $0.5A$ are observed in $i_{fc}(t)$ and $i_{bat}(t)$, respectively which confirm to the design specifications of the MISO converter (section 3.3). These observations imply that the designed current controller performs aptly to implement the EMO1 approach in the PEMFC-battery-HES.

- Fig. 4.8(d) shows that $v_{DC}(t)$ is maintained at the chosen V_{DC}^{ref} of $48V$. Some voltage ripples are also observed at steady-state whose value increases/decreases with increasing/decreasing load. However, the ripples never exceed the pre-specified maximum allowable value of 5% (section 3.3). This observation verifies the appropriate operation of the voltage controller in the regulation of $v_{DC}(t)$ throughout the driving period.

Thus, this simulation study verifies that the proposed EMO1 approach can be implemented for determining the power split in the prototype model of the PEMFC-battery-HES to supply the locomotive load through the use of the PWM controlled MISO converter. In addition to this, the regulation of the DC-bus voltage can also be achieved by the PWM control of the MISO converter switches.

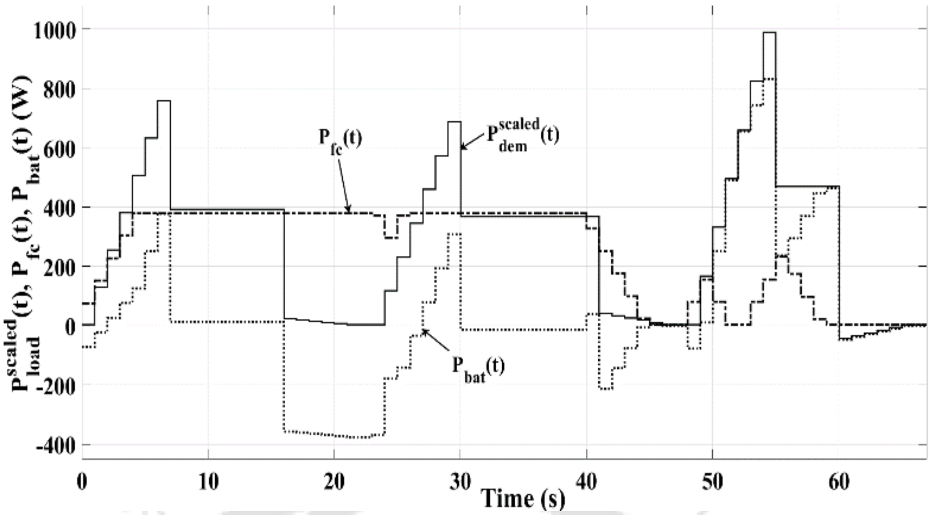
$P_{load}^{scaled}(t)$, $P_{fc}(t)$, $P_{bat}(t)$ (W)
1000
800
600
400
200
0
-200
-400
$P_{fc}(t)$
$P_{dem}^{scaled}(t)$
$P_{bat}(t)$
0
10
20
30
40
50
60
Time (s)

(a)

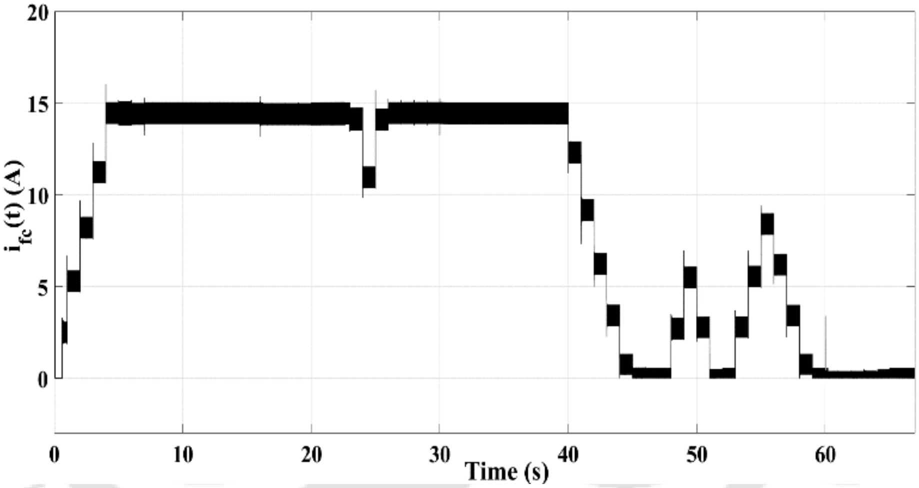
$i_{fc}(t)$ (A)
20
15
10
5
0
0
10
20
30
40
50
60
Time (s)

(b)

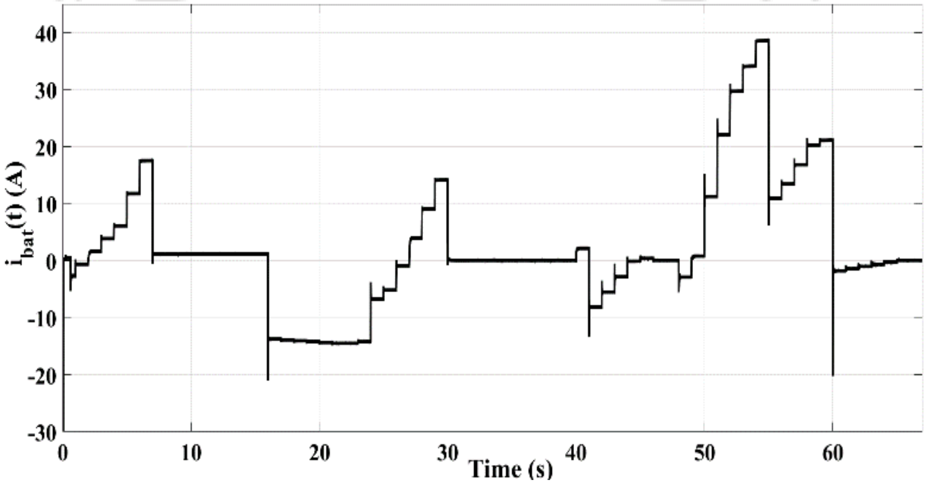
$i_{bat}(t)$ (A)
40
30
20
10
0
-10
-20
-30
0
10
20
30
40
50
60
Time (s)

(c)

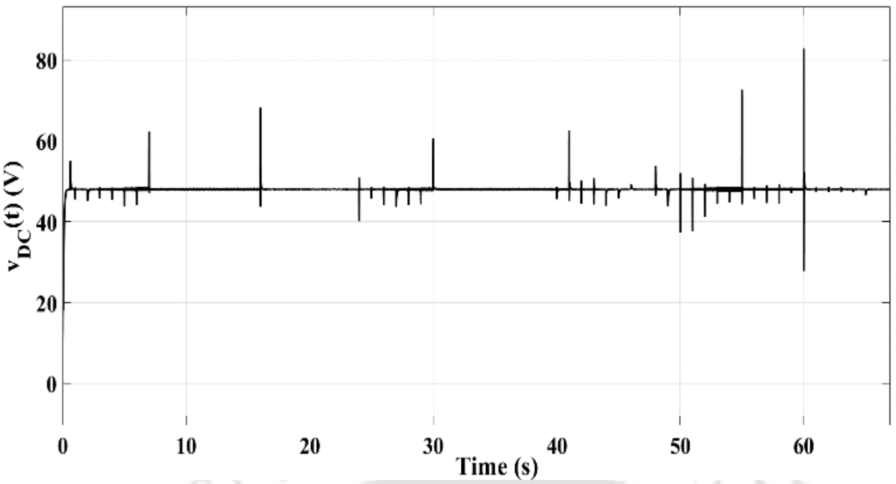

(d)

Fig. 4.8: Plot depicting the variation of power, current and DC-bus voltage following the EMO1 approach for the reduced scale scenario of drive cycle 1: (a) $P_{load}^{scaled}(t)$, $P_{fc}(t)$, $P_{bat}(t)$, (b) $i_{fc}(t)$, (c) $i_{bat}(t)$ and (d) $v_{DC}(t)$.

4.3. EMO2 approach

In this section, the EMO2 approach is proposed to determine the optimal power split in the PEMFC-battery-HES to supply the locomotive load. Simulation studies are also carried out to examine the performance of the proposed EMO2 approach.

4.3.1. Mathematical formulation of the EMO2 approach

This section presents the mathematical formulation of the EMO2 approach. Similar to the EMO1 approach, the EMO2 approach also aims to determine the power references for the PEMFC for each loading point of the dynamically varying locomotive power demand with the objective function of the minimization of the PEMFC fuel consumption during the driving period. However, the limit on state-of-health (SOH) deterioration of the battery is additionally considered as one of the operational constraints of optimization. The EMO2 approach is formulated as a discrete non-linear optimization problem as follows:

$$Minimise\ f(x) = m_{H_2} = \sum_{t=t_0}^{t_f} \frac{P_{fc}(t)}{LHV\eta_{fc}} \Delta t \tag{4.13}$$

$$where, x = P_{fc}(t) \tag{4.14}$$

$$subject\ to$$

$$P_{fc}(t) + P_{bat}(t) = P_{load}(t) \tag{4.15}$$

$$\frac{\Delta P_{fc}}{\Delta t} \leq R_{max} \tag{4.16}$$

$$P_{fc}^{min} \leq P_{fc}(t) \leq P_{fc}^{rated} \tag{4.17}$$

$$SOC_{min} \leq SOC(t) \leq SOC_{max} \tag{4.18}$$

$$0 \leq \{\Delta SOH_{bat} = SOH_{bat}(t_0) - SOH_{bat}(t_f)\} \leq \Delta SOH_{bat,max} \tag{4.19}$$

$$\Delta SOH_{bat,max} = \frac{1}{N_{trip} N_{bat}} \tag{4.20}$$

Where, ΔSOH_{bat} is the change in battery SOH; $SOH_{bat}(t_0)$ $\{SOH_{bat}(t_f)\}$ is the battery SOH at the beginning (end) of the driving period; $\Delta SOH_{bat,max}$ is the maximum deterioration in the battery SOH per trip; N_{trip} is the number of trips of the passenger train per day; and N_{bat} is the battery lifetime. The value of $\Delta SOH_{bat,max}$ is computed in Eq. (4.20) assuming that the SOH of the battery before use as 1. In this study, a model based on energy-throughput [151] is adopted to represent the battery durability or lifetime. According to this model, the $SOH_{bat}(t)$ is defined as a function of the number of cycles, $N(c)$. The $N(c)$, in turn, is a function of the battery output power, and cell temperature. Thus, considering the lossless operation of the battery, the $SOH_{bat}(t)$ is mathematically defined as follows:

$$SOH_{bat}(t) = SOH_{bat}(t_0) - \sum_{t=t_0}^{t} \frac{P_{bat}(t)}{2N(c)E(t_0)} \Delta t \tag{4.21}$$

$$c(t) = \frac{3600 P_{bat}(t)}{E(t_0)} \tag{4.22}$$

$$N(c) = \frac{V_{OC} A(c)}{E(t_0)} \tag{4.23}$$

$$A(c) = \left\{ \frac{\Delta E}{B(c) e^{\left(\frac{-E_a(c)}{RT}\right)}} \right\}^{1/z} \tag{4.24}$$

$$E_a(c) = 31700 - 370.3c(t) \tag{4.25}$$

$$B(c) = -48c(t)^3 + 1200c(t)^2 - 9400c(t) + 36000 \tag{4.26}$$

Where, $E(t_0)$ is the initial battery energy; $c(t)$ is the battery c-rate; V_{OC} is the open circuit voltage of the battery; $A(c)$ is the total amount of throughput in the battery; ΔE is the change in battery energy; $E_a(c)$ is the activation energy of battery, R is the universal gas constant; T is the cell temperature; and z is the power law factor. Eq. (4.24) is the Arrhenius law equation, and Eq. (4.26) is obtained from the method of curve fitting on the experimental data [151]. The values of

$SOH_{bat}(t_0)$, z, ΔE, R, and T are considered to be 1, 0.55, 100%, 8.31*J/mol/K*, and 313*K*, respectively.

4.3.2. Solution strategy for the EMO2 approach

The EMO2 model is executed using GAMS. For this, the mathematical model formulated in sub-section 4.3.1 is fitted into GAMS. The CONOPT solver is used to solve the optimization problem, since it is a kind of non-linear optimization model. Similar to the EMO1 approach, the values of P_{fc}^{rated} and Q_{bat}^{rated} are set at their optimal values of 4.9 MW and 2 MWh, respectively in the EMO2 model. The $SOC(t)$ is allowed to vary in the range of $[SOC_{min}, SOC_{max}]$, i.e., (0.4, 0.6) with $SOC(t_0)$ set as 0.5. Considering the battery replacement in an interval of every 5 years, and a single round trip of the passenger train on a particular route per day, i.e., (N_{trip} = 2), the value of the constraint $\Delta SOH_{bat,max}$ is computed using Eq. (4.20), and is defined in GAMS. Additionally, the data of the dynamically varying $P_{load}(t)$ for the complete driving period is provided as an input to GAMS. The input data is sampled at every 1*s*. The EMO2 approach is now executed to determine the power references for the PEMFC at each loading point of the locomotive power demand.

4.3.3. Results of EMO2 approach

In this sub-section, the dynamic behaviour of the PEMFC and battery to supply the locomotive load while following the EMO2 approach is firstly examined. Thereafter, a comparison of the proposed EMO2 approach with some of the already available energy management approaches for the different drive cycle scenarios is carried out to analyse the competence of the proposed EMO approach.

4.3.3.1. Performance analysis of the EMO2 approach

To examine the dynamic performances of the energy sources following the EMO2 approach, the plots showing the variation of $P_{fc}(t)$ and $P_{bat}(t)$ to supply the dynamically varying $P_{load}(t)$ of drive cycle 1 are shown in Fig. 4.9(a). This figure shows that the PEMFC operates mostly at constant power. However, the constant power operation of the PEMFC varies depending on the locomotive power demand during a particular constant speed driving horizon. The increase/decrease of $P_{fc}(t)$ within $[P_{fc}^{min}, P_{fc}^{rated}]$ is observed during acceleration/deceleration period. The rate of change of $P_{fc}(t)$ is limited by the constraint of R_{max} as defined in Eq. (4.16). On the other hand, the battery charges/discharges throughout the driving period depending on the values of $P_{load}(t)$ and $P_{fc}(t)$. Accordingly, the $SOC(t)$ varies as depicted in Fig. 4.9(b). The $SOC(t)$ rises and falls with small ripples around it. However, the variation in $SOC(t)$ is always maintained within (0.4, 0.6) with $SOC(t_f)$ lying close to SOC_{min}. Similar characteristic variations in $P_{fc}(t)$, $P_{bat}(t)$ and $SOC(t)$ are observed for the drive cycles 2 and 3, and hence, these are not presented in this section.

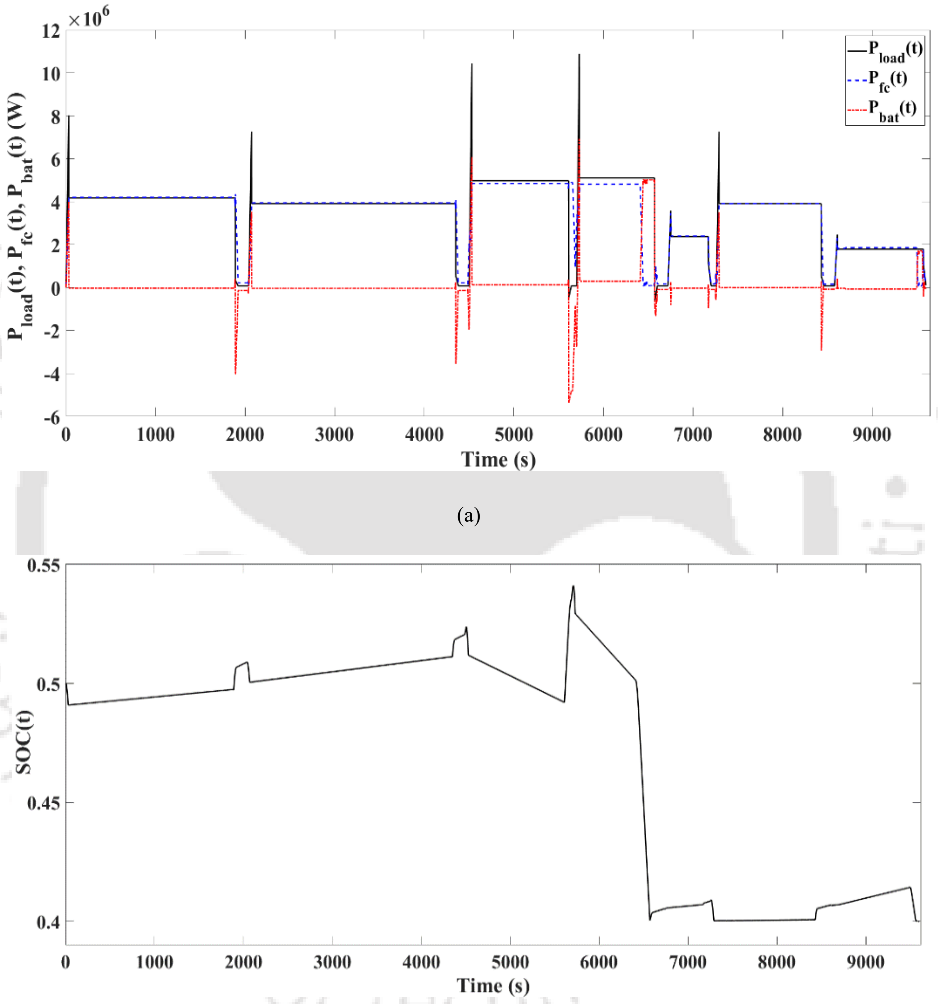

(a)

(b)

Fig. 4.9: Plot depicting the dynamic behaviour of the PEMFC and battery following the EMO2 approach for drive cycle 1: (a) $P_{fc}(t)$, $P_{bat}(t)$, $P_{load}(t)$ and (b) $SOC(t)$.

4.3.3.2. Performance comparison of the EMO2 approach with the existing energy management approaches

To test the efficacy of the proposed EMO2 approach, a comparison study of the EMO2 approach with the two-stage controller [37], [149], state-machine control [36], ECMS [5], LFCS [86], [150] and rule based EMSs [12], (previously reported in the literature) is presented. The comparison among these EMSs is done in terms of their battery $SOC(t)$ variation (Fig. 4.10 and Table 4.5) and the PEMFC hydrogen consumption (Table 4.6) for the different drive cycle scenarios. The following inferences are obtained from this study:

- The two stage controller and state machine control based EMSs (the LFCS and ECMS based EMSs) aim to sustain the $SOC(t)$ variation around $SOC_{max}(SOC_{mean})$. Alternate charging/discharging patterns in the $SOC(t)$ are observed in the rule based EMS with occasional violation of the its limits. This implies that the utilization of the battery capacity to supply the locomotive load is more for the rule based EMS as compared to the two-stage controller, state-machine control, ECMS and LFCS based EMSs. Hence, the rule based EMS results in lesser hydrogen consumption than the other EMSs for drive cycles 1 and 2.
- An exception lies in the drive cycle 3 scenario. For this drive cycle, higher hydrogen consumption of the rule based EMS is observed as compared to the ECMS and LFCS based EMSs. This is because of the charging pattern followed by the battery towards the end of the drive cycle 3 while supplying/absorbing the deficit/excess power. Thus, more amount of PEMFC power is used in the rule based EMS to supply the locomotive load and to charge the battery which subsequently leads to higher hydrogen consumption in the rule based EMS than the ECMS, and LFCS based EMSs. Thus, the rule based EMS may be advantageous over the two-stage controller, state-machine control, ECMS and LFCS based EMSs in terms of reduced hydrogen consumption. But this may not be true for all driving conditions.
- Unlike, the aforementioned EMSs, the proposed EMO2 approach generates the optimal set points for the PEMFC output power so as to minimize the PEMFC hydrogen consumption during the driving period. Thus, it is seen in Table 4.6 that the EMO2 approach results in the least hydrogen consumption. For drive cycle 1, the reduction in hydrogen consumption is 5.11%, 4.51%, 2.14%, 1.75% and 1.56% as compared to the two stage controller, state machine control, ECMS, LFCS and rule based EMSs, respectively. Similarly, for drive cycles 2 and 3, the corresponding reductions in hydrogen consumption are 5.40%, 4.97%, 2.36%, 2.23%, 1.72% and 4.82%, 3.36%, 1.57%, 1.38%, 3.20%, respectively.
- In none of the two stage controller, state machine control, ECMS, LFCS and rule based EMSs, the durability or the SOH maintenance of the energy sources is considered unlike the EMO2 approach. Moreover, since the aforementioned energy management approaches

are based on some pre-defined rules, these may not work for all driving conditions.

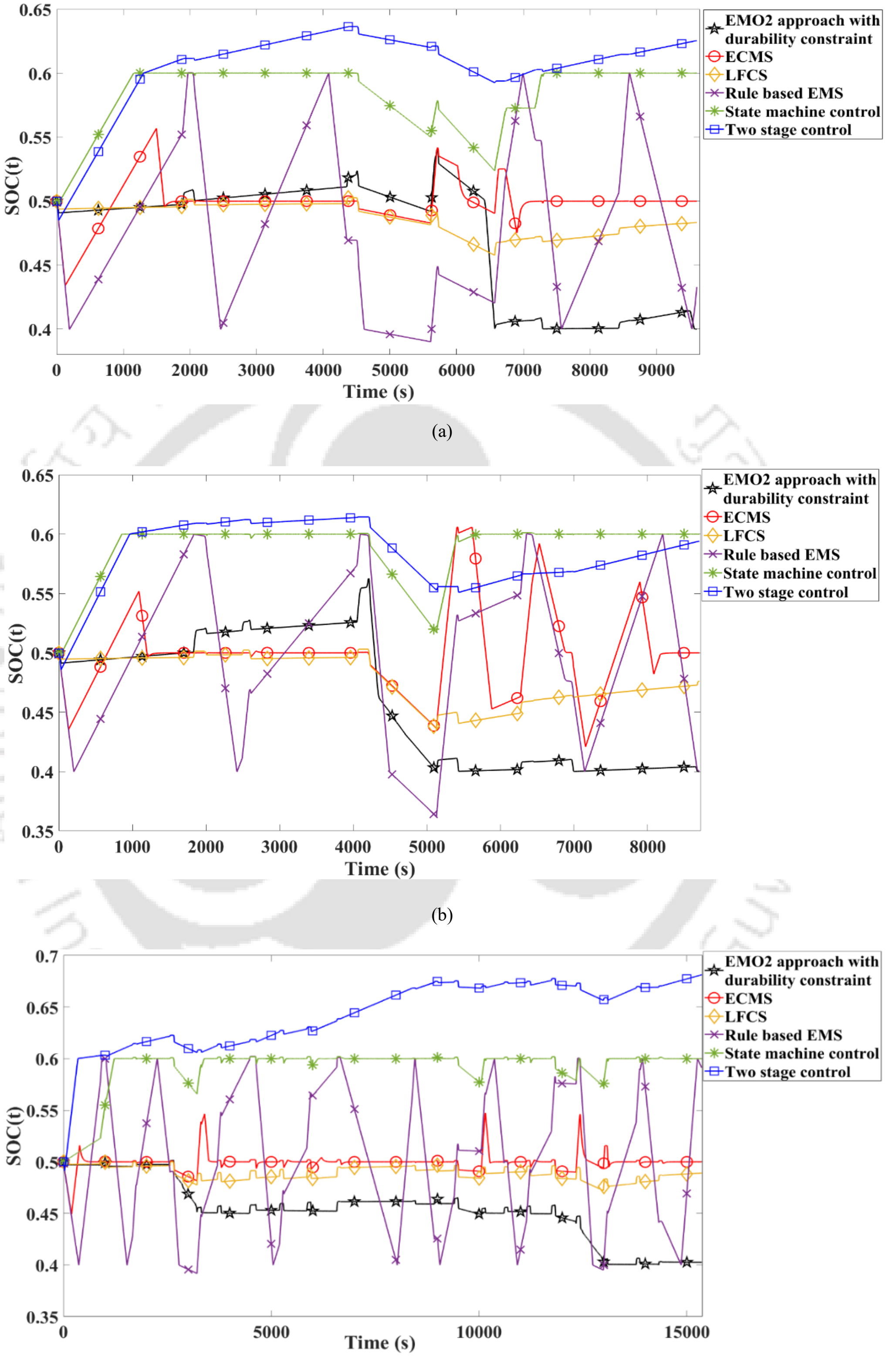

(c)

Fig. 4.10: Comparison among the EMO2 approach and the already available EMSs of literature in terms of their $SOC(t)$ variation under

the dynamically varying locomotive load of the different drive cycles: (a) drive cycle 1, (b) drive cycle 2 and (c) drive cycle 3.

Table 4.5: A case study on the performance analysis of the proposed EMO2 approach and the energy management approaches previously used in literature.

EMS	*Drive cycles*	$SOC(t_f)$	*Remarks*
State-machine control [36]	1	$SOC(t_f) = 0.6$	The battery initially charges to SOC_{max}. Thereafter, $SOC(t)$ varies close to SOC_{max}.
	2		
	3		
Two-stage controller [37], [149]	1	$SOC(t_f) = 0.625$	The $SOC(t)$ fluctuates around SOC_{max} with occasional charging beyond SOC_{max}.
	2	$SOC(t_f) = 0.594$	
	3	$SOC(t_f) = 0.681$	
ECMS [5]	1	$SOC(t_f) = 0.5$	$SOC(t)$ is maintained aroundSOC_{mean} of 0.5 with slight deviations around it.
	2		
	3		
LFCS [86], [150]	1	$SOC(t_f) = 0.483$	$SOC(t)$ varies in a similar way as the ECMS with $SOC(t_f)$ falling slightly below SOC_{max}.
	2	$SOC(t_f) = 0.476$	
	3	$SOC(t_f) = 0.489$	
Rule based EMS [12]	1	$SOC(t_f) = 0.433$	The battery charges, and discharges alternately throughout the driving period.
	2	$SOC(t_f) = 0.4$	
	3	$SOC(t_f) = 0.591$	
Proposed EMO2 approach	1	$SOC(t_f) = 0.405$	The battery initially operates in charging mode, and then in discharging mode with small ripples around $SOC(t)$.
	2	$SOC(t_f) = 0.4$	
	3	$SOC(t_f) = 0.403$	

Table 4.6: The values of the PEMFC hydrogen consumption (in *kg*) for the EMO2 approach and the different EMSs for the different drive cycle scenarios.

EMS	*Drive cycle 1*	*Drive cycle 2*	*Drive cycle 3*
Two-stage controller [37], [149]	590.20	537.02	779.36
State-machine control [36]	586.81	534.81	768.53
ECMS [5]	573.50	521.50	755.20
LFCS [86], [150]	571.30	520.87	753.75
Rule based EMS [12]	570.27	518.28	767.36
Proposed EMO2 approach	561.50	509.50	743.52

4.4 Performance comparison of the EMO2 approach with the EMO1 approach

In this section, the performance comparison of the EMO2 approach with the EMO1 approach is presented. The comparison between the two EMO approaches in terms of their $P_{fc}(t)$ and $SOC(t)$ variation for drive cycle 1 is presented in Fig. 4.11. Likewise, the PEMFC fuel consumption for the different drive cycles are compared for the two EMO approaches in Table 4.7. The following inferences are obtained from this study:

- Following the EMO1 approach, the PEMFC is subjected to frequent changes in its output power while supplying the locomotive load. On the other hand, the EMO2 approach ensures a steady operation of the PEMFC as compared to the EMO1 approach. This characteristic variation in $P_{fc}(t)$ is clearly depicted in Fig. 4.11(a). However, the rate of change of $P_{fc}(t)$ is constrained by R_{max} in both the EMO approaches.
- Fig. 4.11(b) shows that the EMO1 approach results in higher numbers of charging/discharging cycles of the battery within $[SOC_{min}, SOC_{max}]$ of (0.4, 0.6) than the EMO2 approach. This implies that the battery degrades faster while supplying the locomotive power demand in accordance to the EMO1 approach as compared to the EMO2 approach. This is because of the durability constraint considered in the EMO2 approach.
- The EMO2 approach leads to lesser hydrogen consumption than the EMO1 approach. The reduction in hydrogen consumption for the EMO2 approach is observed to be 0.95%, 1.12% and 0.85% for the drive cycle 1, 2 and 3, respectively. This is because following the EMO1 approach, the battery charges close to SOC_{max} of 0.6 for some parts of the drive cycle. This implies that more power is drawn from the PEMFC to supply the locomotive load as well as to charge the battery. On the other hand, the $SOC(t)$ variation in the EMO2 approach lies close to 0.5 and falls to SOC_{min} of 0.4 towards the end of the driving period. In addition to this, the battery is never charged beyond 0.52 throughout the driving horizon. This implies that more power is utilised from the battery than the PEMFC in the EMO2 approach. This subsequently leads to lesser hydrogen consumption of the PEMFC in the EMO2 approach as compared to the EMO1 approach.

Similar dynamic behavior of the PEMFC and battery are observed for the drive cycles 2 and 3, and hence, they are not discussed in this section. Thus, this study verifies that the EMO2 approach with the battery durability constraint is advantageous over the EMO1 approach. However, as compared to the existing energy management approaches, i.e., the two stage controller, state machine control, ECMS, LFCS and rule based EMSs, both the proposed EMO1 and EMO2 approaches exhibit better performances.

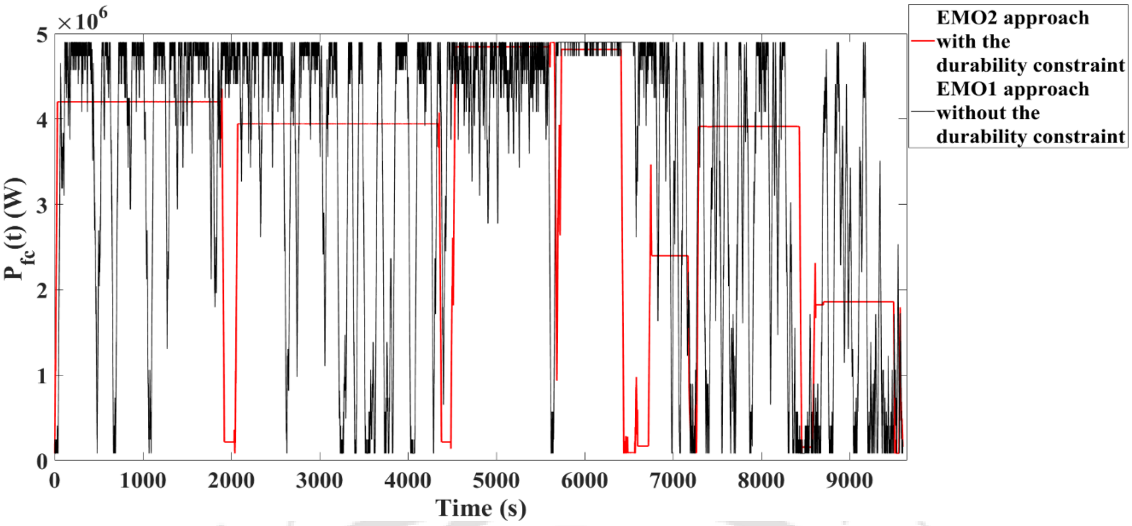

(a)

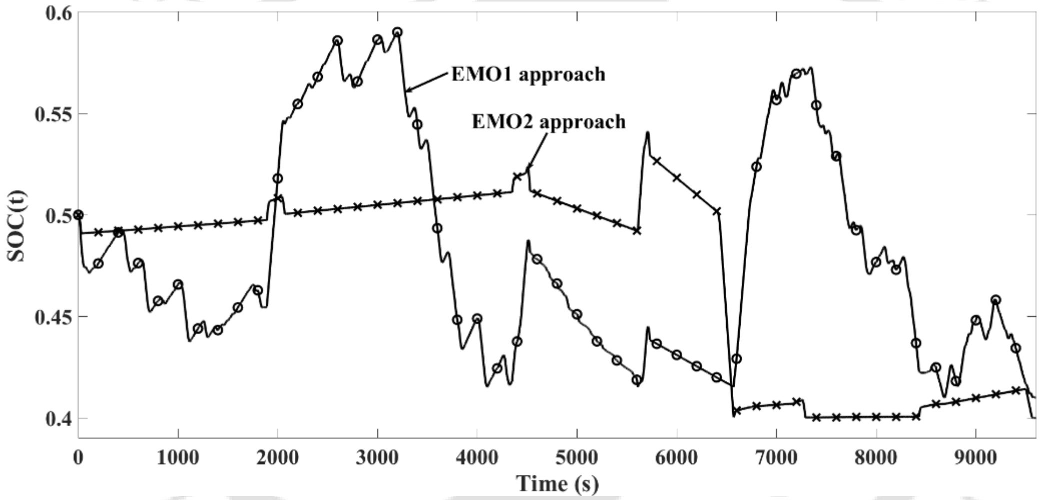

(b)

Fig. 4.11: Comparison between the EMO1 and EMO2 approaches for the dynamically varying locomotive load of drive cycle 1 in terms of their variation in: (a) $P_{fc}(t)$ and (b) $SOC(t)$.

Table 4.7: The values of the PEMFC hydrogen consumption (in *kg*) for the EMO1 and EMO2 approaches under the different drive cycle scenarios.

EMS approaches	*Drive cycle 1*	*Drive cycle 2*	*Drive cycle 3*
EMO1 approach without the durability constraint	566.85	515.21	749.80
EMO2 approach with the durability constraint	561.50	509.50	743.52

4.5. Online Implementation of the proposed EMO approaches using GAMS

In this chapter, the performances of the proposed EMO approaches as offline optimization processes are examined. The implementation of the EMO approaches as online optimization processes using GAMS is also possible. This is because GAMS involves less computational time of about few milliseconds which makes its operation possible for online optimization. The block diagram depicting the process of online EMO using GAMS, starting with the generation of the PEMFC power references to the transfer of data to the controller for the load sharing control in the HES in accordance to the EMS is given in Fig. 4.12. Besides, the data of the dynamically varying locomotive load, the values of $P_{fc}(t)$ and $SOC(t)$ of the previous sampled time also act as the inputs to the proposed EMO approaches. However, some delays in the range of microseconds or nanoseconds (represented by T_{delay}) may incur in the response times of the controller, the communication channels, the DC-DC converter, etc. Considering these time delays, the sampling time of the inputs may be increased to 5 or 10 seconds. This suffices to achieve the online execution of the EMO approaches for the real-time optimal load dispatch to the energy sources.

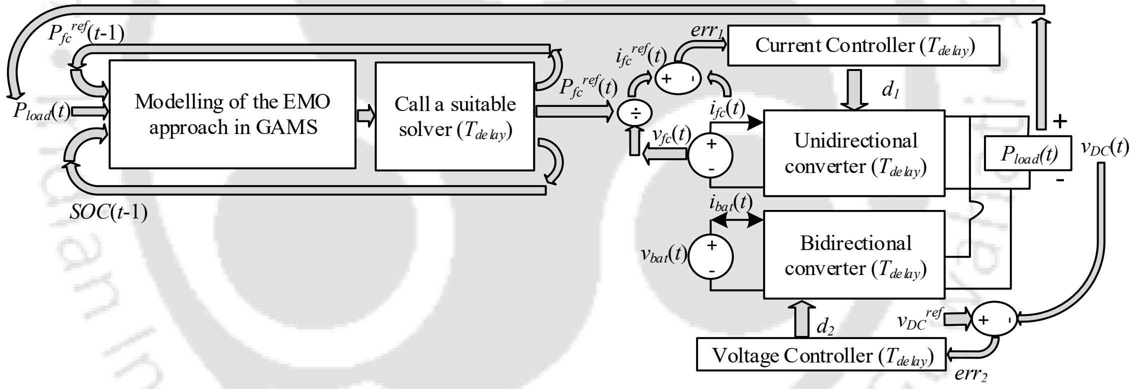

Fig. 4.12: Block diagram depicting the process of online EMO using GAMS.

4.6. Summary of the present work

In this chapter, two different EMO approaches with and without the durability constraints of the energy sources have been developed to achieve the optimal distribution of load in the PEMFC-battery-HES for locomotive applications. The modelling of the PEMFC-battery-HES has been carried out to retrofit the diesel locomotive, WDM-3D which is used to haul the intercity passenger trains in NEFR, Assam, India. Formulated as discrete optimization problems, both the EMO approaches aim to generate the PEMFC power references at each loading point of the locomotive power demand with the objective function of the minimization of the total fuel consumption of the PEMFC. The EMO approaches have been implemented using GAMS, and their effectiveness has been tested through comparison with some of the existing energy management approaches in literature for some practical drive cycle scenarios. The salient outcomes of this research are as follows:

- The proposed EMO approaches resulted in 1% to 5.5% reduction in the PEMFC fuel consumption as compared to the two stage controller, state machine control, ECMS, LFCS and rule based energy management approaches. On an average, the reduction in hydrogen consumption for the proposed EMO approaches is found to be the highest for drive cycle 2 and least for drive cycle 3. Moreover, the reduction in hydrogen consumption is observed to be more for the EMO2 approach as compared to the EMO1 approach.
- The two stage controller, state machine control, ECMS and LFCS based EMSs do not result into the optimum utilization of the battery capacity to supply the locomotive load since these EMSs aim to sustain the battery $SOC(t)$ around some reference values. On the other hand, the battery charges and discharges alternately following the rule based EMS. Thus, the rule based EMS may be advantageous over the two stage controller, state machine control, ECMS and LFCS based EMSs in terms of the reduced hydrogen consumption for certain driving conditions. Unlike the aforementioned energy management approaches, the optimum utilization of the capacity of the energy sources is ensured in the proposed EMO approaches. This is because the battery operates in charging/discharging mode in the proposed EMO approaches depending on the instantaneous values of the PEMFC output power and load, in which the references for the PEMFC output power are generated through optimization.
- In the EMO2 approach, the battery durability model is considered. Hence, the EMO2 approach leads to less number of battery charge/discharge cycles than the EMO1 approach. In addition to this, fewer ripples around the battery $SOC(t)$ variation for the EMO2 approach is also observed. In addition to this, the proposed EMO2 approach ensures a steady operation of the PEMFC unlike the EMO1 approach.

Thus, both the proposed EMO approaches ensure the minimum hydrogen consumption of the PEMFC to supply the locomotive load without compromising the operational dynamics and the durability constraints of the energy sources. However, the EMO2 approach exhibit better performance as compared to EMO1 approach.

Chapter 5

Infrastructure Planning of Hydrogen Refueling Station for the deployment of hydrogen powered locomotives

5.1. Introduction

In transportation, the use of hydrogen fueled vehicles offers a promising solution in relieving the global energy crisis, and protecting the environment. However, the lack of proper refueling infrastructures along with the high cost of fuel production are some of the major problems which hinder the diffusion of hydrogen fueled vehicles in the market. Hence, the same needs to be investigated considering the number and the optimal location of the HRS. In [110], [111], a preliminary study on the commercial viability, and the cost-effectiveness of the HRS infrastructure is carried out. The authors in [112] develop a flow capturing location model (FCLM) for determining the optimal location of the alternative refueling station layout. The FCLM assumes that a vehicle flow along a particular route will be covered if at least one refueling facility is located on that route. Thus, this assumption violates the constraint on the driving range of the vehicles. Over the years, the FCLM is reformulated to formally characterize a wide variety of consumer needs, such as, the hybrid flow capturing plus p-median model proposed in [113]. The authors in [114] present the flow refueling location model (FRLM) which optimally locates the refueling stations on a network so as to maximize the vehicular traffic flow that can be refueled without violating the driving range limitation of the alternative-fuel vehicles. However, the generation of the enormous number of HRS combinations along the longer routes limits the applicability of the traditional FRLM to medium and large sized networks. Hence, to reduce the computational burden, the traditional FRLM is reformulated, and mixed integer programming based FRLMs are presented in [115], [116]. Furthermore, as an extension of the conventional FRLM, the authors in [117], [118] propose to refuel the vehicle trips with a given layout of refueling stations which are scattered not only over the network nodes but also over the candidate sites dispersed along the arcs. However, the FRLMs proposed in the above research are un-capacitated models, i.e., they implicitly assume that a single HRS can refuel an infinite amount of traffic flow. This assumption is practically infeasible, and in view of this, the authors in [119] introduce the capacitated FRLM that limits the amount of traffic flow that any particular HRS can refuel. Likewise, many HRS allocation methodologies are reported in literature, such as, the COBRA model [120], a generalized flow interception location allocation model [121], mixed integer programming method based on vehicle-routing logics [122], [123], the agent-based training system [124], the deviation-flow refueling location model [125], the analytical hierarchy process-binary integer programming based optimization model [126], the fuzzy model [127], the robust centralized planning and bi-level centralized planning models [128], the geographical information systems based site selection method [129], [130], flow interception facility location model [131], and the fuel-travel-back approach [132]. Furthermore, comparison studies are carried out in [132] and [134] to analyze the competitiveness of the p-median models with the flow-refueling models, and the path-based models with the node-based models, respectively. However, in all the above works, the problem of optimal HRS allocation is addressed as a short time planning problem. The authors in [135] present the long term location planning of the HRS network considering the co-dependency between the sales of hydrogen FC vehicles and the number of HRS. For this, an integrated optimization model comprising of the generalized bass diffusion model and the FCLM are proposed in [135]. Thus, literature survey shows that studies on the HRS infrastructure planning for the deployment of hydrogen powered locomotives are not reported so far. To address this research gap, the following objectives are proposed in this chapter:

- Optimal allocation planning of the HRS for the rollout of the hydrogen powered intercity passenger trains in NEFR, Assam, India.
- Formulation of the single-objective and multi-objective optimization approaches to satisfy the constraints and deployment feasibility of the HRS in locomotive applications.
- Development of the solution strategies to be used as the support subroutines in the binary PSO based solution algorithms to solve the optimization problems.

- Investigation of the total investments incurred in the HRS infrastructure development for the different scenarios of installed HRS capacity.

Thus, the present chapter offers novelty in terms of the formulated optimization models, the application area (locomotive), the employed heuristic solution algorithm (binary PSO), and the region under analysis (NEFR, Assam, India).

5.2. Single-objective optimization approach

The present chapter aims to plan the optimal locations of the HRS for the deployment of the hydrogen powered intercity passenger trains to be operational under the department of NEFR, in Assam, India. To do this, the problem of optimal HRS allocation is firstly addressed as a single-objective optimization approach. The existing network of intercity railway stations of Assam [140] is considered as the potential base layout for the installation of the HRS. In Assam, there are total 18 intercity railway routes and 231 stations located on these routes. An overview of the intercity railway routes of Assam is shown in Fig. 5.1. The details of the routes, i.e., the origin-destination terminuses, number of intermediate stations, and traffic flow, expressed in terms of the total number of passenger trains operating per day are listed in Table 5.1.

Table 5.1: Details of the intercity railway routes of NEFR, Assam, India.

Sl. No.	*Railway route*	*Distance (in km)*	*No. of intermediate stations*	*Traffic flow*
1	GHY to NBQ via. Guagachha	157	20	4
2	GHY to NBQ via. Goalpara town	182	17	2
3	DBB to KYQ	280	19	2
4	LMG to GHY	181	24	2
5	LMG to TSK	337	35	2
6	JTTN to TSK	175	25	2
7	GHY to MBO	160	27	2
8	SLGR to DBRT	100	11	2
9	DKGN to BHNG	63	6	2
10	DKGN to MZS	345	40	2
11	RNY to DKGN	142	16	2
12	DKGN to RPAN	19	2	1
13	RPAN to RNY	123	13	2
14	GHY to NBQ	157	15	2
15	SCL to MSSN	60	11	4
16	BPB to DLCR	71	14	2
17	SCL to DLCR	100	9	2
18	DBRG to MZS	121	12	2

NBQ: New Bongaigaon Junction; GHY: Guwahati; DBB: Dhubri; KYQ: Kamakhya Junction; LMG: Lumding Junction; TSK: Tinsukia Junction; JTTN: Jorhat town; MBO: Mairabari; SLGR: Simaluguri Junction; DBRT: Dibrugarh Town; DKGN: Dekargaon; BHNG: Bhalukpong; MZS: Murkongselek; RNY: Rangiya Junction; RPAN: Rangapara North Junction; SCL: Silchar; MSSN: Maishashan; BPB: Badarpur Junction; DLCR: Dullabcherra; DBRG: Dibrugarh

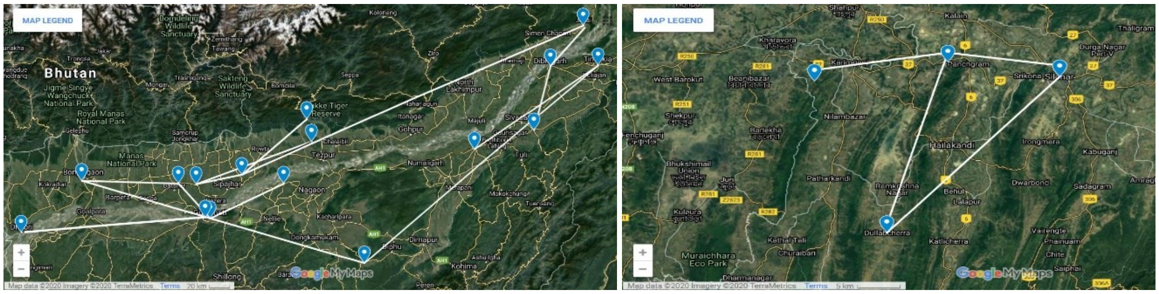

(a) (b)

Fig. 5.1: An overview of the railway routes of intercity passenger trains operating under the Department of NEFR, in Assam, India: (a) Brahmaputra valley, and (b) Barak valley.

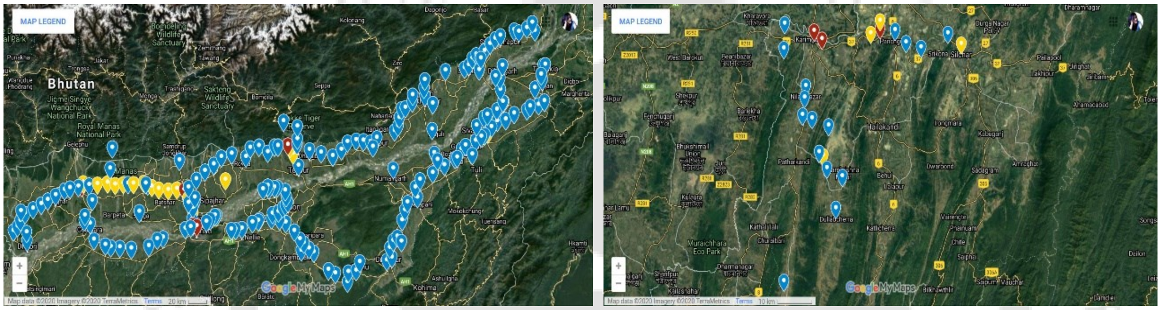

(a) (b)

Fig. 5.2: The segregation of the railway stations into different *TZ*s with the blue, yellow and red pins indicating the light, medium and heavy traffic areas, respectively: (a) Brahmaputra valley, and (b) Barak valley.

5.2.1. Formulation of the single-objective optimization approach

In this sub-section, a single-objective optimization approach is developed to determine the optimal locations of the HRS to be able to meet the fuel needs of the hydrogen powered passenger trains operating on the different intercity railway routes in Assam, India. Since investment cost is a vital aspect of HRS infrastructure planning, therefore, the optimization approach is formulated with the objective function of the minimization of the total cost of ownership (*TCO*) of the HRS over a specified planning period of T_{plan} years. The mathematical model of the optimization approach is given below:

$$Minimise\ f(x) = TCO = \sum_{k\in K}\left(CC_k + MC_k + C^{ct}_{refuel,k} + C^{proj}_{refuel,k}\right)x_k \tag{5.1}$$

$$where, x = x_{k|k\in K} \tag{5.2}$$

$$MC_k = HRS_{cap,k}73125\left(HRS_{cap,k}\right)^{-0.853}T_{plan} \tag{5.3}$$

$$C^{ct}_{refuel,k} = fuel_k PV_{H_2} N_{refuel,k} \tag{5.4}$$

$$N_{refuel,k} = \frac{365}{fuel_k} f_{q,k} tank_{cap} \tag{5.5}$$

$$C^{proj}_{refuel,k} = \frac{fuel_k FV_{H_2}}{(1+r_{H_2})^{(T_{plan}-1)}} N^{proj}_{refuel,k} \tag{5.6}$$

$$N^{proj}_{refuel,k} = \frac{365}{fuel_k} f_{q,k} tank_{cap}(T_{plan}-1) \tag{5.7}$$

$subject\ to$

$$x_{k|k\in N_{end}} = 1 \tag{5.8}$$

$$FC_{k,k_{next}} = \frac{D_{k,k_{next}|k,k_{next}\in N_q \& x_k, x_{k_{next}}=1}}{D_{range}} \leq 0.9 \tag{5.9}$$

$$\sum_{k\in K} x_k \leq HRS^{max} \tag{5.10}$$

$$\sum_{q\in Q} f_q y_q = TF \tag{5.11}$$

$$x_k, y_q \in \{0,1\} \tag{5.12}$$

Where, q and k are the indices representing the intercity railway routes and potential sites (the network of railway terminuses) for HRS allocation, respectively; Q and K are the set of all the intercity railway routes and the potential railway sites of Assam, India; CC_k, MC_k, $HRS_{cap,k}$, $C^{ct}_{refuel,k}$ ($C^{proj}_{refuel,k}$), $N_{refuel,k}$ ($N^{proj}_{refuel,k}$) and $fuel_k$ are the capital cost, maintenance cost, capacity (in *kg/day*), cost of HRS refueling in the current {projected $(T_{plan}-1)$} year(s), frequency of HRS refueling for the current (projected) year(s), and the amount of hydrogen (in *kg*) required for refueling the HRS located at the *k*th potential site, respectively; x_k is a binary variable which assumes the value of 1 if a HRS is located at the *k*th potential site, otherwise 0; PV_{H_2} (FV_{H_2}) is the current (future) cost of the hydrogen fuel considered as 3.25 *$/kg* (2.3 *$/kg* by 2050) [152]; r_{H_2} is the discounting rate of hydrogen fuel assumed to be 10% [152]; f_q is the traffic flow along the route, *q*; $f_{q,k}$ is the traffic flow of *q*th route to be refueled by the HRS located at the *k*th potential site; $tank_{cap}$ is the fuel tank capacity of the train (in *kg*); N_{end} is the set of all the origin-destination terminuses; $FC_{k,k_{next}}$ is the fraction of locomotive fuel tank capacity consumed while travelling a distance of $D_{k,k_{next}}$ between two nearby HRS located at the potential sites, *k* and k_{next}; N_q is the set of all the potential sites on the route, *q*; D_{range} is the driving range of the train (in *kg*); HRS^{max} is the maximum number of HRS to be installed in a given layout of potential railway sites; y_q is a binary variable which takes the value of 1 if f_q is refueled by the HRS, otherwise 0; and *TF* is the total traffic flow of the intercity passenger trains operating in NEFR, Assam, India. Equation (5.1) is the objective function of the optimization approach which aims to minimize the TCO of the HRS layout. The TCO includes the summation of the capital cost, the maintenance cost and the total cost of HRS refueling for T_{plan} of 30 years. The x_k is the optimizing or the decision variable as given in Eq. (5.2). According to the report published by NREL in [153], both CC_k and MC_k vary with $HRS_{cap,k}$. The mathematical equation to approximate the variation of MC_k with $HRS_{cap,k}$ is given in Eq. (5.3). In the present work, the $HRS_{cap,k}$ is chosen depending on the traffic flow through the k^{th} terminus. For this, the intercity passenger train traffic is divided into light (1 to 4 trains per day), medium (5 to 7 trains per day) and heavy (8 to 12 trains per day) traffic, and accordingly the railway stations are segregated depending on their location in the different traffic zones (*TZ*). The segregation of the railway stations into the areas of light, medium and heavy traffic are clearly depicted by the blue, yellow and red pins, respectively in Fig. 5.2 using GoogleMap. Observation of this figure shows that majority of the railway stations of Assam, almost 88.26% are located in the areas with light traffic. The remaining 9.05% and 2.69% of the total railway stations are distributed between the medium and heavy *TZ*s, respectively. Thereafter, to fulfill the refueling requirements of light/medium and heavy traffic, the $HRS_{cap,k}$ of 450 *kg/day* and 1500 *kg/day*, respectively are chosen for deployment. The values of CC_k for 450 *kg/day* and 1500 *kg/day* HRS are obtained from [153] as 2.8 *m$* and 5.055 *m$*, respectively. The current and the estimated costs of HRS refueling for the specified T_{plan} are defined in Eqs. (5.4-5.5) and (5.6-5.7), respectively. These equations are derived assuming that each HRS has to supply an amount of fuel which is equal to the full tank capacity ($tank_{cap}$ in *kg*) of each train passing through it. Equation (5.8) is a constraint that ensures that a HRS be mandatorily located at the origin and destination terminuses of all the railway routes. This is because unlike the vehicular traffic, the passenger trains halt at the end terminuses for a duration of at least 1 to 2 hours before starting the journey anew [140]. This gives sufficient time for the refueling of the trains, and consequently ensures that the trains commence on a new journey with a full tank of fuel. This will further reduce the refueling requirements at the intermediate stations, and consequently the number of HRS installation at the intermediate stations along a railway route. Next, the D_{range} limitation of the hydrogen powered trains is expressed in terms of $FC_{k,k_{next}}$ in Eq. (5.9). Thus, following this constraint, the HRS are allocated along a route such that the train never consumes more than 90% of its $tank_{cap}$ while travelling from one HRS to another. Equation (5.10) imposes an upper limit on the total number of HRS to be installed in a layout of potential railway sites. The requisite of supplying the fuel requirements of all the intercity passenger trains is taken care of by the constraint defined in Eq. (5.11). The constraint defined in Eq. (5.12) indicates the binary nature of the variables, x_k and y_q.

5.2.2. *Solution strategy for the single-objective optimization approach*

In this sub-section, the solution strategies used to solve the problem of optimal HRS allocation are discussed.

5.2.2.1. Subroutine

A subroutine is developed that calculates the objective function value(s) while simultaneously satisfying the operational constraints of the optimization model. The steps of the subroutine are summarized below:

1) For each $k \epsilon N_{end}$, the subroutine will set $x_k = 1$, indicating that the HRS are located at all the origin-destination terminuses of the railway routes.
2) Next, for each route, q the subroutine will check if $D_{k,k_{next}}/D_{range}$ satisfies the constraint (5.9). If this constraint is violated for any path segment between two nearby HRS along q, then y_q is set to 0, and vice versa. Thus, $y_q = 0$ $(y_q = 1)$ implies that the given HRS layout does not suffice (suffices) to refuel the traffic flow, f_q.
3) The step 2 is repeated for all $q \epsilon Q$.
4) Thereafter, the uncaptured f_q are penalized while calculating the objective function value(s) as given in Eq. (5.13).
5) Likewise, $penalty_2$ is imposed in Eq. (5.13) if Eq. (5.10) is violated.

$$obj = \begin{cases} f_i(x) + penalty_1\left(TF - \sum_{q\epsilon Q} f_q y_q\right) + penalty_2, if\ \sum_{k\epsilon K} x_k > HRS^{max} \\ f_i(x) + penalty_1\left(TF - \sum_{q\epsilon Q} f_q y_q\right), otherwise \end{cases} \tag{5.13}$$

Where, i is the index representing the number of objective functions of optimization. For the single-objective optimization approach, $f_i(x)$ represents the single-objective function defined in Eq. (5.1). The flowchart of the subroutine is shown in Fig. 5.3. The designed subroutine is incorporated in the heuristic search based solution algorithm to determine the optimal solution set of the HRS layout.

5.2.2.2. Binary Particle Swarm Optimization

As discussed in section 2.3.2, the PSO is a population-based meta-heuristic search technique that iteratively tries to iteratively tries to improve a candidate solution with regard to the objective function value(s) to be optimized. Each particle in PSO represents a candidate solution whose position and velocity vectors are updated in every iteration. In this study, the binary PSO proposed by Kennedy et. al. in [154] is implemented, since the proposed optimization model involves the binary decision variable, x_k. In binary PSO, the particle's position vector can only take either of the binary values, 0 or 1. The velocity and the position update equations are given as follows:

$$V_{ij}^{iter} = V_{ij}^{iter-1} + c_1 rand_1\left(pbest_{ij}^{iter-1} - S_{ij}\right) + c_2 rand_2\left(gbest_{ij}^{iter-1} - S_{ij}\right) \tag{5.14}$$

$$S_{ij} = \begin{cases} 1, rand(k) < f\left(V_{ij}^{iter}\right) \\ 0, otherwise \end{cases} \tag{5.15}$$

$$f\left(V_{ij}\right) = \frac{1}{1+e^{-V_{ij}^{iter}}} \tag{5.16}$$

Where, *iter* is the iteration number; $V_{ij}^{iter}(S_{ij}^{iter})$ is the velocity (position) of the j^{th} dimension of the i^{th} particle in *iter*th iteration; *rand*, *rand*$_1$ and *rand*$_2$ are random numbers between [0,1]; and c_1 and c_2 are the learning factors. Equation (5.16) is adopted from [155].

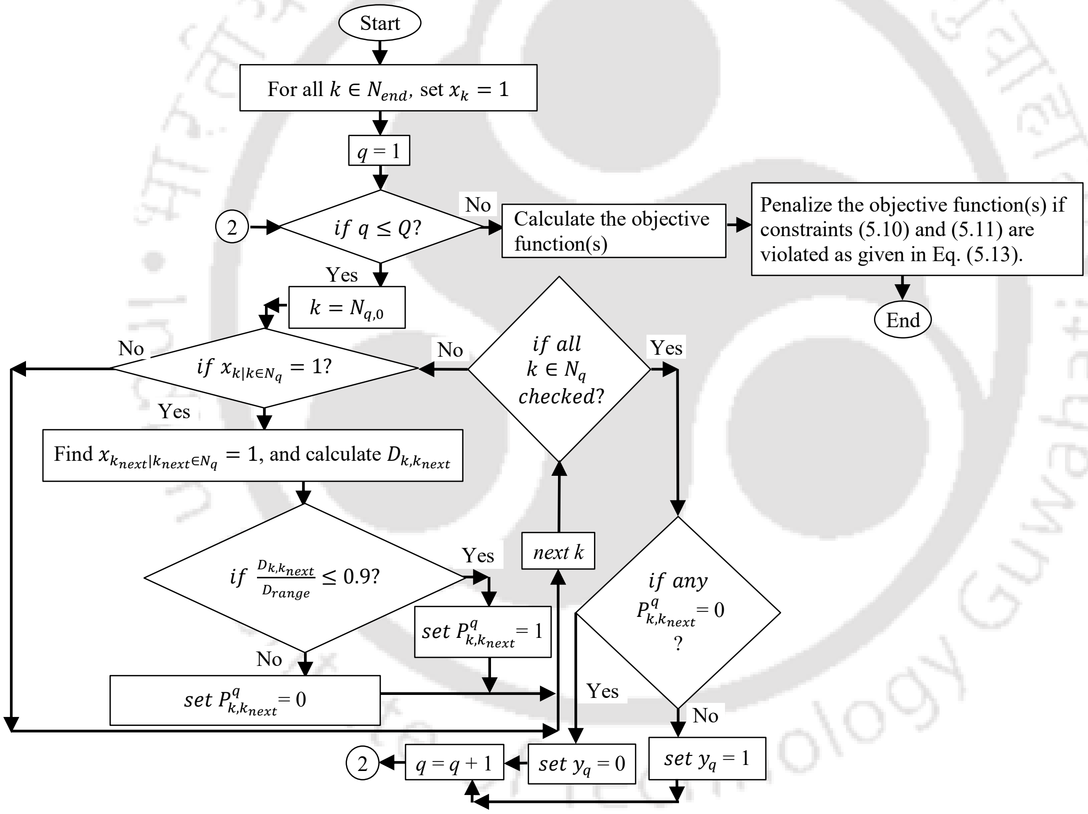

Where, $N_{q,0}$, and $P^q_{k,k_{next}}$ are the origin terminus, and the path segment between k^{th}, and k^{th}_{next} potential sites of the route, q, respectively.

Fig. 5.3: Flowchart of the subroutine.

5.2.3. *Results of single-objective optimization*

The results obtained from computer simulation study are discussed in this section. The present work aims to determine an optimal HRS layout which is technically sufficient to supply the fuel needs of the hydrogen powered intercity passenger trains to be functional under the Department of NEFR, Assam, India. For initial deployment, the conventional diesel run passenger trains are assumed to be replaced by the hydrogen powered passenger trains similar to the Hydroflex which is currently operational in United Kingdom [156]. The Hydroflex has a D_{range} of 85 to 115 km with a $tank_{cap}$ of 20 kg. The real time data of the intercity railway traffic of Assam, India [140] acts as the input to the optimization approach. The value of HRS^{max} is taken as 116, i.e., the total number of installed HRS is limited to less than 50% of the total existing potential railway sites of Assam, India. The parameters of binary PSO, i.e., n_{pop}, $iter^{max}$ and learning factors are set as 1000, 100 and 0.2, respectively. These values are optimized by taking multiple simulation runs.

5.2.3.1. Analysis of the HRS layout obtained using optimization

The single-objective optimization approach is solved using binary PSO to obtain the layout of HRS for the different values of D_{range} of the hydrogen powered passenger train between 85 to 115 km. The simulation results show that the number of installed HRS in a given layout of potential sites decreases with the increase in the D_{range} of the train. This is because larger the D_{range}, greater is the distance that the train can be travel on a single tank of hydrogen fuel. Consequently, the refueling requirements of the trains at the intermediate stations reduce which eventually leads to the decrease in the number of HRS installations. This observation is clearly validated in Table 5.2, where the number of HRS in a given layout reduces by almost 7.35%, 12.7% and 10.9%, respectively as D_{range} is increased from 85 to 115 km in steps of 10 km. To further illustrate the refueling choices provided by a HRS layout obtained using optimization along the different intercity railway routes of Assam, India, the HRS layout obtained for the locomotive D_{range} of 85 km is investigated. The corresponding refueling options are depicted in Table 5.3. Furthermore, the distribution of the HRS along the network of potential railway sites of Assam, India is displayed using GoogleMap in Fig. 5.4. In this figure, a blue pin represents a potential site for HRS allocation. The red pin depicts the presence of a HRS at the potential site, which is otherwise represented by the blue pin. The observations of Table 5.3 and Fig. 5.4 are as follows:

- The HRS layout obtained through optimization is capable of supplying the fuel needs of all the passenger trains travelling along the different intercity railway routes of Assam.
- Besides the HRS allocation at the intermediate stations within the D_{range} limit of the train, the HRS are also situated at the origin-destination terminuses of the railway routes. This is clearly validated by the results presented in Table 5.3. In this table, it is observed that the HRS are located at New Bongaigaon Juntion and Guwahati of Route 1, Guwahati and New

Bonagiagaon Junction of Route 2, Dhubri and Kamakhya Junction of Route 3, Lumding Junction and Guwahati of Route 4, Lumding Junction and Tinsukia Junction of Route 5, Jorhat and Tinsukia Junctionof Route 6, Guwhati and Mairabari of Roue 7, etc. These terminuses are the end stations of the respective railway routes. In addition to this, the distance between two nearby HRS location is found to be less than the D_{range} of 85km. Thus, in Route 1, the distance between the HRS locations at New Bongaigaon Junction and Patiladaha is 27.4km, Patiladaha and Nizsariha Halt is 42.5km, and so on. Similar observations are obtained for the remaining railway routes of Assam.

- The total number of HRS installed in the given layout of potential railway sites is 68. This implies that the HRS are located at about 29.5% of the total existing railway terminuses of Assam, India.

Thus, the obtained HRS layout is optimal, and confirms to the constraints (5.8 - 5.11) of the optimization model.

Table 5.2: Variation in the number of HRS installation in a given layout of potential railway sites with the locomotive D_{range}.

Driving range (km)	85	95	105	115
Total no. of HRS	68	63	55	49

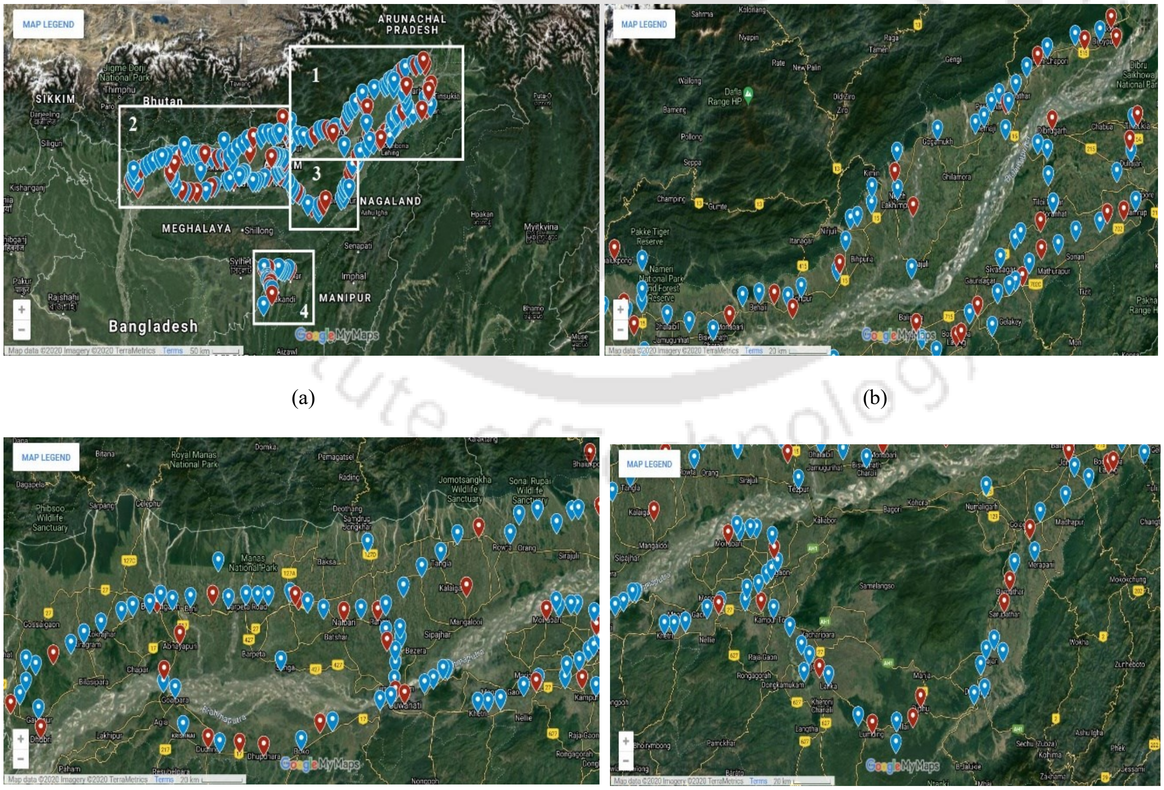

(a)

(b)

(c)

(d)

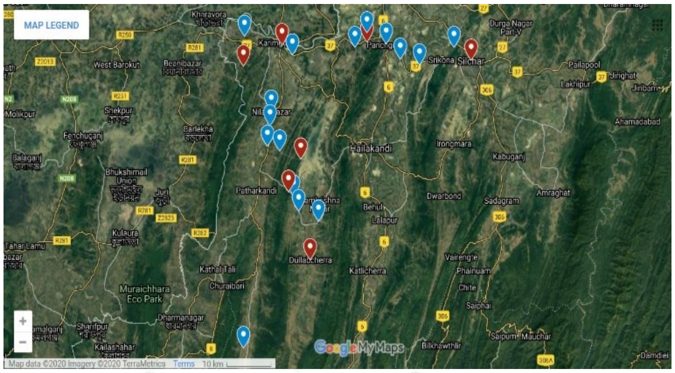

(e)

Fig. 5.4: An overview of the HRS distribution along the network of potential railway sites (represented by the blue pins) of Assam, India as obtained in Table 5.3, with the red pins depicting the presence of a HRS at a site: (a) general view of Assam, (b) part 1, (c) part 2, (d) part 3 and (e) part 4.

Table 5.3: Details of the optimal locations of the HRS at the potential railway terminuses along the different intercity railway routes of Assam, India as per the HRS layout obtained through optimization for the case of $85km\ D_{range}$ of the train.

Sl. No.	*Route*	*Railway terminuses where the HRS are located along with the distance between them*
1	GHY to NBQ via Guagachha	New Bongaigaon Junction - 27.4 *km* - Patiladaha - 42.5 *km* - Nizsariha Halt - 22.5 *km* - Nalbari - 16.6 *km* - Rangiya Junction - 40.9 *km* - Kamakhya Junction - 6.8 *km* - Guwahati.
2	GHY to NBQ via Goalpara town	Guwahati - 6.8 *km* - Kamakhya Junction - 48.6 *km* - Bamuni Gaon -16 *km* - Singra - 9.5 *km* - Dhup Dhara - 9.2 *km* - Rangjuli -20.4 *km* - Dudhnoi -38.7 *km* - Jogighopa - 15.9 *km* - Abhayapuri Asam - 17.4 *km* - New Bongaigaon Junction.
3	DBB to KYQ	Dhubri - 19.8 *km* - Golakganj Junction - 31.3 *km* - Tipkai - 53.7 *km* - New Bongaigaon Junction - 17.4 *km* - Abhayapuri Asam - 15.9 *km* - Jogighopa - 38.6 *km* - Dudhnoi - 55 *km* - Bamuni Gaon - 48.5 *km* - Kamakhya Junction.
4	LMG to GHY	Lumding Junction - 37.8 *km* - Dhalpukhuri - 43 *km* - Laopani - 23.9 *km* - Dharamtul - 11.2 *km* – Aujuri - 64.6 *km* - Guwahati
5	LMG to TSK	Lumding Junction - 23.1 *km* - Nailalung - 9.4 *km* - Diphu - 73.2 *km* - Sarupathar - 9.5 *km* - Barpathar - 24.4 *km* - Furkating Junction - 48.6 *km* - Nakachari - 17.5 *km* - Amguri Junction - 26.1 *km* - Simaluguri Junction - 13.5 *km* - Lakwa - 47.2 *km* - Borhat - 44 *km* - Tinsukia Junction.
6	JTTN to TSK	Jorhat - 26.8 *km* - Nakachari - 5.7 *km* - Lahing - 11.9 *km* - Amguri Junction - 26.1 *km* - Simaluguri Junction - 13.4 *km* - Lakwa - 42.4 *km* - Baruanagar - 4.8 *km* - Borhat - 10.4 *km* - Balimara - 18.9 *km* - Bordubi road - 14.6 *km* - Tinsukia Junction
7	GHY to MBO	Guwahati - 64.6 *km* - Aujuri - 11.2 *km* - Dharamtul - 50 *km* - Rupahigaon - 34 *km* - Mairabari.
8	SLGR to DBRT	Simaluguri Junction - 43 *km* - Sepon - 51.1 *km* - Dibrugarh - 5.7 *km* - Dibrugarh Town
9	DKGN to BHNG	Dekargaon - 4.2 *km* - Bindukuri - 14.7 *km* - Rangapara North Junction - 43.7 *km* - Bhalukpong
10	DKGN to MZS	Dekargaon - 4.2 *km* - Bindukuri - 14.7 *km* - Rangapara North Junction - 60.1 *km* - Monabari - 23 *km* - Helem - 28.5 *km* - Dubia - 13.6 *km* - Tatibahar - 55.7 *km* - Lilabari - 17 *km* - Baginadi – 10 *km* - Subansiri - 20.4 *km* - Bordoloni - 32.2 *km* - Sisibargaon - 23.8 *km* - Dipa - 25.1 *km* - Laimekuri - 17 *km* - Murkongselek
11	RNY to DKGN	Rangiya Junction - 61.2 *km* - Udalguri - 61.5 *km* - Rangapara North Junction - 14.7 *km* - Bindukuri - 4.2 *km* - Dekargaon

12	DKGN to RPAN	Dekargaon - 4.2 *km* - Bindukuri - 14.7 *km* - Rangapara North Junction
13	RPAN to RNY	Rangapara North Junction - 61.5 *km* - Udalguri - 61.3 *km* - Rangiya Junction
14	GHY to NBQ	Guwahati - 6.8 *km* - Kamakhya Junction - 40.8 *km* - Rangiya Junction - 16.6 *km* - Nalbari - 65.1 *km* - Patiladaha - 27.5 *km* - New Bongaigaon Junction
15	SCL to MSSN	Silchar - 29.4 *km* - Badarpur Junction - 20.1 *km* - Karimganj Junction - 10.6 *km* - Maishashan
16	BPB to DLCR	Badarpur Junction - 20.1 *km* - Karimganj Junction - 29.6 *km* - Phakhoagram - 6.1 *km* – Bazarghat - 14.7 *km* - Dullabcherra
17	SCL to DLCR	Silchar - 29.4 *km* - Badarpur Junction - 20.1 *km* - Karimganj Junction - 29.6 *km* - Phakhoagram - 6.1 *km* – Bazarghat - 14.7 *km* - Dullabcherra
18	DBRG to MZS	Dibrugarh - 55 *km* - Sisibargaon - 23.7 *km* - Dipa - 25.1 *km* - Laimekuri - 17 *km* - Murkongselek

5.2.3.2. Analysis of the cost of infrastructure planning of the HRS

In this sub-section, the cost of HRS infrastructure planning is investigated. For this study, three different scenarios of installed HRS capacity are considered.

- Case I: As mentioned in section 5.2.1, the $HRS_{cap,k}$ is chosen depending on the traffic flow through the k^{th} terminus in this case. To fulfil the refuelling requirements of the light/medium and heavy traffic, the $HRS_{cap,k}$ of 450 *kg/day* with CC_k of 2.8 *m$*, and $HRS_{cap,k}$ of 1500 *kg/day* with CC_k of 5.055 *m$*, respectively are chosen for deployment.
- Case II: The second case assume the installation of HRS with uniform capacities of 450 *kg/day* at the terminuses of the optimal HRS layout irrespective of the traffic flow.
- Case III: The third case considers HRS with uniform capacities of 1500 *kg/day* to be constructed at the terminuses of the optimal HRS layout irrespective of the traffic flow.

A comparison among the three cases in terms of their *TCO* is then carried out to examine the more suitable option of HRS deployment among them. The present study considers the HRS layout obtained for the locomotive D_{range} of 85 *km*.

5.2.3.2.1. Analysis of the capital and maintenance costs of the HRS

For the case I of HRS deployment, the capital and maintenance costs of the HRS for T_{plan} of 30 years are obtained through optimization. For cases II and III, the corresponding costs are calculated using Eqs. (5.1 - 5.3). The obtained cost values are listed in Table 5.4. Observation of this table presents the following inferences:

- Both the capital and maintenance costs are found to be the least (highest) for the case II (case III) of HRS deployment. This is because for the cases II and III, the HRS with the least and the highest capacities are installed at the terminuses of the optimal HRS layout under consideration. Consequently, larger the $HRS_{cap,k}$, higher are the values of the capital and maintenance costs.

- Case I scenario of HRS deployment incurs a total investment that lies intermediate to the cases II and III.
- As compared to case I, the total capital costs are found to be 7.64% lower and 66.58% higher for case II and case III, respectively. Similarly, the corresponding reduction and rise in the maintenance costs are observed to be 1.95% and 17.03%, respectively.

The above observations show that the case II scenario of 450 *kg/day* installed HRS capacity is the most feasible option in view of the least capital investment and maintenance cost.

Table 5.4: Calculated values of the Capital, and Maintenance Costs of the HRS layout under observation (Fig. 5.4 and Table 5.3).

Case I				*Case II*		*Case III*	
$\sum CC_k$ *(m$)*		$\sum MC_k$ *(m$)*		$\sum CC_k$ *(in m$)*	$\sum MC_k$ *(in m$)*	$\sum CC_k$ *(in m$)*	$\sum MC_k$ *(in m$)*
450 *kg/day*	1500 *kg/day*	450 *kg/day*	1500 *kg/day*	190.40	366.20	343.74	437.10
170.80	35.35	328.50	45				
Total = 206.15		Total = 373.50					

Table 5.5: Calculated values of the Refueling Costs of the HRS layout under observation (Fig. 5.4 and Table 5.3).

No. of HRS in different TZ {fuel to be supplied by the HRS per day =$f_q.tank_{cap}$ (in kg/day) }	*Case I*			*Case II*			*Case III*		
	$HRS_{cap,k}$ *(in kg/day)*	$N_{refuel,k}$ + $N_{refuel,k}^{proj}$	$C_{refuel,k}^{ct}$ + $C_{refuel,k}^{proj}$ *(in m$)*	$HRS_{cap,k}$ *(in kg/day)*	$N_{refuel,k}$ + $N_{refuel,k}^{proj}$	$C_{refuel,k}^{ct}$ + $C_{refuel,k}^{proj}$ *(in m$)*	$HRS_{cap,k}$ *(in kg/day)*	$N_{refuel,k}$ + $N_{refuel,k}^{proj}$	$C_{refuel,k}^{ct}$ + $C_{refuel,k}^{proj}$ *(in m$)*
2 (1*20)	450	16+470	0.05+0.06	450	16+470	0.05+0.06	1500	5+141	0.05+0.06
30 (2*20)	450	32+941	1.42+1.84	450	32+941	1.42+1.84	1500	10+282	1.42+1.84
23 (4*20)	450	65+1882	2.18+2.82	450	65+1882	2.18+2.82	1500	19+565	2.18+2.82
4 (6*20)	450	97+2823	0.57+0.74	450	97+2823	0.57+0.74	1500	29+847	0.57+0.74
2 (7*20)	450	114+3293	0.33+0.43	450	114+3293	0.33+0.43	1500	34+988	0.33+0.43
2 (8*20)	1500	39+1129	0.38+0.50	450	130+3764	0.38+0.50	1500	39+1129	0.38+0.50
1 (9*20)	1500	44+1270	0.21+0.28	450	146+4234	0.21+0.28	1500	44+1270	0.21+0.28
3 (10*20)	1500	49+1411	0.71+0.92	450	162+4704	0.71+0.92	1500	49+1411	0.71+0.92
3 (10*20)	1500	58+1694	0.28+0.37	450	195+5645	0.28+0.37	1500	58+1694	0.28+0.37
		=15427	=14.09		=28713	=14.09		=8614	=14.09

5.2.3.2.2. *Analysis of the refueling requirements of the HRS*

In this sub-section, the refueling requirements of the HRS are investigated. The cost of HRS refueling is calculated in terms of the delivery cost of hydrogen to the HRS. For case I, the values of $C_{refuel,k}^{ct}$ and $C_{refuel,k}^{proj}$ are obtained from the solution presented by the optimization approach. For the remaining cases, the refueling costs are calculated using Eqs. (5.4 - 5.7). These values are listed in Table 5.5. In addition to this, the $N_{refuel,k}$ and $N_{refuel,k}^{proj}$ are also determined and are listed in this table. The interpretations of this study are:

- Similar investments of around 14.09 *m$* are incurred in the refueling of the HRS for T_{plan} of 30 years for all the cases of HRS deployment.
- The difference lies in the frequency of HRS refueling for the three cases. With the increase in HRS capacity, the need for frequent refueling of the HRS decreases, and vice versa. This variation is clearly validated in Table 5.5. With respect to the 450 *kg/day* HRS, nearly 70% reduction in the frequency of HRS refueling with capacity of 1500 *kg/day* is observed in the different *TZ*s.
- The summation of the refueling frequencies of the HRS in the given layout for cases II and III are almost 86.12% higher and 44.16% lower, respectively as compared to that of the case I scenario of HRS deployment.

The above observations imply that installing HRS with uniform capacity of 1500 *kg/day* at all the optimal terminuses of the given layout leads to an overall reduction in the HRS refueling requirements but with the same refueling investment incurred for the current and the projected years. Hence, from the point of view of reduced HRS refueling, the third scenario is the most favorable option for deployment. However, although the cases II and III of HRS deployment are most suited for obtaining minimum capital investments and reduced HRS refueling requirements, respectively, to meet the requirements of optimum *TCO*, the case I scenario of HRS installation is the most feasible choice.

5.3. Multi-objective optimization approach

The problem of optimal HRS allocation is addressed as a multi-objective optimization approach in this section. The formulation of the multi-objective optimization model, the solution strategies used to solve the optimization problem and the simulation results are discussed here.

5.3.1. Formulation of the multi-objective optimization approach

In the multi-objective optimization approach, two cost functions are considered, namely the *TCO* (which defined as the summation of the capital and maintenance costs of the HRS), and the cost of HRS refueling for a specified T_{plan}. Both the CC_k and MC_k vary with $HRS_{cap,k}$ and the number of HRS. Increased number of HRS installations in a given layout of potential railway sites with higher $HRS_{cap,k}$ leads to a higher value of TCO, and vice versa. However, a layout with larger number of installed HRS will provide more refueling options for the passenger trains while operating on the different routes. This reduces the amount of fuel utilized from a particular HRS on a daily basis to supply the fuel needs of the passenger trains. This, in turn, increases the duration beyond which the HRS will run out of hydrogen fuel. Hence, the frequency of refueling of the HRS, and subsequently the cost of HRS refueling reduces for a layout with larger number of HRS installations. Thus, the TCO and average cost of HRS refueling, $HRS_{refuel,cost}^{avg}$ of a given layout of HRS conflict each other in terms of its variation with the number of HRS installations. Therefore, in this section, the multi-objective optimization approach is formulated with the objective functions of simultaneous minimization of the TCO and $HRS_{refuel,cost}^{avg}$ over a specified planning period of T_{plan} years. A notable assumption of the proposed multi-objective optimization approach that the passenger trains are refueled from its utilized tank capacity to its full tank capacity during its halt at each HRS before commencing on the journey anew. The mathematical model of the optimization approach is given below:

$$Minimise \begin{cases} f_1(x) = TCO = \sum_{k \in K} (CC_k + MC_k) x_k \\ f_2(x) = HRS_{refuel,cost}^{avg} = \frac{\sum_{k \in K} \left(C_{refuel,k}^{ct} + C_{refuel,k}^{proj} \right) x_k}{\sum_{k \in K} x_k} \end{cases} \tag{5.17}$$

$$where, x = x_{k|k \in K} \tag{5.18}$$

$$MC_k = HRS_{cap,k} 73125 \left(HRS_{cap,k} \right)^{-0.853} T_{plan} \tag{5.19}$$

$$C_{refuel,k}^{ct} = fuel_k PV_{H_2} N_{refuel,k} \tag{5.20}$$

$$N_{refuel,k} = \frac{365}{fuel_k} \sum_{q \in Q} HRS_{cap,used,k}^{q} \tag{5.21}$$

$$C_{refuel,k}^{proj} = \frac{fuel_k FV_{H_2}}{(1+r)^{\left(T_{plan} - 1 \right)}} N_{refuel,k}^{proj} \tag{5.22}$$

$$N_{refuel,k}^{proj} = \frac{365}{fuel_k} \left(T_{plan} - 1 \right) \sum_{q \in Q} HRS_{cap,used,k}^{q} \tag{5.23}$$

$$HRS_{cap,used,k}^{q} = \frac{D_{k,k_{prev}|k,k_{prev} \in N_q \& x_k, x_{k_{prev}} = 1}}{D_{range}} tank_{cap} \tag{5.24}$$

$$subject\ to$$

$$x_{k|k \in N_{end}} = 1 \tag{5.25}$$

$$FC_{k,k_{next}} = \frac{D_{k,k_{next}|k,k_{next}\in N_q \& x_k,x_{k_{next}}=1}}{D_{range}} \leq 0.9 \tag{5.26}$$

$$\sum_{k\in K} x_k \leq HRS^{max} \tag{5.27}$$

$$\sum_{q\in Q} f_q y_q = TF \tag{5.28}$$

$$x_k, y_q \in \{0,1\} \tag{5.29}$$

Equation (1) defines the objective functions of the multi-objective optimization approach, i.e., the simultaneous minimization of the TCO and $HRS^{avg}_{refuel,cost}$ for the specified planning period. While the TCO includes the summation of the capital and maintenance costs of the HRS, the $HRS^{avg}_{refuel,cost}$ is the average of the summation of $C^{ct}_{refuel,k}$ and $C^{proj}_{refuel,k}$ of the HRS for a T_{plan} of 30 years. It is to be noted that while calculating $C^{ct}_{refuel,k}$ and $C^{proj}_{refuel,k}$ in the single-objective optimization approach, it is assumed that each HRS has to supply an amount of fuel which is equal to the full tank capacity, $tank_{cap}$ of each train passing through the HRS. However, while operating on a railway route in real time from one station to another, the entire $tank_{cap}$ may not be utilized. Instead, the amount of locomotive fuel consumption is proportional to the ratio of the distance travelled between two nearby HRS and D_{range} of the train. Thus, the HRS located at a potential site, k along a route, q will have to supply an amount of fuel to the train which is equal to the distance travelled by the train to reach the present location, k from a HRS located at a previous railway station, k_{prev} along the route, q. Thus, Eqs. (5.5) and (5.7) are reformulated by replacing the term $(f_{q,k} tank_{cap})$ by $\left(\sum_{q\in Q} HRS^{q}_{cap,used,k}\right)$ in Eqs. (5.21) and (5.23). The term $HRS^{q}_{cap,used,k}$ represents the amount of $HRS_{cap,k}$ utilized in supplying the fuel needs of the passenger train passing through the kth potential site along the qth railway route. The mathematical definition of $HRS^{q}_{cap,used,k}$ is given in Eq. (5.24). The constraints defined in Eqs. (5.25 - 5.29) is the same as that of the single-objective optimization approach, and are already discussed in section 5.2.1.

5.3.2. Solution strategy for the multi-objective optimization approach

It is already mentioned in section 2.4.2 that a vital aspect of a multi-objective optimization approach is to obtain the Pareto optimal set of solutions with better diversity among them. This depends on the selection of *pbest* and *gbest* which in turn depends on the fitness assignment scheme. In this section, the SPEA2-based multi-objective binary PSO (MOBPSO) is used for assigning the particles' fitness values. The pseudo-codes for the SPEA2-based MOBPSO used to solve the multi-objective optimization problem are depicted in Fig. 5.5. Each particle of SPEA2-based MOBPSO encodes the information of the binary variable, x_k. The subroutine of Fig. 5.3 is incorporated as the support sub-routine in the solution algorithm. In the subroutine, the term $f_i(x)$ of Eq. (5.13) represents the dual-objective functions defined in Eq. (5.17).

```
Begin
Generate initial population of particles;
Obtain the initial non-dominated solutions and store them in elite archive;
While $iter \leq iter^{max}$
    For $i = 1{:}n_{pop}$
        Update particle velocity and position using Eqs. (5.14-5.16);
        Call the subroutine of Fig.5.3;
        Calculate objective functions and assign the finesses using SPEA2;
    End for
    Find the new set of non-dominated solutions;
    Update the elite archive;
    iter=iter+1;
End while
Elite archive contains the optimal solution sets of HRS layout.
End
```

Fig.5.5: Pseudo-codes of SPEA2-based MOBPSO solution algorithm.

5.3.3. Results of multi-objective optimization

In this section, the simulation results of multi-objective optimization approach are presented and discussed. The present work aims to determine an optimal HRS layout which is technically sufficient to supply the fuel needs of the hydrogen powered intercity passenger trains to be functional under the Department of NEFR in Assam, India. To solve the optimization problem, the hydrogen powered trains similar to the Hydroflex are considered for initial deployment. The optimization is carried out for the three different cases of installed HRS capacity (defined in section 5.2.3.2.2). The real time data of the intercity railway traffic of Assam, India [27] is taken as the input. The values of D_{range} and HRS^{max} set as 85 *km* and 116, respectively. The values of SPEA2-based MOBPSO parameters, i.e., n_{pop} and $iter^{max}$ are taken as 3000 and 100, respectively. These values are optimized after taking multiple simulation runs.

5.3.3.1. Analysis of the TCO and refueling requirements of the HRS

The multi-objective optimization approach is solved using SPEA2-based MOBPSO to obtain the Pareto optimal set of solutions in which each solution represents a HRS layout for a particular value of *TCO* and $HRS^{avg}_{refuel,cost}$. Three different Pareto fronts are obtained, one for each case of HRS deployment, and are shown in Fig. 5.6. Three solutions of the Pareto front are chosen, and their corresponding details are listed in Table 5.6. For all the cases, the $Solution_{1,case}$ ($Solution_{3,case}$) corresponds to the highest (lowest) of $HRS^{avg}_{refuel,cost}$ and lowest (highest) values of TCO. The $Solution_{2,case}$ is an intermediate solution. The total number of HRS installed in a given layout of potential railway sites for all the solution sets are also given in Table 5.6. Furthermore, to study the variation in the frequency of HRS refueling with $HRS_{cap,k}$, the values $\sum_{k\in TZ}\left(N_{refuel,k} + N^{proj}_{refuel,k}\right)$ of the HRS located in the different traffic zones for $Solution_{2,1}$, $Solution_{2,2}$ and $Solution_{2,3}$ are obtained, and are presented in Table 5.7. The following inferences are obtained from this study:

- $Solution_{1,case}$ ($Solution_{3,case}$) presents the network with the smallest (largest) number of HRS installations for all the cases of HRS deployment. For case I, the total number of HRS installed in a given layout increases by 9.40% and 20.83% for $Solution_{2,1}$ and $Solution_{3,1}$, respectively as compared to $Solution_{1,1}$. Likewise, for cases II and III, the corresponding increase in the number of HRS are found to be 8.25%, 19.60% and 6.10%, 17.20%, respectively.
- Larger the number of installed HRS in a given layout, higher (lower) is the value of the TCO ($HRS^{avg}_{refuel,cost}$). Hence, the values of TCO are the smallest for $Solution_{1,case}$ and increases by 9.15% (20.32%) for $Solution_{2,1}$ ($Solution_{3,1}$), 8.25% (19.58%) for $Solution_{2,2}$ ($Solution_{3,2}$) and 6.06% (17.17%) for $Solution_{2,3}$ ($Solution_{3,3}$). On the other hand, the HRS layout corresponding to $Solution_{1,case}$ results in the highest values of $HRS^{avg}_{refuel,cost}$. As compared to $Solution_{1,case}$, the decrease in the value of $HRS^{avg}_{refuel,cost}$ is observed to be 8.57% (17.24%) for $Solution_{2,1}$ ($Solution_{3,1}$), 7.62% (16.38%) for $Solution_{2,2}$ ($Solution_{3,2}$) and 5.72% (14.66%) for $Solution_{2,3}$ ($Solution_{3,3}$).
- The TCO increases proportionally with $HRS_{cap,k}$. Hence, for $Solution_{2,case}$ and $Solution_{3,case}$ which are having the same number of HRS installations in a given layout, the values of TCO are found to be almost 2.30% and 40.22% higher for cases I and III, respectively than the corresponding value of TCO for the case II scenario of HRS deployment. This is because the case II assumes the installation of the smallest $HRS_{cap,k}$ of 450 *kg/day* at the terminuses of the optimal HRS layout.
- The variation in the frequency and the cost of HRS refuelling are inversely proportional to $HRS_{cap,k}$. This observation is clearly depicted in Table 5.7. Since, as per case III, the HRS of the largest capacity of 1500 *kg/day* is chosen for deployment, hence, the summation of

the refuelling frequencies of all the HRS is the lowest for this case. Although the number of HRS corresponding to $Solution_{2,case}$ is the same for all the cases of HRS deployment, the total refuelling frequencies of the HRS for cases I and II are observed to be 3.2 and 3.33 times higher in comparison to case III, respectively.

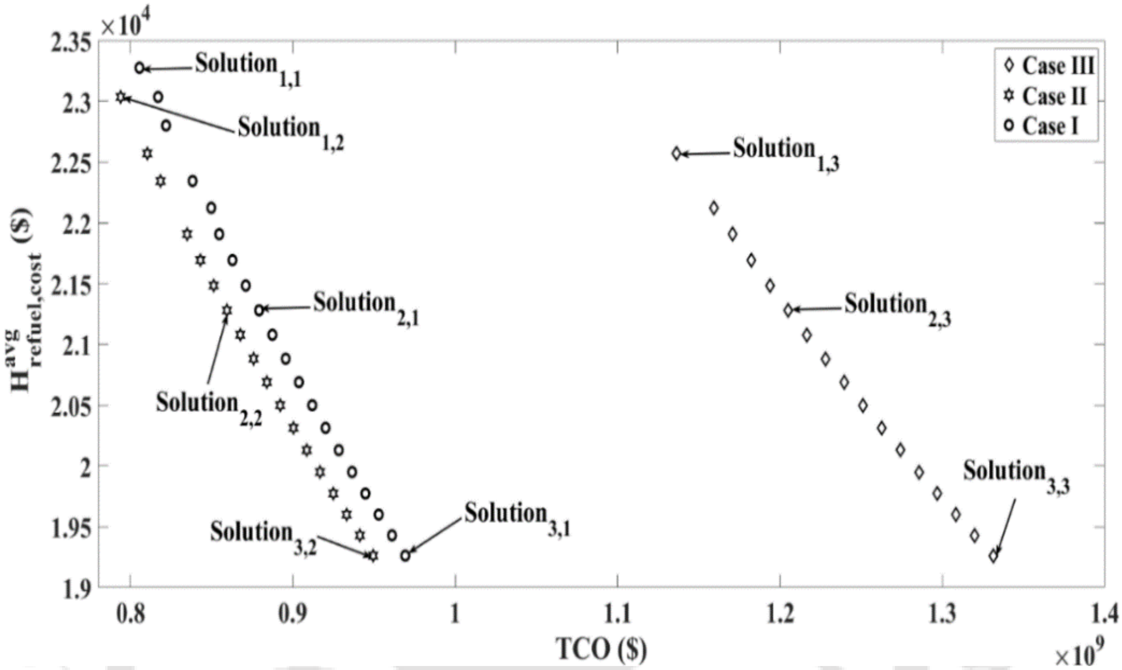

Fig. 5.6: Pareto fronts obtained with SPEA2-based MOPSO for the different cases of HRS deployment.

Table 5.6: Details of the values of *TCO* and $HRS^{avg}_{refuel,cost}$ for the solution sets of Fig. 5.6.

Case I			
Solution sets	*TCO (m$)*	$HRS^{avg}_{refuel,cost}$ *($)*	*Total HRS*
$Solution_{1,1}$	805.54	23275	90 (450 kg/day) + 6 (1500 kg/day) = 96
$Solution_{2,1}$	879.21	21280	99 (450 kg/day) + 6 (1500 kg/day) = 105
$Solution_{3,1}$	969.25	19262	110 (450 kg/day) + 6 (1500 kg.day) = 116
Case II			
Solution sets	*TCO (m$)*	$HRS^{avg}_{refuel,cost}$ *($)*	*Total HRS of 450 kg/day*
$Solution_{2,1}$	794.00	23035	97
$Solution_{2,2}$	859.50	21280	105
$Solution_{3,2}$	949.50	19262	116
Case III			
Solution sets	*TCO (m$)*	$HRS^{avg}_{refuel,cost}$ *($)*	*Total HRS of 1500 kg/day*
$Solution_{3,1}$	1136.30	22570	99
$Solution_{3,2}$	1205.20	21280	105
$Solution_{3,3}$	1331.40	19262	116

Table 5.7: Comparison among the three cases in terms of their HRS refueling frequencies for the HRS layout corresponding to $Solution_{2,case}$.

Traffic flow in TZ	*Case I*	*Case II*	*Case III*
	$\sum_{k \in TZ} \left(N_{refuel,k} + N_{refuel,k}^{T_{plan}-1}\right)$	$\sum_{k \in TZ} \left(N_{refuel,k} + N_{refuel,k}^{T_{plan}-1}\right)$	$\sum_{k \in TZ} \left(N_{refuel,k} + N_{refuel,k}^{T_{plan}-1}\right)$
1	$286 \vert_{\sum(k \in TZ)=3}$	$93 \vert_{\sum(k \in TZ)=1}$	$55 \vert_{\sum(k \in TZ)=2}$
2	$6519 \vert_{\sum(k \in TZ)=50}$	$6615 \vert_{\sum(k \in TZ)=51}$	$1885 \vert_{\sum(k \in TZ)=45}$
3	$409 \vert_{\sum(k \in TZ)=2}$	$56 \vert_{\sum(k \in TZ)=1}$	$57 \vert_{\sum(k \in TZ)=1}$
4	$9480 \vert_{\sum(k \in TZ)=32}$	$8727 \vert_{\sum(k \in TZ)=36}$	$2719 \vert_{\sum(k \in TZ)=38}$
6	$1621 \vert_{\sum(k \in TZ)=9}$	$1646 \vert_{\sum(k \in TZ)=6}$	$606 \vert_{\sum(k \in TZ)=11}$
7	$370 \vert_{\sum(k \in TZ)=3}$	$369 \vert_{\sum(k \in TZ)=3}$	$32 \vert_{\sum(k \in TZ)=1}$
8	$118 \vert_{\sum(k \in TZ)=1}$	$688 \vert_{\sum(k \in TZ)=2}$	$234 \vert_{\sum(k \in TZ)=2}$
9	$37 \vert_{\sum(k \in TZ)=1}$	$124 \vert_{\sum(k \in TZ)=1}$	$116 \vert_{\sum(k \in TZ)=1}$
10	$207 \vert_{\sum(k \in TZ)=3}$	$1599 \vert_{\sum(k \in TZ)=3}$	$310 \vert_{\sum(k \in TZ)=3}$
12	$26 \vert_{\sum(k \in TZ)=1}$	$119 \vert_{\sum(k \in TZ)=1}$	$36 \vert_{\sum(k \in TZ)=1}$
Total	19073	19980	5994

5.3.3.2. Analysis of the HRS layout obtained using SPEA2-based MOPSO

In this sub-section, the refueling choices provided by a HRS layout which is obtained using the multi-objective optimization approach along the different intercity railway routes of Assam, India is investigated. For this, the HRS layout corresponding to $Solution_{2,1}$ of the Pareto front is considered. The corresponding refueling options are listed in Table 5.8. In addition to this, the distribution of the HRS along the network of potential railway sites of Assam, India is depicted by the red pins using GoogleMap in Fig. 5.7. The observations of this study are as follows:

- The HRS layout obtained using optimization is capable of supplying the fuel needs of the passenger trains travelling along the different intercity railway routes of NEFR, Assam, India.
- The HRS are located at the end stations of each of the railway routes giving sufficient time for the trains to refuel its tank before starting the journey anew. For example, in Route 1, the HRS are located at the end terminuses which are New Bongaigaon Junction and Guwahati.
- The HRS are also located at the intermediate stations of the railway routes within the D_{range} limit of the train so that the train never runs out of fuel while travelling on these routes. Thus, in Route 1 it is seen the distance between New Bongaigaon Junction and Bijni is 17.2 km, between Bijni and Patiladaha is 10.2 km, between Patiladaha and Sorupeta is 27.9 km and so

on. Similar distribution of HRS within D_{range} of 85 km is observed in the remaining railway routes of Assam.

- The total number of HRS is limited to 105 which is less than the pre-specified HRS^{max} value of 116.

Thus, the above study shows that similar to the single-objective optimization approach, the HRS layout obtained using multi-objective optimization is optimal, and confirms to the constraints defined in Eqs. (5.25 - 5.29) of the optimization model. Similar features are also exhibited by the remaining solutions of the Pareto front, and hence, they are not discussed in this chapter.

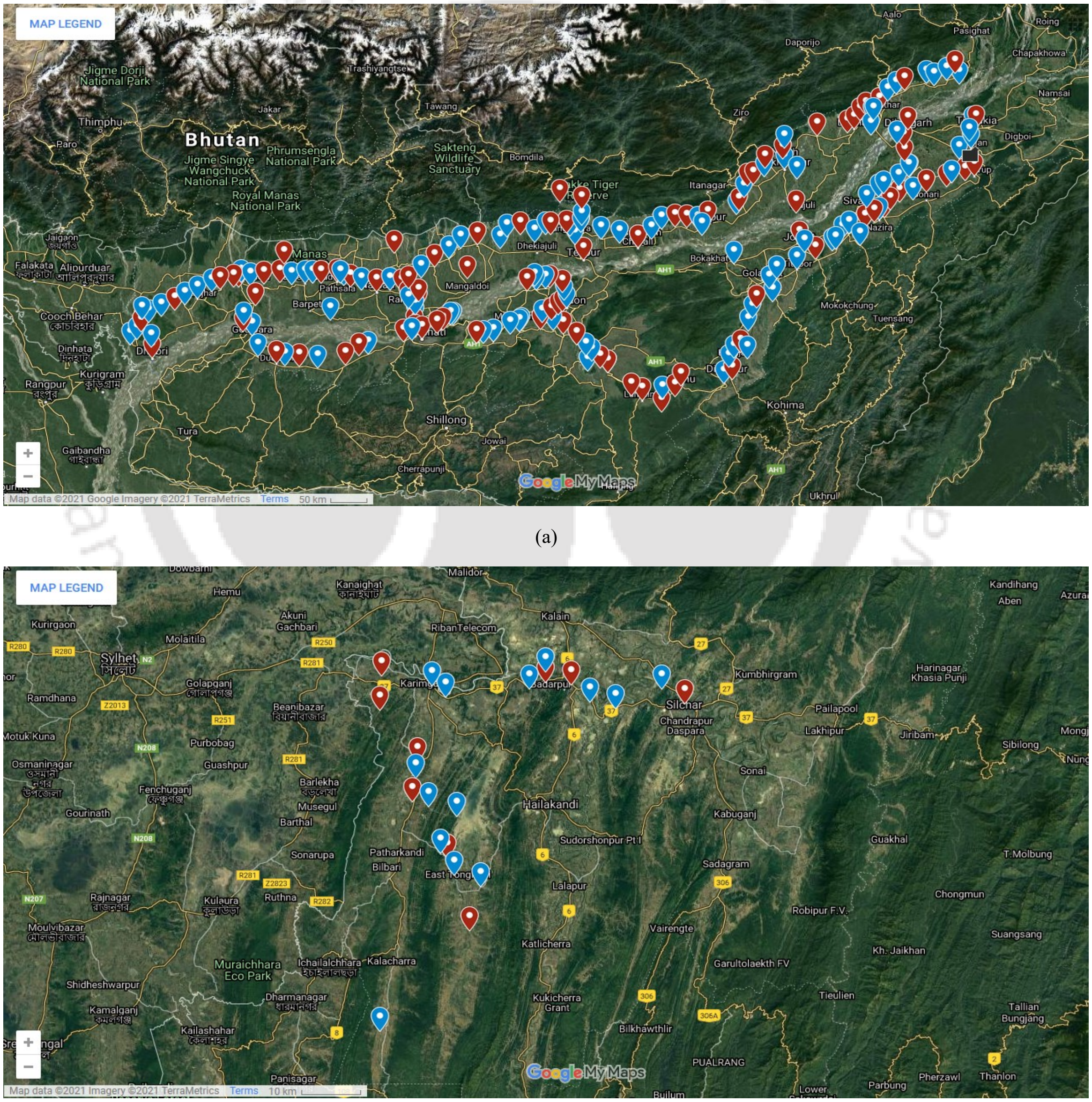

(a)

(b)

Fig. 5.7: An overview of the distribution of the HRS provided in Table 5.8 in the layout of potential railway terminuses of Assam, India

with the red pins denoting the presence of a HRS at a potential railway site: (a) Brahmaputra valley and (b) Barak valley.

Table 5.8: Details of the optimal locations of the HRS at the potential railway terminuses along the different intercity railway routes of Assam, India as per the HRS layout of $Solution_{2,1}$ of the Pareto front.

Sl. No.	*Route*	*Intermediate stations with the bold font representing the stations where HRS are located*
1	GHY to NBQ via. Guagachha	New Bongaigaon Junction -17.2 *km* - Bijni -10.2 *km* - Patiladaha -27.9 *km* - Sorupeta -10 *km* - Pathsala -9.5 *km* - Tihu -17.6 *km* - Nalbari -16.6 *km* - Rangiya Junction -10.1 *km* - Kendukona -5.3 *km* - Baihata -18.3 *km* - Agthori -7.2 *km* - Kamakhya Junction -6.8 *km* - Guwahati.
2	GHY to NBQ via Goalpara town	Guwahati -6.8 *km* - Kamakhya Junction -13.3 *km* - Azara -35.5 *km* - Bamuni Gaon -7.8 *km* - Boko -26.9 *km* - Rangjuli -20.4 *km* - Dudhnoi -28.1 *km* - Pancharatna -26.5 *km* - Abhayapuri Asam -9 *km* - Majgaon Assam -8.4 *km* - New Bongaigaon Junction.
3	DBB to KYQ	Dhubri -32 *km* - Basbari -26.7 *km* - Sapatgram -34.3 *km* - Basugaon -7.5 *km* - Dangtal -4.3 *km* - New Bongaigaon Junction -17.4 *km* - Abhayapuri Asam -54.5 *km* - Dudhnoi -55 *km* - Bamuni Gaon -35.2 *km* - Azara -13.3 *km* - Kamakhya Junction.
4	LMG to GHY	Lumding Junction -8.4 *km* - Patharkola -22.2 *km* - Lanka -7.2 *km* - Dhalpukhuri -23.6 *km* - Jamunamukh -10.9 *km* - Kampur -17.2 *km* - Chaparmukh Junction -26.4 *km* - Aujuri -19.3 *km* - Kamrup Khetri -18.7 *km* - Panbari -12.7 *km* - Panikhaiti -5.5 *km* - Narangi -8.4 *km* - Guwahati
5	LMG to TSK	Lumding Junction -6.9 *km* - Barlangfer -16.2 *km* - Nailalung -9.4 *km* - Diphu -37 *km* - Dimapur -20.2 *km* - Chongajan -33.4 *km* - Bhilgaon -6.7 *km* - Jamguri -47.9 *km* - Mariani Junction -39.5 *km* - Namti Ali -14.6 *km* - Simaluguri Junction -13.5 *km* - Lakwa -20.5 *km* - Bhojo -13.9 *km* - Sapekhati -12.8 *km* - Borhat -5.3 *km* - Namrup -38.7 *km* - Tinsukia Junction.
6	TSK to JTTN	Tinsukia Junction -33.5 *km* - Balimara -5.1 *km* - Namrup -5.3 *km* - Borhat -12.8 *km* - Sapekhati -13.9 *km* - Bhojo -20.5 *km* - Lakwa -6.9 *km* - Mahutgaon -6.5 *km* - Simaluguri Junction -7.6 *km* - Mezenga -7 *km* - Namti Ali -55.9 *km* - Jorhat
7	GHY to MBO	Guwahati -8.4 *km* - Narangi -5.5 *km* - Panikhaiti -12.7 *km* - Panbari -18.7 *km* - Kamrup Khetri -19.3 *km* - Aujuri -26.4 *km* - Chaparmukh Junction -11.5 *km* - Phulaguri -5.4 *km* - Bebejia -2 *km* - Senchoa Junction -25.9 *km* - Juriagaon -3.9 *km* - Dagaon -5.4 *km* - Balikotia -14.7 *km* - Mairabari.
8	SLGR to DBRT	Simaluguri Junction -38.2 *km* - Mohkhuti -26.8 *km* - Khowang -10 *km* - Lepetkata -24.8 *km* - Dibrugarh Town
9	DKGN to BHNG	Dekargaon -18.9 *km* - Rangapara North Junction -22.6 *km* - Gamani -21.1 *km* - Bhalukpong
10	DKGN to MZS	Dekargaon -18.9 *km* - Rangapara North Junction -50.8 *km* - Viswanath Chariali -25.6 *km* - Bedeti -6.7 *km* - Helem -18.9 *km* - Gohpur -23.2 *km* - Tatibahar -17.4 *km* - Harmuti Junction -3.9 *km* - Tanijan -16 *km* - Silanibari -18.4 *km* - Lilabari -35.3 *km* - Gogamukh -19.8 *km* - Jiadhal -5.7 *km* - Dhemaji -7.6 *km* - Moridhal -4.6 *km* - Sripani -34.5 *km* - Simen Chapari -38 *km* - Murkongselek
11	RNY to DKGN	Rangiya Junction -4.9 *km* - Khandikar -23.2 *km* - Khoirabari -33.1 *km* - Udalguri -28.8 *km* - Hugrajuli -22.1 *km* - New Missamari -10.6 *km* - Rangapara North Junction -18.9 *km* - Dekargaon
12	DKGN to RPAN	Dekargaon -18.9 *km* - Rangapara North Junction
13	RPAN to RNY	Rangapara North Junction -10.6 *km* - New Missamari -22.1 *km* - Hugrajuli -28.8 *km* - Udalguri -33.2 *km* - Khoirabari -23.2 *km* - Khandikar -4.9 *km* - Rangiya Junction
14	GHY to NBQ	Guwahati -6.8 *km* - Kamakhya Junction -30.7 *km* - Kendukona -10.1 *km* - Rangiya Junction -16.6 *km* - Nalbari -17.6 *km* - Tihu -9.6 *km* - Pathsala -10 *km* - Sorupeta -27.9 *km* - Patiladaha -10.2 *km* - Bijni -17.3 *km* - New Bongaigaon Junction
15	SCL to MSSN	Silchar -24.2 *km*- Panchgram -5.2 *km*- Badarpur Junction -14 *km*- Chargola -16.7 *km*- Maishashan

16	BPB to DLCR	Badarpur Junction -14 *km* - Chargola -14.2 *km* - Suprakandi -5.9 *km* - Nilambazar -7.5 *km* - Baraigram Junction -28.9 *km* - Dullabcherra
17	SCL to DLCR	Silchar -29.4 *km* - Badarpur Junction -34.1 *km* - Nilambazar -7.4 *km* - Baraigram Junction -28.9 *km* - Dullabcherra
18	DBRG to MZS	Dibrugarh -48.4 *km* - Sripani -34.4 *km* - Simen Chapari -38 *km* - Murkongselek

5.4. Summary of the present work

In order to address the concern of environmental pollution and diminishing fossil fuel reserve, the hydrogen powered locomotives have been proposed to retrofit the conventional diesel locomotives which are currently used to haul the intercity passenger trains operational under the Department of NEFR in Assam, India. However, the deployment of hydrogen powered passenger trains requires a proper refueling infrastructure. In view of this, an attempt has been made in the present chapter to determine the optimal locations of the HRS for the rollout of the hydrogen powered intercity passenger trains in Assam, India. To do this, the single-objective optimization approach has been firstly formulated with the objective function of the minimization of the *TCO* of the HRS. The *TCO* includes the capital cost, the maintenance cost, and the cost of refueling of the HRS for the specified planning period. Next, the cost function has been split into two contradictory components. The first cost component is the *TCO* comprising of the capital and maintenance cost of the HRS. The second cost component is the cost of HRS refueling for the specified planning period. Both these costs functions conflict each other in terms of their variation with the number and the capacity of the HRS. To address this issue, the multi-objective optimization approach has been developed which aims to simultaneously minimize the aforementioned cost components, i.e., the *TCO* and the cost of HRS refueling. Both, the optimization problems have been solved using the real-time data of the intercity railway traffic of NEFR, Assam as the input, and the binary PSO based the solution algorithms. Three different cases of installed HRS capacity has been considered in this study. The salient outcomes of this research are:

- The optimization approaches present the different combinations of HRS layout which are capable of supplying the fuel needs of all the passenger trains travelling on the intercity railway routes of Assam, India.
- The total number of HRS installed in a given layout decreases with the increase in the driving range of the train.
- Investigation on the HRS infrastructure development showed that a HRS of lower capacity requires frequent refueling, and vice versa. Likewise, the frequency and cost of HRS

refueling reduce with the increase in the number of HRS. However, the capital and maintenance costs increase with the increase in the capacity and the number of HRS installations.

- The proposed multi-objective optimization approach provides a set of alternative solutions with different number and combinations of the HRS layout from which a planner can select a solution according to the budget of capital and operational expenditures.

Chapter 6

Conclusions and Future Work

In the recent years, with rapid industrialization and diminishing fossil fuel reserve, the global energy sector is drifting fast towards renewable energy. In transportation, the PEMFC is turning out to be a viable replacement for the fossil fuel driven internal combustion engines. The PEMFC is a green energy technology that runs on hydrogen fuel. But owing to its technical drawbacks of slow dynamic response, high cost, FC starvation, flooding, etc., the use of PEMFC with some ESS, such as, the battery, SC, etc. to form a HES is always preferred. The ESS has the capability to withstand larger load dynamics without affecting its lifetime, and to absorb/store the excess energy for future use. However, the optimal component sizing of the PEMFC based HES, and/or the development of an efficient EMS are important factors that determine the competence of the PEMFC based HES in terms of its capital and operational costs. Hence, the same forms an important area of research. In Chapter 1, a comprehensive review of the research related to the application of the PEMFC based HES in transportation has been provided. The concerned research area has been classified based on the topology of the PEMFC based HES, the transportation areas, the field of study, i.e., the development of the control approaches, DO, and/or EMO approaches, and the different solution strategies employed in these studies. However, the application of PEMFC is not just limited to transportation alone. There are several research papers where the PEMFC based HES is implemented in micro-grid, power generation system, desalination system, and in various portable applications, such as, the laptop, uninterrupted power supply, etc. These papers have been thoroughly discussed in Chapter 1. Among all the aforementioned papers, there are very few research articles where the use of PEMFC based HES in locomotive applications has been reported. In none of these papers, the formulation of some optimization approaches to determine the optimal sizes of the HES components or the development of the EMO approaches for the optimal distribution of load in the HES have been presented. Thus, this thesis is basically concentrated on the development of a competent PEMFC-battery-HES with reduced investment and operational costs for locomotive applications. In ordinary situations, the electric locomotives are a good option for replacing the diesel locomotives since they are pollution free and can power a longer train for much greater distance and at faster speeds than its diesel engine counterpart. Hence, the electrification of the locomotives has been going on in several parts of India except for the North Eastern region of the country. The first electric locomotive came into operation in Assam in 2021. Moreover, almost two-thirds of the North Eastern area is hilly terrain interspersed with valleys and plains [157]. The electrification of locomotives is not a feasible option in these hilly areas. On the other hand, considering the pace of investment in the FC sector, the cost of PEMFC is expected to come down significantly in the near future. Moreover, hydrogen production is one of the largest growing industry of the twentieth century as it is turning out to be a potential substitute for the fossil fuels, especially in transportation applications. However, since hydrogen contains less energy per unit volume than all other fuels, transporting, storing, and delivering it to the end-user become more expensive on a per gasoline gallon equivalent basis. Thus, engineers all around the globe are working on low-cost production technologies to make the resulting hydrogen cost competitive with the conventional transportation fuels. According to the new report from Hydrogen Council [158], the cost of hydrogen production is predicted to fall drastically by up to 60% by 2030. Thus, in due course of time, the PEMFC powered locomotives will serve as a competent green energy solution that can deliver the same power, range, reliability and cost-effectiveness as the conventional diesel locomotives. Besides, converting the diesel locomotives to hydrogen powered locomotives will be far more cost-effective than electrifying the railway tracks with overhead catenary wires. This is one of the reasons why the commercial deployment of the hydrogen powered passenger trains have already started in several European countries, such as Germany, United Kingdom, etc. Keeping this in mind, the rollout of the PEMFC-battery-HES powered locomotives in the NEFR region, Assam, India has been considered in this thesis. However, the deployment of hydrogen fueled locomotives requires a proper refueling infrastructure along with the cost-effective methods of fuel production. In view of this, the optimal allocation planning of the HRS for the commercial rollout of the hydrogen powered passenger trains has been addressed in Chapter 5 of this thesis. Thus, the contributions of this thesis are summarized as follows:

- In Chapter 2, the formulation of the DO approaches to optimise the sizes of the PEMFC and battery that constitute a HES capable of driving the intercity passenger trains in NEFR, Assam, India has been presented. The objective of the DO approaches is to minimise the cost of deployment of the PEMFC-battery-HES in locomotives. The problem of DO has been addressed as single-objective and multi-objective optimization approaches. Simulation study shows that the sizes of the PEMFC and battery obtained through optimization are primarily dependent on the choice of EMS, the driving conditions, and the slope of the railway track in which the train is operating. Among the different values of the PEMFC and battery sizes, the largest size of the energy sources that suffice to supply the locomotive power demand under the different driving conditions can be chosen for deployment in real-time. Besides, the proposed multi-objective optimization approach presented the planner with a set of alternative solutions with different sizes of the PEMFC-battery-HES components considering the trade-off between the capital and operational investments incurred in its deployment.

- In Chapter 3, the design of the PWM control approaches for the MISO-DC/DC boost converter has been carried out to meet the requirements of the application of the PEMFC-battery-HES powered locomotives, i.e., the regulation of the DC-bus voltage, and the power flow control in the HES in accordance to the EMS. The performances of the PWM control approaches have been tested for a practical drive cycle scenario through computer simulation, and on the experimental setup of the HES. For both the studies, the reduced scaled prototype models of the PEMFC-battery-HES and the MISO converter have been developed. The MISO converter has been designed to supply a peak locomotive load of $150W$ with operating DC-bus voltage at $48V$. The PWM controllers have been developed using the mathematical concept of Venable K-factor. Both the simulation and hardware results show that the designed PWM controlled MISO converter operates satisfactorily to provide the desired performances. However, the average power demand and the operating DC-bus voltage of a locomotive in real-time application varies around 2 to $5MW$ and 1500 to $2800V$, respectively. Accordingly, the proposed prototype of the MISO converter and the PEMFC-battery-HES can be scaled up to develop the real setup of the HES for locomotives. However, in the design of a PEMFC-battery-HES of such high power and voltage ratings, the issues related to the high voltage protection, space management, etc. need to be given due attention.

- In Chapter 4, the problem of optimal load distribution in the PEMFC-battery-HES for locomotive applications has been addressed. For this, two different EMO approaches have been formulated, i.e., the EMO1 and EMO2 approaches without and with the durability constraints of the energy sources, respectively. The EMO approaches have been executed using GAMS. The performance comparison of the proposed EMO approaches with some of the already available energy management approaches in literature verifies the proficiency of both the EMO approaches in the reduction of hydrogen consumption without compromising the operational dynamics and the durability of the energy sources. However, the EMO2 approach exhibits better performance as compared to the EMO1 approach both in terms of reduced hydrogen consumption of the PEMFC and improved dynamic response of the energy sources.

- In Chapter 5, the optimal allocation planning of the HRS to meet the constraints of the rollout of the hydrogen powered passenger trains in NEFR, Assam, India has been presented. For this, the single-objective and multi-objective optimization approaches have been formulated. The basic goal behind these optimization approaches to minimize the cost of deployment of the HRS. Both the optimization problems have been solved using the real-time data of the intercity railway traffic of NEFR, Assam, India as the input, and binary PSO based solution algorithms. Investigation on the HRS infrastructure planning shows that a HRS of lower capacity requires frequent refuelling, and vice-versa. Likewise, the frequency and the cost of refuelling of the HRS reduce with the increase in the number of HRS installed in a given layout of potential railway sites. On the contrary, the capital and maintenance costs increase with the capacity and the number of HRS. Thus, the capital and maintenance cost of the HRS and the cost of HRS refueling conflict each other in terms of their variation with the number and the capacity of the HRS. In view of this, the proposed multi-objective optimization approach provides the Pareto optimal set of solutions with different combinations of the HRS layout from which a planner can selected a solution based on the budget of capital and operational expenditures.

There are many practical aspects related to the use of PEMFC-battery-HES in locomotive applications which need to be investigated in future. The present study has been carried out assuming that the size and weight of the PEMFC-battery-HES powered locomotives are similar to that of the diesel locomotive class, WDM-3D. In Chapter 2, the ratings of the PEMFC and battery have been optimized so as to minimize the total cost of the HES. However, the location of the hybrid energy sources on the locomotive is a big concern as it increases the weight and drag of the train. Besides, although hydrogen is important as a new source of energy, it is clear that the key challenge in developing the hydrogen fueled technologies is its storage. This is because the hydrogen is a highly inflammable gas that requires it being handled with great care. Hence, the storage and safety concerns of hydrogen needs thorough investigation. In [159]–[161], the authors review the various storage methods for hydrogen. These methods can be sub-categorized into physical based storage and material based hydrogen storage. Examples of physical based storage include the high-pressure gas cylinders, liquid hydrogen in cryogenic tanks, etc. Examples of the material based hydrogen storage are the physical sorption of hydrogen on materials with a large specific surface area, chemical sorption of hydrogen on interstitial sites in a host metal, chemically bonded in covalent and ionic compounds, etc. Besides, the authors also highlight the potential for improvement and the physical limitations in each of the aforementioned hydrogen storage methods for on-board applications in [159]–[161]. In [162], the authors present a review of hydrogen storage systems that are relevant for mobility applications. The authors mention that the high-pressure compressed gas cylinders are by-far the most feasible storage option for mobility applications as compared to other technologies. Furthermore, the FC applications generally require adequate performance to be maintained over long periods of time. The U.S. Department of Energy [109] has set ultimate targets for FC system lifetime at 8,000 hours for light-duty vehicles, 30000 hours for heavy-duty trucks, and 80000 hours for distributed power systems. To achieve this target, it is very crucial to understand the mechanisms related to FC degradation and to develop methods that can mitigate these problems. However, the PEMFC durability has not been studied in the present thesis. Besides, in Chapter 3, the performances of the PWM control approaches have been tested for the implementation of a simple rule-based EMS. The experimental verification of the competence of the proposed PWM control approaches for the real-time implementation of the EMO approaches that are developed in Chapter 4 needs to be carried out. Keeping this in mind, some of the studies to be included as a future extension of the present work are mentioned below:

- ***Combined DO and EMO for the PEMFC-battery-HES***: In Chapter 2, the DO problem has been formulated in order to minimise the capital and operational costs of the HES. The optimization of the size and weight of the HES driven locomotive including the storage of hydrogen have not been carried out. These factors translate into the design needs for the PEMFC-battery-HES driven locomotives. In view of this, the combined DO and EMO problem of the HES needs to be formulated in order to optimise its size, weight and the storage of hydrogen fuel besides minimising the capital and operational costs of the PEMFC-battery-HES powered locomotives.

- ***Experimental verification of the EMO approaches as online optimization***: In chapter 4, the proposed EMO approaches have been implemented as offline optimization processes, i.e., the distribution of the load in the PEMFC-battery-HES is done by the EMO approaches for some pre-defined or predicted drive cycle scenarios of intercity passenger trains operating in Indian railways. The online execution of the EMO approaches for the real-time optimal load dispatch to the energy sources is also possible, and has been discussed in section 4.5. However, the performance analysis of the proposed EMO approaches as online optimization processes on a real-time hardware setup of the PEMFC-battery-HES has not been carried out. Hence, the same needs to be investigated.

- ***EMO considering the durability model of the PEMFC***: The EMO2 approach proposed in chapter 4 has been developed considering the durability model of the battery alone. However, similar to the battery, the PEMFC's performance also tends to deteriorate gradually during its lifetime. This is due to the various physical and chemical changes which take place with usage and with age until eventually the PEMFC is no longer usable. Hence, the modelling of the PEMFC's *SOH* in terms of the depletion in the active cell area of the PEMFC is required. Moreover, the proposed EMO2 approach can be reformulated to incorporate the PEMFC durability model, and its performance can be tested for both offline/online energy management in the PEMFC-battery-HES for locomotive applications.

- ***Use of SC-battery as ESS in the PEMFC based HES*****:** In this thesis, the DO, EMO and control of the PEMFC-battery-HES powered locomotives have been addressed so far. However, besides the battery, the SC also provides a promising performance for use an ESS. Hence, in the future work, the SC can be integrated in the HES to form a PEMFC-battery-SC-HES. The problems of DO, EMO, and control of the PEMFC-battery-SC-HES can be investigated for locomotive applications. Moreover, a quantitative comparison between the two PEMFC based HES topologies, i.e. the PEMFC-battery and PEMFC-battery-SC can also be carried out in terms of the capital and operational expenditures.

Bibliography

[1] F. Barbir, *PEM Fuel Cells: Theory and Practice*, Second. Elsevier Inc., 2013.

[2] G. Pede, A. Iacobazzi, S. Passerini, A. Bobbio, and G. Botto, “FC vehicle hybridisation: an affordable solution for an energy-efficient FC powered drive train,” *Journal of Power Sources*, vol. 125, no. 2, pp. 280–291, Jan. 2004, doi: 10.1016/j.jpowsour.2003.07.018.

[3] H. T. Yap, N. Schofield, and C. M. Bingham, “Hybrid energy/power sources for electric vehicle traction systems,” in *Second International Conference on Power Electronics, Machines and Drives (PEMD 2004).*, Mar. 2004, vol. 1, pp. 61-66 Vol.1. doi: 10.1049/cp:20040260.

[4] D. Feroldi, M. Serra, and J. Riera, “Design and Analysis of Fuel-Cell Hybrid Systems Oriented to Automotive Applications,” *IEEE Transactions on Vehicular Technology*, vol. 58, no. 9, pp. 4720–4729, Nov. 2009, doi: 10.1109/TVT.2009.2027241.

[5] Y. Guezennec, Ta-Young Choi, G. Paganelli, and G. Rizzoni, “Supervisory control of fuel cell vehicles and its link to overall system efficiency and low-level control requirements,” in *Proceedings of the 2003 American Control Conference, 2003.*, Jun. 2003, vol. 3, pp. 2055–2061 vol.3. doi: 10.1109/ACC.2003.1243377.

[6] W. Zhang, J. Li, L. Xu, and M. Ouyang, “Optimization for a fuel cell/battery/capacity tram with equivalent consumption minimization strategy,” *Energy Conversion and Management*, vol. 134, pp. 59–69, Feb. 2017, doi: 10.1016/j.enconman.2016.11.007.

[7] X. Wang, F. Peng, D. Wang, and X. Li, “Development of a hydrogen consumption optimization based dynamic penalty control strategy for a PEMFC-LIB-SC hybrid tramway,” in *2017 IEEE Conference on Energy Internet and Energy System Integration (EI2)*, Nov. 2017, pp. 1–6. doi: 10.1109/EI2.2017.8245382.

[8] P. Garcia, L. M. Fernandez, C. A. Garcia, and F. Jurado, “Energy Management System of Fuel-Cell-Battery Hybrid Tramway,” *IEEE Transactions on Industrial Electronics*, vol. 57, no. 12, pp. 4013–4023, Dec. 2010, doi: 10.1109/TIE.2009.2034173.

[9] P. J. Corral-Vega, P. García-Triviño, and L. M. Fernández-Ramírez, “Design, modelling, control and techno-economic evaluation of a fuel cell/supercapacitors powered container crane,” *Energy*, vol. 186, p. 115863, Nov. 2019, doi: 10.1016/j.energy.2019.115863.

[10] W. Andari, M. S. B. YAHIA, H. Allagui, and A. Mami, “Modeling and Simulation of PEM Fuel Cell/Supercapacitor hybrid power sources for an electric vehicle,” in *2019 10th International Renewable Energy Congress (IREC)*, Mar. 2019, pp. 1–6. doi: 10.1109/IREC.2019.8754584.

[11] A. Tahri *et al.*, “Management of fuel cell power and supercapacitor state-of-charge for electric vehicles,” *Electric Power Systems Research*, vol. 160, pp. 89–98, Jul. 2018, doi: 10.1016/j.epsr.2018.02.003.

[12] G. Napoli, S. Micari, G. Dispenza, S. Di Novo, V. Antonucci, and L. Andaloro, “Development of a fuel cell hybrid electric powertrain: A real case study on a Minibus application,” *International Journal of Hydrogen Energy*, vol. 42, no. 46, pp. 28034–28047, Nov. 2017, doi: 10.1016/j.ijhydene.2017.07.239.

[13] A. Behdani and M. R. Naseh, “Power management and nonlinear control of a fuel cell–supercapacitor hybrid automotive vehicle with working condition algorithm,” *International Journal of Hydrogen Energy*, vol. 42, no. 38, pp. 24347–24357, Sep. 2017, doi: 10.1016/j.ijhydene.2017.07.197.

[14] F.-C. Wang and W.-H. Fang, “The development of a PEMFC hybrid power electric vehicle with automatic sodium borohydride hydrogen generation,” *International Journal of Hydrogen Energy*, vol. 42, no. 15, pp. 10376–10389, Apr. 2017, doi: 10.1016/j.ijhydene.2017.03.040.

[15] D. Gao, Z. Jin, J. Zhang, J. Li, and M. Ouyang, “Development and performance analysis of a hybrid fuel cell/battery bus with an axle integrated electric motor drive system,” *International Journal of Hydrogen Energy*, vol. 41, no. 2, pp. 1161–1169, Jan. 2016, doi: 10.1016/j.ijhydene.2015.10.046.

[16] Z. Mokrani, D. Rekioua, N. Mebarki, T. Rekioua, and S. Bacha, “Energy management of battery-PEM Fuel cells Hybrid energy storage system for electric vehicle,” in *2016 International Renewable and Sustainable Energy Conference (IRSEC)*, Nov. 2016, pp. 985–990. doi: 10.1109/IRSEC.2016.7984073.

[17] H. Aouzellag, K. Ghedamsi, and D. Aouzellag, “Energy management and fault tolerant control strategies for fuel cell/ultra-capacitor hybrid electric vehicles to enhance autonomy, efficiency and life time of the fuel cell system,” *International Journal of Hydrogen Energy*, vol. 40, no. 22, pp. 7204–7213, Jun. 2015, doi: 10.1016/j.ijhydene.2015.03.132.

[18] V. Roda, J. Carroquino, L. Valiño, A. Lozano, and F. Barreras, “Remodeling of a commercial plug-in battery electric vehicle to a hybrid configuration with a PEM fuel cell,” *International Journal of Hydrogen Energy*, vol. 43, no. 35, pp. 16959–16970, Aug. 2018, doi: 10.1016/j.ijhydene.2017.12.171.

[19] N. Mebarki, T. Rekioua, Z. Mokrani, D. Rekioua, and S. Bacha, "PEM fuel cell/ battery storage system supplying electric vehicle," *International Journal of Hydrogen Energy*, vol. 41, no. 45, pp. 20993–21005, Dec. 2016, doi: 10.1016/j.ijhydene.2016.05.208.

[20] H. Fathabadi, "Novel fuel cell/battery/supercapacitor hybrid power source for fuel cell hybrid electric vehicles," *Energy*, vol. 143, pp. 467–477, Jan. 2018, doi: 10.1016/j.energy.2017.10.107.

[21] I. Lachhab and L. Krichen, "An improved energy management strategy for FC/UC hybrid electric vehicles propelled by motor-wheels," *International Journal of Hydrogen Energy*, vol. 39, no. 1, pp. 571–581, Jan. 2014, doi: 10.1016/j.ijhydene.2013.10.064.

[22] L. Xu, J. Li, J. Hua, X. Li, and M. Ouyang, "Adaptive supervisory control strategy of a fuel cell/battery-powered city bus," *Journal of Power Sources*, vol. 194, no. 1, pp. 360–368, Oct. 2009, doi: 10.1016/j.jpowsour.2009.04.074.

[23] D. Bouquain, B. Blunier, and A. Miraoui, "A hybrid fuel cell/battery wheelchair — modeling, simulation and experimentation," in *2008 IEEE Vehicle Power and Propulsion Conference*, Sep. 2008, pp. 1–6. doi: 10.1109/VPPC.2008.4677671.

[24] P. Thounthong, S. Raël, B. Davat, and I. Sadli, "A control strategy of fuel cell/battery hybrid power source for electric vehicle applications," in *2006 37th IEEE Power Electronics Specialists Conference*, Jun. 2006, pp. 1–7. doi: 10.1109/pesc.2006.1712067.

[25] M. Ouyang, L. Xu, J. Li, L. Lu, D. Gao, and Q. Xie, "Performance comparison of two fuel cell hybrid buses with different powertrain and energy management strategies," *Journal of Power Sources*, vol. 163, no. 1, pp. 467–479, Dec. 2006, doi: 10.1016/j.jpowsour.2006.09.033.

[26] B. Allaoua, K. Asnoune, and B. Mebarki, "Energy management of PEM fuel cell/ supercapacitor hybrid power sources for an electric vehicle," *International Journal of Hydrogen Energy*, vol. 42, no. 33, pp. 21158–21166, Aug. 2017, doi: 10.1016/j.ijhydene.2017.06.209.

[27] W. Wu, J. S. Partridge, and R. W. G. Bucknall, "Stabilised control strategy for PEM fuel cell and supercapacitor propulsion system for a city bus," *International Journal of Hydrogen Energy*, vol. 43, no. 27, pp. 12302–12313, Jul. 2018, doi: 10.1016/j.ijhydene.2018.04.114.

[28] L. Andaloro, G. Napoli, F. Sergi, G. Dispenza, and V. Antonucci, "Design of a hybrid electric fuel cell power train for an urban bus," *International Journal of Hydrogen Energy*, vol. 38, no. 18, pp. 7725–7732, Jun. 2013, doi: 10.1016/j.ijhydene.2012.08.116.

[29] D. F. Pereira, F. D. C. Lopes, and E. H. Watanabe, "Nonlinear Model Predictive Control for the Energy Management of Fuel Cell Hybrid Electric Vehicles in Real-Time," *IEEE Transactions on Industrial Electronics*, pp. 1–1, 2020, doi: 10.1109/TIE.2020.2979528.

[30] J. P. Torreglosa, P. García, L. M. Fernández, and F. Jurado, “Predictive Control for the Energy Management of a Fuel-Cell–Battery–Supercapacitor Tramway,” *IEEE Transactions on Industrial Informatics*, vol. 10, no. 1, pp. 276–285, Feb. 2014, doi: 10.1109/TII.2013.2245140.

[31] J. Chen and Q. Song, “A Decentralized Energy Management Strategy for a Fuel Cell/Supercapacitor-Based Auxiliary Power Unit of a More Electric Aircraft,” *IEEE Transactions on Industrial Electronics*, vol. 66, no. 7, pp. 5736–5747, Jul. 2019, doi: 10.1109/TIE.2018.2866042.

[32] B. Amrouche, T. Otmane Cherif, M. Ghanes, and K. Iffouzar, “A passivity-based controller for coordination of converters in a fuel cell system used in hybrid electric vehicle propelled by two seven phase induction motor,” *International Journal of Hydrogen Energy*, vol. 42, no. 42, pp. 26362–26376, Oct. 2017, doi: 10.1016/j.ijhydene.2017.08.099.

[33] H. Zhang, X. Li, X. Liu, and J. Yan, “Enhancing fuel cell durability for fuel cell plug-in hybrid electric vehicles through strategic power management,” *Applied Energy*, vol. 241, pp. 483–490, May 2019, doi: 10.1016/j.apenergy.2019.02.040.

[34] K. Ettihir, M. Higuita Cano, L. Boulon, and K. Agbossou, “Design of an adaptive EMS for fuel cell vehicles,” *International Journal of Hydrogen Energy*, vol. 42, no. 2, pp. 1481–1489, Jan. 2017, doi: 10.1016/j.ijhydene.2016.07.211.

[35] Y. Wang, Z. Sun, and Z. Chen, “Energy management strategy for battery/supercapacitor/fuel cell hybrid source vehicles based on finite state machine,” *Applied Energy*, vol. 254, p. 113707, Nov. 2019, doi: 10.1016/j.apenergy.2019.113707.

[36] L. M. Fernandez, P. Garcia, C. A. Garcia, and F. Jurado, “Hybrid electric system based on fuel cell and battery and integrating a single dc/dc converter for a tramway,” *Energy Conversion and Management*, vol. 52, no. 5, pp. 2183–2192, May 2011, doi: 10.1016/j.enconman.2010.12.028.

[37] S. Ramy, A. Hatem, and A. Mami, “Study and design of a power management system using two-stage controller for PEM fuel cell vehicles,” in *2016 7th International Renewable Energy Congress (IREC)*, Mar. 2016, pp. 1–6. doi: 10.1109/IREC.2016.7478904.

[38] Y. B. Kim and S. J. Kang, “Time delay control for fuel cells with bidirectional DC/DC converter and battery,” *International Journal of Hydrogen Energy*, vol. 35, no. 16, pp. 8792–8803, Aug. 2010, doi: 10.1016/j.ijhydene.2010.05.022.

[39] Y. Tang, W. Yuan, M. Pan, and Z. Wan, “Experimental investigation on the dynamic performance of a hybrid PEM fuel cell/battery system for lightweight electric vehicle application,” *Applied Energy*, vol. 88, no. 1, pp. 68–76, Jan. 2011, doi: 10.1016/j.apenergy.2010.07.033.

[40] Z. Yu, D. Zinger, and A. Bose, “An innovative optimal power allocation strategy for fuel cell, battery and supercapacitor hybrid electric vehicle,” *Journal of Power Sources*, vol. 196, no. 4, pp. 2351–2359, Feb. 2011, doi: 10.1016/j.jpowsour.2010.09.057.

[41] A. A. Ferreira, J. A. Pomilio, G. Spiazzi, and L. de A. Silva, "Energy Management Fuzzy Logic Supervisory for Electric Vehicle Power Supplies System," *IEEE Transactions on Power Electronics*, vol. 23, no. 1, pp. 107–115, Jan. 2008, doi: 10.1109/TPEL.2007.911799.

[42] K.-S. Jeong, W.-Y. Lee, and C.-S. Kim, "Energy management strategies of a fuel cell/battery hybrid system using fuzzy logics," *Journal of Power Sources*, vol. 145, no. 2, pp. 319–326, Aug. 2005, doi: 10.1016/j.jpowsour.2005.01.076.

[43] M. Tekin, D. Hissel, M.-C. Pera, and J. M. Kauffmann, "Energy-Management Strategy for Embedded Fuel-Cell Systems Using Fuzzy Logic," *IEEE Trans. Ind. Electron.*, vol. 54, no. 1, pp. 595–603, Feb. 2007, doi: 10.1109/TIE.2006.885471.

[44] Xiangjun Li, Liangfei Xu, Jianfeng Hua, Jianqiu Li, and Minggao Ouyang, "Control algorithm of fuel cell/battery hybrid vehicular power system," in *2008 IEEE Vehicle Power and Propulsion Conference*, Sep. 2008, pp. 1–6. doi: 10.1109/VPPC.2008.4677613.

[45] D. Gao, Z. Jin, and Q. Lu, "Energy management strategy based on fuzzy logic for a fuel cell hybrid bus," *Journal of Power Sources*, vol. 185, no. 1, pp. 311–317, Oct. 2008, doi: 10.1016/j.jpowsour.2008.06.083.

[46] Q. Li, W. Chen, Y. Li, S. Liu, and J. Huang, "Energy management strategy for fuel cell/battery/ultracapacitor hybrid vehicle based on fuzzy logic," *International Journal of Electrical Power & Energy Systems*, vol. 43, no. 1, pp. 514–525, Dec. 2012, doi: 10.1016/j.ijepes.2012.06.026.

[47] G. Zhang, W. Chen, and Q. Li, "Modeling, optimization and control of a FC/battery hybrid locomotive based on ADVISOR," *International Journal of Hydrogen Energy*, vol. 42, no. 29, pp. 18568–18583, Jul. 2017, doi: 10.1016/j.ijhydene.2017.04.172.

[48] J.-J. Hwang, J.-S. Hu, and C.-H. Lin, "Design of a range extension strategy for power decentralized fuel cell/battery electric vehicles," *International Journal of Hydrogen Energy*, vol. 40, no. 35, pp. 11704–11712, Sep. 2015, doi: 10.1016/j.ijhydene.2015.04.026.

[49] C. Xie, X. Xu, P. Bujlo, D. Shen, H. Zhao, and S. Quan, "Fuel cell and lithium iron phosphate battery hybrid powertrain with an ultracapacitor bank using direct parallel structure," *Journal of Power Sources*, vol. 279, pp. 487–494, Apr. 2015, doi: 10.1016/j.jpowsour.2015.01.029.

[50] O. Erdinc, B. Vural, and M. Uzunoglu, "A wavelet-fuzzy logic based energy management strategy for a fuel cell/battery/ultra-capacitor hybrid vehicular power system," *Journal of Power Sources*, vol. 194, no. 1, pp. 369–380, Oct. 2009, doi: 10.1016/j.jpowsour.2009.04.072.

[51] Q. Li, W. Chen, Z. Liu, M. Li, and L. Ma, "Development of energy management system based on a power sharing strategy for a fuel cell-battery-supercapacitor hybrid tramway," *Journal of Power Sources*, vol. 279, pp. 267–280, Apr. 2015, doi: 10.1016/j.jpowsour.2014.12.042.

[52] W. Obaid, A. Hamid, and C. Ghenai, “Hybrid PEM Fuel-Cell-Solar Power System Design for Electric Boat with MPPT System and Fuzzy Energy Management,” in *2019 International Conference on Communications, Signal Processing, and their Applications (ICCSPA)*, Mar. 2019, pp. 1–7. doi: 10.1109/ICCSPA.2019.8713646.

[53] K. Simmons, Y. Guezennec, and S. Onori, “Modeling and energy management control design for a fuel cell hybrid passenger bus,” *Journal of Power Sources*, vol. 246, pp. 736–746, Jan. 2014, doi: 10.1016/j.jpowsour.2013.08.019.

[54] N. P. Reddy, D. Pasdeloup, M. K. Zadeh, and R. Skjetne, “An Intelligent Power and Energy Management System for Fuel Cell/Battery Hybrid Electric Vehicle Using Reinforcement Learning,” in *2019 IEEE Transportation Electrification Conference and Expo (ITEC)*, Jun. 2019, pp. 1–6. doi: 10.1109/ITEC.2019.8790451.

[55] W.-S. Lin and C.-H. Zheng, “Energy management of a fuel cell/ultracapacitor hybrid power system using an adaptive optimal-control method,” *Journal of Power Sources*, vol. 196, no. 6, pp. 3280–3289, Mar. 2011, doi: 10.1016/j.jpowsour.2010.11.127.

[56] L. Xu, M. Ouyang, J. Li, F. Yang, L. Lu, and J. Hua, “Optimal sizing of plug-in fuel cell electric vehicles using models of vehicle performance and system cost,” *Applied Energy*, vol. 103, pp. 477–487, Mar. 2013, doi: 10.1016/j.apenergy.2012.10.010.

[57] X. Liu, D. Diallo, and C. Marchand, “Design methodology of fuel cell electric vehicle power system,” in *2008 18th International Conference on Electrical Machines*, Sep. 2008, pp. 1–6. doi: 10.1109/ICELMACH.2008.4800034.

[58] O. Hegazy and J. V. Mierlo, “Particle Swarm Optimization for optimal powertrain component sizing and design of fuel cell hybrid electric vehicle,” in *2010 12th International Conference on Optimization of Electrical and Electronic Equipment*, May 2010, pp. 601–609. doi: 10.1109/OPTIM.2010.5510447.

[59] M. Jain, C. Desai, N. Kharma, and S. S. Williamson, “Optimal powertrain component sizing of a fuel cell plug-in hybrid electric vehicle using multi-objective genetic algorithm,” in *2009 35th Annual Conference of IEEE Industrial Electronics*, Nov. 2009, pp. 3741–3746. doi: 10.1109/IECON.2009.5415111.

[60] J. Bauman and M. Kazerani, “An Analytical Optimization Method for Improved Fuel Cell–Battery–Ultracapacitor Powertrain,” *IEEE Transactions on Vehicular Technology*, vol. 58, no. 7, pp. 3186–3197, Sep. 2009, doi: 10.1109/TVT.2009.2014843.

[61] J. Lopes, J. A. Pomilio, and P. A. V. Ferreira, “Optimal sizing of batteries and ultracapacitors for fuel cell electric vehicles,” in *IECON 2011 - 37th Annual Conference of the IEEE Industrial Electronics Society*, Nov. 2011, pp. 4603–4608. doi: 10.1109/IECON.2011.6120068.

[62] Y. Wu and H. Gao, “Optimization of Fuel Cell and Supercapacitor for Fuel-Cell Electric Vehicles,” *IEEE Transactions on Vehicular Technology*, vol. 55, no. 6, pp. 1748–1755, Nov. 2006, doi: 10.1109/TVT.2006.883764.

[63] A. R. Miller and J. Peters, “Fuelcell hybrid locomotives: applications and benefits,” in *Proceedings of the 2006 IEEE/ASME Joint Rail Conference*, Apr. 2006, pp. 287–293. doi: 10.1109/RRCON.2006.215320.

[64] M. Kim, Y.-J. Sohn, W.-Y. Lee, and C.-S. Kim, “Fuzzy control based engine sizing optimization for a fuel cell/battery hybrid mini-bus,” *Journal of Power Sources*, vol. 178, no. 2, pp. 706–710, Apr. 2008, doi: 10.1016/j.jpowsour.2007.12.047.

[65] R. T. Doucette and M. D. McCulloch, “A comparison of high-speed flywheels, batteries, and ultracapacitors on the bases of cost and fuel economy as the energy storage system in a fuel cell based hybrid electric vehicle,” *Journal of Power Sources*, vol. 196, no. 3, pp. 1163–1170, Feb. 2011, doi: 10.1016/j.jpowsour.2010.08.100.

[66] F. Odeim, J. Roes, and A. Heinzel, “Power Management Optimization of a Fuel Cell/Battery/Supercapacitor Hybrid System for Transit Bus Applications,” *IEEE Transactions on Vehicular Technology*, vol. 65, no. 7, pp. 5783–5788, Jul. 2016, doi: 10.1109/TVT.2015.2456232.

[67] C. Li, G. Zheng, and G. Liu, “A real-time optimization control strategy for power management in fuel cell/battery hybrid power sources,” in *Proceedings of 2012 UKACC International Conference on Control*, Sep. 2012, pp. 845–850. doi: 10.1109/CONTROL.2012.6334742.

[68] N. Marx, D. Hissel, F. Gustin, L. Boulon, and K. Agbossou, “On the sizing and energy management of an hybrid multistack fuel cell – Battery system for automotive applications,” *International Journal of Hydrogen Energy*, vol. 42, no. 2, pp. 1518–1526, Jan. 2017, doi: 10.1016/j.ijhydene.2016.06.111.

[69] J. Bernard, S. Delprat, F. Buechi, and T. M. Guerra, “Global Optimisation in the power management of a Fuel Cell Hybrid Vehicle (FCHV),” in *2006 IEEE Vehicle Power and Propulsion Conference*, Sep. 2006, pp. 1–6. doi: 10.1109/VPPC.2006.364289.

[70] V. Paladini, T. Donateo, A. de Risi, and D. Laforgia, “Super-capacitors fuel-cell hybrid electric vehicle optimization and control strategy development,” *Energy Conversion and Management*, vol. 48, no. 11, pp. 3001–3008, Nov. 2007, doi: 10.1016/j.enconman.2007.07.014.

[71] L. Xu, F. Yang, J. Li, M. Ouyang, and J. Hua, “Real time optimal energy management strategy targeting at minimizing daily operation cost for a plug-in fuel cell city bus,” *International Journal of Hydrogen Energy*, vol. 37, no. 20, pp. 15380–15392, Oct. 2012, doi: 10.1016/j.ijhydene.2012.07.074.

[72] S. Ahmadi and S. M. T. Bathaee, “Multi-objective genetic optimization of the fuel cell hybrid vehicle supervisory system: Fuzzy logic and operating mode control strategies,” *International Journal of Hydrogen Energy*, vol. 40, no. 36, pp. 12512–12521, Sep. 2015, doi: 10.1016/j.ijhydene.2015.06.160.

[73] L. Xu, M. Ouyang, J. Li, F. Yang, L. Lu, and J. Hua, “Application of Pontryagin’s Minimal Principle to the energy management strategy of plugin fuel cell electric vehicles,” *International Journal of Hydrogen Energy*, vol. 38, no. 24, pp. 10104–10115, Aug. 2013, doi: 10.1016/j.ijhydene.2013.05.125.

[74] Q. Li, W. Huang, W. Chen, Y. Yan, W. Shang, and M. Li, “Regenerative braking energy recovery strategy based on Pontryagin’s minimum principle for fell cell/supercapacitor hybrid locomotive,” *International Journal of Hydrogen Energy*, vol. 44, no. 11, pp. 5454–5461, Feb. 2019, doi: 10.1016/j.ijhydene.2018.10.115.

[75] F. Odeim, J. Roes, L. Wülbeck, and A. Heinzel, “Power management optimization of fuel cell/battery hybrid vehicles with experimental validation,” *Journal of Power Sources*, vol. 252, pp. 333–343, Apr. 2014, doi: 10.1016/j.jpowsour.2013.12.012.

[76] K. Ettihir, L. Boulon, and K. Agbossou, “Optimization-based energy management strategy for a fuel cell/battery hybrid power system,” *Applied Energy*, vol. 163, pp. 142–153, Feb. 2016, doi: 10.1016/j.apenergy.2015.10.176.

[77] T. Fletcher, R. Thring, and M. Watkinson, “An Energy Management Strategy to concurrently optimise fuel consumption & PEM fuel cell lifetime in a hybrid vehicle,” *International Journal of Hydrogen Energy*, vol. 41, no. 46, pp. 21503–21515, Dec. 2016, doi: 10.1016/j.ijhydene.2016.08.157.

[78] N. Bizon, “Real-time optimization strategies of Fuel Cell Hybrid Power Systems based on Load-following control: A new strategy, and a comparative study of topologies and fuel economy obtained,” *Applied Energy*, vol. 241, pp. 444–460, May 2019, doi: 10.1016/j.apenergy.2019.03.026.

[79] S. Kelouwani, K. Agbossou, Y. Dubé, and L. Boulon, “Fuel cell Plug-in Hybrid Electric Vehicle anticipatory and real-time blended-mode energy management for battery life preservation,” *Journal of Power Sources*, vol. 221, pp. 406–418, Jan. 2013, doi: 10.1016/j.jpowsour.2012.08.016.

[80] R. Álvarez Fernández, S. Corbera Caraballo, F. Beltrán Cilleruelo, and J. A. Lozano, “Fuel optimization strategy for hydrogen fuel cell range extender vehicles applying genetic algorithms,” *Renewable and Sustainable Energy Reviews*, vol. 81, pp. 655–668, Jan. 2018, doi: 10.1016/j.rser.2017.08.047.

[81] Z. Sun, Y. Wang, Z. Chen, and X. Li, “Min-max game based energy management strategy for fuel cell/supercapacitor hybrid electric vehicles,” *Applied Energy*, vol. 267, p. 115086, Jun. 2020, doi: 10.1016/j.apenergy.2020.115086.

[82] N. Bizon and P. Thounthong, “Real-time strategies to optimize the fueling of the fuel cell hybrid power source: A review of issues, challenges and a new approach,” *Renewable and Sustainable Energy Reviews*, vol. 91, pp. 1089–1102, Aug. 2018, doi: 10.1016/j.rser.2018.04.045.

[83] A. Chauvin, A. Hijazi, E. Bideaux, and A. Sari, “Cost Optimization for Plug-In Integration in a Hybrid Electric Mini-Excavator with Mixed-Integer Linear Programming,” in *2015 IEEE Vehicle Power and Propulsion Conference (VPPC)*, Oct. 2015, pp. 1–6. doi: 10.1109/VPPC.2015.7352923.

[84] A. Chauvin, A. Hijazi, E. Bideaux, and A. Sari, “Combinatorial approach for sizing and optimal energy management of HEV including durability constraints,” in *2015 IEEE 24th International Symposium on Industrial Electronics (ISIE)*, Jun. 2015, pp. 1236–1241. doi: 10.1109/ISIE.2015.7281649.

[85] M.-J. Kim and H. Peng, “Power management and design optimization of fuel cell/battery hybrid vehicles,” *Journal of Power Sources*, vol. 165, no. 2, pp. 819–832, Mar. 2007, doi: 10.1016/j.jpowsour.2006.12.038.

[86] M. Jain, C. Desai, and S. S. Williamson, “Genetic algorithm based optimal powertrain component sizing and control strategy design for a fuel cell hybrid electric bus,” in *2009 IEEE Vehicle Power and Propulsion Conference*, Sep. 2009, pp. 980–985. doi: 10.1109/VPPC.2009.5289740.

[87] A. Ravey, R. Roche, B. Blunier, and A. Miraoui, “Combined optimal sizing and energy management of hybrid electric vehicles,” in *2012 IEEE Transportation Electrification Conference and Expo (ITEC)*, Jun. 2012, pp. 1–6. doi: 10.1109/ITEC.2012.6243420.

[88] B. Geng, J. K. Mills, and D. Sun, “Combined power management/design optimization for a fuel cell/battery plug-in hybrid electric vehicle using multi-objective particle swarm optimization,” *Int.J Automot. Technol.*, vol. 15, no. 4, pp. 645–654, Jun. 2014, doi: 10.1007/s12239-014-0067-x.

[89] J. Bernard, S. Delprat, F. N. Buchi, and T. M. Guerra, “Fuel-Cell Hybrid Powertrain: Toward Minimization of Hydrogen Consumption,” *IEEE Transactions on Vehicular Technology*, vol. 58, no. 7, pp. 3168–3176, Sep. 2009, doi: 10.1109/TVT.2009.2014684.

[90] R. K. Sharma and S. Mishra, “Dynamic Power Management and Control of a PV PEM Fuel-Cell-Based Standalone ac/dc Microgrid Using Hybrid Energy Storage,” *IEEE Transactions on Industry Applications*, vol. 54, no. 1, pp. 526–538, Jan. 2018, doi: 10.1109/TIA.2017.2756032.

[91] L. Valverde, C. Bordons, and F. Rosa, “Integration of Fuel Cell Technologies in Renewable-Energy-Based Microgrids Optimizing Operational Costs and Durability,” *IEEE Transactions on Industrial Electronics*, vol. 63, no. 1, pp. 167–177, Jan. 2016, doi: 10.1109/TIE.2015.2465355.

[92] A. Kafetzis, C. Ziogou, K. D. Panopoulos, S. Papadopoulou, P. Seferlis, and S. Voutetakis, “Energy management strategies based on hybrid automata for islanded microgrids with renewable sources, batteries and hydrogen,” *Renewable and Sustainable Energy Reviews*, vol. 134, p. 110118, Dec. 2020, doi: 10.1016/j.rser.2020.110118.

[93] H. Fathabadi, “Novel standalone hybrid solar/wind/fuel cell/battery power generation system,” *Energy*, vol. 140, pp. 454–465, Dec. 2017, doi: 10.1016/j.energy.2017.08.098.

[94] A. Maleki and F. Pourfayaz, “Sizing of stand-alone photovoltaic/wind/diesel system with battery and fuel cell storage devices by harmony search algorithm,” *Journal of Energy Storage*, vol. 2, pp. 30–42, Aug. 2015, doi: 10.1016/j.est.2015.05.006.

[95] A. Maleki and A. Askarzadeh, “Comparative study of artificial intelligence techniques for sizing of a hydrogen-based stand-alone photovoltaic/wind hybrid system,” *International Journal of Hydrogen Energy*, vol. 39, no. 19, pp. 9973–9984, Jun. 2014, doi: 10.1016/j.ijhydene.2014.04.147.

[96] S. M. Hakimi and S. M. Moghaddas-Tafreshi, “Optimal sizing of a stand-alone hybrid power system via particle swarm optimization for Kahnouj area in south-east of Iran,” *Renewable Energy*, vol. 34, no. 7, pp. 1855–1862, Jul. 2009, doi: 10.1016/j.renene.2008.11.022.

[97] A. Maleki and M. A. Rosen, “Design of a cost-effective on-grid hybrid wind–hydrogen based CHP system using a modified heuristic approach,” *International Journal of Hydrogen Energy*, vol. 42, no. 25, pp. 15973–15989, Jun. 2017, doi: 10.1016/j.ijhydene.2017.01.169.

[98] B. Li, R. Roche, D. Paire, and A. Miraoui, “Sizing of a stand-alone microgrid considering electric power, cooling/heating, hydrogen loads and hydrogen storage degradation,” *Applied Energy*, vol. 205, pp. 1244–1259, Nov. 2017, doi: 10.1016/j.apenergy.2017.08.142.

[99] A. Maleki, “Design and optimization of autonomous solar-wind-reverse osmosis desalination systems coupling battery and hydrogen energy storage by an improved bee algorithm,” *Desalination*, vol. 435, pp. 221–234, Jun. 2018, doi: 10.1016/j.desal.2017.05.034.

[100] L. Bartolucci, S. Cordiner, V. Mulone, and S. Pasquale, “Fuel cell based hybrid renewable energy systems for off-grid telecom stations: Data analysis and system optimization,” *Applied Energy*, vol. 252, p. 113386, Oct. 2019, doi: 10.1016/j.apenergy.2019.113386.

[101] M. Y. El-Sharkh, M. Tanrioven, A. Rahman, and M. S. Alam, “Impact of hydrogen production on optimal economic operation of a grid-parallel PEM fuel cell power plant,” *Journal of Power Sources*, vol. 153, no. 1, pp. 136–144, Jan. 2006, doi: 10.1016/j.jpowsour.2005.03.187.

[102] M. Y. El-Sharkh, A. Rahman, and M. S. Alam, “Evolutionary programming-based methodology for economical output power from PEM fuel cell for micro-grid application,” *Journal of Power Sources*, vol. 139, no. 1, pp. 165–169, Jan. 2005, doi: 10.1016/j.jpowsour.2004.07.011.

[103] R. Dufo-López, J. L. Bernal-Agustín, and J. Contreras, “Optimization of control strategies for stand-alone renewable energy systems with hydrogen storage,” *Renewable Energy*, vol. 32, no. 7, pp. 1102–1126, Jun. 2007, doi: 10.1016/j.renene.2006.04.013.

[104] T. Yalcinoz and M. S. Alam, “Improved dynamic performance of hybrid PEM fuel cells and ultracapacitors for portable applications,” *International Journal of Hydrogen Energy*, vol. 33, no. 7, pp. 1932–1940, Apr. 2008, doi: 10.1016/j.ijhydene.2008.01.027.

[105] C. A. Ramos-Paja, A. Romero, R. Giral, J. Calvente, and L. Martinez-Salamero, “Mathematical analysis of hybrid topologies efficiency for PEM fuel cell power systems design,” *International Journal of Electrical Power & Energy Systems*, vol. 32, no. 9, pp. 1049–1061, Nov. 2010, doi: 10.1016/j.ijepes.2010.01.032.

[106] Y. Zhan, Y. Guo, J. Zhu, and L. Li, “Performance comparison of input current ripple reduction methods in UPS applications with hybrid PEM fuel cell/supercapacitor power sources,” *International Journal of Electrical Power & Energy Systems*, vol. 64, pp. 96–103, Jan. 2015, doi: 10.1016/j.ijepes.2014.07.020.

[107] Y. Zhan, H. Wang, and J. Zhu, “Modelling and control of hybrid UPS system with backup PEM fuel cell/battery,” *International Journal of Electrical Power & Energy Systems*, vol. 43, no. 1, pp. 1322–1331, Dec. 2012, doi: 10.1016/j.ijepes.2012.03.046.

[108] E. Irmak and N. Güler, “Application of a boost based multi-input single-output DC/DC converter,” in *2017 IEEE 6th International Conference on Renewable Energy Research and Applications (ICRERA)*, Nov. 2017, pp. 955–961. doi: 10.1109/ICRERA.2017.8191200.

[109] “Fuel Cells,” *Energy.gov*. https://www.energy.gov/eere/fuelcells/fuel-cells (accessed Jul. 30, 2021).

[110] S. C.-R. [1], A. Colmenar-Santos, C. Perez-Molina, and F. Mur-Perez, “A hydrogen refuelling stations infrastructure deployment for cities supported on fuel cell taxi roll-out,” *Energy*, vol. 148, pp. 1018–1031, 2018.

[111] [2] M. Iordache, D. Schitea, and I. Iordache, “Hydrogen refuelling station infrastructure roll-up, an indicative assessment of the commercial viability and profitability in the Member States of Europe Union,” *International Journal of Hydrogen Energy*, vol. 42, no. 50, pp. 29629–29647, 2017.

[112] M. J. Hodgson, “A Flow-Capturing Location-Allocation Model,” *Geographical Analysis*, vol. 22, no. 3, pp. 270–279, 1990, doi: https://doi.org/10.1111/j.1538-4632.1990.tb00210.x.

[113] M. J. Hodgson and K. E. Rosing, “A network location-allocation model trading off flow capturing andp-median objectives,” *Ann Oper Res*, vol. 40, no. 1, pp. 247–260, Dec. 1992, doi: 10.1007/BF02060480.

[114] M. Kuby and S. Lim, “The flow-refueling location problem for alternative-fuel vehicles,” *Socio-Economic Planning Sciences*, vol. 39, no. 2, pp. 125–145, Jun. 2005, doi: 10.1016/j.seps.2004.03.001.

[115] I. Capar and M. Kuby, “An efficient formulation of the flow refueling location model for alternative-fuel stations,” *IIE Transactions*, vol. 44, no. 8, pp. 622–636, Aug. 2012, doi: 10.1080/0740817X.2011.635175.

[116] S. A. MirHassani and R. Ebrazi, “A Flexible Reformulation of the Refueling Station Location Problem,” *Transportation Science*, vol. 47, no. 4, pp. 617–628, Sep. 2012, doi: 10.1287/trsc.1120.0430.

[117] M. Kuby and S. Lim, “Location of Alternative-Fuel Stations Using the Flow-Refueling Location Model and Dispersion of Candidate Sites on Arcs,” *Netw Spat Econ*, vol. 7, no. 2, pp. 129–152, Jun. 2007, doi: 10.1007/s11067-006-9003-6.

[118] I. Capar, M. Kuby, V. J. Leon, and Y.-J. Tsai, “An arc cover–path-cover formulation and strategic analysis of alternative-fuel station locations,” *European Journal of Operational Research*, vol. 227, no. 1, pp. 142–151, May 2013, doi: 10.1016/j.ejor.2012.11.033.

[119] C. Upchurch, M. Kuby, and S. Lim, “A Model for Location of Capacitated Alternative-Fuel Stations,” *Geographical Analysis*, vol. 41, no. 1, pp. 85–106, 2009, doi: https://doi.org/10.1111/j.1538-4632.2009.00744.x.

[120] R. L. Church, “COBRA: A New Formulation of the Classic p-Median Location Problem,” *Annals of Operations Research*, vol. 122, no. 1, pp. 103–120, Sep. 2003, doi: 10.1023/A:1026142406234.

[121] W. Zeng, I. Castillo, and M. J. Hodgson, “A Generalized Model for Locating Facilities on a Network with Flow-Based Demand,” *Netw Spat Econ*, vol. 10, no. 4, pp. 579–611, Dec. 2010, doi: 10.1007/s11067-008-9073-8.

[122] Y.-W. Wang and C.-C. Lin, “Locating road-vehicle refueling stations,” *Transportation Research Part E: Logistics and Transportation Review*, vol. 45, no. 5, pp. 821–829, Sep. 2009, doi: 10.1016/j.tre.2009.03.002.

[123] Y.-W. Wang and C.-R. Wang, “Locating passenger vehicle refueling stations,” *Transportation Research Part E: Logistics and Transportation Review*, vol. 46, no. 5, pp. 791–801, Sep. 2010, doi: 10.1016/j.tre.2009.12.001.

[124] T. Ma, J. Zhao, S. Xiang, Y. Zhu, and P. Liu, “An Agent-Based Training System for Optimizing the Layout of AFVs’ Initial Filling Stations,” *JASSS*, vol. 17, no. 4, p. 6, 2014.

[125] J.-G. Kim and M. Kuby, “The deviation-flow refueling location model for optimizing a network of refueling stations,” *International Journal of Hydrogen Energy*, vol. 37, no. 6, pp. 5406–5420, Mar. 2012, doi: 10.1016/j.ijhydene.2011.08.108.

[126] J. J. Brey, A. F. Carazo, and R. Brey, “Using AHP and binary integer programming to optimize the initial distribution of hydrogen infrastructures in Andalusia,” *International Journal of Hydrogen Energy*, vol. 37, no. 6, pp. 5372–5384, Mar. 2012, doi: 10.1016/j.ijhydene.2011.08.040.

[127] F. Ferdowsi and M. Nasiri, “Refueling station location problem under uncertain environment,” *Annals of Optimization Theory and Practice*, vol. 1, no. 2, pp. 35–45, May 2018, doi: 10.22121/aotp.2018.129441.1012.

[128] M. Miralinaghi, Y. Lou, B. B. Keskin, A. Zarrinmehr, and R. Shabanpour, “Refueling station location problem with traffic deviation considering route choice and demand uncertainty,” *International Journal of Hydrogen Energy*, vol. 42, no. 5, pp. 3335–3351, Feb. 2017, doi: 10.1016/j.ijhydene.2016.12.137.

[129] F. C. Fang and N. Torres, “Analysis of hydrogen station network using geographic information systems,” in *2011 14th International IEEE Conference on Intelligent Transportation Systems (ITSC)*, Oct. 2011, pp. 834–839. doi: 10.1109/ITSC.2011.6082933.

[130] D. Messaoudi, N. Settou, B. Negrou, S. Rahmouni, B. Settou, and I. Mayou, “Site selection methodology for the wind-powered hydrogen refueling station based on AHP-GIS in Adrar, Algeria,” *Energy Procedia*, vol. 162, pp. 67–76, Apr. 2019, doi: 10.1016/j.egypro.2019.04.008.

[131] A. Shukla, J. Pekny, and V. Venkatasubramanian, “An optimization framework for cost effective design of refueling station infrastructure for alternative fuel vehicles,” *Computers & Chemical Engineering*, vol. 35, no. 8, pp. 1431–1438, Aug. 2011, doi: 10.1016/j.compchemeng.2011.03.018.

[132] Z. Lin, J. Ogden, Y. Fan, and C.-W. Chen, “The fuel-travel-back approach to hydrogen station siting,” *International Journal of Hydrogen Energy*, vol. 33, no. 12, pp. 3096–3101, Jun. 2008, doi: 10.1016/j.ijhydene.2008.01.040.

[133] C. Upchurch and M. Kuby, “Comparing the p-median and flow-refueling models for locating alternative-fuel stations,” *Journal of Transport Geography*, vol. 18, no. 6, pp. 750–758, Nov. 2010, doi: 10.1016/j.jtrangeo.2010.06.015.

[134] Y. Honma and M. Kuby, “Node-based vs. path-based location models for urban hydrogen refueling stations: Comparing convenience and coverage abilities,” *International Journal of Hydrogen Energy*, vol. 44, no. 29, pp. 15246–15261, Jun. 2019, doi: 10.1016/j.ijhydene.2019.03.262.

[135] Y. Li, F. Cui, and L. Li, “An integrated optimization model for the location of hydrogen refueling stations,” *International Journal of Hydrogen Energy*, vol. 43, no. 42, pp. 19636–19649, Oct. 2018, doi: 10.1016/j.ijhydene.2018.08.215.

[136] A. Maleki and M. A. Rosen, “Design of a cost-effective on-grid hybrid wind–hydrogen based CHP system using a modified heuristic approach,” *International Journal of Hydrogen Energy*, vol. 42, no. 25, pp. 15973–15989, Jun. 2017, doi: 10.1016/j.ijhydene.2017.01.169.

[137] A. A. Pesaran, G. Kim, and J. D. Gonder, “PEM Fuel Cell Freeze and Rapid Startup Investigation,” p. 204, 2005.

[138] “Instruction manual of the North–East Frontier Railway, Indian railway.”

[139] “[IRFCA] Indian Railways FAQ: Rolling Stock - III (Weight Comparison Tables).” https://www.irfca.org/faq/faq-stock3.html (accessed Feb. 09, 2021).

[140] “https://indiarailinfo.com”.

[141] X. Wu, B. Cao, X. Li, J. Xu, and X. Ren, “Component sizing optimization of plug-in hybrid electric vehicles,” *Applied Energy*, vol. 88, no. 3, pp. 799–804, Mar. 2011, doi: 10.1016/j.apenergy.2010.08.018.

[142] “Section 3.4 Fuel Cells – Department of Energy.” [Online]. Available: https:// www. energy. gov/ sites/prod/ files/ 2016/06/f32/fcto_myrdd_fuel_cells_0.pdf

[143] J. Kennedy and R. Eberhart, “Particle swarm optimization,” in *Proceedings of ICNN’95 - International Conference on Neural Networks*, Nov. 1995, vol. 4, pp. 1942–1948 vol.4. doi: 10.1109/ICNN.1995.488968.

[144] Y. Shi and R. Eberhart, “A modified particle swarm optimizer,” in *1998 IEEE International Conference on Evolutionary Computation Proceedings. IEEE World Congress on Computational Intelligence (Cat. No.98TH8360)*, May 1998, pp. 69–73. doi: 10.1109/ICEC.1998.699146.

[145] E. Zitzler, M. Laumanns, and L. Thiele, “SPEA2: Improving the strength pareto evolutionary algorithm,” Eidgenössische Technische Hochschule Zürich (ETH), Institut für Technische Informatik und Kommunikationsnetze (TIK), Working Paper, 2001. doi: 10.3929/ethz-a-004284029.

[146] S. Ganguly, N. C. Sahoo, and D. Das, “Mono- and multi-objective planning of electrical distribution networks using particle swarm optimization,” *Applied Soft Computing*, vol. 11, no. 2, pp. 2391–2405, Mar. 2011, doi: 10.1016/j.asoc.2010.09.002.

[147] H. Dean Venable, “The K factor: a new mathematical tool for stability analysis and synthesis,” presented at the 10th Proceedings of POWERCON, 1983.

[148] “Manual of NEXA 1200 PEMFC system.” https://www.ien.eu/uploads/tx_etim/Datenblatt_Nexa1200_EN _1109.pdf

[149] V. Sezer, M. Gokasan, and S. Bogosyan, “A Novel ECMS and Combined Cost Map Approach for High-Efficiency Series Hybrid Electric Vehicles,” *IEEE Transactions on Vehicular Technology*, vol. 60, no. 8, pp. 3557–3570, Oct. 2011, doi: 10.1109/TVT.2011.2166981.

[150] “ADVISOR Documentation.” http://adv-vehicle-sim.sourceforge.net/advisor_doc.html (accessed Apr. 22, 2021).

[151] S. Ebbesen, P. Elbert, and L. Guzzella, “Battery State-of-Health Perceptive Energy Management for Hybrid Electric Vehicles,” *IEEE Transactions on Vehicular Technology*, vol. 61, no. 7, pp. 2893–2900, Sep. 2012, doi: 10.1109/TVT.2012.2203836.

[152] M. Singh, J. Moore, and W. Shadis, “Hydrogen Demand, Production, and Cost by Region to 2050,” 2005.

[153] M. Melaina and M. Penev, “Hydrogen Station Cost Estimates: Comparing Hydrogen Station Cost Calculator Results with other Recent Estimates,” National Renewable Energy Lab. (NREL), Golden, CO (United States), NREL/TP-5400-56412, Sep. 2013. doi: https://doi.org/10.2172/1260510.

[154] J. Kennedy and R. C. Eberhart, “A discrete binary version of the particle swarm algorithm,” in *Computational Cybernetics and Simulation 1997 IEEE International Conference on Systems, Man, and Cybernetics*, Oct. 1997, vol. 5, pp. 4104–4108 vol.5. doi: 10.1109/ICSMC.1997.637339.

[155] Y. P. Mathur, R. Kumar, and A. Pawde, “A binary particle swarm optimisation for generating optimal schedule of lateral canals,” *The IES Journal Part A: Civil & Structural Engineering*, vol. 3, no. 2, pp. 111–118, May 2010, doi: 10.1080/19373261003619936.

[156] “HydroFLEX Hydrogen-powered Train, United Kingdom.” https://www.railway-technology.com/projects/hydroflex-hydrogen-train (accessed Mar. 09, 2021).

[157] “Northeast India,” *Wikipedia*. Jul. 27, 2021. Accessed: Jul. 27, 2021. [Online]. Available: https://en.wikipedia.org/w/index.php?title=Northeast_India&oldid=1035724260

[158] “Green hydrogen costs projected to decrease by up to 60% by 2030,” *pv magazine International*. https://www.pv-magazine.com/2020/01/28/green-hydrogen-costs-projected-to-decrease-by-up-to-60-by-2030/ (accessed Jul. 30, 2021).

[159] C. Tarhan and M. A. Çil, “A study on hydrogen, the clean energy of the future: Hydrogen storage methods,” *Journal of Energy Storage*, vol. 40, p. 102676, Aug. 2021, doi: 10.1016/j.est.2021.102676.

[160] R. Moradi and K. M. Groth, “Hydrogen storage and delivery: Review of the state of the art technologies and risk and reliability analysis,” *International Journal of Hydrogen Energy*, vol. 44, no. 23, pp. 12254–12269, May 2019, doi: 10.1016/j.ijhydene.2019.03.041.

[161] S. Niaz, T. Manzoor, and A. H. Pandith, “Hydrogen storage: Materials, methods and perspectives,” *Renewable and Sustainable Energy Reviews*, vol. 50, pp. 457–469, Oct. 2015, doi: 10.1016/j.rser.2015.05.011.

[162] E. Rivard, M. Trudeau, and K. Zaghib, “Hydrogen Storage for Mobility: A Review,” *Materials*, vol. 12, no. 12, Art. no. 12, Jan. 2019, doi: 10.3390/ma12121973.

Lists of Publications

Journals:

[1] U. Sarma and S. Ganguly, “Determination of the component sizing for the PEM fuel cell-battery hybrid energy system for locomotive application using particle swarm optimization,” *Journal of Energy Storage*, vol. 19, pp. 247-259, 2018.

[2] U. Sarma and S. Ganguly, “Design optimisation for component sizing using multi-objective particle swarm optimisation and control of PEM fuel cell-battery hybrid energy system for locomotive application,” *IET Electrical Systems in Transportation*, vol. 10, pp. 52-61, 2020.

Conferences:

[1] U. Sarma and S. Ganguly, "Determination of Rating Requirement for Fuel-Cell-Battery Hybrid Energy System to Substitute the Diesel Locomotives of Indian Railway," *2017 14th IEEE India Council International Conference (INDICON)*, Roorkee, 2017, pp. 1-6.

[2] U. Sarma and S. Ganguly, "Modelling and cost-benefit analysis of PEM fuel-cell-battery hybrid energy system for locomotive application," *2018 Technologies for Smart-City Energy Security and Power (ICSESP)*, Bhubaneswar, 2018, pp. 1-5.

[3] U. Sarma and S. Ganguly, "Modelling of the PEM Fuel Cell and Design of a Closed Loop Control Based DC-DC Boost Converter for Locomotive Application," *2019 IEEE Milan PowerTech*, Milan, Italy, 2019, pp. 1-6.

[4] U. Sarma and S. Ganguly, “Modelling of the PEM fuel cell and design of a peak current control based DC-DC boost converter for locomotive application,” *2019 IEEE Transportation Electrification Conference (ITEC-India)*, Dec. 2019, pp. 1–6.

[5] U. Sarma, S. Ganguly, and A. Dutta, “Determination of the component sizes and analysis of the operational cost of PEM Fuel Cell-Battery Hybrid Energy System to Retrofit the Diesel Locomotives of Indian Railway,” *2019 8th International Conference on Power Systems (ICPS)*, Dec. 2019, pp. 1–6.

Submitted journals:

[1] U. Sarma and S. Ganguly, “Optimal allocation planning of hydrogen refueling stations for running hydrogen powered locomotives in Indian railway using multi-objective particle swarm optimization,” submitted to *Journal of Rail Transport Planning & Management.*

[2] U. Sarma and S. Ganguly, “An Energy Management Optimization Approach for PEM Fuel Cell-Battery Hybrid Energy System for Railway Applications,” submitted to *Journal of Energy Storage.*

[3] U. Sarma and S. Ganguly, “An Optimization Based Energy Management Strategy for PEM Fuel Cell-Battery Hybrid Energy System for Locomotive Applications,” submitted after first revision to *Transactions of the Indian National Academy of Engineering.*

[4] U. Sarma and S. Ganguly, “Allocation planning of the hydrogen refueling stations for the deployment of hydrogen powered locomotives in Indian North East Frontier Railway,” submitted to *Transactions of the Indian National Academy of Engineering.*

Author's Biography

Upasana Sarma was born on 8 October 1991 at Nagaon in Assam, India. She obtained Bachelor of Technology degree in Electrical Engineering from National Institute of Technology, Silchar in 2014. She received Master of Technology degree in Power and Energy Systems Engineering from National Institute of Technology, Silchar in 2016. She joined the Ph.D. programme in the Department of Electronics and Electrical Engineering, Indian Institute of Technology Guwahati in 2016. Her research interest includes the fuel cell and renewable energy, hybrid energy system, energy management approaches, e-mobility, power system, soft computing and optimization, etc.